Numerical investigation of the flow-body interaction of thin flexible foils and ambient flow

by

Benjamin S.H. Connell

Submitted to the Department of Mechanical Engineering
in partial fulfillment of the requirements for the degree of

Doctor of Philosophy in Ocean Engineering

at the

MASSACHUSETTS INSTITUTE OF TECHNOLOGY

June 2006

Author ....
Department of Mechanical Engineering
February 24, 2006

Certified by ....
Dick K.P. Yue
Professor of Mechanical and Ocean Engineering
Thesis Supervisor

Accepted by ....
Lallit Anand
Chairman, Department Committee on Graduate Students

Numerical investigation of the flow-body interaction of thin flexible foils and ambient flow

by

Benjamin S.H. Connell

Submitted to the Department of Mechanical Engineering
on February 24, 2006, in partial fulfillment of the
requirements for the degree of
Doctor of Philosophy in Ocean Engineering

Abstract

Flow-induced flapping of flexible thin bodies is oft observed in our day-to-day lives in phenomena such as flag flapping, and is important in a host of engineering applications. Despite its prevalence, however, this fundamental problem of fluid-structure interaction is not very well understood. Use of flexible control surfaces in ocean vehicles holds promise for achieving the efficiencies and maneuverability of waterborne animals, but requires an understanding of the natural responses of flexible foils and the associated physics. Likewise, industrial applications such as the handling of flexible textiles and paper benefit from improved understanding of the relationship between the system parameters and the anticipated response of the body. The present work furthers the understanding of the passive flapping problem through the development and application of a nonlinear computational simulation capability. Examining the flapping problem over a wide range of system parameters and responses indicates the influences and trends of the system behavior, and allows investigation of relevant physical mechanisms in the fluid-structure interaction.

To pursue this study, the fluid-structure direct simulation (FSDS) capability is developed, coupling a Navier-Stokes fluid-dynamic solver to a geometrically nonlinear thin-body structural solver. The coupled solver is developed in both two dimensions and three dimensions, where the thin foil is free to spanwise variation as a nonlinear plate. The viscous fluid dynamics are solved on a moving grid fitted to the structural boundary. Fluid forcing to the structure is calculated at this boundary and used as external forcing to the structural equations of motion. As both the fluid dynamic and structural solvers use fully implicit backwards difference time integration, they must be solved simultaneously. An iterative approach is used for the simultaneous solution, converging to structural equilibrium with a divergence-free flow field.

A detailed study of the canonical problem of a thin flexible foil in uniform flow is first performed in two dimensions, using linear analysis and FSDS simulation, and examining the stability and natural responses as a function of the system parameters. The three relevant nondimensional parameters governing the problem are the Reynolds number, $Re = VL/\nu$; the structure-to-fluid mass ratio, $\mu = \rho_s h/(\rho_f L)$;

and the nondimensional bending rigidity, $K_B = EI/(\rho_f V^2 L^3)$. The flag problem, which has been the subject of recent experimental and numerical studies, is at the limit of vanishing bending rigidity, where the physics are governed by the two parameters of Reynolds number and mass ratio. We find stability of the system to increase for decreasing Reynolds number, decreasing mass ratio, and increasing bending rigidity. Three distinct regimes of response are observed, (I) fixed-point stability, (II) limit-cycle flapping, and (III) chaotic flapping, in order of decreasing stability. Characteristics of the dynamic interaction between the fluid and structure are considered with the modal response and associated flow wake, and the mechanics of the significant physical phenomena of stability hysteresis and chaotic snapping are investigated in detail. The linear analysis is extended to examine the stability of the three-dimensional problem and indicates an increase in stability with spanwise wavenumber. Simulations confirm the relationship between spanwise variation and stability, and display the three-dimensional flapping response and associated wake. Fundamental three-dimensional modes of a spanwise standing wave, spanwise traveling wave, and two-dimensional flapping are revealed along with their unique wake patterns, and the evolution of the system to hybrid modes is displayed.

Through this work, we identify for the first time the relationship between the relevant nondimensional parameters of the passive flapping system and the response through the three distinct regimes. The comprehensive study provides new understanding of the physical mechanisms associated with the regime transitions and the flapping dynamics, including chaotic snapping. FSDS allows a first investigation of the three-dimensional passive flapping problem, identifying the stability characteristics and modes of response. The detailed examination and enhanced understanding of the relationship between the relevant nondimensional parameters and the kinematics, forcing, and wake characteristics for the system of a passive flexible foil in uniform flow allows for better engineering of flexible foils for both passive and active applications.

Thesis Supervisor: Dick K.P. Yue
Title: Professor of Mechanical and Ocean Engineering

Acknowledgments

I would first like to thank Professor Dick K.P. Yue for his excellent guidance in this research, and in the course of my studies at MIT. I am also very grateful to the other members of the thesis committee, Professor Michael S. Triantafyllou and Dr. Franz S. Hover of MIT, Professor George E. Karniadakis of Brown University, and Professor Lian Shen of Johns Hopkins University, who have all been very helpful and generous with their time.

Thank you to the people who helped me get organized and on track with my early research at MIT, Susan Brown, Xiang Zhang, and Len Imas. I received extensive guidance throughout my research from Kelli Hendrickson, Lian Shen, and Yuming Liu, and I am very appreciative of the time and effort that entailed. Particular thanks to Kelli for putting up with the occasional appearance of my stubborn side in discussing some of the finer points of CFD, and whatever else. Thanks also to Alex Techet, who was always good to talk to about vortices, and has the good sense to drop everything and throw a party once in a while. I'd like to thank the array of office-mates who were always good for a chat, Sean, Kelli, and the series of Matts (Walter, Watts, Unger) who have cycled through recently. I am indebted to the people who have held together the VFRL lab and who never get appreciated enough, particularly Kelli Hendrickson and Guangyu Wu, and also to George Papaioannou who somehow tackled the Microway cluster. Thanks to all the people of the VFRL lab, towtank, and water tunnel, who are a terrific bunch to talk hydro with.

I'd like to thank my family (who seem to value over-education) for always offering the right amount of encouragement and advice through this process. I'm very happy with course I've taken so far in my adult life, and I credit my parents, brother, and sister for shaping my decision making process. Thank you to my in-laws, the Jauchs, for their support and patience, and for never asking when I'm finishing. Of course, a resounding thank you to my wife, Cristina, whose support never foundered, and whose patience is seemingly infinite. She is an inspiration to me for so many reasons, most recently for bringing forth our beautiful little Estelle.

This research was supported by the Office of Naval Research, in part through the National Defense Science and Engineering Graduate Fellowship Program of the American Society for Engineering Education. Many thanks to these agencies for their support.

Contents

List of Figures

List of Tables

Chapter 1

Introduction

1.1 Motivation

Many problems of interest to ocean engineers involve the characteristics of the interaction between a body and the surrounding fluid. Historically, the approach to design has been through steady flow considerations. These considerations resulted in streamlined ships and underwater vessels with design of propulsors and control surfaces following steady flow assumptions. Though allowances were certainly made for performance in unsteady conditions (surface waves, maneuvering, etc.), the characteristics of the unsteady hydrodynamics have not been understood well enough to allow for their exploitation in design.

The value of understanding the unsteady hydrodynamics about an engineered body in some key problems of ocean engineering is clear. In displaying the distinct advantage in terms of propulsive efficiency associated with swimming animals, Sir James Gray in 1936 triggered an interest in the physical mechanisms associated with fish-like swimming [25]. It was apparent that biological evolution had arrived at an efficient method of propulsion based on unsteady hydrodynamics which are only now becoming understood. Another realm of unsteady hydrodynamics of great interest to ocean engineers involves harmonic forcing of offshore structures (flow-induced oscillation), particularly those associated with oil-drilling operations. As engineering limits continue to be pushed by the oil industry, a greater understanding of the potential harmonic loading on the structures is needed to ensure safety and economy.

A problem presented to an ocean engineer involving the interaction between a body and its surrounding fluid will always be constrained by conservation of energy and conservation of momentum. The design challenge to the engineer is likely to be some optimization within these limits. For instance, an underwater vehicle would ideally maximize the desired momentum imparted to the body with a minimum of energy expenditure. To realize such optimization, the structural characteristics of the body must be considered. The purpose of the present study is to gain insight into the mechanisms of momentum and energy exchange between a flexible thin foil and the surrounding fluid. An enhanced understanding of the natural response of such a body in a flow enables structural tuning of flexible foils in engineering practice.

1.2 Previous Studies

The lack of full understanding of many problems involving unsteady viscous hydrodynamics comes from the difficulty involved in performing the investigations. As evolution in technology continues to advance both experimental and computational capabilities, further studies are performed which feed back to engineering designs.

The previously mentioned realms of fish-like swimming and flow-induced oscillation have both been the focus of a number of research projects throughout the past forty years. There are many very rich realizations of the problems which have been studied both experimentally and computationally. An extensive overview of relevant prior work is covered in Chapter 2.

The studies of flow-induced oscillation usually involve free kinematics, where the body motion results from hydrodynamic forcing and the body structural properties. The fish-like swimming studies, on the other hand, involve imposed kinematics. A gap exists in the study of vorticity control for desired momentum transfer (fish-like swimming) through the tuning of an elastically responding body.

1.3 Objective

As a flexible body is moving within a flow field, there is an ongoing exchange of energy between the body and the surrounding fluid. Hydrodynamic energy can be stored in the structure and released at a later time. Structural energy can be moved to a new location on the body by release and recovery in a convecting flow field.

Taking the study of vortical flow control beyond the realm of strict body kinematics and into the realm of fluid-structure interaction should change the engineering approach. Instead of a problem of direct actuation of the kinematics, the approach should involve exploitation of resonant behavior and tuned energy exchange.

Some of the most basic canonical problems of the energy exchange between large-scale vorticity and flexible structures have yet to be studied in detail. The present study uses a simple structure, a thin flexible foil, and examines the natural responses in a uniform inflow. The intention is to gain an understanding of the behavior of the flow-body interaction, the natural modal response and dynamic interaction. Such knowledge of how the fluid and structure will interact is paramount to exploiting the characteristics of the system for engineering purposes.

While suppression of the onset of turbulence is one possible consequence of the manipulation of the near-body vortical flow field, this is beyond the scope of the proposed work. The focus of the proposed study is to be the interaction of large-scale vortical structures with a flexible body.

1.4 The Computational Approach

In order to pursue this study, we develop a coupled fluid-structure direct simulation (FSDS). The fluid-dynamic direct simulation (FDS) is a finite-difference solution to the Navier–Stokes equations solved on a grid fitted to a mobile thin body. Fluid-dynamic forcing on the body surface is calculated and used as input to a finite-difference structural-dynamic direct simulation (SDS). The structural solver is geometrically nonlinear, able to take on arbitrary configurations. Both the FDS and SDS are implicit, requiring iteration between the two for convergence at each time step.

The FDS is an implicit direct solution to the Navier–Stokes equations using primitive variables $(p, \boldsymbol{v})$ on a moving collocated grid. An O-grid is used for calculation of the equations of motion in cartesian form, and the transformation of these equations from physical to computational space accommodates the motion of the grid. As the simulation is of a very thin body, grid clustering must be used at the body ends to allow smooth calculation around these sharp edges. Grid generation is through an elliptic solver, with clustering source terms calculated from an algebraically generated grid. A full description and derivation of the FDS approach are given in Chapter 3.

The SDS is an implicit structural solver designed to allow arbitrary orientation and configuration of the thin body, and offer stability through a range of external forcing scenarios. While the primary interest is in inextensible bodies, finite extensional rigidity is incorporated into the SDS to ensure a robust capability able to accommodate loss of positive tension. The equations of motion are derived in cartesian coordinates using Hamilton's Principle, linearizing around small body thickness and extensional strain. Coupling of the SDS to the FDS for an implicit FSDS simulation uses an iterative approach for simultaneous convergence of the two solvers. An assumed added mass is used in the iterative procedure to stabilize the system for cases of very low structural mass. A full description and derivation of the SDS approach and the coupling to the FDS are given in Chapter 4.

Extensive verification and validation of the components of the numerical model is performed. This consists of individual consideration of the FDS and SDS, as well as the coupled FSDS. A number of different comparisons are made to previous experimental and computational studies, displaying the physical accuracy and robustness of the simulation. Convergence testing is made with both the FDS and SDS, displaying the second-order or near second-order convergence of the error with both time step and grid size. This validation of the numerical model is detailed in Chapter 5.

1.5 Natural Response of a Flexible Foil

An extensive study into the natural response of the thin foil in a uniform inflow is performed in two dimensions. An understanding of the relevant nondimensional parameters, and their influence to the system is gained through a linear analysis of the coupled system. A systematic series of FSDS simulations is then performed, using the linear analysis for guidance.

In the 'flag' limit of very low bending rigidity, the restoring force is dominated by the flow-induced tension in the body. The linear analysis indicates that in this limit the parameters guiding the problem are the ratio of structural to fluid mass, and the Reynolds number. We find that, for a fixed Reynolds number $O(10^3)$, increasing the mass ratio transitions the system through three distinct regimes of response. For the lowest mass ratios the foil is stable straight. Intermediate mass ratios experience period-one limit-cycle flapping, increasing in amplitude with mass ratio. Higher mass ratios experience chaotic flapping, with transition to chaos occurring when the Strouhal number reaches $St \simeq 0.2-0.3$, the natural wake frequency. Chaotic flapping includes intermittent snapping events marked by loss of positive tension and dynamic buckling. Both lower Reynolds number and higher bending rigidity are predicted to increase the stability of the system by increasing the restoring force, and the FSDS results confirm this behavior with an upward shift to the critical mass ratios. The full two-dimensional analysis and FSDS results presentation are covered in Chapter 6.

The stability analysis is extended to the three-dimensional problem in Chapter 7, indicating the influence of three-dimensionality on the problem. It is shown that strictly two-dimensional modes are the least stable, with stability increasing with increasing spanwise wavenumber. A targeted set of three-dimensional FSDS simulations confirm the stability prediction, while indicating the natural three-dimensional responses of the passive flapping system. Fundamental flapping modes of spanwise standing wave, spanwise travelling wave, and two-dimensional flapping are found, with natural response of the system including hybrid modes. The description of the three-dimensional analysis and interpretation of the FSDS-3D results is given in

Chapter 7

The analyses and results of Chapters 6 and 7 present the relationship between the relevant nondimensional parameters and response of the system of a passive thin foil in a uniform stream. The responses include the fixed-point stability, limit-cycle flapping, and chaotic flapping, as well as the onset and characterization of three-dimensional flapping modes. An understanding of the relationship of the natural response to the system parameters is important to a host of engineering problems, allowing design to specific regimes. Opportunities for further work on this problem with the FSDS capability exist, particularly in further exploring the three-dimensional flapping evolution, and in studying the role of flexibility with driven flapping foils.

Chapter 2

Background

As computational and experimental capabilities have advanced, numerous doors have opened, allowing the study of a host of problems involving unsteady interaction of bodies and the surrounding fluid. Two major considerations for unsteady flow about a body concern the study of fish-like swimming and the study of flow-induced oscillation. Historically, these two realms have been treated independently. As the present work involves a fusion of these two categories, there are many relevant past studies concerning both. The following listing and descriptions of previous work are meant to set the context, displaying how the present work fits into communal engineering goals.

2.1 Flow-induced Oscillation

2.1.1 Overview

The study of flow-induced oscillation of elastic bodies has seen significant attention, owing to the necessity of its consideration in a host of engineering situations. From the waving of a flag to the famous collapse of the Tacoma Narrows Bridge to fatigue on a vibrating car antenna to the annoying slapping of halyards on flagpoles and sailboat masts, the consequences of flow-induced oscillations surround us. Engineers designing buildings, bridges, and offshore structures have to be very cognizant of the phenomena of flow-induced oscillation, and design accordingly. The importance of these problems is reflected by the content of the *Journal of Fluids and Structures*, much of which is dedicated to these types of problems. Robert Blevins' 1977 volume *Flow-induced Vibration*, updated and republished in 1990 [10], gives an excellent description of the causes for flow induced vibration, associated problems and solutions. There is seemingly no end to the types of flow-induced oscillation problems encountered by engineers, many of them in ocean engineering.

2.1.2 Vortex-induced Vibration (VIV)

A good deal of the work in flow-induced oscillations has to do with unsteady forcing deriving from vortex shedding from a bluff body. At many engineering Reynolds numbers, the stable wake configuration of a bluff body in steady flow derives from the alternate shedding of vortices from the top and bottom of the body. This periodic alternate shedding results in a strong oscillating lift force, with a weaker oscillatory component to the drag force. Clearly, if the natural frequency of oscillation of an elastic body is close to the frequency of unsteady hydrodynamic forcing, there is potential for large, possibly damaging, oscillations. In fact, when the frequencies are in the same neighborhood, the vortex shedding and resulting oscillatory forcing adopts the natural frequency of the structure, a phenomenon called *lock-in.* Experimental and numerical studies displaying these phenomena are covered in a 1979 review by Sarpkaya [52] and a 1984 review by Bearman [7]. One early study of particular interest is a 1967 experimental investigation by Koopmann [33]. Conducting experiments with a driven oscillating cylinder Koopmann accomplished remarkably clear flow visualization displaying the changes to the vortex wake structure due to the cylinder motion.

The recent work in VIV benefits significantly from current advancement of computational capabilities [36]. These advances now allow for fully 3D turbulent viscous simulations of flow about flexible cylinders undergoing vortex-induced vibration. The work of Blackburn et. al. [9] displays that computational capabilities have moved us into the realm where 3D viscous simulations can be compared to experiments performed at the equivalent Reynolds number.

Earlier experimental work by Brika et. al. [11] investigated the free oscillation amplitude of a flexible cylinder as the shedding frequency was adjusted up to and past the structural natural frequency. The vortex wake associated with different responses was considered. Viscous numerical simulations of such a flexible cylinder at low Reynolds numbers were later performed by Newman and Karniadakis [44]. These simulations expanded considerably the capabilities of flow visualization and force determination. A very detailed study of the three dimensional structure of the wake associated with the different responses was performed. Evangelinos et. al. extended this investigation to higher, turbulent, Reynolds numbers, allowing for comparison with an empirically determined formula used for drag prediction in engineering [19].

This work in vortex-induced vibration shows how the relationship between the natural frequency of the structure and the natural frequency of fluid affects the response and downstream flow pattern. Combinations of different flow patterns about a single body are shown to exist in cases of tapered bodies [60][28], and bodies in shear flows [41]. As the natural hydrodynamic frequency is a function of the body size and ambient flow, changing either of these should change the near-body flow structure. These studies look at the associated forcing, showing the manner in which variation of body form can influence the momentum exchange in the oscillation process. There is great value in such studies as the forcing implications that come from body form and structural properties can be used in engineering practice.

2.1.3 Flapping Bodies

The study of flapping bodies examines how a passive flexible body responds to a flow about it. An early study of Paidoussis [47] treats the problem of the stability and response of a flexible cylinder in axial flow, both theoretically and experimentally. He notes the destabilizing effect of increasing the flow velocity through what is essentially the Kelvin-Helmholtz instability, balanced against the restoring effect of tension and bending rigidity of the flexible body. Predictions and observation of a streamwise travelling-wave flapping solution are found, similar to the motion of swimming fish observed by Gray [24]. Paidoussis emphasizes the importance of the nonlinear effects neglected in the theoretical model when considering the unstable response of the experiments. Subsequent work of Triantafyllou [63] examines the nature of the travelling-wave linear instability in further detail. Coene [13] extends the Paidoussis theoretical analysis to that of a thin membrane. For this case, the contribution of the flow is different in that the added mass can no longer be considered sectionally with strip theory, but becomes a function of the mode of oscillation. The case of constant tension of the membrane is considered, and experiments are performed with paper strips pulled at both ends. Critical values of the tension, below which flapping is realized, are found experimentally to be in good agreement with theory. Two important considerations for the flag-flapping problem not incorporated in these studies are the interaction of the flow wake, and the varying tension along the length associated with the fluid-dynamic forcing.

Including the existence and influence of the flow wake adds considerable complexity to the theoretical treatment. Such an analysis including the shedding of wake vortices is presented by Argentina & Mahadevan [4]. The approach details a method for including finite-length effects, and analysis is given for a particular case which simplifies the formulation. Trends are predicted for the flapping frequency and critical flow speed above which flapping is realized. In this case the added mass is much smaller than the structural mass, the flow speed is much larger than the flapping velocity, and the bending rigidity dominates the structural restoring force, conditions which do not obtain for the regime of interest in the present study. Continued work with the wake effect linear formulation which broadens the scope of the analysis would contribute to understanding the physics of a larger class of flag-flapping problems.

The difficulties and assumptions of theoretical treatment are avoided through the use of experiments and numerical simulations. The experiment of Zhang *et al.* [76], using a filament in a flowing soap film, allowed the effects of wake flow and varying structural tension. Using a film to maintain two-dimensionality, the experiment observed both stable and unstable response, depending on the filament length. As length increased, the filament became unstable, displaying a streamwise travelling-wave response. The flapping amplitude was observed to diminish toward the leading edge, where the tension due to viscous forcing and gravity was highest. A length region of bistability was observed, where sufficiently large perturbation could transform the system from stable to unstable response. Flow visualization allowed a look at the near-body flow characteristics, and the vortical flow pattern in the wake. A sinuous pattern of alternating vorticity was observed on the scale of the body motion, consisting of a series of smaller-scale vortices alternating in sign with position in the wake.

Two distinct approaches to numerically simulating the Zhang soap film experiments have been made by Zhu & Peskin [79] [80] and Farnell *et al.* [21] [20]. The Farnell work treats the filament as pendulum of many links connected by springs and dashpots. Such treatment requires tuning of the model, and it is indicated that further work is required in determining the accuracy of the approach. The Zhu & Peskin numerical study uses the immersed boundary method to couple a nonlinear filament with bending and extensional rigidity to a Navier–Stokes solver. The study replicates the trends found in the experiment. These include the transition to unstable flapping for longer filaments and the existence of a bistable region. Flow visualization indicates that the small scale vortical structures observed in the experiment were not apparent in the simulations, an anticipated result with the Reynolds number having been reduced from 20 000 in the experiment to 200 in the simulation. It is noted that removing the filament mass results in an always stable filament. Beyond this observation, the variation parameter used for the soap film studies is the dimensional filament length.

The experimental investigation of paper flutter in a wind tunnel of Watanabe *et al.* [70] indicates the particular importance of this flapping problem to paper moving through a printing press. Through a series of experiments, the stabilizing effects of decreasing flow velocity, decreasing length, decreasing mass, and increasing bending rigidity were presented. Again, a bistable region was discovered in the transition from stable to unstable flapping modes. Increasing the flow speed from the critical point, the flapping amplitude and Strouhal number were found to increase, both approaching asymptotic values in the established flapping regime. While the Watanabe *et al.* experiments were performed in air, the recent work of Shelley *et al.* [54] details similar experiments performed in a water tunnel. These experiments in water required special treatment to bring the membrane mass up to a sufficient value to realize flapping. Similar results to those of the air experiments were found for stability, response, and bistability with varying the flow velocity.

There is still much to be done in terms of understanding the complex viscous hydrodynamics associated with flapping instabilities of both 2D and 3D bodies in flow. It is very likely that the structural characteristics of swimming animals exploit such flapping instabilities to minimize energy expenditure in swimming motion. Gaining a better understanding of this process is very important step to moving forward with engineering for fish-like swimming.

2.2 Flow Control

Flow control is at root of engineering hydrodynamics. Controlling the flow about an engineered body will control the hydrodynamic forcing, often a primary concern. Ship streamlining, for instance, serves to delay separation and reduce the drag force. Vehicle control surfaces are designed to create local hydrodynamic forces by inducing a lift force on a foil. These are examples of flow control through steady hydrodynamics. The characteristics of such problems have been studied in great detail. P.K. Chang's 1976 volume *Control of Flow Separation* [12] covers a wide range of topics and methods relating to control of flow about bodies from the steady flow perspective. Beyond the problem of profile design for controlled separation, there is also discussion of the effectiveness of active methods such as sucking/blowing for control of near-body flow.

Unsteady flow control concerns influencing the evolution of body-generated vorticity. The advantage of controlling the unsteady hydrodynamics has lead to a number of studies, described below. The majority of these are experimental or numerical, owing to the difficult nonlinear nature of the equations governing the physics.

2.2.1 Control of Vortex Interaction with Bodies

A key component to the proposed study is the idea of controlling the interaction of large-scale vortical flow with a flexible body. Consequently, topics of considerable importance include the manner in which vortices interact with bodies. A 1998 review by Rockwell [51] explains the mechanisms and consequences of different types of vortex-body interactions. The findings of a number of important numerical and experimental studies are covered. Of particular relevance to the proposed research is the parallel interaction of vortices with the body. The work of Gopalkrishnan et. al. [23] displayed the ability of a heaving and pitching foil to alter the organization of a parallel interacting vortex street in several different ways. The momentum transfer associated with each of the reorganizations is of particular interest.

The simplest form of parallel interaction is that of a vortex dipole incident on a wall. The interaction of the two vortices exerts a mutual influence that results in translation of the pair. As such, interaction of the vortices with the body is achieved without any body motion or external flow. As the vortices approach a no-slip boundary such as a wall, reverse vorticity is generated at the wall boundary layer. Pairing of the wall generated vorticity with each of the incident vortices eventually causes them to translate back up away from the wall. Koumoutsakos investigated control of this vortex rebound phenomenon with a 2D numerical study [34]. By measuring the pressure gradients on the wall to determine vorticity flux, blowing and suction were used to control the near-wall vorticity. The simulations displayed the clear manipulation that could be made to the flow, allowing annihilation of the vortices, or sustaining the attachment of the vortices to the wall.

A number of studies have examined the interaction of such a vortex dipole with the free surface [46][15][16]. These are interesting for the energy exchange between the vortices and the free surface elevation. A particularly relevant study of this problem by Tsai and Yue [67] included the effect of varying surface tension on the interaction. It was found that, in the case of nonconstant surface tension, the internal dynamics of the surface strongly affected the nature of the underlying flow. The achievable effects included strong generation of vorticity at the free surface. This study demonstrates that a tuning of the structural properties of the free surface can control the transformation of energy in the surface to vortical energy in the underlying flow. Such a phenomenon is analogous to the tuning of the structural properties of a body to direct the vorticity evolution.

2.2.2 Fish-like Swimming Overview

The human inclination to borrow engineering ideas from nature is much greater for things that we can't do than for things that we can. While early attempts at flight used biological models, we had long accomplished the feat of moving a vehicle through the water. With no pressing engineering need, the application of biological ideas to water vehicles was much more of a scientific pursuit. In the 1930's, Sir James Gray published his series of "Studies in animal locomotion" in the *Journal of Experimental Biology.* Among detailed study of the kinematics of swimming fish [24], this also included a power study of the swimming of a dolphin[25]. The results of this power study would become known as *Gray's Paradox*, the understanding of which continues to be a focal point for much research. Gray estimated the power generation capability of a dolphin and compared it to the power required to tow a rigid dolphin body. The power needed to tow the rigid body was found to be seven times the capability of the dolphin's muscles. The indication was that there was something fundamentally different about the unsteady motion of the body through the water which enabled much greater efficiency.

Subsequent numerical analyses were triggered by the work and interest of Gray. Early studies included slender-body approaches by G.I. Taylor in 1952 [57] and James Lighthill in 1960 [37]. T.Y. Wu, in 1961, published a 2D potential flow approach to the problem (treating the 2D fish as a waving plate) [75]. All of these early works explained mechanisms through which a waving motion can propel an aquatic body. The mechanisms for the 3D (Lighthill and Taylor) and 2D (Wu) explanations are, however, different. While the Lighthill and Taylor work describes transfer of momentum from a moving slender body to the fluid using hydrodynamic coefficients, the Wu model solves the inviscid governing equations with the appropriate boundary conditions to display the thrust wake generated behind a swimming body with large span. As detailed in a recent numerical study [82], both of these mechanisms are important, and play a role in the hydrodynamics of fish swimming. The analyses of Lighthill and Wu are the fundamentals of what is understood of the hydrodynamics of fish-like swimming, and continue to be points of reference for present-day experimentalists and computational fluid dynamicists.

A contrasting of Lighthill's 1969 review of work in fish-like swimming [38] and the subsequent 2000 review of Triantafyllou [66], displays the clear impact of technological advances on the capabilities for studying unsteady hydrodynamics. The Lighthill review has its focus heavily on observed fish kinematics and early simple numerical approaches (as the Lighthill, Taylor, and Wu models) to predict the hydrodynamic consequences. The Triantafyllou review describes recent work using modern experimental and computational techniques to gain a detailed understanding of the hydrodynamics about such swimming bodies. Experimental techniques require lasers, digital cameras, and modern computers, while the computational techniques require enormous computational power for 3D simulations which are becoming more elaborate as technology allows.

2.2.3 Simple Oscillatory Problems

The idea behind flow control by fish-like swimming is that there is some natural frequency to the hydrodynamics in its interaction with the body. Through tuned periodic motion of the body, the unsteady natural hydrodynamics are controlled to some engineering benefit. A relatively simple example of this is found in the experiments of Tokumaru and Dimotakis in which they used rotary oscillations of a cylinder to control the vortex shedding wake characteristics [62]. This study demonstrated that such oscillations could yield a very significant 80% decrease in drag.

Another simplified realization of oscillatory body motion similar to swimming fish is that of a waving plate. The problem, first characterized by Wu's 2D potential flow model, has since been examined for viscous flows both numerically and experimentally.

It has been shown both in experiments [56][59], and through 3D numerical simulations [77] [55] that the motion of a waving wall determines the characteristics of the near body flow. Not only was it displayed that the separation and subsequent recirculation can be controlled, but a reduction of the turbulence intensity in the boundary layer was also shown to be a consequence of the swimming motion.

2.2.4 Flapping Foils

While the waving plate studies display how near-body flow can be controlled, they do not treat how the hydrodynamic energy, in the form of vortical structures, is organized for its eventual release from the near-body region. This organization and release of vorticity into the wake has consequences in terms of the momentum exchange between the fluid and the body. There is a range of controlling parameters for this problem when treated in two dimensions, which increases for the three-dimensional problem. These include the body section, pitch amplitude and frequency, point of rotation, heave amplitude and frequency, and phase between heave and pitch. Of course, the nature of the harmonic forcing (usually taken as sinusoidal) and the Reynolds number are also important parameters. Studies of this problem include investigations covering a wide range of these parameters.

A 1989 experimental study of Koochesfahani used dye injection flow visualization and Laser Doppler Velocimetry to characterize the flow and forcing characteristics associated with an oscillatory pitching motion of a NACA0012 foil section [32]. The results indicated wake vortex patterns associated with net drag, net thrust, and net zero streamwise forcing. Work of Triantafyllou et.al. combining theory from stability analysis with experimentally obtained forcing measurements determined a parametric range for creation of a thrusting vortex wake with combined heave and pitch motion [65][64]. Followup work of Anderson et. al. [3][2] included experimental flow visualization using Digital Partical Image Velocimetry (DPIV). This visualization allowed for detailed insight into how varying the kinematics of the foil influenced the generation and interaction of near-body vorticity, such information not available with the wake visualization of Koochesfahani. Of particular interest and relation to fish-like swimming is the use of the trailing edge of the foil to distribute and contribute to vorticity generated at the leading edge. This relates to the manner in which fish use their large tails to manipulate vorticity generated upstream on the body. Further experimental study by Read [50] examined in detail the relationship between the heave and pitch kinematics and the hydrodynamic forcing and propulsive efficiency.

Ramamurti and Sandberg [49] recently repeated some of the Koochesfahani and Anderson experiments with 2D viscous numerical simulations. The simulations allow a detailed look at the near-body flow characteristics in conjunction with the exact time history of the hydrodynamic forcing, but such analysis was only touched upon briefly. The numerical work of Wang [69] and recent work of Guglielmini and Blondeaux [26] do utilize the advantage of numerical simulations by examining the relationship between hydrodynamic forcing and the evolution of the flow-body interaction. Wang discusses the changes in the forcing due to the separation of the leading and trailing edge bound vortices. The analysis allows identification of an optimal foil stroke as one operating in a thrust window which allows generous growth of the trailing edge vortex without full separation of the leading edge bound vorticity. Such a study is a clear example of the distinct advantage of viscous numerical simulations, the ability to examine the details of near body flow and how these relate to momentum exchange between the fluid and body.

2.2.5 Real Fish Kinematics

Other experimental and numerical pursuits have been of a real fish form and kinematics. The most significant of these studies have come within the past several years. Wolfgang et.al. [74] combined experimental work of DPIV on a live fish with inviscid numerical simulations of the same fish. The study displays how body kinematics are used to organize near-body vorticity for the purpose of straight-line swimming and fast turning. An extension of the inviscid numerical study by Zhu et. al. [82] encompassed a more detailed look at the near-body flow and wake characteristics resulting from different body forms and kinematics.

Though unsteady viscous numerical simulations are computationally expensive, they can be performed for small Reynolds number flows. One clear advantage of a viscous simulation is the availability of complete and accurate hydrodynamic forcing information for any point on the body. Such simulations have been performed in both 2D and 3D for a swimming tadpole [40][39]. As it used a truly viscous model, this work was able to describe the tail interaction with flow structures generated upstream without relying on viscous modeling for vorticity generation and separation. Specialized kinematics matched to the body form of a tadpole were determined to manipulate the near-body flow for optimal swimming efficiency. Such a determination was made possible by the availability of the details of the ongoing momentum exchange between the body and the surrounding fluid.

The work of Barret et. al. [5] consisted of the building of a robotic fish, the *Robotuna*. A parametric study of kinematics was pursued, examining the power requirements for propulsion of the Robotuna. It was determined that the power required to propel the fish through the optimized swimming motion was less than that needed to tow the rigid fish body. This study was experimental confirmation of the "drag reduction" ideas initiated by Gray's paradox.

2.2.6 The Future of Fish-like Swimming

The works described above portray a clear picture of how oscillatory body kinematics affect near-body flow and wake characteristics and resultant forcing on the body. There is certainly room for further study on the momentum exchange consequences of fish-like swimming body motions, particularly in bringing to a close the understanding of the reasons for Gray's paradox. One significant mechanism of importance which is not addressed in any of the above studies is the role of the structural characteristics of the body in motion. It's almost certain that, through evolution, the structural characteristics of fish have been tuned for natural modes of oscillation coupled with hydrodynamics which provide maximum benefit. To fully realize the advantages of fish-like swimming, engineers will have to investigate, understand, and exploit this process. Due to the difficult nonlinear nature of the hydrodynamics, such an understanding of the fluid-structure interaction involved in fish-like swimming must come from experimental and computational studies.

2.3 Tuning the Fluid-Structure Interaction for Engineering

There is very little work to date concerning attempts to tune and/or drive an elastic body in fluid for specific engineering functions. However, this is a key component of the process through which fish are able to achieve such high efficiencies. Recent work of Beal investigated the swimming patterns of live fish in an incoming periodic vortex wake [6]. A tendency for the fish to swim through the wake in a consistent manner suggested an efficient interaction between the structurally oscillating body and the flow-body hydrodynamics. This was confirmed when a euthenized fish was shown to actually accelerate through the wake with a similar passive oscillation. Such a phenomenon is an indication of the importance of properly tuning a structure so desired forcing can result with minimal energy expenditure.

2.3.1 Energy Extraction

One potential realization of a tuned interaction between a flow and elastic body would be in the pursuit of extracting energy from an ambient flow. Just as propellers have a tradition as the primary propulsory mechanism, they are used for the purpose of energy extraction. Knowing from Gray's work of the advantages of a new paradigm for propulsion, the possibility of such advantages for energy extraction should also be considered. Recent work by Allen and Smits details an experiment in which a flexible piezoelectric membrane flaps in the wake of a bluff body for the purpose of energy capture [1]. Tests were run varying the dimensions and structural properties of the membrane with the goal of maximizing the membrane's strain for maximum power generation. Further pursuit of this concept might well prove useful, particularly as it may be used in the same mechanisms designed for driven swimming motion.

2.3.2 Beam Fish

In similar experimental studies McHenry et. al. [42] and McLetchie [43] used elastic fish bodies driven harmonically in pitch at a single point to investigate swimming fish as actuated structures. The McHenry study was essentially of the observed kinematics of the elastic fish. The fish was put in a free-swimming state (zero drag/thrust), and the kinematics were compared to those of real fish. With the determination that the model was unable to match the fish kinematics through a range of swimming speeds without altering the bending stiffness, they concluded that real fish must be able to alter their structural properties. McLetchie's work was essentially a power study. The power required to harmonically drive and drag the fish was measured so that the swimming efficiency could be exactly determined. Though dragging the passive fish was found to be more efficient in this experiment, parameters for efficient free swimming and power requirement for large thrust were determined. A continuation of the McLetchie study with more involved structural tuning for desired swimming kinematics could potentially realize dramatic improvements in efficiency.

2.3.3 Status of the Field

It's inevitable that there will be a surge in work involving control of the interaction between flexible bodies and ambient flow for engineering purposes. The natural world demonstrates the clear benefits of such control, and we are only now obtaining the capabilities to begin to understand them. Studies of fish-like swimming involving live fish or imposed kinematics have demonstrated vortical flow mechanisms involved in the process. A deeper understanding of the natural interaction of the elastically responding foil body and the ambient flow is now sought. The present study seeks to identify the key parameters and physical mechanisms in the range of natural responses of the flexible foil fluid-structure interaction.

Chapter 3

The Fluid-dynamic Direct Simulation (FDS)

The following details the development and characteristics of the fluid-dynamic direct simulation (FDS) component of the coupled fluid-structure numerical solver. The final product allows for direct solution of the unsteady Navier-Stokes equations in three dimensions using primitive variables (p, $\vec{v}$). The equations are solved implicitly using a moving collocated grid. Such treatment allows for iterative coupling with implicit structural equations to be described later.

The FDS was developed using the Periodic Waving Plate Model of Xiang Zhang [77] as a template. The Periodic Waving Plate Model is a 3D finite-difference direct numerical simulation of the Navier-Stokes equations. The computer code of the present study differs from that of the waving plate code on a fundamental level in that the mapping between the physical and computational domains is not the same. While the Periodic Waving Plate Model required one of the three cross-sectional planes in the physical domain to project a 2D cartesian coordinate system, the present model was developed with no such requirement. For this reason, the coordinate dependencies between the physical and computational domain are more involved. The resulting governing equations, mapped from the physical to computational domain, are considerably more complicated. The reward for this added complexity is that the present model is very robust in terms of the body geometries about which the flow

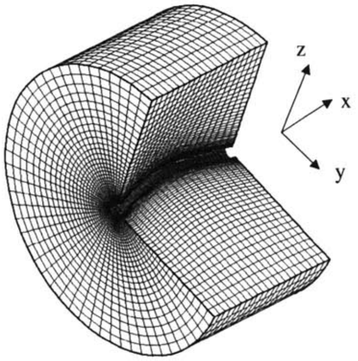

Figure 3-1: Shows physical domain with cutout displaying grid.

can be solved. Other important methodological differences include implementation of second-order time integration, consistency of the pressure solver with the velocity field for divergence control, enforcement of pressure solveability, inclusion of a method for handling grid motion, and parallelization of the computer code in two directions for high wall clock efficiency.

3.1 Domains and Mappings

The following defines the physical system which is to be modelled, and the framework through which this system must be solved. The need for generating the solution in a simple computational domain and the manner of transformation are addressed.

3.1.1 The Physical Domain

The physical domain refers to the actual physical system which is to be simulated. This domain will be demonstrated as a curved length of body (in this case a cylinder) enclosed by a large outer boundary as shown in figure 3-1. The outer boundary is the far-field boundary, through which flow is permitted, while the inner boundary is the solid body around which the flow must travel. A three-dimensional grid as shown represents the points at which the flow field is calculated.

A two-dimensional cross-section shown in figure 3-2 shows a slice of the physical

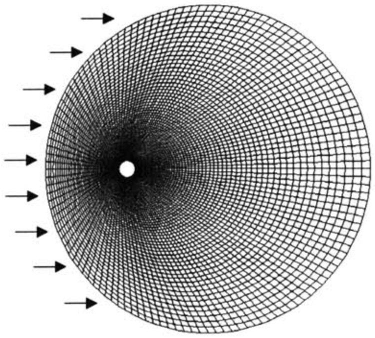

Figure 3-2: Cross-section of grid with center cylinder displaced. Arrows represent an inflow condition at the outer boundary.

domain with the corresponding computational grid. In this figure, there is a large displacement of the inner cylinder from the center of the physical domain. Such an upstream displacement with an inflow as shown would allow for a larger downstream wake area to be calculated. The increasing resolution of the grid toward the inner cylinder represents the importance of accurately solving the flow at the body boundary.

The three cartesian coordinates in the physical domain are shown in figure 3-1. It's clear that only one of these cartesian coordinates, the x-direction, is aligned with the grid. While the problem of a straight cylinder lends itself to calculation in cylindrical coordinates, a model permitting variable displacement of an arbitrarily shaped inner boundary would make this more difficult than with the cartesian coordinates used.

3.1.2 The Computational Domain

The problem of the need for a complicated curvilinear coordinate system is approached by defining a computational domain. In this domain the directions are aligned exactly with the grid. The grid lines radiating from the inner cylinder to the outer cylinder are designated the direction ρ, the lines circumscribing the inner cylinder are designated the direction θ, and the axial direction is designated ξ.

Figure 3-3 shows the mapping of the physical domain to the computational domain. In this computational domain the grid spacing in each grid direction remains

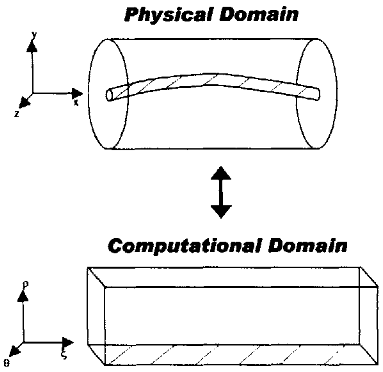

Figure 3-3: Sketch of the mapping of the physical domain to the computational domain.

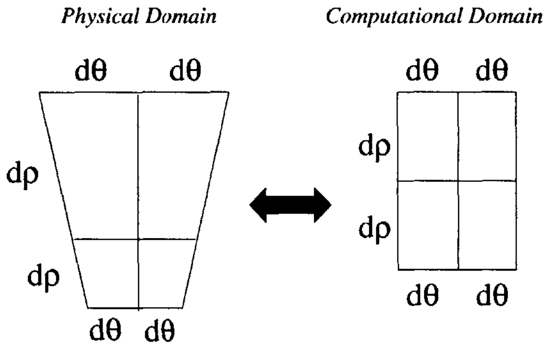

Figure 3-4: Detailed section of grid mapping. Shows the phenomenon of mapping non-constant to constant grid spacing.

constant, while it clearly does not in the physical domain. Figure 3-4 displays this concept of mapping non-constant grid spacing to constant grid spacing.

3.1.3 Mapping Equations from the Physical to Computational Domain

The dynamics of the system are represented through governing differential equations in the physical domain. These equations are to be solved, however, in the computational domain, requiring a mapping of the equations from one domain to another.

Discretization of Derivatives: Need to Map Derivatives

Differential equations are solved computationally by discretization. The discretized equation on the grid can then be put into matrix form with the appropriate boundary conditions and solved. For the following example first-order system,

$$\begin{aligned} \frac{\partial f}{\partial \zeta} &= K \\ \zeta &= [0, 1, 2, 3] \\ f(0) &= 10, \end{aligned} \tag{3.1}$$

the first derivative is approximated with a backwards finite difference expression,

$$\frac{f_i - f_{i-1}}{\Delta\zeta} = K. \tag{3.2}$$

The system can now be put into matrix form as

$$\begin{bmatrix} 1 & 0 & 0 & 0 \\ -1 & 1 & 0 & 0 \\ 0 & -1 & 1 & 0 \\ 0 & 0 & -1 & 1 \end{bmatrix} \begin{bmatrix} f_0 \\ f_1 \\ f_2 \\ f_3 \end{bmatrix} = \begin{bmatrix} 10 \\ K \cdot \Delta\zeta \\ K \cdot \Delta\zeta \\ K \cdot \Delta\zeta \end{bmatrix} \tag{3.3}$$

and this $A\vec{x} = \vec{b}$ system is solved as $\vec{x} = A^{-1}\vec{b}$.

The expressions $\frac{\partial f}{\partial x}$, $\frac{\partial f}{\partial y}$, and $\frac{\partial f}{\partial z}$ can not be translated so simply to finite differences on the computational grid shown in figure 3-1. The mappings of these derivatives to the computational domain must first be defined.

Development of Mapping and Grid Metrics

The mappings are developed for a general physical domain which does not require the inner boundary to be either straight or stationary. Thus, these mappings can handle a vibrating flexible body. The coordinate dependencies are

$$\begin{array}{cc} x(\xi) & \xi(x) \\ y(\xi,\rho,\theta,\tau) & \rho(x,y,z,t) \\ z(\xi,\rho,\theta,\tau) & \theta(x,y,z,t) \\ t(\tau) & \tau(t) \end{array}. \tag{3.4}$$

Here, time is represented in the physical domain by t and in the computational domain by τ. We need to map derivatives in the cartesian coordinates of the physical domain to derivatives in the computational domain. This can be achieved using the chain rule,

$$\begin{aligned} \frac{\partial f}{\partial x} &= \frac{\partial f}{\partial \xi}\frac{\partial \xi}{\partial x} + \frac{\partial f}{\partial \rho}\frac{\partial \rho}{\partial x} + \frac{\partial f}{\partial \theta}\frac{\partial \theta}{\partial x} \\ \frac{\partial f}{\partial y} &= \frac{\partial f}{\partial \rho}\frac{\partial \rho}{\partial y} + \frac{\partial f}{\partial \theta}\frac{\partial \theta}{\partial y} \\ \frac{\partial f}{\partial z} &= \frac{\partial f}{\partial \rho}\frac{\partial \rho}{\partial z} + \frac{\partial f}{\partial \theta}\frac{\partial \theta}{\partial z} \\ \frac{\partial f}{\partial t} &= \frac{\partial f}{\partial \rho}\frac{\partial \rho}{\partial t} + \frac{\partial f}{\partial \theta}\frac{\partial \theta}{\partial t} + \frac{\partial f}{\partial \tau}\frac{\partial \tau}{\partial t}. \end{aligned} \tag{3.5}$$

In these expressions, the derivatives relating the two domains appear as changes of computational coordinates in the physical domain. However, we want to calculate in the computational domain, so would prefer derivatives of physical coordinates in the computational domain. To achieve this we use the chain rule in the opposite direction and manipulate the expressions algebraically,

$$\begin{aligned} \frac{\partial f}{\partial \xi} &= \frac{\partial f}{\partial x}\frac{\partial x}{\partial \xi} + \frac{\partial f}{\partial y}\frac{\partial y}{\partial \xi} + \frac{\partial f}{\partial z}\frac{\partial z}{\partial \xi} \\ \frac{\partial f}{\partial \rho} &= \frac{\partial f}{\partial y}\frac{\partial y}{\partial \rho} + \frac{\partial f}{\partial z}\frac{\partial z}{\partial \rho} \\ \frac{\partial f}{\partial \theta} &= \frac{\partial f}{\partial y}\frac{\partial y}{\partial \theta} + \frac{\partial f}{\partial z}\frac{\partial z}{\partial \theta} \\ \frac{\partial f}{\partial \tau} &= \frac{\partial f}{\partial y}\frac{\partial y}{\partial \tau} + \frac{\partial f}{\partial z}\frac{\partial z}{\partial \tau} + \frac{\partial f}{\partial t}\frac{\partial t}{\partial \tau}. \end{aligned} \tag{3.6}$$

In the mapping used, $t = \tau$ so that $t_\tau = 1$. The equations are rewritten in a cleaner form prior to manipulation,

$$f_\xi = x_\xi f_x + y_\xi f_y + z_\xi f_z \tag{3.7}$$

$$f_\rho = y_\rho f_y + z_\rho f_z \tag{3.8}$$

$$f_\theta = y_\theta f_y + z_\theta f_z \tag{3.9}$$

$$f_\tau = y_\tau f_y + z_\tau f_z + f_t. \tag{3.10}$$

Multiplying equation 3.9 by z_ρ and subtracting it from the product of equation 3.8 and z_θ, we obtain

$$\begin{aligned}(z_\theta f_\rho - z_\rho f_\theta) &= (z_\theta y_\rho - z_\rho y_\theta) f_y \\ f_y &= \frac{z_\theta f_\rho - z_\rho f_\theta}{z_\theta y_\rho - z_\rho y_\theta}.\end{aligned} \tag{3.11}$$

This is now an expression for a generic y-derivative in terms of only derivatives taken in the computational domain. Similarly, the product of equation 3.9 and y_ρ is subtracted from the product of equation 3.8 and y_θ, yielding

$$\begin{aligned}(y_\theta f_\rho - y_\rho f_\theta) &= (y_\theta z_\rho - y_\rho z_\theta) f_z \\ f_z &= \frac{y_\theta f_\rho - y_\rho f_\theta}{y_\theta z_\rho - y_\rho z_\theta}.\end{aligned} \tag{3.12}$$

We define the cross-sectional Jacobian as

$$J = y_\rho z_\theta - y_\theta z_\rho. \tag{3.13}$$

The y and z-derivative terms can then be rewritten,

$$f_y = \frac{1}{J}(z_\theta f_\rho - z_\rho f_\theta) \tag{3.14}$$

$$f_z = \frac{1}{J}(-y_\theta f_\rho + y_\rho f_\theta). \tag{3.15}$$

An equation for f_x can now be formed from equation 3.7 by substituting in equations 3.14 and 3.15,

$$\begin{aligned} f_x &= \frac{1}{x_\xi}\left[f_\xi - y_\xi \frac{1}{J}(z_\theta f_\rho - z_\rho f_\theta) - z_\xi \frac{1}{J}(-y_\theta f_\rho + y_\rho f_\theta)\right] \\ f_x &= \frac{1}{x_\xi}\left[f_\xi + \frac{1}{J}[(-y_\xi z_\theta + z_\xi y_\theta) f_\rho + (y_\xi z_\rho - z_\xi y_\rho) f_\theta]\right]. \end{aligned} \tag{3.16}$$

The following definitions are employed,

$$YTZX = \frac{1}{x_\xi}(y_\theta z_\xi - y_\xi z_\theta) \tag{3.17}$$

$$YXZR = \frac{1}{x_\xi}(y_\xi z_\rho - y_\rho z_\xi), \tag{3.18}$$

and the generic x-derivative is thus expressed as

$$f_x = \frac{1}{x_\xi} f_\xi + \frac{1}{J}[YTZX\, f_\rho + YXZR\, f_\theta]. \tag{3.19}$$

Derivatives in time in the physical domain are mapped to the computational domain through equation 3.10,

$$f_t = f_\tau - y_\tau f_y - z_\tau f_z. \tag{3.20}$$

The derivatives y_τ and z_τ denote how the y and z values of a particular grid point change in time. By this definition, these are simply the velocity components of the grid in physical space,

$$v_g = \frac{\partial y}{\partial \tau} \qquad w_g = \frac{\partial z}{\partial \tau}. \tag{3.21}$$

We now have the collection of first derivatives in space and time mapped from the physical to computational domain,

$$\frac{\partial f}{\partial x} = \frac{1}{x_\xi}\frac{\partial f}{\partial \xi} + \frac{1}{J}\left(YTZX\frac{\partial f}{\partial \rho} + YXZR\frac{\partial f}{\partial \theta}\right) \tag{3.22}$$

$$\frac{\partial f}{\partial y} = \frac{1}{J}\left(z_\theta \frac{\partial f}{\partial \rho} - z_\rho \frac{\partial f}{\partial \theta} \right) \tag{3.23}$$

$$\frac{\partial f}{\partial z} = \frac{1}{J}\left(-y_\theta \frac{\partial f}{\partial \rho} + y_\rho \frac{\partial f}{\partial \theta} \right) \tag{3.24}$$

$$\begin{aligned} \frac{\partial f}{\partial t} &= \frac{\partial f}{\partial \tau} - v_g \frac{\partial f}{\partial y} - w_g \frac{\partial f}{\partial z} \\ &= \frac{\partial f}{\partial \tau} - \frac{1}{J}\left[v_g \left(z_\theta \frac{\partial f}{\partial \rho} - z_\rho \frac{\partial f}{\partial \theta} \right) + w_g \left(-y_\theta \frac{\partial f}{\partial \rho} + y_\rho \frac{\partial f}{\partial \theta} \right) \right] . \end{aligned} \tag{3.25}$$

The mappings for derivatives which make up a first-order differential equation are now defined. Derivatives of the physical space variables on the computational grid are the components of these mappings, and we refer to these as the grid metrics.

Second Order Mapping

In order to obtain mappings for second derivatives, expressions of equations 3.22, 3.23, and 3.24 are plugged back into themselves. Keeping in mind that all of the metrics are functions of computational space, the expressions get somewhat lengthy.

Considering $g = \frac{\partial f}{\partial x}$, to obtain $\frac{\partial g}{\partial x}$ the expression of equation 3.22 is used on itself,

$$\begin{aligned} \frac{\partial^2 f}{\partial x^2} = \frac{\partial g}{\partial x} &= \frac{1}{x_\xi} g_\xi + \left(\frac{YTZX}{J} \right) g_\rho + \left(\frac{YXZR}{J} \right) g_\theta \\ &= \frac{1}{x_\xi} \left[\frac{1}{x_\xi} f_{\xi\xi} + \left(\frac{YTZX}{J} \right)_\xi f_\rho + \left(\frac{YTZX}{J} \right) f_{\xi\rho} + \left(\frac{YXZR}{J} \right)_\xi f_\theta + \left(\frac{YXZR}{J} \right) f_{\xi\theta} \right] \\ &+ \left(\frac{YTZX}{J} \right) \left[\frac{1}{x_\xi} f_{\xi\rho} + \left(\frac{YTZX}{J} \right)_\rho f_\rho + \left(\frac{YTZX}{J} \right) f_{\rho\rho} + \left(\frac{YXZR}{J} \right)_\rho f_\theta \right. \\ &+ \left. \left(\frac{YXZR}{J} \right) f_{\rho\theta} \right] + \left(\frac{YXZR}{J} \right) \left[\frac{1}{x_\xi} f_{\xi\theta} + \left(\frac{YTZX}{J} \right)_\theta f_\rho + \left(\frac{YTZX}{J} \right) f_{\rho\theta} \right. \\ &+ \left. \left(\frac{YXZR}{J} \right)_\theta f_\theta + \left(\frac{YXZR}{J} \right) f_{\theta\theta} \right] . \end{aligned} \tag{3.26}$$

In the same manner, $\frac{\partial^2 f}{\partial y^2}$ is obtained by using equation 3.23 on itself, and $\frac{\partial^2 f}{\partial z^2}$ from using equation 3.24 on itself,

$$\frac{\partial^2 f}{\partial y^2} = \frac{\partial g}{\partial y} = \left(\frac{z_\theta}{J} \right) g_\rho - \left(\frac{z_\rho}{J} \right) g_\theta$$

$$
\begin{aligned}
&= \left(\frac{z_\theta}{J}\right)\left[\left(\frac{z_\theta}{J}\right)_\rho f_\rho + \left(\frac{z_\theta}{J}\right) f_{\rho\rho} - \left(\frac{z_\rho}{J}\right)_\rho f_\theta - \left(\frac{z_\rho}{J}\right) f_{\rho\theta}\right] \\
&- \left(\frac{z_\rho}{J}\right)\left[\left(\frac{z_\theta}{J}\right)_\theta f_\rho + \left(\frac{z_\theta}{J}\right) f_{\rho\theta} - \left(\frac{z_\rho}{J}\right)_\theta f_\theta - \left(\frac{z_\rho}{J}\right) f_{\theta\theta}\right],
\end{aligned}
\tag{3.27}
$$

$$
\begin{aligned}
\frac{\partial^2 f}{\partial z^2} = \frac{\partial g}{\partial z} &= -\left(\frac{y_\theta}{J}\right) g_\rho + \left(\frac{y_\rho}{J}\right) g_\theta \\
&= -\left(\frac{y_\theta}{J}\right)\left[-\left(\frac{y_\theta}{J}\right)_\rho f_\rho - \left(\frac{y_\theta}{J}\right) f_{\rho\rho} + \left(\frac{y_\rho}{J}\right)_\rho f_\theta + \left(\frac{y_\rho}{J}\right) f_{\rho\theta}\right] \\
&+ \left(\frac{y_\rho}{J}\right)\left[-\left(\frac{y_\theta}{J}\right)_\theta f_\rho - \left(\frac{y_\theta}{J}\right) f_{\rho\theta} + \left(\frac{y_\rho}{J}\right)_\theta f_\theta + \left(\frac{y_\rho}{J}\right) f_{\theta\theta}\right].
\end{aligned}
\tag{3.28}
$$

The expression for the Laplacian $\nabla^2 f = f_{xx} + f_{yy} + f_{zz}$ can be defined from equations 3.26-3.28. This is most easily organized by grouping terms as

$$
\begin{aligned}
\nabla^2 f &= f_{xx} + f_{yy} + f_{zz} \\
&= CXX\, f_{\xi\xi} + CXR\, f_{\xi\rho} + CXT\, f_{\xi\theta} + CRR\, f_{\rho\rho} + CRT\, f_{\rho\theta} \\
&+ CTT\, f_{\theta\theta} + CR\, f_\rho + CT\, f_\theta
\end{aligned}
\tag{3.29}
$$

$$
\begin{aligned}
CXX &= \frac{1}{x_\xi^2} \\
CXR &= \frac{2}{x_\xi}\frac{YTZX}{J} \\
CXT &= \frac{2}{x_\xi}\frac{YXZR}{J} \\
CRR &= \left(\frac{YTZX}{J}\right)^2 + \left(\frac{z_\theta}{J}\right)^2 + \left(\frac{y_\theta}{J}\right)^2 \\
CRT &= 2\frac{YTZX \cdot YXZR}{J^2} - 2\frac{z_\rho z_\theta}{J^2} - 2\frac{y_\rho y_\theta}{J^2} \\
CTT &= \left(\frac{YXZR}{J}\right)^2 + \left(\frac{z_\rho}{J}\right)^2 + \left(\frac{y_\rho}{J}\right)^2
\end{aligned}
\tag{3.30}
$$

$$\begin{aligned} CR = &\frac{1}{x_\xi}\left(\frac{YTZX}{J}\right)_\xi + \left(\frac{YTZX}{J}\right)\left(\frac{YTZX}{J}\right)_\rho + \left(\frac{YXZR}{J}\right)\left(\frac{YTZX}{J}\right)_\theta \\ &+ \left(\frac{z_\theta}{J}\right)\left(\frac{z_\theta}{J}\right)_\rho - \left(\frac{z_\rho}{J}\right)\left(\frac{z_\theta}{J}\right)_\theta + \left(\frac{y_\theta}{J}\right)\left(\frac{y_\theta}{J}\right)_\rho - \left(\frac{y_\rho}{J}\right)\left(\frac{y_\theta}{J}\right)_\theta \end{aligned}$$

$$\begin{aligned} CT = &\frac{1}{x_\xi}\left(\frac{YXZR}{J}\right)_\xi + \left(\frac{YTZX}{J}\right)\left(\frac{YXZR}{J}\right)_\rho + \left(\frac{YXZR}{J}\right)\left(\frac{YXZR}{J}\right)_\theta \\ &- \left(\frac{z_\theta}{J}\right)\left(\frac{z_\rho}{J}\right)_\rho + \left(\frac{z_\rho}{J}\right)\left(\frac{z_\rho}{J}\right)_\theta - \left(\frac{y_\theta}{J}\right)\left(\frac{y_\rho}{J}\right)_\rho + \left(\frac{y_\rho}{J}\right)\left(\frac{y_\rho}{J}\right)_\theta. \end{aligned}$$

These expressions of equation 3.30 are also considered metrics of the grid, used in the mapping to the computational domain.

First and second derivatives can now be mapped from the physical domain to the computational domain. With these mappings a second-order differential equation defined in the physical domain can be transferred to the computational domain and solved with finite differencing. Expressing the equations as differences in term of ξ, ρ, and θ, a matrix system like that of equation 3.3 can be formed.

3.1.4 Grid Generation

Two methods are used in generating the computational grid to be used, depending on the complexity of the geometry of the problem being solved. For simple geometries such as the cylinder of figure 3-2, or for straight rigid foils, the grid is generated algebraically. A function will position the grid point in physical space according to its index. In practice, the points at the inner and outer boundaries are defined, and interior points are smoothed between the two. Accommodation is made near the boundaries to ensure that the grid is boundary normal. Clustering is used at the inner boundary, placing points in sufficient density for boundary layer resolution. For foils with sharp edges, clustering is also used at the ends to resolve the smallest scales associated with the hydrodynamics around the edge. Such clustering is shown in the series of plots of figure 3-5.

For complicated geometries involving flexible bodies experiencing large curvature, the algebraic grid generation fails. Such failure is due to excessive skewing of the

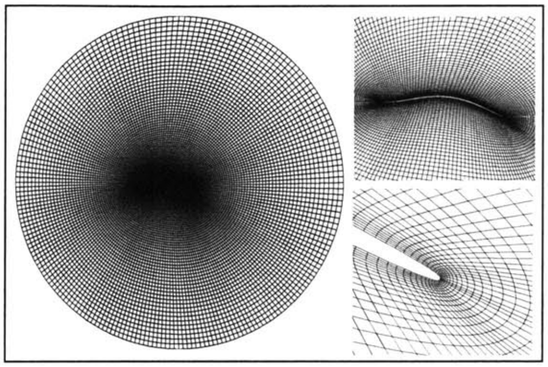

Figure 3-5: Shows grid resolution around a thin foil. The clustering around the sharp trailing edge ensures resolution of the smallest length scales.

grid, or the grid overlapping itself. An alternative form of grid generation used is the solving of an elliptic equation in order to establish a well spaced grid. The popular method detailed in Thompson et. al. [61] is used. We have

$$\frac{\partial^2 \rho}{\partial y^2} + \frac{\partial^2 \rho}{\partial z^2} = P(\rho, \theta) \tag{3.31}$$

$$\frac{\partial^2 \theta}{\partial y^2} + \frac{\partial^2 \theta}{\partial z^2} = Q(\rho, \theta), \tag{3.32}$$

which reduces to

$$\alpha y_{\rho\rho} - 2\beta y_{\rho\theta} + \gamma y_{\theta\theta} + J^2(P y_\rho + Q y_\theta) = 0 \tag{3.33}$$

$$\alpha z_{\rho\rho} - 2\beta z_{\rho\theta} + \gamma z_{\theta\theta} + J^2(P z_\rho + Q z_\theta) = 0 \tag{3.34}$$

$$\alpha = y_\theta^2 + z_\theta^2, \quad \beta = y_\rho y_\theta + z_\rho z_\theta, \quad \gamma = y_\rho^2 + z_\rho^2. \tag{3.35}$$

The grid which is generated and its clustering characteristics depends on the source terms, $P(\rho, \theta)$ and $Q(\rho, \theta)$. In our application, these source terms are found by first algebraically generating a grid about a straight body with the desired clustering characteristics. The values of $P(\rho, \theta)$ and $Q(\rho, \theta)$ are then calculated on this grid from the expressions of equations 3.31 and 3.32. These calculated source terms of $P(\rho, \theta)$ and $Q(\rho, \theta)$ are then fixed for the duration of the simulation, influencing the elliptic solver to generate grids with the desired clustering characteristics about the nonlinearly moving body. This method is successful in maintaining the desired grid characteristics, while avoiding the grid failure which occurs when using an algebraic grid generator with large body displacements.

3.2 Governing Equations

With the computational domain and required mappings established, the next step is to define the differential equations which govern the dynamics of the system. The equations of motion used for this viscous incompressible fluid are the Navier-Stokes equations. They are to be solved in the primitive variables of velocity and pressure.

3.2.1 The Navier-Stokes Equations

The Navier-Stokes equations describe a force balance of a fluid particle in terms of inertia, viscous stresses, and the pressure gradient. For the three-dimensional model of the present study there are three equations, one for the force balance in each direction.

The equations can be written in vector form, and in dimensional terms the non-conservative form is

$$\frac{\partial \vec{v}}{\partial t} + (\vec{v} \cdot \vec{\nabla})\vec{v} = -\frac{1}{\rho_f}\nabla p + \nu \nabla^2 \vec{v}. \tag{3.36}$$

Here, ρ_f is the fluid density and ν is the kinematic viscosity, both of which are assumed to be constant. The following nondimensionalizations are employed using the body length-scale L, and the input flow V,

$$\begin{aligned} \vec{v}^* &= \frac{\vec{v}}{V} \\ t^* &= \frac{t}{L/V} \\ \vec{x}^* &= \frac{\vec{x}}{L} \\ p^* &= \frac{p}{\rho_f V^2}. \end{aligned} \tag{3.37}$$

Now, equation 3.36 can be rewritten in nondimensional form as

$$\frac{V^2}{L}\frac{\partial \vec{v}^*}{\partial t^*} + \frac{V^2}{L}(\vec{v}^* \cdot \vec{\nabla}^*)\vec{v}^* = -\frac{V^2}{L}\nabla^* p^* + \frac{\nu V}{L^2}\nabla^{2*}\vec{v}^*, \tag{3.38}$$

and dividing by V^2/L and defining the Reynolds number as $Re = VL/\nu$ we obtain

$$\frac{\partial \vec{v}^*}{\partial t^*} + (\vec{v}^* \cdot \vec{\nabla}^*)\vec{v}^* = -\nabla^* p^* + \frac{1}{Re}\nabla^{2*}\vec{v}^*. \tag{3.39}$$

The superscripts denoting nondimensional variables are eliminated for convenience, and all equations are considered to be nondimensional henceforth,

$$\frac{\partial \vec{v}}{\partial t} + (\vec{v} \cdot \vec{\nabla})\vec{v} = -\vec{\nabla} p + \frac{1}{Re}\nabla^2 \vec{v}. \tag{3.40}$$

The three momentum equations are written in expanded form as

$$u_t + u\,u_x + v\,u_y + w\,u_z = -p_x + \frac{1}{Re}\nabla^2 u \tag{3.41}$$

$$v_t + u\,v_x + v\,v_y + w\,v_z = -p_y + \frac{1}{Re}\nabla^2 v \tag{3.42}$$

$$w_t + u\,w_x + v\,w_y + w\,w_z = -p_z + \frac{1}{Re}\nabla^2 w. \tag{3.43}$$

Using the mappings of equations 3.22-3.30, the Navier-Stokes equations can be mapped into the computational domain as

$$\begin{aligned}
&u_\tau + u\{\frac{1}{x_\xi}u_\xi + \frac{1}{J}[YTZX\,u_\rho + YXZR\,u_\theta]\} + (v - v_g)\{\frac{1}{J}[z_\theta u_\rho - z_\rho u_\theta]\} \\
&+(w - w_g)\{\frac{1}{J}[-y_\theta u_\rho + y_\rho u_\theta]\} = \\
&-\{\frac{1}{x_\xi}p_\xi + \frac{1}{J}[YTZX\,p_\rho + YXZR\,p_\theta]\} \\
&+\frac{1}{Re}(CXX\,u_{\xi\xi} + CXR\,u_{\xi\rho} + CXT\,u_{\xi\theta} + CRR\,u_{\rho\rho} \\
&+CRT\,u_{\rho\theta} + CTT\,u_{\theta\theta} + CR\,u_\rho + CT\,u_\theta)
\end{aligned} \tag{3.44}$$

$$v_\tau + u\{\frac{1}{x_\xi}v_\xi + \frac{1}{J}[YTZX\,v_\rho + YXZR\,v_\theta]\} + (v - v_g)\{\frac{1}{J}[z_\theta v_\rho - z_\rho v_\theta]\}$$

$$\begin{aligned}
&+(w-w_g)\{\frac{1}{J}[-y_\theta v_\rho + y_\rho v_\theta]\} = \\
&-\{\frac{1}{J}[z_\theta p_\rho - z_\rho p_\theta]\} \\
&+\frac{1}{Re}(CXX\, v_{\xi\xi} + CXR\, v_{\xi\rho} + CXT\, v_{\xi\theta} + CRR\, v_{\rho\rho} \\
&+CRT\, v_{\rho\theta} + CTT\, v_{\theta\theta} + CR\, v_\rho + CT\, v_\theta)
\end{aligned} \tag{3.45}$$

$$\begin{aligned}
w_\tau + u\{\frac{1}{x_\xi} w_\xi &+ \frac{1}{J}[YTZX\, w_\rho + YXZR\, w_\theta]\} + (v-v_g)\{\frac{1}{J}[z_\theta w_\rho - z_\rho w_\theta]\} \\
&+(w-w_g)\{\frac{1}{J}[-y_\theta w_\rho + y_\rho w_\theta]\} = \\
&-\{\frac{1}{J}[-y_\theta p_\rho + y_\rho p_\theta]\} \\
&+\frac{1}{Re}(CXX\, w_{\xi\xi} + CXR\, w_{\xi\rho} + CXT\, w_{\xi\theta} + CRR\, w_{\rho\rho} \\
&+CRT\, w_{\rho\theta} + CTT\, w_{\theta\theta} + CR\, w_\rho + CT\, w_\theta).
\end{aligned} \tag{3.46}$$

3.2.2 The Problem of Pressure: Conservation of Mass

With the velocity equations defined, the velocity can be determined for a given pressure field. The problem now consists of determining the appropriate pressure field.

For a grid size N, the problem has $4 \cdot N$ unknowns as (u, v, w, p) at each grid point. However, the Navier-Stokes equations give only $3 \cdot N$ equations. The fourth equation used to make the system determinate is the conservation of mass. Mass conservation in an incompressible fluid is expressed as a divergence-free velocity field,

$$\vec{\nabla} \cdot \vec{v} = u_x + v_y + w_z = 0, \tag{3.47}$$

which ensures that the mass in an infinitesimal control volume is conserved. The expression of equation 3.47 applied at each grid point offers us the N missing equations which allow us to solve the system.

It seems that it might be possible through finite differencing to form a matrix equation, $A\vec{x} = \vec{b}$, with the column vectors having $4N$ entries representing the four variables at each grid point. Even beyond the complexity of constructing the A

matrix for the mapped three-dimensional problem, the nonlinearity in the momentum equation makes such a linear construction impossible for a fully implicit scheme.

Methods for numerically solving these equations have been the object of much attention. The course of many is to find a route from conservation of mass, equation 3.47, to a determination of the pressure field. Essentially, a pressure field is required that, when used in the Navier-Stokes equations, ensures mass conservation. As such, the pressure field is a function of the velocity field, and the velocity field is a function of the pressure field. For the fully implicit scheme being used, the pressure and velocity need to be solved simultaneously. This is accomplished using an iterative procedure.

3.2.3 Development of the Pressure Equation in Continuous Form

A Poisson equation for the pressure is arrived at by taking the divergence of the vector form of the Navier-Stokes equations 3.40,

$$\vec{\nabla} \cdot \vec{\nabla} p = \vec{\nabla} \cdot \left[-\frac{\partial \vec{v}}{\partial t} - (\vec{v} \cdot \vec{\nabla})\vec{v} + \frac{1}{Re}\nabla^2 \vec{v} \right]. \tag{3.48}$$

The right-hand-side of the equation 3.48 is expanded as

$$\vec{\nabla} \cdot \vec{\nabla} p = -\frac{\partial(\vec{\nabla} \cdot \vec{v})}{\partial t} - \vec{\nabla} \cdot [(\vec{v} \cdot \vec{\nabla})\vec{v}] + \frac{1}{Re}\nabla^2(\vec{\nabla} \cdot \vec{v}). \tag{3.49}$$

Applying conservation of mass, the first and last terms of the right-hand-side of Equation 3.49 disappear, so that

$$\vec{\nabla} \cdot \vec{\nabla} p = -\vec{\nabla} \cdot [(\vec{v} \cdot \vec{\nabla})\vec{v}]. \tag{3.50}$$

The result is a Poisson equation for a pressure field which enforces mass conservation in the Navier-Stokes equations. While the development in continuous form is straightforward, it becomes more complicated in discrete form. Careful matching of the discrete pressure and velocity equations is needed in order to maintain accuracy of mass conservation. These details are given in § 3.3.

3.2.4 Boundary Conditions in Continuous Form

As with the example problem of equation 3.1, boundary conditions are needed to solve for the velocity and pressure fields. For these second order differential equations there are two choices for nonperiodic boundary conditions. The Dirichlet condition specifies the values of the variable at the boundaries, while the Neumann condition specifies the variable's derivative at the boundary.

Periodic boundary conditions are used for the ξ and θ-directions. This simply means that the domain is considered to connect to itself in these directions. This is easily conceived for the θ or circumferential direction in figure 3-2. For the ξ-direction, the minimum and maximum x in figure 3-1 are considered to connect.

Velocity Boundary Condition

Both Dirichlet and Neumann conditions can be specified for the velocity field. For the inner solid boundary we use a Dirichlet no-slip, no-flux condition. At the outer boundary we use a combination of Dirichlet and Neumann conditions according to location. A Dirichlet condition is specified upstream as the inflow boundary, setting the ambient flow parameter, while Neumann conditions are set at the outflow boundary to minimize influence of the boundary on the downstream wake.

Pressure Boundary Condition

For a domain periodic in the ξ and θ-directions, a pressure boundary condition is required only at the inner and outer extent of the ρ-direction. A Neumann pressure boundary condition in this direction follows directly from the formulation of the pressure system which ensures a divergence-free velocity field. The exact form is discussed later in § 3.3.3, but the relation between the normal pressure derivative and that in the ρ-direction is shown below.

The Neumann condition for the pressure derivative in the normal direction in physical space is given as

$$p_n = x_n p_x + y_n p_y + z_n p_z. \tag{3.51}$$

Consider the surface tangential directions to be τ_1 in the circumferential direction and τ_2 in the axial direction, giving the geometric relations

$$\begin{aligned}
y_{\tau_1} &= \frac{y_\theta}{\sqrt{y_\theta^2 + z_\theta^2}} \\
z_{\tau_1} &= \frac{z_\theta}{\sqrt{y_\theta^2 + z_\theta^2}} \\
x_{\tau_2} &= \frac{x_\xi}{\sqrt{x_\xi^2 + y_\xi^2 + z_\xi^2}} \\
y_{\tau_2} &= \frac{y_\xi}{\sqrt{x_\xi^2 + y_\xi^2 + z_\xi^2}} \\
z_{\tau_2} &= \frac{z_\xi}{\sqrt{x_\xi^2 + y_\xi^2 + z_\xi^2}}.
\end{aligned} \tag{3.52}$$

The cartesian components of the outward facing normal are expressed in terms of these relations,

$$\begin{aligned}
x_n &= y_{\tau_2} z_{\tau_1} - z_{\tau_2} y_{\tau_1} \\
y_n &= -x_{\tau_2} z_{\tau_1} \\
z_n &= x_{\tau_2} y_{\tau_1}.
\end{aligned} \tag{3.53}$$

The relations of equation 3.52 are used in equation 3.53 to form an expression for the normal pressure derivative from equation 3.51 as

$$p_n = \frac{-x_\xi}{\sqrt{x_\xi^2 + y_\xi^2 + z_\xi^2}\sqrt{y_\theta^2 + z_\theta^2}} \left[\frac{y_\theta z_\xi - y_\xi z_\theta}{x_\xi} p_x + z_\theta p_y - y_\theta p_z \right]. \tag{3.54}$$

The pressure derivatives in physical space are written in terms of derivatives in computational space using the relations of equations 3.22-3.24. With terms grouped according to the pressure derivatives we find

$$p_n = \frac{-x_\xi}{\sqrt{x_\xi^2 + y_\xi^2 + z_\xi^2}\sqrt{y_\theta^2 + z_\theta^2}} \left[\frac{YTZX}{x_\xi} p_\xi + \left(\frac{YTZX^2}{J} + \frac{z_\theta^2}{J} + \frac{y_\theta^2}{J} \right) p_\rho + \right. \qquad (3.55)$$
$$\left. \left(\frac{YTZX \cdot YXZR}{J} - \frac{z_\theta z_\rho}{J} - \frac{y_\theta y_\rho}{J} \right) p_\theta \right] .$$

This expression for the normal derivative will be used for comparison to the Neumann boundary condition of p_ρ, derived from the discrete mass conservation in § 3.3.3.

3.3 The Discrete Equations

Now that the form of the continuous equations has been laid out, the discrete equations are to be developed. The second-order time and space discretizations are described, with analysis of the associated error. The discrete pressure equation is discussed in terms of the associated error to the mass conservation.

3.3.1 Time Integration

There are a number of implicit, explicit, and combined time integration schemes which are used in solving the Navier-Stokes equations. Fully implicit schemes require simultaneous solution of the velocity and pressure, which are functions of each other and must be solved in iterative fashion. Explicit schemes avoid the need for such iteration, but have a time-step restriction for stability. Fractional-step methods ease this time-step restriction by treating the viscous term implicitly, but maintain explicit treatment of the convective term. As such, these methods have stability restrictions associated with flux over the grid during the span of a time step. For the very fine grids used to resolve flow at the boundaries and sharp edges in the present study, a fully implicit method was needed to avoid excessive restriction on the time step.

For the following analysis we will consider the Navier-Stokes momentum equations in the form

$$\frac{\partial \vec{v}}{\partial \tau} = \vec{G}(\vec{v}, p, \vec{v}_g). \tag{3.56}$$

Here, τ is used to emphasize that the time derivative is being taken on the computational grid which, in general, can be moving with velocity $\vec{v}_g$. With the distinction made clear, t will be substituted for τ henceforth.

Second-Order Backwards Euler (BDF-2)

The simple Second-Order Backwards Euler or BDF-2 implicit scheme was used. This stable scheme has second-order accuracy and in semi-discrete form is written

$$\frac{3\vec{v}^{n+1} - 4\vec{v}^{n} + \vec{v}^{n-1}}{2\Delta t} = \vec{G}^{n+1}. \tag{3.57}$$

In order to confirm the accuracy of this scheme we take a Taylor Series expansion of the left-hand side of the semi-discrete equation,

$$\begin{aligned} \frac{3\vec{v}^{n+1} - 4\vec{v}^{n} + \vec{v}^{n-1}}{2\Delta t} &= \frac{1}{2\Delta t}[3\vec{v}^{n+1} \\ &-4\vec{v}^{n+1} + 4\Delta t\vec{v}_t^{n+1} - 4\frac{1}{2}\Delta t^2\vec{v}_{tt}^{n+1} + 4\frac{1}{6}\Delta t^3\vec{v}_{ttt}^{n+1} + O(\Delta t^4) \\ &+\vec{v}^{n+1} - (2\Delta t)\vec{v}_t^{n+1} + \frac{1}{2}(2\Delta t)^2 - \frac{1}{6}(2\Delta t)^3\vec{v}_{ttt}^{n+1} + O(\Delta t^4)] \\ &= \vec{v}_t^{n+1} - \frac{\Delta t^2}{3}\vec{v}_{ttt}^{n+1} + O(\Delta t^3). \end{aligned} \tag{3.58}$$

The semi-discrete equation can thus be shown to differ from the continuous equation by a second-order error as

$$\vec{v}_t^{n+1} = \vec{G}^{n+1} + \frac{1}{3}\vec{v}_{ttt}^{n+1}\Delta t^2. \tag{3.59}$$

The Navier-Stokes equations can now be written in semi-discrete form for the

BDF-2 scheme,

$$\frac{3\vec{v}^{n+1} - 4\vec{v}^{n} + \vec{v}^{n-1}}{2\Delta t} = -((\vec{v}^{n+1} - \vec{v}_g^{n+1}) \cdot \nabla)\vec{v}^{n+1} - \nabla p^{n+1} + \frac{1}{Re}\nabla^2 \vec{v}^{n+1}. \tag{3.60}$$

Similarly, the semi-discrete Poisson equation is formed for the pressure,

$$\nabla \cdot \nabla p^{n+1} = \nabla \cdot ((\vec{v}^{n+1} - \vec{v}_g^{n+1}) \cdot \nabla)\vec{v}^{n+1}. \tag{3.61}$$

Forming the fully discrete form of this pressure equation is somewhat more complicated, as assurance that the pressure yields a mass-conserving velocity is required. This is treated in detail in § 3.3.3.

3.3.2 Spatial Discretization

The discretizations taken in space are all at least second order. General derivatives are taken with central differences. Boundary derivatives are taken as second-order one-sided differences.

First Derivatives

Error of the first derivative central difference for a function $f(x)$ is

$$\begin{aligned}\frac{f_{i+1} - f_{i-1}}{2\Delta x} &= \frac{1}{2\Delta x}[f_i + \Delta x\ f_i' + \frac{1}{2}\Delta x^2 f_i'' + \frac{1}{6}\Delta x^3 f_i''' + O(\Delta x^4) \\ &\quad -f_i + \Delta x\ f_i' - \frac{1}{2}\Delta x^2 f_i'' + \frac{1}{6}\Delta x^3 f_i''' + O(\Delta x^4)] \\ &= f_i' + \frac{1}{6}\Delta x^2 f_i'''.\end{aligned} \tag{3.62}$$

Error for the backwards and forwards one-sided differences are

Backwards:

$$\begin{aligned}\frac{3f_i - 4f_{i-1} + f_{i-2}}{2\Delta x} &= \frac{1}{2\Delta x}[3f_i \\ &\quad -4f_i + 4\Delta x\ f_i' - \frac{4}{2}\Delta x^2 f_i'' + \frac{4}{6}\Delta x^3 f_i''' + O(\Delta x^4)\end{aligned}$$

$$\begin{aligned}&+f_i - 2\Delta x\ f_i' + \frac{1}{2}(2\Delta x)^2 f_i'' - \frac{1}{6}(2\Delta x)^3 f_i''' + O(\Delta x^4)] \\ &= f_i' - \frac{1}{3}\Delta x^2 f_i'''\end{aligned} \tag{3.63}$$

Forwards:

$$\begin{aligned}\frac{-3f_i + 4f_{i+1} - f_{i+2}}{2\Delta x} &= \frac{1}{2\Delta x}[-3f_i \\ &4f_i + 4\Delta x\ f_i' + \frac{4}{2}\Delta x^2 f_i'' + \frac{4}{6}\Delta x^3 f_i''' + O(\Delta x^4) \\ &-f_i - 2\Delta x\ f_i' - \frac{1}{2}(2\Delta x)^2 f_i'' - \frac{1}{6}(2\Delta x)^3 f_i''' + O(\Delta x^4)] \\ &= f_i' - \frac{1}{3}\Delta x^2 f_i'''.\end{aligned} \tag{3.64}$$

Second Derivatives

Second-order forms are also used for the second derivatives, both for center differences and one-sided differences at the boundaries, as

Center:

$$\begin{aligned}\frac{f_{i+1} - 2f_i + f_{i-1}}{\Delta x^2} &= \frac{1}{\Delta x^2}[\\ &f_i + \Delta x\ f_i' + \frac{1}{2}\Delta x^2 f_i'' + \frac{1}{6}\Delta x^3 f_i''' + \frac{1}{24}\Delta x^4 f_i'''' + O(\Delta x^5) \\ &-2f_i + f_i - \Delta x\ f_i' + \frac{1}{2}\Delta x^2 f_i'' - \frac{1}{6}\Delta x^3 f_i''' + \frac{1}{24}\Delta x^4 f_i'''' + O(\Delta x^5)] \\ &= f_i'' + \frac{1}{12}\Delta x^2 f_i''''\end{aligned} \tag{3.65}$$

Backwards:

$$\begin{aligned}\frac{2f_i - 5f_{i-1} + 4f_{i-2} - f_{i-3}}{\Delta x^2} &= \frac{1}{\Delta x^2}[2f_i \\ &-5f_i + 5\Delta x\ f_i' - \frac{5}{2}\Delta x^2 f_i'' + \frac{5}{6}\Delta x^3 f_i''' - \frac{5}{24}\Delta x^4 f_i'''' + O(\Delta x^5) \\ &+4f_i - 4(2\Delta x) f_i' + \frac{4}{2}(2\Delta x)^2 f_i'' - \frac{4}{6}(2\Delta x)^3 f_i''' + \frac{4}{24}(2\Delta x)^4 f_i'''' + O(\Delta x^5) \\ &-f_i + (3\Delta x) f_i' - \frac{1}{2}(3\Delta x)^2 f_i'' + \frac{1}{6}(3\Delta x)^3 f_i''' - \frac{1}{24}(3\Delta x)^4 f_i'''' + O(\Delta x^5)] \\ &= f_i'' - \frac{11}{12}\Delta x^2 f_i''''\end{aligned} \tag{3.66}$$

Forwards:

$$\begin{aligned}\frac{2f_i - 5f_{i+1} + 4f_{i+2} - f_{i+3}}{\Delta x^2} &= \frac{1}{\Delta x^2}[2f_i \\ &-5f_i - 5\Delta x\ f_i' - \frac{5}{2}\Delta x^2 f_i'' - \frac{5}{6}\Delta x^3 f_i''' - \frac{5}{24}\Delta x^4 f_i'''' + O(\Delta x^5) \\ &+4f_i + 4(2\Delta x)f_i' + \frac{4}{2}(2\Delta x)^2 f_i'' + \frac{4}{6}(2\Delta x)^3 f_i''' + \frac{4}{24}(2\Delta x)^4 f_i'''' + O(\Delta x^5) \\ &-f_i - (3\Delta x)f_i' - \frac{1}{2}(3\Delta x)^2 f_i'' - \frac{1}{6}(3\Delta x)^3 f_i''' - \frac{1}{24}(3\Delta x)^4 f_i'''' + O(\Delta x^5)] \\ &= f_i'' - \frac{11}{12}\Delta x^2 f_i''''. \end{aligned} \tag{3.67}$$

Mixed derivatives involve using the second order first derivatives twice,

$$\begin{aligned}\frac{\partial^2 f}{\partial x \partial y} = \frac{f_{y_{i+1}} - f_{y_{i-1}}}{2\Delta x} &= (f_{y_i} + \frac{1}{6}\Delta y^2 f_{yyy_i})_x + \frac{1}{6}\Delta x^2 f_{yxxx_i} \\ &= f_{xy_i} + \frac{1}{6}\Delta y^2 f_{xyyy_i} + \frac{1}{6}\Delta x^2 f_{yxxx_i}. \end{aligned} \tag{3.68}$$

Upwinding

Stability of the convective term in the Navier-Stokes equation cannot be understood by linear analysis. Nonlinear instability of the high wave number modes is often countered by introduction of numerical dissipation with an upwinding scheme. Discrete spatial derivatives taken are based more heavily on information upstream of the point of interest. The biased upwinding scheme used contains a third-order dissipation term as

For $u > 0$:

$$u\frac{\partial f}{\partial x} = u\frac{f_{i+2} - 2f_{i+1} + 9f_i - 10f_{i-1} + 2f_{i-2}}{6\Delta x} \tag{3.69}$$

For $u \leq 0$:

$$u\frac{\partial f}{\partial x} = u\frac{-2f_{i+2} + 10f_{i+1} - 9f_i + 2f_{i-1} - f_{i-2}}{6\Delta x}, \tag{3.70}$$

where

$$\begin{aligned} u\frac{f_{i+2} - 2f_{i+1} + 9f_i - 10f_{i-1} + 2f_{i-2}}{6\Delta x} &= u\frac{1}{6\Delta x}[\\ f_i + (2\Delta x)f_i' + \frac{1}{2}(2\Delta x)^2 f_i'' &+ \frac{1}{6}(2\Delta x)^3 f_i''' + \frac{1}{24}(2\Delta x)^4 f_i'''' + \frac{1}{120}(2\Delta x)^5 f_i''''' \end{aligned}$$

$$
\begin{aligned}
&-2f_i - 2\Delta x f_i' - \frac{2}{2}\Delta x^2 f_i'' - \frac{2}{6}\Delta x^3 f_i''' - \frac{2}{24}\Delta x^4 f_i'''' - \frac{2}{120}\Delta x^5 f_i''''' + 9f_i \\
&-10f_i + 10\Delta x f_i' - \frac{10}{2}\Delta x^2 f_i'' + \frac{10}{6}\Delta x^3 f_i''' - \frac{10}{24}\Delta x^4 f_i'''' + \frac{10}{120}\Delta x^5 f_i''''' \\
&+2f_i - 2(2\Delta x) f_i' + \frac{2}{2}(2\Delta x)^2 f_i'' - \frac{2}{6}(2\Delta x)^3 f_i''' + \frac{2}{24}(2\Delta x)^4 f_i'''' - \frac{2}{120}(2\Delta x)^5 f_i''''' \\
&+O(\Delta x^6)] \\
&= u\frac{1}{6\Delta x}[6\Delta x f_i' + \frac{36}{24}\Delta x^4 f_i'''' - \frac{24}{120}\Delta x^5 f_i''''' + O(\Delta x^6)] \\
&= u[f_i' + \frac{1}{4}\Delta x^3 f_i'''' - \frac{1}{30}\Delta x^4 f_i'''''] \qquad (3.71)
\end{aligned}
$$

and

$$
\begin{aligned}
u\frac{-2f_{i+2} + 10f_{i+1} - 9f_i + 2f_{i-1} - 1f_{i-2}}{6\Delta x} &= u\frac{1}{6\Delta x}[\\
&-2f_i - 2(2\Delta x) f_i' - \frac{2}{2}(2\Delta x)^2 f_i'' - \frac{2}{6}(2\Delta x)^3 f_i''' - \frac{2}{24}(2\Delta x)^4 f_i'''' - \frac{2}{120}(2\Delta x)^5 f_i''''' \\
&+10f_i + 10\Delta x f_i' + \frac{10}{2}\Delta x^2 f_i'' + \frac{10}{6}\Delta x^3 f_i''' + \frac{10}{24}\Delta x^4 f_i'''' + \frac{10}{120}\Delta x^5 f_i''''' - 9f_i \\
&+2f_i - 2\Delta x f_i' + \frac{2}{2}\Delta x^2 f_i'' - \frac{2}{6}\Delta x^3 f_i''' + \frac{2}{24}\Delta x^4 f_i'''' - \frac{2}{120}\Delta x^5 f_i''''' \\
&-f_i + (2\Delta x) f_i' - \frac{1}{2}(2\Delta x)^2 f_i'' + \frac{1}{6}(2\Delta x)^3 f_i''' - \frac{1}{24}(2\Delta x)^4 f_i'''' + \frac{1}{120}(2\Delta x)^5 f_i''''' \\
&+O(\Delta x^6)] \\
&= u\frac{1}{6\Delta x}[6\Delta x f_i' - \frac{36}{24}\Delta x^4 f_i'''' - \frac{24}{120}\Delta x^5 f_i''''' + O(\Delta x^6)] \\
&= u[f_i' - \frac{1}{4}\Delta x^3 f_i'''' - \frac{1}{30}\Delta x^4 f_i''''']. \qquad (3.72)
\end{aligned}
$$

The scheme used is therefore third-order accurate with leading order dissipation error and a fourth-order dispersion error.

In both equations 3.71 and 3.72, the convective term with leading error appears as

$$u\ f' + |u|\frac{1}{4}\Delta x^3 f''''. \qquad (3.73)$$

Considering f as a collection of wavenumber modes of the velocity field, the convective term can be rewritten as

$$f = \sum_j \hat{f}_j e^{ik_j x} \quad \rightarrow \quad u\, f' + |u|\frac{1}{4}\Delta x^3 f'''' = u\, f' - |u|\frac{1}{4}\Delta x^3 f'' \sum_j k_j^2. \tag{3.74}$$

Using the leading order discretization error of only this convective term, the Navier-Stokes equation, equation 3.40, is rewritten to display the effect of this error on the spectrum of wavenumber modes,

$$\frac{\partial \vec{v}}{\partial t} + (\vec{v} \cdot \vec{\nabla})\vec{v} = -\vec{\nabla} p + \left(\frac{1}{Re} + |\vec{v}|\frac{1}{4}\Delta x^3 \sum_j k_j^2 \right) \nabla^2 \vec{v}. \tag{3.75}$$

The strength of the artificial dissipation introduced by the upwinding of the convective term is a function of the wavenumber. Order-one wavenumbers will be dissipated as Δx^3, while wavenumbers of order $1/\Delta x$ (wavelength order of the grid spacing) will be dissipated as Δx. Such numerical dissipation controls the nonlinear instability associated with inability to resolve the high wavenumbers. This is done with minimal nonphysical effect to the lower wavenumber modes.

Treatment of the upwinding is complicated somewhat by the use of nonorthogonal coordinates. There is a need to group the terms of the convective portion of the mapped Navier-Stokes equations, equations 3.44-3.46, into the multipliers of $\vec{v}_\xi$, $\vec{v}_\rho$, and $\vec{v}_\theta$,

$$\begin{aligned} \vec{v}_\tau + \left[\frac{1}{x_\xi} u \right] \vec{v}_\xi + \left[\frac{uYTZX + (v - v_g)z_\theta - (w - w_g)y_\theta}{J} \right] \vec{v}_\rho + \\ \left[\frac{uYXZR - (v - v_g)z_\rho + (w - w_g)y_\rho}{J} \right] \vec{v}_\theta = -\vec{\nabla} p + \frac{1}{Re}\nabla^2 \vec{v}. \end{aligned} \tag{3.76}$$

The sign of the multipliers A, B, and C, as defined below, determines the stencil of the derivatives in the ξ, ρ, and θ-directions, respectively, according to equations 3.69 and 3.70,

$$A = \frac{1}{x_\xi} u$$

$$B = \frac{uYTZX + (v - v_g)z_\theta - (w - w_g)y_\theta}{J}$$
$$C = \frac{uYXZR - (v - v_g)z_\rho + (w - w_g)y_\rho}{J}. \tag{3.77}$$

3.3.3 The Discrete Poisson Equation

It can be recalled from the development of the pressure Poisson equation, equations 3.49 and 3.50, that a pressure field which ensures mass conservation is desired. This was previously shown in continuous form, but things become complicated in the discrete derivation.

Deriving the Discrete Pressure Equation

For a pressure field which forces the discrete divergence to be zero, the divergence error will be second order. This is shown below in cartesian coordinates, with $\mathcal{D}$ representing the discrete center difference representation of ∇,

$$\vec{\mathcal{D}} \cdot \vec{v} = \vec{\nabla} \cdot \vec{v} + \frac{1}{6}\Delta x^2 u''' + \frac{1}{6}\Delta y^2 v''' + \frac{1}{6}\Delta z^2 w''' = 0$$
$$\longrightarrow \quad \vec{\nabla} \cdot \vec{v} = -\frac{1}{6}\Delta x^2 u''' - \frac{1}{6}\Delta y^2 v''' - \frac{1}{6}\Delta z^2 w'''. \tag{3.78}$$

Thus, there is some error to the mass conservation due to the discrete vector operator $\mathcal{D}$. This error will be designated e_1,

$$e_1 = -\frac{1}{6}\Delta x^2 u''' - \frac{1}{6}\Delta y^2 v''' - \frac{1}{6}\Delta z^2 w'''. \tag{3.79}$$

For the curvilinear coordinates used, $\mathcal{D}$ needs to be expressed in the computational domain. The expressions of equations 3.22, 3.23, and 3.24 are employed, requiring the use of the grid metrics. If these metrics were available in exact form from analytic expressions there would be no error associated with them. However, the metrics are calculated numerically on the grid using the second-order discretizations discussed earlier. For this reason, the error given by e_1 on the curvilinear grid actually comes from the product of second-order expressions. Such a product will retain second-order accuracy, so that

$$e_1 = O(\Delta^2). \tag{3.80}$$

The error in mass conservation due to the discrete divergence is not the only associated error. With the implicit scheme used, the velocity and pressure are solved in an iterative fashion which will be detailed later. From such a scheme there will be an error associated with not having obtained exact convergence of the solution. This convergence error is a function of the tolerance being used, and will be designated e_2.

In deriving the fully discrete Poisson equation, a time step is designated for the discrete operator $\mathcal{D}$, as the grid metrics on a moving grid are a function of time. We first rewrite equation 3.60 with the discrete operators indicating the fully-discrete Navier-Stokes equation,

$$\begin{aligned}&\frac{3\vec{v}^{n+1} - 4\vec{v}^{n} + \vec{v}^{n-1}}{2\Delta t} = \\ &\quad -((\vec{v}^{n+1} - \vec{v}_g^{n+1}) \cdot \mathcal{D}_u{}^{n+1})\vec{v}^{n+1} - \mathcal{D}^{n+1}p^{n+1} + \frac{1}{Re}\mathcal{L}^{n+1}\vec{v}^{n+1}.\end{aligned} \tag{3.81}$$

Here, $\mathcal{L}$ is the discrete Laplacian which applies the second-order spatial discretizations of equations 3.29 and 3.30. The upwinding operator is designated by $\mathcal{D}_u$. The terms of the discrete Navier-Stokes equation are then rearranged as

$$\frac{3}{2\Delta t}\vec{v}^{n+1} = -\mathcal{D}^{n+1}p^{n+1} + \vec{F}, \tag{3.82}$$

where

$$\vec{F} = \frac{4\vec{v}^{n} - \vec{v}^{n-1}}{2\Delta t} - ((\vec{v}^{n+1} - \vec{v}_g^{n+1}) \cdot \mathcal{D}_u{}^{n+1})\vec{v}^{n+1} + \frac{1}{Re}\mathcal{L}^{n+1}\vec{v}^{n+1}. \tag{3.83}$$

The discrete divergence operator at time $n+1$ is applied to equation 3.82,

$$\frac{3}{2\Delta t}\mathcal{D}^{n+1} \cdot \vec{v}^{n+1} = -\mathcal{D}^{n+1} \cdot \mathcal{D}^{n+1}p^{n+1} + \mathcal{D}^{n+1} \cdot \vec{F}. \tag{3.84}$$

Forcing the right-hand side of equation 3.84 to be zero makes the discrete divergence zero. It should be noted that the viscous term of the velocity Laplacian is not included on the left-hand side. This is due to the following inequality for the fully discrete transformed equations,

$$\mathcal{D} \cdot (\mathcal{L}\vec{v}) \neq \mathcal{L}(\mathcal{D} \cdot \vec{v}). \tag{3.85}$$

Likewise, the earlier velocity terms from the time derivative are not included on the left-hand side, as the discrete divergence operator applied is not from the same time step as these velocities.

If a pressure field is found which ensures that the right-hand side of equation 3.84 disappears, then the mass error will be limited to $e_1 + e_2$. This seems at first relatively straightforward, a matter of ensuring that the discretization is chosen properly in the pressure Poisson equation.

Consider the one-dimensional case where $\mathcal{D}^{n+1} f_i = A_i(f_{i+1} - f_{i-1})/2\Delta x$ so that equation 3.84 is

$$\frac{3}{2\Delta t} A_i \frac{u_{i+1} - u_{i-1}}{2\Delta x} = -A_i \frac{A_{i+1} \frac{p_{i+2} - p_i}{2\Delta x} - A_{i-1} \frac{p_i - p_{i-2}}{2\Delta x}}{2\Delta x} + A_i \frac{F_{i+1} - F_{i-1}}{2\Delta x}. \tag{3.86}$$

Thus, the pressure equation which yields zero discrete divergence can be written in discrete form as

$$\frac{A_i}{4\Delta x^2} (A_{i+1} p_{i+2} - A_{i+1} p_i - A_{i-1} p_i + A_{i-1} p_{i-2}) = A_i \frac{F_{i+1} - F_{i-1}}{2\Delta x} = \sigma_i, \tag{3.87}$$

or

$$\widetilde{\mathcal{L}5}\; p_i = \sigma_i. \tag{3.88}$$

Here, $\widetilde{\mathcal{L}5}$ represents the discrete pressure Laplacian operator taken over a five point stencil. With such a discrete operator, it's clear to see that neighboring pressure points are uncoupled from each other, a phenomenon that extends to two and three-dimensional formulations. It's important to understand the nature of this decoupling in solving the pressure system. Use of a compact three point stencil does couple all of the neighboring points, but eliminates the consistency between the pressure and velocity solutions. Such lack of consistency manifests as an error in the discrete divergence. In order to maintain the consistency and not introduce any error to the discrete divergence, the five point scheme is used. Global coupling between the 'independent' grids is obtained in the solution procedure through the boundary treatment and the desingularization method, as will be later described in § 3.4.

Forming the Pressure Coefficients

Now the exact expression for $\widetilde{\mathcal{L}5}p$ on the three-dimensional transformed grid is to be formed. This is done by plugging equations 3.22, 3.23, and 3.24 into themselves. However, unlike with the Laplacian used in the viscous term, the $\widetilde{\mathcal{L}5}$ rules for forming the coefficients must be carefully followed to ensure consistency with the discrete Navier-Stokes equations and discrete mass conservation. Three indices are (i, j, k), assumed to be centered in the fully discrete representation if not otherwise indicated. For the x-direction we have

$$\mathcal{D}_x\mathcal{D}_x p = \mathcal{D}_x\left[\frac{1}{x_\xi}p_\xi + \frac{YTZX}{J}p_\rho + \frac{YXZR}{J}p_\theta\right] = AX + BX + CX, \tag{3.89}$$

where

$$\begin{aligned}
AX &= \frac{1}{x_\xi^2}p_{\xi\xi} + \frac{1}{x_\xi}\left(\frac{YTZX}{J}p_\rho\right)_\xi + \frac{1}{x_\xi}\left(\frac{YXZR}{J}p_\theta\right)_\xi \\
&= \frac{1}{x_\xi^2}\frac{p_{i+2} - 2p_i + p_{i-2}}{4\Delta\xi^2} + \frac{1}{x_\xi}\frac{1}{2\Delta\xi}\left(\frac{YTZX_{i+1}}{J_{i+1}}\right)\frac{p_{i+1,j+1} - p_{i+1,j-1}}{2\Delta\rho} - \\
&\quad \frac{1}{x_\xi}\frac{1}{2\Delta\xi}\left(\frac{YTZX_{i-1}}{J_{i-1}}\right)\frac{p_{i-1,j+1} - p_{i-1,j-1}}{2\Delta\rho} + \\
&\quad \frac{1}{x_\xi}\frac{1}{2\Delta\xi}\left(\frac{YXZR_{i+1}}{J_{i+1}}\right)\frac{p_{i+1,k+1} - p_{i+1,k-1}}{2\Delta\theta} - \\
&\quad \frac{1}{x_\xi}\frac{1}{2\Delta\xi}\left(\frac{YXZR_{i-1}}{J_{i-1}}\right)\frac{p_{i-1,k+1} - p_{i-1,k-1}}{2\Delta\theta}
\end{aligned} \tag{3.90}$$

$$\begin{aligned} BX &= \frac{YTZX}{J}\left[\frac{1}{x_\xi}p_{\xi\rho} + \left(\frac{YTZX}{J}p_\rho\right)_\rho + \left(\frac{YXZR}{J}p_\theta\right)_\rho\right] \\ &= \frac{YTZX}{J}[\frac{1}{x_\xi}\frac{p_{i+1,j+1} - p_{i-1,j+1} - p_{i+1,j-1} + p_{i-1,j-1}}{4\Delta\xi\Delta\rho} + \\ &\frac{1}{2\Delta\rho}\left(\frac{YTZX_{j+1}}{J_{j+1}}\right)\frac{p_{j+2} - p_j}{2\Delta\rho} - \frac{1}{2\Delta\rho}\left(\frac{YTZX_{j-1}}{J_{j-1}}\right)\frac{p_j - p_{j-2}}{2\Delta\rho} + \\ &\frac{1}{2\Delta\rho}\left(\frac{YXZR_{j+1}}{J_{j+1}}\right)\frac{p_{j+1,k+1} - p_{j+1,k-1}}{2\Delta\theta} - \frac{1}{2\Delta\rho}\left(\frac{YXZR_{j-1}}{J_{j-1}}\right)\frac{p_{j-1,k+1} - p_{j-1,k-1}}{2\Delta\theta}] \end{aligned} \tag{3.91}$$

$$\begin{aligned} CX &= \frac{YXZR}{J}\left[\frac{1}{x_\xi}p_{\xi\theta} + \left(\frac{YTZX}{J}p_\rho\right)_\theta + \left(\frac{YXZR}{J}p_\theta\right)_\theta\right] \\ &= \frac{YXZR}{J}[\frac{1}{x_\xi}\frac{p_{i+1,k+1} - p_{i-1,k+1} - p_{i+1,k-1} + p_{i-1,k-1}}{4\Delta\xi\Delta\theta} + \\ &\frac{1}{2\Delta\theta}\left(\frac{YTZX_{k+1}}{J_{k+1}}\right)\frac{p_{j+1,k+1} - p_{j-1,k+1}}{2\Delta\rho} - \frac{1}{2\Delta\theta}\left(\frac{YTZX_{k-1}}{J_{k-1}}\right)\frac{p_{j+1,k-1} - p_{j-1,k-1}}{2\Delta\rho} + \\ &\frac{1}{2\Delta\theta}\left(\frac{YXZR_{k+1}}{J_{k+1}}\right)\frac{p_{k+2} - p_k}{2\Delta\theta} - \frac{1}{2\Delta\theta}\left(\frac{YXZR_{k-1}}{J_{k-1}}\right)\frac{p_k - p_{k-2}}{2\Delta\theta}]. \end{aligned} \tag{3.92}$$

For the y-direction we have

$$\mathcal{D}_y\mathcal{D}_y p = \mathcal{D}_y\left[\frac{z_\theta}{J}p_\rho - \frac{z_\rho}{J}p_\theta\right] = AY + BY, \tag{3.93}$$

where

$$\begin{aligned} AY &= \frac{z_\theta}{J}\left[\left(\frac{z_\theta}{J}p_\rho\right)_\rho - \left(\frac{z_\rho}{J}p_\theta\right)_\rho\right] \\ &= \frac{z_\theta}{J}[\frac{1}{2\Delta\rho}\left(\frac{z_{\theta\,j+1}}{J_{j+1}}\right)\frac{p_{j+2} - p_j}{2\Delta\rho} - \frac{1}{2\Delta\rho}\left(\frac{z_{\theta\,j-1}}{J_{j-1}}\right)\frac{p_j - p_{j-2}}{2\Delta\rho} - \\ &\frac{1}{2\Delta\rho}\left(\frac{z_{\rho\,j+1}}{J_{j+1}}\right)\frac{p_{j+1,k+1} - p_{j+1,k-1}}{2\Delta\theta} + \frac{1}{2\Delta\rho}\left(\frac{z_{\rho\,j-1}}{J_{j-1}}\right)\frac{p_{j-1,k+1} - p_{j-1,k-1}}{2\Delta\theta}] \end{aligned} \tag{3.94}$$

$$\begin{aligned} BY &= -\frac{z_\rho}{J}\left[\left(\frac{z_\theta}{J}p_\rho\right)_\theta - \left(\frac{z_\rho}{J}p_\theta\right)_\theta\right] \\ &= -\frac{z_\rho}{J}[\frac{1}{2\Delta\theta}\left(\frac{z_{\theta\,k+1}}{J_{k+1}}\right)\frac{p_{j+1,k+1} - p_{j-1,k+1}}{2\Delta\rho} - \frac{1}{2\Delta\theta}\left(\frac{z_{\theta\,k-1}}{J_{k-1}}\right)\frac{p_{j+1,k-1} - p_{j-1,k-1}}{2\Delta\rho} - \\ &\frac{1}{2\Delta\theta}\left(\frac{z_{\rho\,k+1}}{J_{k+1}}\right)\frac{p_{k+2} - p_k}{\Delta\theta} + \frac{1}{2\Delta\theta}\left(\frac{z_{\rho\,k-1}}{J_{k-1}}\right)\frac{p_k - p_{k-2}}{2\Delta\theta}]. \end{aligned} \tag{3.95}$$

For the z-direction we have

$$\mathcal{D}_z\mathcal{D}_z p = \mathcal{D}_z\left[-\frac{y_\theta}{J}p_\rho + \frac{y_\rho}{J}p_\theta\right] = AZ + BZ, \tag{3.96}$$

where

$$\begin{aligned} AZ &= -\frac{y_\theta}{J}\left[\left(-\frac{y_\theta}{J}p_\rho\right)_\rho + \left(\frac{y_\rho}{J}p_\theta\right)_\rho\right] \\ &= -\frac{y_\theta}{J}[-\frac{1}{2\Delta\rho}\left(\frac{y_{\theta\, j+1}}{J_{j+1}}\right)\frac{p_{j+2}-p_j}{2\Delta\rho} + \frac{1}{2\Delta\rho}\left(\frac{y_{\theta\, j-1}}{J_{j-1}}\right)\frac{p_j-p_{j-2}}{2\Delta\rho} + \\ &\frac{1}{2\Delta\rho}\left(\frac{y_{\rho\, j+1}}{J_{j+1}}\right)\frac{p_{j+1,k+1}-p_{j+1,k-1}}{2\Delta\theta} - \frac{1}{2\Delta\rho}\left(\frac{y_{\rho\, j-1}}{J_{j-1}}\right)\frac{p_{j-1,k+1}-p_{j-1,k-1}}{2\Delta\theta}] \end{aligned} \tag{3.97}$$

$$\begin{aligned} BZ &= \frac{y_\rho}{J}\left[\left(-\frac{y_\theta}{J}p_\rho\right)_\theta + \left(\frac{y_\rho}{J}p_\theta\right)_\theta\right] \\ &= \frac{y_\rho}{J}[-\frac{1}{2\Delta\theta}\left(\frac{y_{\theta\, k+1}}{J_{k+1}}\right)\frac{p_{j+1,k+1}-p_{j-1,k+1}}{2\Delta\rho} + \frac{1}{2\Delta\theta}\left(\frac{y_{\theta\, k-1}}{J_{k-1}}\right)\frac{p_{j+1,k-1}-p_{j-1,k-1}}{2\Delta\rho} + \\ &\frac{1}{2\Delta\theta}\left(\frac{y_{\rho\, k+1}}{J_{k+1}}\right)\frac{p_{k+2}-p_k}{2\Delta\theta} - \frac{1}{2\Delta\theta}\left(\frac{y_{\rho\, k-1}}{J_{k-1}}\right)\frac{p_k-p_{k-2}}{2\Delta\theta}]. \end{aligned} \tag{3.98}$$

The pressure stencil involves nineteen points with the following coefficients,

$$\begin{aligned} C_{i,j,k} &= -\frac{1}{x_\xi^2}\frac{2}{4\Delta\xi^2} \\ &-\frac{YTZX_{i,j,k}}{J_{i,j,k}}\frac{1}{4\Delta\rho^2}\left(\frac{YTZX_{i,j+1,k}}{J_{i,j+1,k}}\right) - \frac{YTZX_{i,j,k}}{J_{i,j,k}}\frac{1}{4\Delta\rho^2}\left(\frac{YTZX_{i,j-1,k}}{J_{i,j-1,k}}\right) \\ &-\frac{YXZR_{i,j,k}}{J_{i,j,k}}\frac{1}{4\Delta\theta^2}\left(\frac{YXZR_{i,j,k+1}}{J_{i,j,k+1}}\right) - \frac{YXZR_{i,j,k}}{J_{i,j,k}}\frac{1}{4\Delta\theta^2}\left(\frac{YXZR_{i,j,k-1}}{J_{i,j,k-1}}\right) \\ &-\frac{z_{\theta\, i,j,k}}{J_{i,j,k}}\frac{1}{4\Delta\rho^2}\left(\frac{z_{\theta\, i,j+1,k}}{J_{i,j+1,k}}\right) - \frac{z_{\theta\, i,j,k}}{J_{i,j,k}}\frac{1}{4\Delta\rho^2}\left(\frac{z_{\theta\, i,j-1,k}}{J_{i,j-1,k}}\right) \\ &-\frac{z_{\rho\, i,j,k}}{J_{i,j,k}}\frac{1}{4\Delta\theta^2}\left(\frac{z_{\rho\, i,j,k+1}}{J_{i,j,k+1}}\right) - \frac{z_{\rho\, i,j,k}}{J_{i,j,k}}\frac{1}{4\Delta\theta^2}\left(\frac{z_{\rho\, i,j,k-1}}{J_{i,j,k-1}}\right) \\ &-\frac{y_{\theta\, i,j,k}}{J_{i,j,k}}\frac{1}{4\Delta\rho^2}\left(\frac{y_{\theta\, i,j+1,k}}{J_{i,j+1,k}}\right) - \frac{y_{\theta\, i,j,k}}{J_{i,j,k}}\frac{1}{4\Delta\rho^2}\left(\frac{y_{\theta\, i,j-1,k}}{J_{i,j-1,k}}\right) \\ &-\frac{y_{\rho\, i,j,k}}{J_{i,j,k}}\frac{1}{4\Delta\theta^2}\left(\frac{y_{\rho\, i,j,k+1}}{J_{i,j,k+1}}\right) - \frac{y_{\rho\, i,j,k}}{J_{i,j,k}}\frac{1}{4\Delta\theta^2}\left(\frac{y_{\rho\, i,j,k-1}}{J_{i,j,k-1}}\right) \end{aligned} \tag{3.99}$$

$$C_{i+2,j,k} = \frac{1}{x_\xi^2}\frac{1}{4\Delta\xi^2} \tag{3.100}$$

$$C_{i+1,j+1,k} = \frac{1}{x_\xi}\frac{1}{4\Delta\xi\Delta\rho}\frac{YTZX_{i+1,j,k}}{J_{i+1,j,k}} + \frac{1}{x_\xi}\frac{1}{4\Delta\xi\Delta\rho}\frac{YTZX_{i,j,k}}{J_{i,j,k}} \tag{3.101}$$

$$C_{i+1,j-1,k} = -\frac{1}{x_\xi}\frac{1}{4\Delta\xi\Delta\rho}\frac{YTZX_{i+1,j,k}}{J_{i+1,j,k}} - \frac{1}{x_\xi}\frac{1}{4\Delta\xi\Delta\rho}\frac{YTZX_{i,j,k}}{J_{i,j,k}} \tag{3.102}$$

$$C_{i+1,j,k+1} = \frac{1}{x_\xi}\frac{1}{4\Delta\xi\Delta\theta}\frac{YXZR_{i+1,j,k}}{J_{i+1,j,k}} + \frac{1}{x_\xi}\frac{1}{4\Delta\xi\Delta\theta}\frac{YXZR_{i,j,k}}{J_{i,j,k}} \tag{3.103}$$

$$C_{i+1,j,k-1} = -\frac{1}{x_\xi}\frac{1}{4\Delta\xi\Delta\theta}\frac{YXZR_{i+1,j,k}}{J_{i+1,j,k}} - \frac{1}{x_\xi}\frac{1}{4\Delta\xi\Delta\theta}\frac{YXZR_{i,j,k}}{J_{i,j,k}} \tag{3.104}$$

$$C_{i-2,j,k} = \frac{1}{x_\xi^2}\frac{1}{4\Delta\xi^2} \tag{3.105}$$

$$C_{i-1,j+1,k} = -\frac{1}{x_\xi}\frac{1}{4\Delta\xi\Delta\rho}\frac{YTZX_{i-1,j,k}}{J_{i-1,j,k}} - \frac{1}{x_\xi}\frac{1}{4\Delta\xi\Delta\rho}\frac{YTZX_{i,j,k}}{J_{i,j,k}} \tag{3.106}$$

$$C_{i-1,j-1,k} = \frac{1}{x_\xi}\frac{1}{4\Delta\xi\Delta\rho}\frac{YTZX_{i-1,j,k}}{J_{i-1,j,k}} + \frac{1}{x_\xi}\frac{1}{4\Delta\xi\Delta\rho}\frac{YTZX_{i,j,k}}{J_{i,j,k}} \tag{3.107}$$

$$C_{i-1,j,k+1} = -\frac{1}{x_\xi}\frac{1}{4\Delta\xi\Delta\theta}\frac{YXZR_{i-1,j,k}}{J_{i-1,j,k}} - \frac{1}{x_\xi}\frac{1}{4\Delta\xi\Delta\theta}\frac{YXZR_{i,j,k}}{J_{i,j,k}} \tag{3.108}$$

$$C_{i-1,j,k-1} = \frac{1}{x_\xi}\frac{1}{4\Delta\xi\Delta\theta}\frac{YXZR_{i-1,j,k}}{J_{i-1,j,k}} + \frac{1}{x_\xi}\frac{1}{4\Delta\xi\Delta\theta}\frac{YXZR_{i,j,k}}{J_{i,j,k}} \tag{3.109}$$

$$\begin{aligned} C_{i,j+2,k} = {} & \frac{YTZX_{i,j,k}}{J_{i,j,k}}\frac{1}{4\Delta\rho^2}\left(\frac{YTZX_{i,j+1,k}}{J_{i,j+1,k}}\right) + \frac{z_{\theta\, i,j,k}}{J_{i,j,k}}\frac{1}{4\Delta\rho^2}\left(\frac{z_{\theta\, i,j+1,k}}{J_{i,j+1,k}}\right) \\ & + \frac{y_{\theta\, i,j,k}}{J_{i,j,k}}\frac{1}{4\Delta\rho^2}\left(\frac{y_{\theta\, i,j+1,k}}{J_{i,j+1,k}}\right) \end{aligned} \tag{3.110}$$

$$\begin{aligned} C_{i,j+1,k+1} = {} & \frac{YTZX_{i,j,k}}{J_{i,j,k}}\frac{1}{4\Delta\rho\Delta\theta}\frac{YXZR_{i,j+1,k}}{J_{i,j+1,k}} + \frac{YXZR_{i,j,k}}{J_{i,j,k}}\frac{1}{4\Delta\rho\Delta\theta}\frac{YTZX_{i,j,k+1}}{J_{i,j,k+1}} \\ & - \frac{z_{\theta\, i,j,k}}{J_{i,j,k}}\frac{1}{4\Delta\rho\Delta\theta}\frac{z_{\rho\, i,j+1,k}}{J_{i,j+1,k}} - \frac{z_{\rho\, i,j,k}}{J_{i,j,k}}\frac{1}{4\Delta\rho\Delta\theta}\frac{z_{\theta\, i,j,k+1}}{J_{i,j,k+1}} \\ & - \frac{y_{\theta\, i,j,k}}{J_{i,j,k}}\frac{1}{4\Delta\rho\Delta\theta}\frac{y_{\rho\, i,j+1,k}}{J_{i,j+1,k}} - \frac{y_{\rho\, i,j,k}}{J_{i,j,k}}\frac{1}{4\Delta\rho\Delta\theta}\frac{y_{\theta\, i,j,k+1}}{J_{i,j,k+1}} \end{aligned} \tag{3.111}$$

$$
\begin{aligned}
C_{i,j+1,k-1} = & -\frac{YTZX_{i,j,k}}{J_{i,j,k}}\frac{1}{4\Delta\rho\Delta\theta}\frac{YXZR_{i,j+1,k}}{J_{i,j+1,k}} - \frac{YXZR_{i,j,k}}{J_{i,j,k}}\frac{1}{4\Delta\rho\Delta\theta}\frac{YTZX_{i,j,k-1}}{J_{i,j,k-1}} \\
& + \frac{z_{\theta\, i,j,k}}{J_{i,j,k}}\frac{1}{4\Delta\rho\Delta\theta}\frac{z_{\rho\, i,j+1,k}}{J_{i,j+1,k}} + \frac{z_{\rho\, i,j,k}}{J_{i,j,k}}\frac{1}{4\Delta\rho\Delta\theta}\frac{z_{\theta\, i,j,k-1}}{J_{i,j,k-1}} \\
& + \frac{y_{\theta\, i,j,k}}{J_{i,j,k}}\frac{1}{4\Delta\rho\Delta\theta}\frac{y_{\rho\, i,j+1,k}}{J_{i,j+1,k}} + \frac{y_{\rho\, i,j,k}}{J_{i,j,k}}\frac{1}{4\Delta\rho\Delta\theta}\frac{y_{\theta\, i,j,k-1}}{J_{i,j,k-1}}
\end{aligned}
\tag{3.112}
$$

$$
\begin{aligned}
C_{i,j-2,k} = & \frac{YTZX_{i,j,k}}{J_{i,j,k}}\frac{1}{4\Delta\rho^2}\left(\frac{YTZX_{i,j-1,k}}{J_{i,j-1,k}}\right) + \frac{z_{\theta\, i,j,k}}{J_{i,j,k}}\frac{1}{4\Delta\rho^2}\left(\frac{z_{\theta\, i,j-1,k}}{J_{i,j-1,k}}\right) \\
& + \frac{y_{\theta\, i,j,k}}{J_{i,j,k}}\frac{1}{4\Delta\rho^2}\left(\frac{y_{\theta\, i,j-1,k}}{J_{i,j-1,k}}\right)
\end{aligned}
\tag{3.113}
$$

$$
\begin{aligned}
C_{i,j-1,k+1} = & -\frac{YTZX_{i,j,k}}{J_{i,j,k}}\frac{1}{4\Delta\rho\Delta\theta}\frac{YXZR_{i,j-1,k}}{J_{i,j-1,k}} - \frac{YXZR_{i,j,k}}{J_{i,j,k}}\frac{1}{4\Delta\rho\Delta\theta}\frac{YTZX_{i,j,k+1}}{J_{i,j,k+1}} \\
& + \frac{z_{\theta\, i,j,k}}{J_{i,j,k}}\frac{1}{4\Delta\rho\Delta\theta}\frac{z_{\rho\, i,j-1,k}}{J_{i,j-1,k}} + \frac{z_{\rho\, i,j,k}}{J_{i,j,k}}\frac{1}{4\Delta\rho\Delta\theta}\frac{z_{\theta\, i,j,k+1}}{J_{i,j,k+1}} \\
& + \frac{y_{\theta\, i,j,k}}{J_{i,j,k}}\frac{1}{4\Delta\rho\Delta\theta}\frac{y_{\rho\, i,j-1,k}}{J_{i,j-1,k}} + \frac{y_{\rho\, i,j,k}}{J_{i,j,k}}\frac{1}{4\Delta\rho\Delta\theta}\frac{y_{\theta\, i,j,k+1}}{J_{i,j,k+1}}
\end{aligned}
\tag{3.114}
$$

$$
\begin{aligned}
C_{i,j-1,k-1} = & \frac{YTZX_{i,j,k}}{J_{i,j,k}}\frac{1}{4\Delta\rho\Delta\theta}\frac{YXZR_{i,j-1,k}}{J_{i,j-1,k}} + \frac{YXZR_{i,j,k}}{J_{i,j,k}}\frac{1}{4\Delta\rho\Delta\theta}\frac{YTZX_{i,j,k-1}}{J_{i,j,k-1}} \\
& - \frac{z_{\theta\, i,j,k}}{J_{i,j,k}}\frac{1}{4\Delta\rho\Delta\theta}\frac{z_{\rho\, i,j-1,k}}{J_{i,j-1,k}} - \frac{z_{\rho\, i,j,k}}{J_{i,j,k}}\frac{1}{4\Delta\rho\Delta\theta}\frac{z_{\theta\, i,j,k-1}}{J_{i,j,k-1}} \\
& - \frac{y_{\theta\, i,j,k}}{J_{i,j,k}}\frac{1}{4\Delta\rho\Delta\theta}\frac{y_{\rho\, i,j-1,k}}{J_{i,j-1,k}} - \frac{y_{\rho\, i,j,k}}{J_{i,j,k}}\frac{1}{4\Delta\rho\Delta\theta}\frac{y_{\theta\, i,j,k-1}}{J_{i,j,k-1}}
\end{aligned}
\tag{3.115}
$$

$$
\begin{aligned}
C_{i,j,k+2} = & \frac{YXZR_{i,j,k}}{J_{i,j,k}}\frac{1}{4\Delta\theta^2}\left(\frac{YXZR_{i,j,k+1}}{J_{i,j,k+1}}\right) + \frac{z_{\rho\, i,j,k}}{J_{i,j,k}}\frac{1}{4\Delta\theta^2}\left(\frac{z_{\rho\, i,j,k+1}}{J_{i,j,k+1}}\right) \\
& + \frac{y_{\rho\, i,j,k}}{J_{i,j,k}}\frac{1}{4\Delta\theta^2}\left(\frac{y_{\rho\, i,j,k+1}}{J_{i,j,k+1}}\right)
\end{aligned}
\tag{3.116}
$$

$$
\begin{aligned}
C_{i,j,k-2} = & \frac{YXZR_{i,j,k}}{J_{i,j,k}}\frac{1}{4\Delta\theta^2}\left(\frac{YXZR_{i,j,k-1}}{J_{i,j,k-1}}\right) + \frac{z_{\rho\, i,j,k}}{J_{i,j,k}}\frac{1}{4\Delta\theta^2}\left(\frac{z_{\rho\, i,j,k-1}}{J_{i,j,k-1}}\right) \\
& + \frac{y_{\rho\, i,j,k}}{J_{i,j,k}}\frac{1}{4\Delta\theta^2}\left(\frac{y_{\rho\, i,j,k-1}}{J_{i,j,k-1}}\right).
\end{aligned}
\tag{3.117}
$$

The discrete source term, the right-hand-side, comes from the application of $\mathcal{D}\cdot\vec{F}$, and is written

$$
\begin{aligned}
\sigma = {} & \frac{1}{x_\xi}\frac{F_{x_{i+1}} - F_{x_{i-1}}}{2\Delta\xi} + \frac{YTZX}{J}\frac{F_{x_{j+1}} - F_{x_{j-1}}}{2\Delta\rho} + \frac{YXZR}{J}\frac{F_{x_{k+1}} - F_{x_{k-1}}}{2\Delta\theta} \\
& + \frac{z_\theta}{J}\frac{F_{y_{j+1}} - F_{y_{j-1}}}{2\Delta\rho} - \frac{z_\rho}{J}\frac{F_{y_{k+1}} - F_{y_{k-1}}}{2\Delta\theta} - \frac{y_\theta}{J}\frac{F_{z_{j+1}} - F_{z_{j-1}}}{2\Delta\rho} + \frac{y_\rho}{J}\frac{F_{z_{k+1}} - F_{z_{k-1}}}{2\Delta\theta}.
\end{aligned}
\tag{3.118}
$$

Treatment at the Boundary

The Neumann pressure boundary condition must be constructed in such a way as to maintain consistency between the velocity and pressure systems. It's important to consider the effect of the boundary derivative enforced on this consistency at the point adjacent to the boundary. In fact, the boundary derivative component of the adjacent point pressure equation is used exactly as the boundary condition.

The implementation of the boundary condition is first illustrated in a two-dimensional cartesian system with boundary in the y-direction. The momentum equation is written as

$$
\mathcal{D}p = a\vec{v} + \vec{F}. \tag{3.119}
$$

The pressure equation is found by taking the discrete divergence of the above equation,

$$
\mathcal{D}\cdot\mathcal{D}p = a\mathcal{D}\cdot\vec{v} + \mathcal{D}\cdot\vec{F}. \tag{3.120}
$$

Interior points would normally have mass conservation enforced by setting the velocity divergence term to zero. For the case adjacent to the boundary the equation is expanded, using $\mathcal{PY}$ to represent the boundary derivative,

$$
\begin{aligned}
& \frac{p_{i+2} - 2p_i + p_{i-2}}{4\Delta^2} + \frac{\frac{p_{j+2}-p_j}{2\Delta} - \mathcal{PY}_{j-1}}{2\Delta} = \\
& a\left[\frac{u_{i+1} - u_{i-1}}{2\Delta} + \frac{v_{j+1} - v_{j-1}}{2\Delta}\right] + \left[\frac{F_{x_{i+1}} - F_{x_{i-1}}}{2\Delta} + \frac{F_{y_{j+1}} - F_{y_{j-1}}}{2\Delta}\right].
\end{aligned}
\tag{3.121}
$$

The boundary condition is then taken as that part of the above expression evaluated on the boundary,

$$\frac{1}{2\Delta}\mathcal{P}\mathcal{Y}_{j-1} = a\frac{v_{j-1}}{2\Delta} + \frac{F_{y_{j-1}}}{2\Delta}. \tag{3.122}$$

Now, equation 3.121 is rewritten with the divergence term set to zero, so that it enforces mass conservation,

$$\begin{gathered} \frac{p_{i+2} - 2p_i + p_{i-2}}{4\Delta^2} + \frac{\frac{p_{j+2}-p_j}{2\Delta} - \mathcal{P}\mathcal{Y}_{j-1}}{2\Delta} = \\ [\frac{F_{x_{i+1}} - F_{x_{i-1}}}{2\Delta} + \frac{F_{y_{j+1}} - F_{y_{j-1}}}{2\Delta}], \end{gathered} \tag{3.123}$$

and substituting for $\mathcal{P}\mathcal{Y}$ from equation 3.122,

$$\begin{gathered} \frac{p_{i+2} - 2p_i + p_{i-2}}{4\Delta^2} + \frac{p_{j+2} - p_j}{4\Delta^2} = \\ a\frac{v_{j-1}}{2\Delta} + [\frac{F_{x_{i+1}} - F_{x_{i-1}}}{2\Delta} + \frac{F_{y_{j+1}}}{2\Delta}]. \end{gathered} \tag{3.124}$$

The equations 3.124 and 3.122 are those to be solved on the boundary-adjacent and boundary points, ensuring mass conservation. A second-order forward derivative would be used for the discrete formulation of the boundary pressure derivative $\mathcal{P}\mathcal{Y}$, reflecting that equation 3.122 is just an expression of the momentum equation normal to the boundary.

Another way to consider this method is starting from the expression of the discrete divergence,

$$\mathcal{D} \cdot \vec{v} = \frac{u_{i+1} - u_{i-1}}{2\Delta} + \frac{v_{j+1} - v_{j-1}}{2\Delta}, \tag{3.125}$$

and substituting in from the momentum equation 3.119. The difference at the boundary is that the velocity is given, it is not solved from the momentum equation. For this reason there is no such substitution made at the boundary, instead retaining the boundary velocity term in the boundary-adjacent divergence equation. This results in the boundary-adjacent equation 3.124.

The formulation is now extended to our transformed three-dimensional problem by considering the boundary derivative terms in the boundary-adjacent formulation of the pressure equation from equations 3.90-3.98. The boundary derivatives contain components in all computational directions.

The boundary derivative expression for the lower boundary is

$$\begin{aligned}
&\frac{YTZX}{J}\left(\frac{1}{2\Delta\rho}\frac{1}{x_\xi}p_{\xi_{j-1}}+\frac{1}{2\Delta\rho}\frac{YTZX_{j-1}}{J_{j-1}}p_{\rho_{j-1}}+\frac{1}{2\Delta\rho}\frac{YXZR_{j-1}}{J_{j-1}}p_{\theta_{j-1}}\right) \qquad (3.126)\\
&+\frac{z_\theta}{J}\left(\frac{1}{2\Delta\rho}\frac{z_{\theta\,j-1}}{J_{j-1}}p_{\rho_{j-1}}-\frac{1}{2\Delta\rho}\frac{z_{\rho\,j-1}}{J_{j-1}}p_{\theta_{j-1}}\right)\\
&+\frac{y_\theta}{J}\left(\frac{1}{2\Delta\rho}\frac{y_{\theta\,j-1}}{J_{j-1}}p_{\rho_{j-1}}-\frac{1}{2\Delta\rho}\frac{y_{\rho\,j-1}}{J_{j-1}}p_{\theta_{j-1}}\right)\\
&=\frac{YTZX}{J}\left(-\frac{3}{2\Delta t}\frac{u_{j-1}}{2\Delta\rho}+\frac{F_{x_{j-1}}}{2\Delta\rho}\right)+\frac{z_\theta}{J}\left(-\frac{3}{2\Delta t}\frac{v_{j-1}}{2\Delta\rho}+\frac{F_{y_{j-1}}}{2\Delta\rho}\right)\\
&-\frac{y_\theta}{J}\left(-\frac{3}{2\Delta t}\frac{w_{j-1}}{2\Delta\rho}+\frac{F_{z_{j-1}}}{2\Delta\rho}\right),
\end{aligned}$$

and for the upper boundary is

$$\begin{aligned}
&\frac{YTZX}{J}\left(\frac{1}{2\Delta\rho}\frac{1}{x_\xi}p_{\xi_{j+1}}+\frac{1}{2\Delta\rho}\frac{YTZX_{j+1}}{J_{j+1}}p_{\rho_{j+1}}+\frac{1}{2\Delta\rho}\frac{YXZR_{j+1}}{J_{j+1}}p_{\theta_{j+1}}\right) \qquad (3.127)\\
&+\frac{z_\theta}{J}\left(\frac{1}{2\Delta\rho}\frac{z_{\theta\,j+1}}{J_{j+1}}p_{\rho_{j+1}}-\frac{1}{2\Delta\rho}\frac{z_{\rho\,j+1}}{J_{j+1}}p_{\theta_{j+1}}\right)\\
&+\frac{y_\theta}{J}\left(\frac{1}{2\Delta\rho}\frac{y_{\theta\,j+1}}{J_{j+1}}p_{\rho_{j+1}}-\frac{1}{2\Delta\rho}\frac{y_{\rho\,j+1}}{J_{j+1}}p_{\theta_{j+1}}\right)\\
&=\frac{YTZX}{J}\left(-\frac{3}{2\Delta t}\frac{u_{j+1}}{2\Delta\rho}+\frac{F_{x_{j+1}}}{2\Delta\rho}\right)+\frac{z_\theta}{J}\left(-\frac{3}{2\Delta t}\frac{v_{j+1}}{2\Delta\rho}+\frac{F_{y_{j+1}}}{2\Delta\rho}\right)\\
&-\frac{y_\theta}{J}\left(-\frac{3}{2\Delta t}\frac{w_{j+1}}{2\Delta\rho}+\frac{F_{z_{j+1}}}{2\Delta\rho}\right).
\end{aligned}$$

These lower boundary and upper boundary derivatives are cancelled (added and subtracted, respectively) from the boundary adjacent pressure equations, with the appropriate modifications made to the right-hand-side source terms. This again is just a matter of using the exact boundary velocity in the discrete divergence equation rather than one expressed in terms of the momentum equation. It can now be noted that these pressure derivative expressions are in the physical normal direction as formulated in equation 3.55.

Substituting equations 3.126 and 3.127 into the boundary-adjacent equations gives a modification to both the pressure coefficients and to the source term, just as with the two-dimensional cartesian system. For the lower boundary, the modifications are

$$\begin{aligned}
C_{i,j,k} = & -\frac{1}{x_\xi^2}\frac{2}{4\Delta\xi^2} \\
& -\frac{YTZX_{i,j,k}}{J_{i,j,k}}\frac{1}{4\Delta\rho^2}\left(\frac{YTZX_{i,j+1,k}}{J_{i,j+1,k}}\right) \\
& -\frac{YXZR_{i,j,k}}{J_{i,j,k}}\frac{1}{4\Delta\theta^2}\left(\frac{YXZR_{i,j,k+1}}{J_{i,j,k+1}}\right) - \frac{YXZR_{i,j,k}}{J_{i,j,k}}\frac{1}{4\Delta\theta^2}\left(\frac{YXZR_{i,j,k-1}}{J_{i,j,k-1}}\right) \\
& -\frac{z_{\theta\, i,j,k}}{J_{i,j,k}}\frac{1}{4\Delta\rho^2}\left(\frac{z_{\theta\, i,j+1,k}}{J_{i,j+1,k}}\right) \\
& -\frac{z_{\rho\, i,j,k}}{J_{i,j,k}}\frac{1}{4\Delta\theta^2}\left(\frac{z_{\rho\, i,j,k+1}}{J_{i,j,k+1}}\right) - \frac{z_{\rho\, i,j,k}}{J_{i,j,k}}\frac{1}{4\Delta\theta^2}\left(\frac{z_{\rho\, i,j,k-1}}{J_{i,j,k-1}}\right) \\
& -\frac{y_{\theta\, i,j,k}}{J_{i,j,k}}\frac{1}{4\Delta\rho^2}\left(\frac{y_{\theta\, i,j+1,k}}{J_{i,j+1,k}}\right) \\
& -\frac{y_{\rho\, i,j,k}}{J_{i,j,k}}\frac{1}{4\Delta\theta^2}\left(\frac{y_{\rho\, i,j,k+1}}{J_{i,j,k+1}}\right) - \frac{y_{\rho\, i,j,k}}{J_{i,j,k}}\frac{1}{4\Delta\theta^2}\left(\frac{y_{\rho\, i,j,k-1}}{J_{i,j,k-1}}\right)
\end{aligned} \tag{3.128}$$

$$C_{i+1,j-1,k} = -\frac{1}{x_\xi}\frac{1}{4\Delta\xi\Delta\rho}\frac{YTZX_{i+1,j,k}}{J_{i+1,j,k}} \tag{3.129}$$

$$C_{i-1,j-1,k} = \frac{1}{x_\xi}\frac{1}{4\Delta\xi\Delta\rho}\frac{YTZX_{i-1,j,k}}{J_{i-1,j,k}} \tag{3.130}$$

$$C_{i,j-2,k} = 0 \tag{3.131}$$

$$\begin{aligned}
C_{i,j-1,k+1} = & -\frac{YXZR_{i,j,k}}{J_{i,j,k}}\frac{1}{4\Delta\rho\Delta\theta}\frac{YTZX_{i,j,k+1}}{J_{i,j,k+1}} + \frac{z_{\rho\, i,j,k}}{J_{i,j,k}}\frac{1}{4\Delta\rho\Delta\theta}\frac{z_{\theta\, i,j,k+1}}{J_{i,j,k+1}} \\
& +\frac{y_{\rho\, i,j,k}}{J_{i,j,k}}\frac{1}{4\Delta\rho\Delta\theta}\frac{y_{\theta\, i,j,k+1}}{J_{i,j,k+1}}
\end{aligned} \tag{3.132}$$

$$\begin{aligned}
C_{i,j-1,k-1} = & \frac{YXZR_{i,j,k}}{J_{i,j,k}}\frac{1}{4\Delta\rho\Delta\theta}\frac{YTZX_{i,j,k-1}}{J_{i,j,k-1}} - \frac{z_{\rho\, i,j,k}}{J_{i,j,k}}\frac{1}{4\Delta\rho\Delta\theta}\frac{z_{\theta\, i,j,k-1}}{J_{i,j,k-1}} \\
& -\frac{y_{\rho\, i,j,k}}{J_{i,j,k}}\frac{1}{4\Delta\rho\Delta\theta}\frac{y_{\theta\, i,j,k-1}}{J_{i,j,k-1}}.
\end{aligned} \tag{3.133}$$

The source new source (right-hand-side) for the lower boundary-adjacent point is

$$\begin{aligned}\sigma = \mathcal{D}\cdot\vec{F} &+ \frac{YTZX}{J}\left(-\frac{3}{2\Delta t}\frac{u_{j-1}}{2\Delta\rho}+\frac{F_{x_{j-1}}}{2\Delta\rho}\right) \\ &+\frac{z_\theta}{J}\left(-\frac{3}{2\Delta t}\frac{v_{j-1}}{2\Delta\rho}+\frac{F_{y_{j-1}}}{2\Delta\rho}\right)-\frac{y_\theta}{J}\left(-\frac{3}{2\Delta t}\frac{w_{j-1}}{2\Delta\rho}+\frac{F_{z_{j-1}}}{2\Delta\rho}\right).\end{aligned} \tag{3.134}$$

For the upper boundary, the modifications to the pressure coefficients are

$$\begin{aligned}C_{i,j,k} = &-\frac{1}{x_\xi^2}\frac{2}{4\Delta\xi^2} \\ &-\frac{YTZX_{i,j,k}}{J_{i,j,k}}\frac{1}{4\Delta\rho^2}\left(\frac{YTZX_{i,j-1,k}}{J_{i,j-1,k}}\right) \\ &-\frac{YXZR_{i,j,k}}{J_{i,j,k}}\frac{1}{4\Delta\theta^2}\left(\frac{YXZR_{i,j,k+1}}{J_{i,j,k+1}}\right)-\frac{YXZR_{i,j,k}}{J_{i,j,k}}\frac{1}{4\Delta\theta^2}\left(\frac{YXZR_{i,j,k-1}}{J_{i,j,k-1}}\right) \\ &-\frac{z_{\theta\,i,j,k}}{J_{i,j,k}}\frac{1}{4\Delta\rho^2}\left(\frac{z_{\theta\,i,j-1,k}}{J_{i,j-1,k}}\right) \\ &-\frac{z_{\rho\,i,j,k}}{J_{i,j,k}}\frac{1}{4\Delta\theta^2}\left(\frac{z_{\rho\,i,j,k+1}}{J_{i,j,k+1}}\right)-\frac{z_{\rho\,i,j,k}}{J_{i,j,k}}\frac{1}{4\Delta\theta^2}\left(\frac{z_{\rho\,i,j,k-1}}{J_{i,j,k-1}}\right) \\ &-\frac{y_{\theta\,i,j,k}}{J_{i,j,k}}\frac{1}{4\Delta\rho^2}\left(\frac{y_{\theta\,i,j-1,k}}{J_{i,j-1,k}}\right) \\ &-\frac{y_{\rho\,i,j,k}}{J_{i,j,k}}\frac{1}{4\Delta\theta^2}\left(\frac{y_{\rho\,i,j,k+1}}{J_{i,j,k+1}}\right)-\frac{y_{\rho\,i,j,k}}{J_{i,j,k}}\frac{1}{4\Delta\theta^2}\left(\frac{y_{\rho\,i,j,k-1}}{J_{i,j,k-1}}\right)\end{aligned} \tag{3.135}$$

$$C_{i+1,j+1,k} = \frac{1}{x_\xi}\frac{1}{4\Delta\xi\Delta\rho}\frac{YTZX_{i+1,j,k}}{J_{i+1,j,k}} \tag{3.136}$$

$$C_{i-1,j+1,k} = -\frac{1}{x_\xi}\frac{1}{4\Delta\xi\Delta\rho}\frac{YTZX_{i-1,j,k}}{J_{i-1,j,k}} \tag{3.137}$$

$$C_{i,j+2,k} = 0 \tag{3.138}$$

$$\begin{aligned}C_{i,j+1,k+1} = &\frac{YXZR_{i,j,k}}{J_{i,j,k}}\frac{1}{4\Delta\rho\Delta\theta}\frac{YTZX_{i,j,k+1}}{J_{i,j,k+1}} \\ &-\frac{z_{\rho\,i,j,k}}{J_{i,j,k}}\frac{1}{4\Delta\rho\Delta\theta}\frac{z_{\theta\,i,j,k+1}}{J_{i,j,k+1}} \\ &-\frac{y_{\rho\,i,j,k}}{J_{i,j,k}}\frac{1}{4\Delta\rho\Delta\theta}\frac{y_{\theta\,i,j,k+1}}{J_{i,j,k+1}}\end{aligned} \tag{3.139}$$

$$
\begin{aligned}
C_{i,j+1,k-1} = &-\frac{YXZR_{i,j,k}}{J_{i,j,k}}\frac{1}{4\Delta\rho\Delta\theta}\frac{YTZX_{i,j,k-1}}{J_{i,j,k-1}} \\
&+\frac{z_{\rho\,i,j,k}}{J_{i,j,k}}\frac{1}{4\Delta\rho\Delta\theta}\frac{z_{\theta\,i,j,k-1}}{J_{i,j,k-1}} \\
&+\frac{y_{\rho\,i,j,k}}{J_{i,j,k}}\frac{1}{4\Delta\rho\Delta\theta}\frac{y_{\theta\,i,j,k-1}}{J_{i,j,k-1}}.
\end{aligned}
\tag{3.140}
$$

The modified source for the upper boundary-adjacent point is

$$
\begin{aligned}
\sigma = \mathcal{D}\cdot\vec{F} &- \frac{YTZX}{J}\left(-\frac{3}{2\Delta t}\frac{u_{j+1}}{2\Delta\rho}+\frac{F_{x_{j+1}}}{2\Delta\rho}\right) \\
&-\frac{z_\theta}{J}\left(-\frac{3}{2\Delta t}\frac{v_{j+1}}{2\Delta\rho}+\frac{F_{y_{j+1}}}{2\Delta\rho}\right)+\frac{y_\theta}{J}\left(-\frac{3}{2\Delta t}\frac{w_{j+1}}{2\Delta\rho}+\frac{F_{z_{j+1}}}{2\Delta\rho}\right).
\end{aligned}
\tag{3.141}
$$

With the coefficients and source formed for the boundary-adjacent points, we now turn to the actual Neumann boundary derivative to be used at the boundary point. While the physical normal boundary condition of equation 3.55 was used at the boundary-adjacent points to ensure mass conservation, this condition contains derivatives in the tangential directions ξ and θ. In order to obtain a solvable system a boundary condition is formed in the computational normal direction ρ, using the chain rule,

$$
p_\rho = y_\rho p_y + z_\rho p_z. \tag{3.142}
$$

Substitution is made for p_y and p_z from the Navier-Stokes equations,

$$
p_\rho = y_\rho\left(-\frac{3}{2\Delta t}v+F_y\right)+z_\rho\left(-\frac{3}{2\Delta t}w+F_z\right), \tag{3.143}
$$

and this derivative expression scales to a derivative in physical space as

$$
\frac{1}{\sqrt{y_\rho^2+z_\rho^2}}p_\rho = \frac{1}{\sqrt{y_\rho^2+z_\rho^2}}\left[y_\rho\left(-\frac{3}{2\Delta t}v+F_y\right)+z_\rho\left(-\frac{3}{2\Delta t}w+F_z\right)\right]. \tag{3.144}
$$

The formulation differs from that of the physical normal derivative of equation 3.55 in relation to the difference in direction of ρ to the physical normal direction. Any directional difference in the yz-plane can be removed by gridding accordingly. However, physical normal components in the x-direction necessarily represent a directional difference between p_ρ and the physical normal. At any rate, the boundary condition used is consistent with the Navier-Stokes equations, and does not alter the mass-conservation characteristics in the interior. The discrete form for the lower boundary is

$$\frac{-3p_j + 4p_{j+1} - p_{j+2}}{2\Delta\rho} = y_\rho\left(-\frac{3}{2\Delta t}v + F_y\right) + z_\rho\left(-\frac{3}{2\Delta t}w + F_z\right), \tag{3.145}$$

and for the upper boundary is

$$\frac{3p_j - 4p_{j-1} + p_{j-2}}{2\Delta\rho} = y_\rho\left(-\frac{3}{2\Delta t}v + F_y\right) + z_\rho\left(-\frac{3}{2\Delta t}w + F_z\right). \tag{3.146}$$

Thus, the coefficient and source for the pressure at all points is given. The exact solution method for such a Neumann Poisson equation has some subtleties to be addressed in the following § 3.4.

3.4 The Solution Method

With the discretized pressure and velocity equations formed, the progression of the solution needs to be determined. The present implicit model relies on iterative methods to obtain a solution. Each the velocity field and pressure field are solved using successive over-relaxation (SOR). Additionally, as these two fields are interdependent, they are alternately solved in an iterative fashion until a solution is converged.

3.4.1 Velocity Solution

Solving for the velocity consists of applying SOR to the fully discrete Navier-Stokes equations given earlier in equation 3.81,

$$\frac{3\vec{v}^{n+1} - 4\vec{v}^{n} + \vec{v}^{n-1}}{2\Delta t} = -((\vec{v}^{n+1} - \vec{v}_g^{n+1}) \cdot \mathcal{D}_u{}^{n+1})\vec{v}^{n+1} - \mathcal{D}^{n+1}p^{n+1} + \frac{1}{Re}\mathcal{L}^{n+1}\vec{v}^{n+1} \tag{3.147}$$

Three equations need be solved at each point, one for each velocity component. For a component $u^{n+1}_{i,j,k}$, all occurrences are consolidated on the left-hand side. For the nonlinear term, the occurrence contained in the derivative is used, and we write a single equation as

$$u^{n+1^{p+1}}_{i,j,k} = (1-\omega)u^{n+1^{p}}_{i,j,k} + \omega f(\neq u^{n+1}_{i,j,k}; enlt), \tag{3.148}$$

where the superscript p denotes the previous SOR iteration. The function, $f(\neq u^{n+1}_{i,j,k}; enlt)$, refers to the remainder of the Navier-Stokes equation with terms not equal to $u^{n+1}_{i,j,k}$, excepting the nonlinear term.

The velocity field is solved as such, sequentially running through all non-boundary points until the field converges. The boundary velocities are either given directly by the Dirichlet boundary conditions, or an explicit Neumann outflow condition (using velocities from previous time steps).

3.4.2 Pressure Solution

While the pressure equation is linear, its nineteen point stencil for the Laplacian make it difficult to solve by direct methods, with a single equation formed as

$$\begin{aligned}
&C_{i,j,k}p_{i,j,k} + C_{i+1,j,k}p_{i+1,j,k} + C_{i+1,j+1,k}p_{i+1,j+1,k} + C_{i+1,j-1,k}p_{i+1,j-1,k} \\
&\quad + C_{i+1,j,k+1}p_{i+1,j,k+1} + C_{i+1,j,k-1}p_{i+1,j,k-1} + C_{i-1,j,k}p_{i-1,j,k} + C_{i-1,j+1,k}p_{i-1,j+1,k} \\
&\quad + C_{i-1,j-1,k}p_{i-1,j-1,k} + C_{i-1,j,k+1}p_{i-1,j,k+1} + C_{i-1,j,k-1}p_{i-1,j,k-1} + C_{i,j+1,k}p_{i,j+1,k} \\
&\quad + C_{i,j+1,k+1}p_{i,j+1,k+1} + C_{i,j+1,k-1}p_{i,j+1,k-1} + C_{i,j-1,k}p_{i,j-1,k} + C_{i,j-1,k+1}p_{i,j-1,k+1} \\
&\quad + C_{i,j-1,k-1}p_{i,j-1,k-1} + C_{i,j,k+1}p_{i,j,k+1} + C_{i,j,k-1}p_{i,j,k-1} = \mathcal{D} \cdot \vec{F},
\end{aligned} \tag{3.149}$$

where $\vec{F}$ is given by equation 3.83. SOR is again used to solve for the pressure as

$$p^{n+1^{p+1}}_{i,j,k} = (1-\omega)p^{n+1^{p}}_{i,j,k} + \omega f(\neq p^{n+1}_{i,j,k}). \tag{3.150}$$

Obtaining a Unique Pressure Solution

While the Poisson equation for the pressure is applied to the interior, Neumann boundary conditions are applied at the domain boundaries. The divergence theorem is recalled, and is applied to this problem for the pressure

$$\begin{aligned} &\int\!\!\int\!\!\int_V \nabla \cdot \nabla p \, dV = \int\!\!\int_S \nabla p \cdot \hat{n} \, dS \\ &\int\!\!\int\!\!\int_V \nabla \cdot \nabla p \, dV - \int\!\!\int_S \frac{\partial p}{\partial n} dS = 0, \end{aligned} \tag{3.151}$$

which, for our problem, can be expressed in discrete form as

$$\sum_{i1} \widetilde{\mathcal{L}5}\, p_{i1}\, J \, d\xi \, d\rho \, d\theta \; - \sum_{i2} \frac{1}{\sqrt{y_\rho^2 + z_\rho^2}} \mathcal{D}_\rho p_{i2} \sqrt{y_\theta^2 + z_\theta^2} \, d\theta \, d\xi \approx 0. \tag{3.152}$$

Interior points are represented by $i1$ while boundary points are represented by $i2$. This is rewritten with $\mathcal{G}_i$ representing the discrete operator at a point, and B_i representing the constant multiplier,

$$\begin{aligned} &\sum_i B_i \, \mathcal{G}_i \, p_i \approx 0 \\ &\quad B_i = J_i \, d\xi \, d\rho \, d\theta \;\; ; \;\; \mathcal{G} = \widetilde{\mathcal{L}5} \quad \textit{interior} \\ &\quad B_i = -\frac{\sqrt{y_\theta^2 + z_{\theta i}^2}}{\sqrt{y_\rho^2 + z_{\rho i}^2}} \, d\theta \, d\xi \;\; ; \;\; \mathcal{G} = \mathcal{D}_\rho \quad \textit{boundary.} \end{aligned} \tag{3.153}$$

We now consider the pressure problem in matrix form of $A\vec{x} = \vec{b}$ as

$$\begin{bmatrix} \mathcal{G}_1 \\ \mathcal{G}_2 \\ \mathcal{G}_3 \\ \vdots \\ \mathcal{G}_N \end{bmatrix} \begin{bmatrix} p_1 \\ p_2 \\ p_3 \\ \vdots \\ p_N \end{bmatrix} = \begin{bmatrix} \sigma_1 \\ \sigma_2 \\ \sigma_3 \\ \vdots \\ \sigma_N \end{bmatrix} . \tag{3.154}$$

Equations 3.153 implies singularity of the A matrix. Any row can be formed as a linear combination of the other rows, a redundancy which prohibits a unique solution.

The singularity can be removed by replacing a single equation (row) with one that fixes a point in the solution, eg. $p_{i,j,k} = 0$.

The reality, however, is that the A matrix will not be exactly singular due to discretization error (thus the approximate equal sign in equation 3.153). In order to fix the location of the solution, singularity of the system must be enforced. A correction is added to each equation to force the problem to be singular. We first multiply each row by the appropriate constant,

$$\begin{bmatrix} B_1\mathcal{G}_1 \\ B_2\mathcal{G}_2 \\ B_3\mathcal{G}_3 \\ \vdots \\ B_N\mathcal{G}_N \end{bmatrix} \begin{bmatrix} p_1 \\ p_2 \\ p_3 \\ \vdots \\ p_N \end{bmatrix} = \begin{bmatrix} B_1\sigma_1 \\ B_2\sigma_2 \\ B_3\sigma_3 \\ \vdots \\ B_N\sigma_N \end{bmatrix}. \tag{3.155}$$

The left-hand side and right-hand side should now both sum to almost zero, to the accuracy of the discretization error,

$$\sum_i B_i\,\mathcal{G}_i\,p_i = \sum_i B_i\,\sigma_i \approx 0. \tag{3.156}$$

A correction is added to both sides of every equation,

$$B_j\,\mathcal{G}_j\,p_j - B_j\frac{\sum_i B_i\,\mathcal{G}_i\,p_i}{\sum_i B_i} = B_j\,\sigma_j - B_j\frac{\sum_i B_i\,\sigma_i}{\sum_i B_i}, \tag{3.157}$$

so that now the left-hand side and right-hand side will both sum to exactly zero,

$$\sum_j \left(B_j\,\mathcal{G}_j\,p_j - B_j\frac{\sum_i B_i\,\mathcal{G}_i\,p_i}{\sum_i B_i}\right) = \sum_j \left(B_j\,\sigma_j - B_j\frac{\sum_i B_i\,\sigma_i}{\sum_i B_i}\right) = 0. \tag{3.158}$$

The constant is now divided out in the corrected equation 3.157, to obtain the final form for the corrected equation,

$$\mathcal{G}_j\,p_j - \frac{\sum_i B_i\,\mathcal{G}_i\,p_i}{\sum_i B_i} = \sigma_j - \frac{\sum_i B_i\,\sigma_i}{\sum_i B_i}. \tag{3.159}$$

With singularity of the system now enforced, a condition fixing the solution can be added to the system, and this is discussed below.

An Example Problem

The procedure is demonstrated for a one-dimensional problem on a five-point grid using a compact stencil. The original uncorrected matrix equation is

$$\begin{bmatrix} b_1 & c_1 & 0 & 0 & 0 \\ a_2 & b_2 & c_2 & 0 & 0 \\ 0 & a_3 & b_3 & c_3 & 0 \\ 0 & 0 & a_4 & b_4 & c_4 \\ 0 & 0 & 0 & a_5 & b_5 \end{bmatrix} \begin{bmatrix} p_1 \\ p_2 \\ p_3 \\ p_4 \\ p_5 \end{bmatrix} = \begin{bmatrix} \sigma_1 \\ \sigma_2 \\ \sigma_3 \\ \sigma_4 \\ \sigma_5 \end{bmatrix} . \tag{3.160}$$

The left-hand side correction term of equation 3.159 can be written in terms of multipliers to the pressure at each point as

$$-\frac{\sum_i B_i \mathcal{G}_i p_i}{\sum_i B_i} = \gamma_1 p_1 + \gamma_2 p_2 + \gamma_3 p_3 + \gamma_4 p_4 + \gamma_5 p_5 \tag{3.161}$$

$$\gamma_1 = -\frac{B_1 b_1 + B_2 a_2}{B_1 + B_2 + B_3 + B_4 + B_5}$$

$$etc.$$

We define σ_c as the right-hand side correction,

$$\sigma_c = -\frac{\sum_i B_i \sigma_i}{\sum_i B_i} = -\frac{B_1\sigma_1 + B_2\sigma_2 + B_3\sigma_3 + B_4\sigma_4 + B_5\sigma_5}{B_1 + B_2 + B_3 + B_4 + B_5}, \tag{3.162}$$

and the corrected singular matrix equation can now be written as

$$\begin{bmatrix} b_1+\gamma_1 & c_1+\gamma_2 & \gamma_3 & \gamma_4 & \gamma_5 \\ a_2+\gamma_1 & b_2+\gamma_2 & c_2+\gamma_3 & \gamma_4 & \gamma_5 \\ \gamma_1 & a_3+\gamma_2 & b_3+\gamma_3 & c_3+\gamma_4 & \gamma_5 \\ \gamma_1 & \gamma_2 & a_4+\gamma_3 & b_4+\gamma_4 & c_4+\gamma_5 \\ \gamma_1 & \gamma_2 & \gamma_3 & a_5+\gamma_4 & b_5+\gamma_5 \end{bmatrix} \begin{bmatrix} p_1 \\ p_2 \\ p_3 \\ p_4 \\ p_5 \end{bmatrix} = \begin{bmatrix} \sigma_1+\sigma_c \\ \sigma_2+\sigma_c \\ \sigma_3+\sigma_c \\ \sigma_4+\sigma_c \\ \sigma_5+\sigma_c \end{bmatrix} . \tag{3.163}$$

This system now needs an additional condition to obtain a unique solution. Consider that the solution is to be fixed such that $p_4 = 0$ is enforced. This condition can be imposed by removing a row and replacing it with this equation,

$$\begin{bmatrix} b_1+\gamma_1 & c_1+\gamma_2 & \gamma_3 & \gamma_4 & \gamma_5 \\ a_2+\gamma_1 & b_2+\gamma_2 & c_2+\gamma_3 & \gamma_4 & \gamma_5 \\ \gamma_1 & a_3+\gamma_2 & b_3+\gamma_3 & c_3+\gamma_4 & \gamma_5 \\ 0 & 0 & 0 & 1 & 0 \\ \gamma_1 & \gamma_2 & \gamma_3 & a_5+\gamma_4 & b_5+\gamma_5 \end{bmatrix} \begin{bmatrix} p_1 \\ p_2 \\ p_3 \\ p_4 \\ p_5 \end{bmatrix} = \begin{bmatrix} \sigma_1+\sigma_c \\ \sigma_2+\sigma_c \\ \sigma_3+\sigma_c \\ 0 \\ \sigma_5+\sigma_c \end{bmatrix}. \tag{3.164}$$

An equivalent formulation, conditioned differently, is obtained by subtracting the fixed-point equation from every row,

$$\begin{bmatrix} b_1+\gamma_1 & c_1+\gamma_2 & \gamma_3 & \gamma_4-1 & \gamma_5 \\ a_2+\gamma_1 & b_2+\gamma_2 & c_2+\gamma_3 & \gamma_4-1 & \gamma_5 \\ \gamma_1 & a_3+\gamma_2 & b_3+\gamma_3 & c_3+\gamma_4-1 & \gamma_5 \\ \gamma_1 & \gamma_2 & a_4+\gamma_3 & b_4+\gamma_4-1 & c_4+\gamma_5 \\ \gamma_1 & \gamma_2 & \gamma_3 & a_5+\gamma_4-1 & b_5+\gamma_5 \end{bmatrix} \begin{bmatrix} p_1 \\ p_2 \\ p_3 \\ p_4 \\ p_5 \end{bmatrix} = \begin{bmatrix} \sigma_1+\sigma_c \\ \sigma_2+\sigma_c \\ \sigma_3+\sigma_c \\ \sigma_4+\sigma_c \\ \sigma_5+\sigma_c \end{bmatrix}. \tag{3.165}$$

It's important to choose an implementation which results in good convergence characteristics when applying iterative methods such as in the present case.

Desingularization and Uncoupled Pressure Grids

When dealing with periodic boundary conditions, there is an uncoupling of pressure stencils using the $\widetilde{\mathcal{L}5}$ pressure operator. In this case each independent grid system is treated independently with the procedure of equations 3.156-3.159. With each system corrected to be singular, they are desingularized independently. By fixing the solution with an equivalent desingularization procedure, the grids can be tied together. A straightforward procedure to apply is a mean-zero approach which sets the mean of the pressure (as averaged in computational space) to zero. We enforce this condition at the conclusion of each SOR sweep through the domain.

3.4.3 The Total FDS Solution Procedure

As was discussed earlier, the pressure and velocity are interdependent, yet are solved separately. Consequently, there is a need to iterate between the solution of the two. The method for FDS solution follows the procedure below.

1. Set the grid and the velocity boundary condition for the new time step, initializing the interior velocity and pressure to that of the previous time step.
2. Calculate the Poisson source term and pressure boundary condition from the velocity field.
3. Solve the Poisson equation for the pressure.
4. Solve the Navier-Stokes equations with the new pressure field to update the velocity field.
5. Return to Step 2 unless tolerance is reached in terms of velocity change and mass conservation (3 iterations minimum).
6. Advance time step and return to Step 1.

3.4.4 Parallel Computation

Computation of the procedure described can be quite time consuming on the larger grids required by higher Reynolds numbers. As such, a simple domain decomposition parallelization procedure is used. The periodic directions ξ and θ lend themselves nicely to such decomposition, and were both used. The biggest challenge in such a 2D parallelization is bookkeeping, which can always be overcome with enough care. Passing of data across domain 'seams' (between processors representing adjacent domain blocks) occurs at the end of each subdomain sweep in the iterative SOR solvers. As such, treatment at the seams is Jacobi rather than SOR. These Jacobi seams, and the time of interprocessor communications are the prices paid for the benefit of distributing the calculations.

Chapter 4

The Structural-dynamic Direct Simulation (SDS) and Fluid-dynamic Coupling (FSDS)

This chapter details the formulation, finite-difference discretization, and implementation of the flexible thin-body structural-dynamic direct simulation (SDS). The formulation is nonlinear in terms of displacement, allowing arbitrary orientation and configuration of the body. The approach is described with a detailed look at the validity of the assumptions. Using these assumptions, the equations of motion are derived for the two-dimensional thin-body or filament, and subsequently for a three-dimensional thin-body or plate. Linearizations are indicated around a thin body assumption, small extensional strain, and, for the three-dimensional case, small planar shear strain. As such, the body is constrained to be thin with high extensional rigidity, but can accommodate a range of structural mass and bending stiffness.

4.1 Overview of SDS Formulation and Assumptions

Drawing on the work of Belmonte et. al [8] in their swinging chain study, and a review of nonlinear structural methods by Steve Taylor [58], a two-dimensional nonlinear model based on global cartesian coordinates is derived using Hamilton's Principle. For a robust capability, able to accommodate loss of positive tension (see [65]), we consider finite physical parameters of large modulus and small thickness, corresponding to a body which is slightly extensible with weak bending rigidity. The final derived two-dimensional equations of motion are exactly equivalent to those used for the structural component in the flapping study of Zhu & Peskin [79]. Using the theory and dynamics of linear plates from Shames and Dym [53], the nonlinear model is extended to a three-dimensional thin plate.

The plate is considered to have two tangential directions, s_1 and s_2, and one normal direction, s_3. General expressions for the potential and kinetic energies of the linearly elastic body are

$$V = \frac{1}{2}\int\int\int \tau_{ij}\, \epsilon_{ij} ds_1\, ds_2\, ds_3 \tag{4.1}$$

$$T = \frac{1}{2}\int\int\int \rho \dot{x}_i \dot{x}_i ds_1\, ds_2\, ds_3. \tag{4.2}$$

These expressions are the starting point for derivation of the equations of motion to be used in the computational simulation. Assumptions used in the derivation are,

Thin-body assumption:

- Shear stresses involving the normal direction are ignored
- Rotational inertia about tangential directions is ignored

Small strain assumptions:

- Linearization about small extensional strain
- Linearization about small planar shear strain (3D).

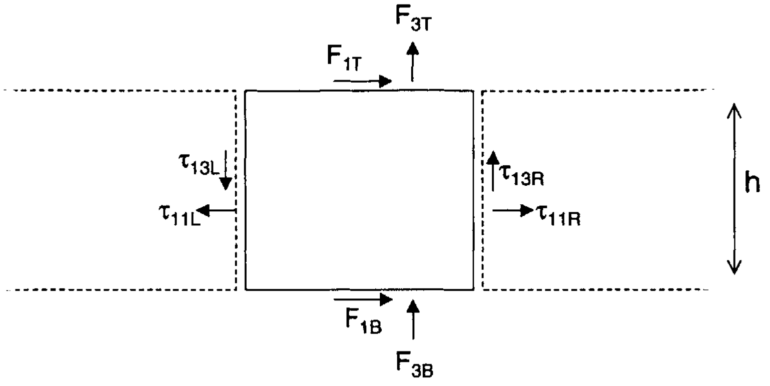

Figure 4-1: Forces on a 2D plate segment with s_1 as the tangential direction and s_3 as the normal direction. The segment has thickness h and length Δs_1, with top, bottom, right, and left sides denoted T, B, R, L.

Selection of simulation parameters is thus made to maintain validity of the assumptions for assurance of solution accuracy.

4.1.1 Thin-body Assumption Justification

In considering only thin bodies, where the thickness is considered much smaller than the lengthscale of body motion and hydrodynamic forcing, it is considered that the shear stresses involving the normal direction, the normal stress in the normal direction, and rotational inertia about the tangential directions can all be ignored. The following offers an explanation of such assumption. For simplicity we show this for a two-dimensional thin plate, considering only the s_1 tangential and s_3 normal directions.

We start by defining a segment of the two-dimensional thin plate, show in figure 4-1. A force equation for each of the two translational directions, and an equation for the moment about the segment center are constructed. The normal force effect of curvature under tension is shown in figure 4-2, and is included in the normal force equation. Two dimensional mass-per-length is given by m. The equations are

$\sum F_1$:

$$m\Delta s_1 \ddot{x}_1 = F_{1T} + F_{1B} + \tau_{11R}h - \tau_{11L}h \tag{4.3}$$

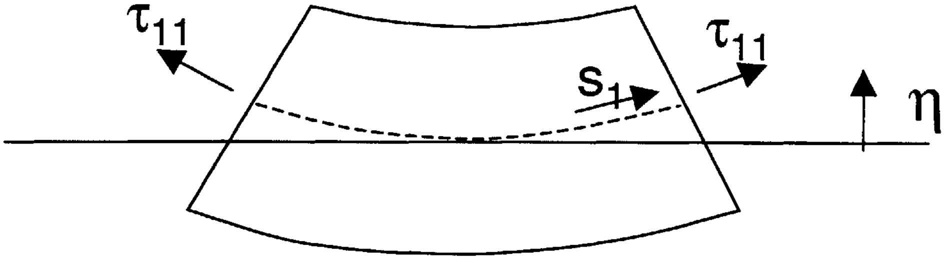

Figure 4-2: The figure shows exaggerated bending of a segment with η as the displacement from the segment center tangent.

$\sum F_3$:

$$m\Delta s_1 \ddot{x}_3 = F_{3T} + F_{3B} + \tau_{13R}h - \tau_{13L}h + \tau_{11R}h\frac{\partial \eta}{\partial s_1}_R - \tau_{11L}h\frac{\partial \eta}{\partial s_1}_L \tag{4.4}$$

$\sum M_c$:

$$\begin{aligned} m\Delta s_1 \frac{1}{12}(h^2 + \Delta s_1^2)\ddot{\theta} &= F_{1T}\frac{h}{2} - F_{1B}\frac{h}{2} \\ &-\tau_{13R}h\frac{\Delta s_1}{2} - \tau_{13L}h\frac{\Delta s_1}{2} + \int_{-\frac{h}{2}}^{\frac{h}{2}} \tau_{11R}(s_3)s_3 ds_3 - \int_{-\frac{h}{2}}^{\frac{h}{2}} \tau_{11L}(s_3)s_3 ds_3. \end{aligned} \tag{4.5}$$

Note that the stresses are considered not a function of s_3 in the force equations, as order-one terms are retained and first-order terms will cancel on integration. However, in the moment equation, dependence on s_3 of τ_{11} is considered for the importance of the first-order expansion terms and cancellation of the order-one terms.

We now consider f as force per length where $f\Delta s_1 = F$. First-order expansions are used to define the right and left-face quantities in terms of those at the center. The top and bottom forcing quantities are retained as is, allowing for force discontinuity across the body thickness. We now have

$\sum F_1$:

$$m\Delta s_1 \ddot{x}_1 = f_{1T}\Delta s_1 + f_{1B}\Delta s_1 + \frac{\partial \tau_{11}}{\partial s_1}\Delta s_1 h \tag{4.6}$$

$\sum F_3$:

$$m\Delta s_1\ddot{x}_3 = f_{3T}\Delta s_1 + f_{3B}\Delta s_1 + \frac{\partial \tau_{13}}{\partial s_1}\Delta s_1 h + \frac{\partial}{\partial s_1}\left(\tau_{11}\frac{\partial \eta}{\partial s_1}\right)\Delta s_1 h \tag{4.7}$$

$\sum M_c$:

$$\begin{aligned} m\Delta s_1\frac{1}{12}(h^2+\Delta s_1^2)\ddot{\theta} &= f_{1T}\Delta s_1\frac{h}{2} - f_{1B}\Delta s_1\frac{h}{2} \\ -\tau_{13}h\Delta s_1 &+ \int_{-\frac{h}{2}}^{\frac{h}{2}} \frac{\partial \tau_{11}(s_3)}{\partial s_1}\Delta s_1 s_3 ds_3. \end{aligned} \tag{4.8}$$

Dividing through by Δs_1 and casting out the Δs_1^2 term, we obtain

$\sum F_1$:

$$m\ddot{x}_1 = f_{1T} + f_{1B} + \frac{\partial \tau_{11}}{\partial s_1}h \tag{4.9}$$

$\sum F_3$:

$$m\ddot{x}_3 = f_{3T} + f_{3B} + \frac{\partial \tau_{13}}{\partial s_1}h + \frac{\partial}{\partial s_1}\left(\tau_{11}\frac{\partial \eta}{\partial s_1}\right)h \tag{4.10}$$

$\sum M_c$:

$$m\frac{h^2}{12}\ddot{\theta} = f_{1T}\frac{h}{2} - f_{1B}\frac{h}{2} - \tau_{13}h + \int_{-\frac{h}{2}}^{\frac{h}{2}} \frac{\partial \tau_{11}(s_3)}{\partial s_1}s_3 ds_3. \tag{4.11}$$

We now consider $\tau_{11}(s_3)$ in the moment equation as a first-order expansion about $s_3 = 0$, denoted as c,

$$\tau_{11}(s_3) = \tau_{11c} + \frac{\partial \tau_{11c}}{\partial s_3}s_3. \tag{4.12}$$

The integral in equation 4.11 can now be evaluated,

$$m\frac{h^2}{12}\ddot{\theta} = f_{1T}\frac{h}{2} - f_{1B}\frac{h}{2} - \tau_{13}h + \frac{\partial}{\partial s_1}\frac{\partial \tau_{11}}{\partial s_3}\frac{h^3}{12}. \tag{4.13}$$

Rearranging, and differentiating with respect to s_1 we obtain

$$\frac{\partial \tau_{13}}{\partial s_1}h = \frac{\partial f_{1T}}{\partial s_1}\frac{h}{2} - \frac{\partial f_{1B}}{\partial s_1}\frac{h}{2} + \frac{\partial^2}{\partial s_1^2}\frac{\partial \tau_{11}}{\partial s_3}\frac{h^3}{12} - m\frac{h^2}{12}\frac{\partial \ddot{\theta}}{\partial s_1}. \tag{4.14}$$

This expression is substituted into equation 4.10,

$$m\ddot{x}_3 = f_{3T} + f_{3B} + \frac{\partial f_{1T}}{\partial s_1}\frac{h}{2} - \frac{\partial f_{1B}}{\partial s_1}\frac{h}{2}$$
$$+\frac{\partial^2}{\partial s_1^2}\frac{\partial \tau_{11}}{\partial s_3}\frac{h^3}{12} - m\frac{h^2}{12}\frac{\partial \ddot{\theta}}{\partial s_1} + \frac{\partial}{\partial s_1}\left(\tau_{11}\frac{\partial \eta}{\partial s_1}\right)h. \tag{4.15}$$

We now examine the relative importance of the terms of equation 4.15. A length scale λ is defined as that characteristic of the body motion and external forcing. We begin by defining τ_{11} and τ_{33} in terms of the modulus of elasticity E and the Poisson ratio ν,

$$\tau_{11} = \frac{E}{1-\nu^2}\left(\epsilon_{11} + \nu\epsilon_{33}\right) \tag{4.16}$$
$$\tau_{33} = \frac{E}{1-\nu^2}\left(\epsilon_{33} + \nu\epsilon_{11}\right). \tag{4.17}$$

A characteristic force per length f varies over the length-scale λ so that $h\tau_{11} \sim f\lambda$ while $\tau_{33} \sim f$. We now have that $\tau_{33}/\tau_{11} \sim h/\lambda$, allowing us to neglect τ_{33} for thin bodies, yielding

$$\tau_{11} = E\epsilon_{11}. \tag{4.18}$$

For a thin body, the strain ϵ_{11} can be written as

$$\epsilon_{11} = \frac{\partial \Delta s1}{\partial s1} - s3\frac{\partial^2 \eta}{\partial s_1^2} = \epsilon_{11_c} - s3\frac{\partial^2 \eta}{\partial s_1^2}. \tag{4.19}$$

The first term indicates the stretch at the centerline, while the second term represents the compression and stretching associated with bending. The second term uses an exact expression for the curvature, as the slope of η is zero at the center of the section (see figure 4-2). Equation 4.15 is now rewritten,

$$m\ddot{x}_3 + m\frac{h^2}{12}\frac{\partial \ddot{\theta}}{\partial s_1} = f_{3T} + f_{3B} + \frac{\partial f_{1T}}{\partial s_1}\frac{h}{2} - \frac{\partial f_{1B}}{\partial s_1}\frac{h}{2}$$
$$-E\frac{h^3}{12}\frac{\partial^4 \eta}{\partial s_1^4} + Eh\frac{\partial}{\partial s_1}\left(\epsilon_{11_c}\frac{\partial \eta}{\partial s_1}\right). \tag{4.20}$$

The variables are normalized by the mass m, typical external forcing value f, and lengthscale of forcing and body motion λ,

$$\begin{aligned} & m\frac{f}{m\lambda}\lambda\ddot{x}_3{}^* + m\frac{h^2}{12}\frac{f}{m\lambda}\frac{1}{\lambda}\frac{\partial\ddot{\theta}^*}{\partial s_1^*} = \\ & \quad ff_{3T}^* + ff_{3B}^* + f\frac{1}{\lambda}\frac{\partial f_{1T}^*}{\partial s_1^*}\frac{h}{2} - f\frac{1}{\lambda}\frac{\partial f_{1B}^*}{\partial s_1^*}\frac{h}{2} \\ & \quad -E\frac{h^3}{12}\frac{1}{\lambda^3}\frac{\partial^4\eta^*}{\partial s_1^{*4}} + Eh\frac{\partial}{\partial s_1^*}\frac{1}{\lambda}\left(\epsilon_{11_c}\frac{\partial\eta^*}{\partial s_1^*}\right). \end{aligned} \tag{4.21}$$

Dividing through by f we obtain

$$\begin{aligned} & \ddot{x}_3{}^* + \frac{1}{12}\frac{h^2}{\lambda^2}\frac{\partial\ddot{\theta}^*}{\partial s_1^*} = \\ & \quad f_{3T}^* + f_{3B}^* + \frac{1}{2}\frac{h}{\lambda}\frac{\partial f_{1T}^*}{\partial s_1^*} - \frac{1}{2}\frac{h}{\lambda}\frac{\partial f_{1B}^*}{\partial s_1^*} \\ & \quad -\frac{E}{f}\frac{h^3}{\lambda^3}\frac{1}{12}\frac{\partial^4\eta^*}{\partial s_1^{*4}} + \frac{E}{f}\frac{h}{\lambda}\frac{\partial}{\partial s_1^*}\left(\epsilon_{11_c}\frac{\partial\eta^*}{\partial s_1^*}\right). \end{aligned} \tag{4.22}$$

The dependence of the terms on the thickness ratio can be seen in equation 4.22. For sufficiently thin bodies, the rotational inertia term can be ignored, as well as those terms associated with moment from shearing at the top and bottom. The importance of the stretching and bending terms is tied to the values of E and ϵ_{11_c}. Nondimensional forms of both the F_1 and F_3 equations are now written,

$$\ddot{x}_1{}^* = f_{1T}^* + f_{1B}^* + \frac{E}{f}\frac{h}{\lambda}\frac{\partial\epsilon_{11_c}}{\partial s_1^*} \tag{4.23}$$

$$\ddot{x}_3{}^* = f_{3T}^* + f_{3B}^* - \frac{E}{f}\frac{h^3}{\lambda^3}\frac{1}{12}\frac{\partial^4\eta^*}{\partial s_1^{*4}} + \frac{E}{f}\frac{h}{\lambda}\frac{\partial}{\partial s_1^*}\left(\epsilon_{11_c}\frac{\partial\eta^*}{\partial s_1^*}\right). \tag{4.24}$$

The first equation tells us that $(E/f)(h/\lambda)\epsilon_{11_c} \sim 1$, so E must be very large for thin bodies to be near inextensible. The second equation indicates that, for the bending term to be significant, then $(1/12)(E/f)(h^3/\lambda^3) \sim 1$. We rewrite the nondimensional F_3 equation using the values $e2$ and $e3$ as the bending and extensional stiffness (nomenclature to be introduced later),

$$\ddot{x}_3^* = f_{3T}^* + f_{3B}^* - e2\frac{\partial^4 \eta^*}{\partial s_1^{*4}} + e3\frac{\partial}{\partial s_1^*}\left(\epsilon_{11_c}\frac{\partial \eta^*}{\partial s_1^*}\right). \tag{4.25}$$

By definition, $e2/e3 \sim h^2/\lambda^2$, so for the thin body assumption to hold it must be true that

$$\sqrt{\frac{e2}{e3}} \ll 1. \tag{4.26}$$

We now look to evaluate the importance of shear stress τ_{13}, writing the moment equation 4.13 without the neglected inertia and external forcing terms,

$$\tau_{13} h = \frac{\partial}{\partial s_1}\frac{\partial \tau_{11}}{\partial s_3}\frac{h^3}{12}, \tag{4.27}$$

which is normalized as

$$\tau_{13}^* = \frac{1}{12}\frac{h}{\lambda}\frac{\partial}{\partial s_1^*}\frac{\partial \tau_{11}^*}{\partial s_3^*}. \tag{4.28}$$

The equation displays that the strength of the shear stress compared to the normal stress is reduced linearly with the thickness parameter.

It has been shown that the dynamics of the system can be considered independent of several factors for sufficiently thin two-dimensional plates. These include the rotational inertia of a segment, the shearing effect of external forces, the shear stress, and the normal stress in the cross-segment direction. Inclusion of the second tangential direction (three-dimensional plate) will not alter the scaling of these effects, so the assumptions remain valid. It's important to note that the planar shear stresses (involving the two tangential directions) are significant and must be included in the three-dimensional formulation, while the planar rotational inertia is captured through the differential treatment in the tangential directions.

4.2 Two-Dimensional Nonlinear Plate Derivation

4.2.1 Potential Energy

We have the following expression for the two-dimensional structural potential energy, using the s_1 tangential direction and the s_3 normal direction,

$$V = \frac{1}{2} \int \int \tau_{ij} \, \epsilon_{ij} ds_1 \, ds_3. \tag{4.29}$$

We use the assumptions justified in the previous section to write

$$\tau_{13} = \tau_{33} = 0. \tag{4.30}$$

The remaining stress is given in terms of the modulus of elasticity E as

$$\tau_{11} = E\epsilon_{11}. \tag{4.31}$$

The potential energy is now rewritten,

$$V = E\frac{1}{2} \int \int \epsilon_{11}^2 ds_1 \, ds_3. \tag{4.32}$$

The strain is now expressed in terms of the global position vector $\vec{x}$ and the tangential and normal directions of the plate,

$$\epsilon_{11} = \left(\left(\frac{\partial \vec{x}}{\partial s_1} \cdot \frac{\partial \vec{x}}{\partial s_1} \right)^{\frac{1}{2}} - 1 \right) - (\pm) s_3 \left(\frac{\partial^2 \vec{x}}{\partial {s_1}^2} \cdot \frac{\partial^2 \vec{x}}{\partial {s_1}^2} \right)^{\frac{1}{2}}. \tag{4.33}$$

The symbol (±) accommodates the direction of the curvature, and will fall out of the formulation. An implicit assumption is that displacements in the normal direction are much bigger than tangential displacements associated extension or compression. This is an assumption of a highly inextensible body.

The expression for ϵ_{11} is used in the potential energy expression,

$$V = E\frac{1}{2}\int_{s_3=-h/2}^{h/2}\int_{s_1=0}^{L_1}[\left(\left(\frac{\partial\vec{x}}{\partial s_1}\cdot\frac{\partial\vec{x}}{\partial s_1}\right)^{\frac{1}{2}}-1\right)^2 \tag{4.34}$$
$$-(\pm)2\left(\left(\frac{\partial\vec{x}}{\partial s_1}\cdot\frac{\partial\vec{x}}{\partial s_1}\right)^{\frac{1}{2}}-1\right)\left(\frac{\partial^2\vec{x}}{\partial {s_1}^2}\cdot\frac{\partial^2\vec{x}}{\partial {s_1}^2}\right)^{\frac{1}{2}}s_3+\left(\frac{\partial^2\vec{x}}{\partial {s_1}^2}\cdot\frac{\partial^2\vec{x}}{\partial {s_1}^2}\right)s_3^2]ds_1\,ds_3,$$

and performing the integration over s_3,

$$V = E\frac{1}{2}\int_{s_1=0}^{L_1}\left[\left(\left(\frac{\partial\vec{x}}{\partial s_1}\cdot\frac{\partial\vec{x}}{\partial s_1}\right)^{\frac{1}{2}}-1\right)^2 h+\left(\frac{\partial^2\vec{x}}{\partial {s_1}^2}\cdot\frac{\partial^2\vec{x}}{\partial {s_1}^2}\right)\frac{h^3}{12}\right]ds_1, \tag{4.35}$$

or

$$V = Eh\int_{s_1=0}^{L_1}\frac{1}{2}\left(\left(\frac{\partial\vec{x}}{\partial s_1}\cdot\frac{\partial\vec{x}}{\partial s_1}\right)^{\frac{1}{2}}-1\right)^2 ds_1+\frac{Eh^3}{12}\int_{s_1=0}^{L_1}\frac{1}{2}\left(\frac{\partial^2\vec{x}}{\partial {s_1}^2}\cdot\frac{\partial^2\vec{x}}{\partial {s_1}^2}\right)ds_1. \tag{4.36}$$

This is our final form of the potential energy for the two-dimensional plate.

4.2.2 The Equations of Motion

In order to obtain the appropriate equations of motion and boundary conditions we need to also define the kinetic energy. Here, in keeping with the assumption of a thin plate, we consider only the linear kinetic energy and neglect the rotational kinetic energy,

$$T = \frac{1}{2}\int_0^{L_1}\rho h\frac{\partial\vec{x}}{\partial t}\cdot\frac{\partial\vec{x}}{\partial t}ds_1. \tag{4.37}$$

With external generalized forces considered as Ξ, the variational indicator is formed,

$$V.I. = \int_{t_1}^{t_2}dt[\delta(T-V)+\sum_j \Xi_j\delta\xi_j]=0 \tag{4.38}$$

$$
\begin{aligned}
V.I. \;=\;& \int_{t_1}^{t_2} dt[\delta(\frac{1}{2}\int_0^{L_1} \rho h \frac{\partial \vec{x}}{\partial t} \cdot \frac{\partial \vec{x}}{\partial t} ds_1 - Eh \int_0^{L_1} \frac{1}{2}\left(\left(\frac{\partial \vec{x}}{\partial s_1} \cdot \frac{\partial \vec{x}}{\partial s_1} \right)^{\frac{1}{2}} - 1 \right)^2 ds_1 \\
-\;& \frac{Eh^3}{12} \int_0^{L_1} \frac{1}{2} \left(\frac{\partial^2 \vec{x}}{\partial {s_1}^2} \cdot \frac{\partial^2 \vec{x}}{\partial {s_1}^2} \right) ds_1) + \int_0^{L_1} \vec{F} \cdot \delta \vec{x}\, ds_1] = 0. \qquad (4.39)
\end{aligned}
$$

The variational indicator contains three terms associated with the kinetic and potential energies. These are denoted as $\Theta_1 \rightarrow \Theta_3$,

$$
\begin{aligned}
\Theta_1 &= \int_{t_1}^{t_2} dt\, \delta \left[\frac{1}{2} \int_0^{L_1} \rho h \frac{\partial \vec{x}}{\partial t} \cdot \frac{\partial \vec{x}}{\partial t} ds_1 \right] \qquad (4.40) \\
&= \rho h \int_{t_1}^{t_2} \int_0^{L_1} \frac{\partial \vec{x}}{\partial t} \cdot \frac{\partial}{\partial t} \delta \vec{x}\, ds_1\, dt \\
&= \rho h \int_0^{L_1} \frac{\partial \vec{x}}{\partial t} \Big|_{t_1}^{t_2} \cdot \delta \vec{x}\, ds_1 - \rho h \int_{t_1}^{t_2} \int_0^{L_1} \frac{\partial^2 \vec{x}}{\partial t^2} \cdot \delta \vec{x}\, ds_1\, dt
\end{aligned}
$$

$$
\begin{aligned}
\Theta_2 &= \int_{t_1}^{t_2} dt\, \delta \left[-Eh \int_0^{L_1} \frac{1}{2} \left(\left(\frac{\partial \vec{x}}{\partial s_1} \cdot \frac{\partial \vec{x}}{\partial s_1} \right)^{\frac{1}{2}} - 1 \right)^2 ds_1 \right] \qquad (4.41) \\
&= -Eh \int_{t_1}^{t_2} \int_0^{L_1} \left(1 - \left(\frac{\partial \vec{x}}{\partial s_1} \cdot \frac{\partial \vec{x}}{\partial s_1} \right)^{\frac{1}{2}} \right) \left(-\frac{1}{2} \right) \left(\frac{\partial \vec{x}}{\partial s_1} \cdot \frac{\partial \vec{x}}{\partial s_1} \right)^{-\frac{1}{2}} 2 \frac{\partial \vec{x}}{\partial s_1} \cdot \frac{\partial}{\partial s_1} \delta \vec{x}\, ds_1\, dt \\
&= -Eh \int_{t_1}^{t_2} \int_0^{L_1} \left(1 - \left(\frac{\partial \vec{x}}{\partial s_1} \cdot \frac{\partial \vec{x}}{\partial s_1} \right)^{-\frac{1}{2}} \right) \frac{\partial \vec{x}}{\partial s_1} \cdot \frac{\partial}{\partial s_1} \delta \vec{x}\, ds_1\, dt \\
&= -Eh \int_{t_1}^{t_2} \left(1 - \left(\frac{\partial \vec{x}}{\partial s_1} \cdot \frac{\partial \vec{x}}{\partial s_1} \right)^{-\frac{1}{2}} \right) \frac{\partial \vec{x}}{\partial s_1} \Big|_0^{L_1} \cdot \delta \vec{x}\, dt \\
&\quad + Eh \int_{t_1}^{t_2} \int_0^{L_1} \frac{\partial}{\partial s_1} \left[\left(1 - \left(\frac{\partial \vec{x}}{\partial s_1} \cdot \frac{\partial \vec{x}}{\partial s_1} \right)^{-\frac{1}{2}} \right) \frac{\partial \vec{x}}{\partial s_1} \right] \cdot \delta \vec{x}\, ds_1\, dt
\end{aligned}
$$

$$
\begin{aligned}
\Theta_3 &= \int_{t_1}^{t_2} dt\, \delta \left[-\frac{Eh^3}{12} \int_0^{L_1} \frac{1}{2} \frac{\partial^2 \vec{x}}{\partial {s_1}^2} \cdot \frac{\partial^2 \vec{x}}{\partial {s_1}^2} ds_1 \right] \qquad (4.42) \\
&= -\frac{Eh^3}{12} \int_{t_1}^{t_2} \int_0^{L_1} \frac{\partial^2 \vec{x}}{\partial {s_1}^2} \cdot \frac{\partial^2}{\partial {s_1}^2} \delta \vec{x}\, ds_1\, dt \\
&= -\frac{Eh^3}{12} \int_{t_1}^{t_2} \int_0^{L_2} \frac{\partial^2 \vec{x}}{\partial {s_1}^2} \Big|_0^{L_1} \cdot \frac{\partial}{\partial s_1} \delta \vec{x}\, dt \\
&\quad + \frac{Eh^3}{12} \int_{t_1}^{t_2} \int_0^{L_1} \frac{\partial^3 \vec{x}}{\partial {s_1}^3} \cdot \frac{\partial}{\partial s_1} \delta \vec{x}\, ds_1\, dt
\end{aligned}
$$

$$
\begin{aligned}
&= -\frac{Eh^3}{12}\int_{t_1}^{t_2}\frac{\partial^2\vec{x}}{\partial {s_1}^2}\Big|_0^{L_1}\cdot\frac{\partial}{\partial s_1}\delta\vec{x}\,dt \\
&+\frac{Eh^3}{12}\int_{t_1}^{t_2}\frac{\partial^3\vec{x}}{\partial {s_1}^3}\Big|_0^{L_1}\cdot\delta\vec{x}\,dt \\
&-\frac{Eh^3}{12}\int_{t_1}^{t_2}\int_0^{L_1}\frac{\partial^4\vec{x}}{\partial {s_1}^4}\cdot\delta\vec{x}\,ds_1\,dt.
\end{aligned}
$$

With the preceding manipulation of the terms of the variational indicator, they can now be grouped to form the equation of motion and boundary conditions,

$$
\begin{aligned}
V.I. = &\int_{t_1}^{t_2}\int_0^{L_1}\vec{\Psi}_1\cdot\delta\vec{x}\,ds_1\,dt \\
&+\int_0^{L_1}\vec{\Psi}_2\Big|_{t_1}^{t_2}\cdot\delta\vec{x}\,ds_1+\int_{t_1}^{t_2}\vec{\Psi}_3\Big|_0^{L_1}\cdot\delta\vec{x}\,dt+\int_{t_1}^{t_2}\vec{\Psi}_4\Big|_0^{L_1}\cdot\frac{\partial}{\partial s_1}\delta\vec{x}\,dt = 0. \quad (4.43)
\end{aligned}
$$

In order for the above expression to hold, all of the $\vec{\Psi}_i$ must be zero. While $\vec{\Psi}_1$ yields the equation of motion, the boundary conditions come from the other $\vec{\Psi}$.

Equation of Motion:

$$
\rho h\frac{\partial^2\vec{x}}{\partial t^2}-Eh\frac{\partial}{\partial s_1}\left[\left(1-\left(\frac{\partial\vec{x}}{\partial s_1}\cdot\frac{\partial\vec{x}}{\partial s_1}\right)^{-\frac{1}{2}}\right)\frac{\partial\vec{x}}{\partial s_1}\right]+\frac{Eh^3}{12}\frac{\partial^4\vec{x}}{\partial {s_1}^4}=\vec{F} \qquad (4.44)
$$

Boundary Conditions:

At $s_1 = 0, L_1$*:*

$$
-Eh\left(1-\left(\frac{\partial\vec{x}}{\partial s_1}\cdot\frac{\partial\vec{x}}{\partial s_1}\right)^{-\frac{1}{2}}\right)\frac{\partial\vec{x}}{\partial s_1}+\frac{Eh^3}{12}\frac{\partial^3\vec{x}}{\partial {s_1}^3}=0 \qquad (4.45)
$$

$$
\frac{\partial^2\vec{x}}{\partial {s_1}^2}=0 \qquad (4.46)
$$

There are thus three independent structural parameters.

$$
\begin{aligned}
e1 &= \rho h \\
e2 &= \frac{Eh^3}{12}
\end{aligned}
$$

$$e3 = Eh \tag{4.47}$$

4.2.3 The Final Two-Dimensional Equations

Equation of Motion:

$$e1\frac{\partial^2 \vec{x}}{\partial t^2} + e2\frac{\partial^4 \vec{x}}{\partial {s_1}^4} - e3\frac{\partial}{\partial s_1}\left[\left(1 - \left(\frac{\partial \vec{x}}{\partial s_1} \cdot \frac{\partial \vec{x}}{\partial s_1}\right)^{-\frac{1}{2}}\right)\frac{\partial \vec{x}}{\partial s_1}\right] = \vec{F} \tag{4.48}$$

Boundary Conditions:

At $s_1 = 0, L_1$*:*

$$-e3\left(1 - \left(\frac{\partial \vec{x}}{\partial s_1} \cdot \frac{\partial \vec{x}}{\partial s_1}\right)^{-\frac{1}{2}}\right)\frac{\partial \vec{x}}{\partial s_1} + e2\frac{\partial^3 \vec{x}}{\partial {s_1}^3} = 0 \tag{4.49}$$

$$\frac{\partial^2 \vec{x}}{\partial {s_1}^2} = 0 \tag{4.50}$$

Definitions:

$$\begin{aligned} e1 &= \rho h \\ e2 &= \frac{Eh^3}{12} \\ e3 &= Eh \end{aligned} \tag{4.51}$$

4.3 Three-Dimensional Nonlinear Plate Derivation

4.3.1 Potential Energy

We have the following expression for the structural potential energy with s_1 and s_2 representing the two tangential directions and s_3 as the normal direction,

$$V = \frac{1}{2}\int\int\int \tau_{ij}\,\epsilon_{ij} ds_1\, ds_2\, ds_3. \tag{4.52}$$

We use the assumptions justified in § 4.1 to write

$$\tau_{13} = \tau_{23} = \tau_{33} = 0. \tag{4.53}$$

The remaining stresses are given in terms of the modulus of elasticity E and the Poisson ratio ν as

$$\tau_{11} = \frac{E}{1-\nu^2}\left(\epsilon_{11} + \nu\epsilon_{22}\right) \tag{4.54}$$

$$\tau_{22} = \frac{E}{1-\nu^2}\left(\epsilon_{22} + \nu\epsilon_{11}\right) \tag{4.55}$$

$$\tau_{12} = \frac{E}{1+\nu}\epsilon_{12} = \frac{E}{1-\nu^2}(1-\nu)\epsilon_{12} \tag{4.56}$$

These expressions indicate an assumption of near orthogonality of the directions s_1 and s_2. Such assumption is a linearization about small shear strain (sine of the angle between the directions is much larger than the cosine of the angle). The potential energy is now rewritten,

$$V = \frac{E}{1-\nu^2}\frac{1}{2}\int\int\int\left[{\epsilon_{11}}^2 + {\epsilon_{22}}^2 + 2\nu\epsilon_{11}\epsilon_{22} + 2(1-\nu){\epsilon_{12}}^2\right] ds_1\, ds_2\, ds_3. \tag{4.57}$$

The strains are written in terms of the position vector $\vec{x}$ and the tangential and normal directions of the plate,

$$\epsilon_{11} = \left(\left(\frac{\partial\vec{x}}{\partial s_1}\cdot\frac{\partial\vec{x}}{\partial s_1}\right)^{\frac{1}{2}} - 1\right) - (\pm_1)s_3\left(\frac{\partial^2\vec{x}}{\partial {s_1}^2}\cdot\frac{\partial^2\vec{x}}{\partial {s_1}^2}\right)^{\frac{1}{2}} \tag{4.58}$$

$$\epsilon_{22} = \left(\left(\frac{\partial\vec{x}}{\partial s_2}\cdot\frac{\partial\vec{x}}{\partial s_2}\right)^{\frac{1}{2}} - 1\right) - (\pm_2)s_3\left(\frac{\partial^2\vec{x}}{\partial {s_2}^2}\cdot\frac{\partial^2\vec{x}}{\partial {s_2}^2}\right)^{\frac{1}{2}} \tag{4.59}$$

$$\epsilon_{12} = \frac{1}{2}\left(\frac{\partial\vec{x}}{\partial s_1}\cdot\frac{\partial\vec{x}}{\partial s_2}\right) - (\pm_3)s_3\left(\frac{\partial^2\vec{x}}{\partial s_1\partial s_2}\cdot\frac{\partial^2\vec{x}}{\partial s_1\partial s_2}\right)^{\frac{1}{2}} \tag{4.60}$$

The symbols $(\pm_i)$ accommodate the direction of the curvature of the tangential directions, and will eventually fall out of the formulation. It is implied by the above that normal displacements are much larger than the in-surface displacements due to the extension and shear strain.

The terms in the integrand are grouped according to their multiplication of s_3,

$$V = \frac{E}{1-\nu^2}\frac{1}{2}\int_{s_3=-h/2}^{h/2}\int_{s_2=0}^{L_2}\int_{s_1=0}^{L_1}\left[\alpha_1 + \alpha_2 s_3 + \alpha_3 s_3^2\right] ds_1\, ds_2\, ds_3, \tag{4.61}$$

and integration over s_3 is performed, yielding

$$V = \frac{E}{1-\nu^2}\frac{1}{2}\int_{s_2=0}^{L_2}\int_{s_1=0}^{L_1}\left[h\alpha_1 + \frac{h^3}{12}\alpha_3\right] ds_1\, ds_2, \tag{4.62}$$

or

$$V = \frac{Eh}{1-\nu^2}\int_0^{L_1}\int_0^{L_2}\frac{1}{2}\alpha_1 ds_1\, ds_2 + \frac{Eh^3}{12(1-\nu^2)}\int_0^{L_1}\int_0^{L_2}\frac{1}{2}\alpha_3 ds_1\, ds_2, \tag{4.63}$$

where the terms α_1 and α_3 are

$$\begin{aligned}\alpha_1 = {} & \left(\left(\frac{\partial\vec{x}}{\partial s_1}\cdot\frac{\partial\vec{x}}{\partial s_1}\right)^{\frac{1}{2}} - 1\right)^2 + \left(\left(\frac{\partial\vec{x}}{\partial s_2}\cdot\frac{\partial\vec{x}}{\partial s_2}\right)^{\frac{1}{2}} - 1\right)^2 \\ & +2\nu\left(\left(\frac{\partial\vec{x}}{\partial s_1}\cdot\frac{\partial\vec{x}}{\partial s_1}\right)^{\frac{1}{2}} - 1\right)\left(\left(\frac{\partial\vec{x}}{\partial s_2}\cdot\frac{\partial\vec{x}}{\partial s_2}\right)^{\frac{1}{2}} - 1\right) + \frac{1-\nu}{2}\left(\frac{\partial\vec{x}}{\partial s_1}\cdot\frac{\partial\vec{x}}{\partial s_2}\right)^2\end{aligned} \tag{4.64}$$

$$\begin{aligned}\alpha_3 = {} & \left(\frac{\partial^2\vec{x}}{\partial {s_1}^2}\cdot\frac{\partial^2\vec{x}}{\partial {s_1}^2}\right) + \left(\frac{\partial^2\vec{x}}{\partial {s_2}^2}\cdot\frac{\partial^2\vec{x}}{\partial {s_2}^2}\right) \\ & +2\nu(\pm_1)(\pm_2)\left(\frac{\partial^2\vec{x}}{\partial {s_1}^2}\cdot\frac{\partial^2\vec{x}}{\partial {s_1}^2}\right)^{\frac{1}{2}}\left(\frac{\partial^2\vec{x}}{\partial {s_2}^2}\cdot\frac{\partial^2\vec{x}}{\partial {s_2}^2}\right)^{\frac{1}{2}} + 2(1-\nu)\left(\frac{\partial^2\vec{x}}{\partial s_1\partial s_2}\cdot\frac{\partial^2\vec{x}}{\partial s_1\partial s_2}\right)\end{aligned} \tag{4.65}$$

We now write a relation which indicates that the second spatial derivatives in both tangential directions are normal to the same surface (again assuming the dominance of the normal displacements over those due to strain). In the equality, the term $(\pm_1)(\pm_2)$ must be employed to accommodate the binary direction of the curvature. The relation is

$$(\pm_1)(\pm_2)\left(\frac{\partial^2\vec{x}}{\partial {s_1}^2}\cdot\frac{\partial^2\vec{x}}{\partial {s_1}^2}\right)^{-\frac{1}{2}}\frac{\partial^2\vec{x}}{\partial {s_1}^2} = \left(\frac{\partial^2\vec{x}}{\partial {s_2}^2}\cdot\frac{\partial^2\vec{x}}{\partial {s_2}^2}\right)^{-\frac{1}{2}}\frac{\partial^2\vec{x}}{\partial {s_2}^2}. \tag{4.66}$$

Premultiplying both sides by $\partial^2\vec{x}/\partial {s_1}^2$ and multiplying through by

$(\partial^2\vec{x}/\partial s_2{}^2 \cdot \partial^2\vec{x}/\partial s_2{}^2)^{1/2}$ we obtain

$$(\pm_1)(\pm_2)\left(\frac{\partial^2\vec{x}}{\partial s_1{}^2}\cdot\frac{\partial^2\vec{x}}{\partial s_1{}^2}\right)^{\frac{1}{2}}\left(\frac{\partial^2\vec{x}}{\partial s_2{}^2}\cdot\frac{\partial^2\vec{x}}{\partial s_2{}^2}\right)^{\frac{1}{2}}=\frac{\partial^2\vec{x}}{\partial s_1{}^2}\cdot\frac{\partial^2\vec{x}}{\partial s_2{}^2}. \tag{4.67}$$

The expression for α_3 is then able to be simplified as

$$\begin{aligned}\alpha_3 = &\left(\frac{\partial^2\vec{x}}{\partial s_1{}^2}\cdot\frac{\partial^2\vec{x}}{\partial s_1{}^2}\right)+\left(\frac{\partial^2\vec{x}}{\partial s_2{}^2}\cdot\frac{\partial^2\vec{x}}{\partial s_2{}^2}\right)\\ &+2\nu\frac{\partial^2\vec{x}}{\partial s_1{}^2}\cdot\frac{\partial^2\vec{x}}{\partial s_2{}^2}+2(1-\nu)\left(\frac{\partial^2\vec{x}}{\partial s_1\partial s_2}\cdot\frac{\partial^2\vec{x}}{\partial s_1\partial s_2}\right).\end{aligned} \tag{4.68}$$

The potential energy is thus expressed through equations 4.63, 4.68, and 4.64.

4.3.2 The Equations of Motion

The kinetic energy is now defined. In keeping with the assumption of a thin plate, we consider only the linear kinetic energy and neglect the rotational kinetic energy, so that

$$T=\frac{1}{2}\int_0^{L_1}\int_0^{L_2}\rho h\frac{\partial\vec{x}}{\partial t}\cdot\frac{\partial\vec{x}}{\partial t}ds_1\,ds_2. \tag{4.69}$$

With external generalized forces considered as Ξ, the variational indicator is formed as

$$V.I.=\int_{t_1}^{t_2}dt[\delta(T-V)+\sum_j \Xi_j\delta\xi_j]=0 \tag{4.70}$$

$$\begin{aligned}V.I.=\int_{t_1}^{t_2}dt[\delta(\frac{1}{2}\int_0^{L_1}\int_0^{L_2}\rho h\frac{\partial\vec{x}}{\partial t}\cdot\frac{\partial\vec{x}}{\partial t}ds_1\,ds_2-\frac{Eh}{1-\nu^2}\int_0^{L_1}\int_0^{L_2}\frac{1}{2}\alpha_1 ds_1\,ds_2\\ -\frac{Eh^3}{12(1-\nu^2)}\int_0^{L_1}\int_0^{L_2}\frac{1}{2}\alpha_3 ds_1\,ds_2)+\int_0^{L_1}\int_0^{L_2}\vec{F}\cdot\delta\vec{x}\,ds_1\,ds_2=0].\end{aligned} \tag{4.71}$$

Considering the expressions of α_1 and α_3, the variational indicator contains nine terms associated with the kinetic and potential energies. These are denoted as $\Theta_1 \rightarrow \Theta_9$,

$$\begin{aligned}
\Theta_1 &= \int_{t_1}^{t_2} dt\, \delta \left[\frac{1}{2} \int_0^{L_1} \int_0^{L_2} \rho h \frac{\partial \vec{x}}{\partial t} \cdot \frac{\partial \vec{x}}{\partial t} ds_1\, ds_2 \right] \\
&= \rho h \int_{t_1}^{t_2} \int_0^{L_1} \int_0^{L_2} \frac{\partial \vec{x}}{\partial t} \cdot \frac{\partial}{\partial t} \delta \vec{x}\, ds_1\, ds_2\, dt \\
&= \rho h \int_0^{L_1} \int_0^{L_2} \frac{\partial \vec{x}}{\partial t}\Big|_{t_1}^{t_2} \cdot \delta \vec{x}\, ds_1\, ds_2 - \rho h \int_{t_1}^{t_2} \int_0^{L_1} \int_0^{L_2} \frac{\partial^2 \vec{x}}{\partial t^2} \cdot \delta \vec{x}\, ds_1\, ds_2\, dt
\end{aligned} \tag{4.72}$$

$$\begin{aligned}
\Theta_2 &= \int_{t_1}^{t_2} dt\, \delta \left[-\frac{Eh}{1-\nu^2} \int_0^{L_1} \int_0^{L_2} \frac{1}{2} \left(\left(\frac{\partial \vec{x}}{\partial s_1} \cdot \frac{\partial \vec{x}}{\partial s_1} \right)^{\frac{1}{2}} - 1 \right)^2 ds_1\, ds_2 \right] \\
&= -\frac{Eh}{1-\nu^2} \int_{t_1}^{t_2} \int_0^{L_1} \int_0^{L_2} \left(1 - \left(\frac{\partial \vec{x}}{\partial s_1} \cdot \frac{\partial \vec{x}}{\partial s_1} \right)^{\frac{1}{2}} \right) \\
&\quad \times \left(-\frac{1}{2} \right) \left(\frac{\partial \vec{x}}{\partial s_1} \cdot \frac{\partial \vec{x}}{\partial s_1} \right)^{-\frac{1}{2}} 2 \frac{\partial \vec{x}}{\partial s_1} \cdot \frac{\partial}{\partial s_1} \delta \vec{x}\, ds_1\, ds_2\, dt \\
&= -\frac{Eh}{1-\nu^2} \int_{t_1}^{t_2} \int_0^{L_1} \int_0^{L_2} \left(1 - \left(\frac{\partial \vec{x}}{\partial s_1} \cdot \frac{\partial \vec{x}}{\partial s_1} \right)^{-\frac{1}{2}} \right) \frac{\partial \vec{x}}{\partial s_1} \cdot \frac{\partial}{\partial s_1} \delta \vec{x}\, ds_1\, ds_2\, dt \\
&= -\frac{Eh}{1-\nu^2} \int_{t_1}^{t_2} \int_0^{L_2} \left(1 - \left(\frac{\partial \vec{x}}{\partial s_1} \cdot \frac{\partial \vec{x}}{\partial s_1} \right)^{-\frac{1}{2}} \right) \frac{\partial \vec{x}}{\partial s_1}\Big|_0^{L_1} \cdot \delta \vec{x}\, ds_2\, dt \\
&\quad + \frac{Eh}{1-\nu^2} \int_{t_1}^{t_2} \int_0^{L_1} \int_0^{L_2} \frac{\partial}{\partial s_1} \left[\left(1 - \left(\frac{\partial \vec{x}}{\partial s_1} \cdot \frac{\partial \vec{x}}{\partial s_1} \right)^{-\frac{1}{2}} \right) \frac{\partial \vec{x}}{\partial s_1} \right] \cdot \delta \vec{x}\, ds_1\, ds_2\, dt
\end{aligned} \tag{4.73}$$

$$\begin{aligned}
\Theta_3 &= -\frac{Eh}{1-\nu^2} \int_{t_1}^{t_2} \int_0^{L_1} \left(1 - \left(\frac{\partial \vec{x}}{\partial s_2} \cdot \frac{\partial \vec{x}}{\partial s_2} \right)^{-\frac{1}{2}} \right) \frac{\partial \vec{x}}{\partial s_2}\Big|_0^{L_2} \cdot \delta \vec{x}\, ds_1\, dt \\
&\quad + \frac{Eh}{1-\nu^2} \int_{t_1}^{t_2} \int_0^{L_1} \int_0^{L_2} \frac{\partial}{\partial s_2} \left[\left(1 - \left(\frac{\partial \vec{x}}{\partial s_2} \cdot \frac{\partial \vec{x}}{\partial s_2} \right)^{-\frac{1}{2}} \right) \frac{\partial \vec{x}}{\partial s_2} \right] \cdot \delta \vec{x}\, ds_1\, ds_2\, dt
\end{aligned} \tag{4.74}$$

$$\Theta_4 = \int_{t_1}^{t_2} dt\, \delta \left[-\frac{Eh}{1-\nu^2} \int_0^{L_1} \int_0^{L_2} \nu \left(\left(\frac{\partial \vec{x}}{\partial s_1} \cdot \frac{\partial \vec{x}}{\partial s_1} \right)^{\frac{1}{2}} - 1 \right) \right. \tag{4.75}$$

$$
\begin{aligned}
&\times \left(\left(\frac{\partial \vec{x}}{\partial s_2} \cdot \frac{\partial \vec{x}}{\partial s_2} \right)^{\frac{1}{2}} - 1 \right) ds_1\, ds_2 \Bigg] \\
&= -\frac{Eh}{1-\nu^2}\nu \int_{t_1}^{t_2} \int_0^{L_1} \int_0^{L_2} \left(\left(\frac{\partial \vec{x}}{\partial s_2} \cdot \frac{\partial \vec{x}}{\partial s_2} \right)^{\frac{1}{2}} - 1 \right) \\
&\quad \times \left(\frac{\partial \vec{x}}{\partial s_1} \cdot \frac{\partial \vec{x}}{\partial s_1} \right)^{-\frac{1}{2}} \frac{\partial \vec{x}}{\partial s_1} \cdot \frac{\partial}{\partial s_1} \delta \vec{x}\, ds_1\, ds_2\, dt \\
&\quad -\frac{Eh}{1-\nu^2}\nu \int_{t_1}^{t_2} \int_0^{L_1} \int_0^{L_2} \left(\left(\frac{\partial \vec{x}}{\partial s_1} \cdot \frac{\partial \vec{x}}{\partial s_1} \right)^{\frac{1}{2}} - 1 \right) \\
&\quad \times \left(\frac{\partial \vec{x}}{\partial s_2} \cdot \frac{\partial \vec{x}}{\partial s_2} \right)^{-\frac{1}{2}} \frac{\partial \vec{x}}{\partial s_2} \cdot \frac{\partial}{\partial s_2} \delta \vec{x}\, ds_1\, ds_2\, dt \\
&= -\frac{Eh}{1-\nu^2}\nu \int_{t_1}^{t_2} \int_0^{L_2} \left(\left(\frac{\partial \vec{x}}{\partial s_2} \cdot \frac{\partial \vec{x}}{\partial s_2} \right)^{\frac{1}{2}} - 1 \right) \left(\frac{\partial \vec{x}}{\partial s_1} \cdot \frac{\partial \vec{x}}{\partial s_1} \right)^{-\frac{1}{2}} \frac{\partial \vec{x}}{\partial s_1} \Big|_0^{L_1} \cdot \delta \vec{x}\, ds_2\, dt \\
&\quad +\frac{Eh}{1-\nu^2}\nu \int_{t_1}^{t_2} \int_0^{L_1} \int_0^{L_2} \\
&\qquad \frac{\partial}{\partial s_1} \left[\left(\left(\frac{\partial \vec{x}}{\partial s_2} \cdot \frac{\partial \vec{x}}{\partial s_2} \right)^{\frac{1}{2}} - 1 \right) \left(\frac{\partial \vec{x}}{\partial s_1} \cdot \frac{\partial \vec{x}}{\partial s_1} \right)^{-\frac{1}{2}} \frac{\partial \vec{x}}{\partial s_1} \right] \cdot \delta \vec{x}\, ds_1\, ds_2\, dt \\
&\quad -\frac{Eh}{1-\nu^2}\nu \int_{t_1}^{t_2} \int_0^{L_1} \left(\left(\frac{\partial \vec{x}}{\partial s_1} \cdot \frac{\partial \vec{x}}{\partial s_1} \right)^{\frac{1}{2}} - 1 \right) \left(\frac{\partial \vec{x}}{\partial s_2} \cdot \frac{\partial \vec{x}}{\partial s_2} \right)^{-\frac{1}{2}} \frac{\partial \vec{x}}{\partial s_2} \Big|_0^{L_2} \cdot \delta \vec{x}\, ds_1\, dt \\
&\quad +\frac{Eh}{1-\nu^2}\nu \int_{t_1}^{t_2} \int_0^{L_1} \int_0^{L_2} \\
&\qquad \frac{\partial}{\partial s_2} \left[\left(\left(\frac{\partial \vec{x}}{\partial s_1} \cdot \frac{\partial \vec{x}}{\partial s_1} \right)^{\frac{1}{2}} - 1 \right) \left(\frac{\partial \vec{x}}{\partial s_2} \cdot \frac{\partial \vec{x}}{\partial s_2} \right)^{-\frac{1}{2}} \frac{\partial \vec{x}}{\partial s_2} \right] \cdot \delta \vec{x}\, ds_1\, ds_2\, dt
\end{aligned}
$$

$$
\begin{aligned}
\Theta_5 &= \int_{t_1}^{t_2} dt\, \delta(-\frac{Eh}{1-\nu^2} \int_0^{L_1} \int_0^{L_2} \frac{1-\nu}{4} \left(\frac{\partial \vec{x}}{\partial s_1} \cdot \frac{\partial \vec{x}}{\partial s_2} \right)^2 ds_1\, ds_2) \qquad (4.76) \\
&= -\frac{Eh}{1-\nu^2} \frac{1-\nu}{2} \int_{t_1}^{t_2} \int_0^{L_1} \int_0^{L_2} \left(\frac{\partial \vec{x}}{\partial s_1} \cdot \frac{\partial \vec{x}}{\partial s_2} \right) \frac{\partial \vec{x}}{\partial s_2} \cdot \frac{\partial}{\partial s_1} \delta \vec{x}\, ds_1\, ds_2\, dt \\
&\quad -\frac{Eh}{1-\nu^2} \frac{1-\nu}{2} \int_{t_1}^{t_2} \int_0^{L_1} \int_0^{L_2} \left(\frac{\partial \vec{x}}{\partial s_1} \cdot \frac{\partial \vec{x}}{\partial s_2} \right) \frac{\partial \vec{x}}{\partial s_1} \cdot \frac{\partial}{\partial s_2} \delta \vec{x}\, ds_1\, ds_2\, dt \\
&= -\frac{Eh}{1-\nu^2} \frac{1-\nu}{2} \int_{t_1}^{t_2} \int_0^{L_2} \left(\frac{\partial \vec{x}}{\partial s_1} \cdot \frac{\partial \vec{x}}{\partial s_2} \right) \frac{\partial \vec{x}}{\partial s_2} \Big|_0^{L_1} \cdot \delta \vec{x}\, ds_2\, dt \\
&\quad +\frac{Eh}{1-\nu^2} \frac{1-\nu}{2} \int_{t_1}^{t_2} \int_0^{L_1} \int_0^{L_2} \frac{\partial}{\partial s_1} \left[\left(\frac{\partial \vec{x}}{\partial s_1} \cdot \frac{\partial \vec{x}}{\partial s_2} \right) \frac{\partial \vec{x}}{\partial s_2} \right] \cdot \delta \vec{x}\, ds_1\, ds_2\, dt
\end{aligned}
$$

$$
\begin{aligned}
&-\frac{Eh}{1-\nu^2}\frac{1-\nu}{2}\int_{t_1}^{t_2}\int_0^{L_1}\left(\frac{\partial\vec{x}}{\partial s_1}\cdot\frac{\partial\vec{x}}{\partial s_2}\right)\frac{\partial\vec{x}}{\partial s_1}\Big|_0^{L_2}\cdot\delta\vec{x}\,ds_1\,dt\\
&+\frac{Eh}{1-\nu^2}\frac{1-\nu}{2}\int_{t_1}^{t_2}\int_0^{L_1}\int_0^{L_2}\frac{\partial}{\partial s_2}\left[\left(\frac{\partial\vec{x}}{\partial s_1}\cdot\frac{\partial\vec{x}}{\partial s_2}\right)\frac{\partial\vec{x}}{\partial s_1}\right]\cdot\delta\vec{x}\,ds_1\,ds_2\,dt
\end{aligned}
$$

$$
\begin{aligned}
\Theta_6 &= \int_{t_1}^{t_2} dt\,\delta(-\frac{Eh^3}{12(1-\nu^2)}\int_0^{L_1}\int_0^{L_2}\frac{1}{2}\frac{\partial^2\vec{x}}{\partial {s_1}^2}\cdot\frac{\partial^2\vec{x}}{\partial {s_1}^2}ds_1\,ds_2)\\
&= -\frac{Eh^3}{12(1-\nu^2)}\int_{t_1}^{t_2}\int_0^{L_1}\int_0^{L_2}\frac{\partial^2\vec{x}}{\partial {s_1}^2}\cdot\frac{\partial^2}{\partial {s_1}^2}\delta\vec{x}\,ds_1\,ds_2\,dt\\
&= -\frac{Eh^3}{12(1-\nu^2)}\int_{t_1}^{t_2}\int_0^{L_2}\frac{\partial^2\vec{x}}{\partial {s_1}^2}\Big|_0^{L_1}\cdot\frac{\partial}{\partial s_1}\delta\vec{x}\,ds_2\,dt\\
&\quad+\frac{Eh^3}{12(1-\nu^2)}\int_{t_1}^{t_2}\int_0^{L_1}\int_0^{L_2}\frac{\partial^3\vec{x}}{\partial {s_1}^3}\cdot\frac{\partial}{\partial s_1}\delta\vec{x}\,ds_1\,ds_2\,dt\\
&= -\frac{Eh^3}{12(1-\nu^2)}\int_{t_1}^{t_2}\int_0^{L_2}\frac{\partial^2\vec{x}}{\partial {s_1}^2}\Big|_0^{L_1}\cdot\frac{\partial}{\partial s_1}\delta\vec{x}\,ds_2\,dt\\
&\quad+\frac{Eh^3}{12(1-\nu^2)}\int_{t_1}^{t_2}\int_0^{L_2}\frac{\partial^3\vec{x}}{\partial {s_1}^3}\Big|_0^{L_1}\cdot\delta\vec{x}\,ds_2\,dt\\
&\quad-\frac{Eh^3}{12(1-\nu^2)}\int_{t_1}^{t_2}\int_0^{L_1}\int_0^{L_2}\frac{\partial^4\vec{x}}{\partial {s_1}^4}\cdot\delta\vec{x}\,ds_1\,ds_2\,dt
\end{aligned}
\tag{4.77}
$$

$$
\begin{aligned}
\Theta_7 &= -\frac{Eh^3}{12(1-\nu^2)}\int_{t_1}^{t_2}\int_0^{L_1}\frac{\partial^2\vec{x}}{\partial {s_2}^2}\Big|_0^{L_2}\cdot\frac{\partial}{\partial s_2}\delta\vec{x}\,ds_1\,dt\\
&\quad+\frac{Eh^3}{12(1-\nu^2)}\int_{t_1}^{t_2}\int_0^{L_1}\frac{\partial^3\vec{x}}{\partial {s_2}^3}\Big|_0^{L_2}\cdot\delta\vec{x}\,ds_1\,dt\\
&\quad-\frac{Eh^3}{12(1-\nu^2)}\int_{t_1}^{t_2}\int_0^{L_1}\int_0^{L_2}\frac{\partial^4\vec{x}}{\partial {s_2}^4}\cdot\delta\vec{x}\,ds_1\,ds_2\,dt
\end{aligned}
\tag{4.78}
$$

$$
\begin{aligned}
\Theta_8 &= \int_{t_1}^{t_2} dt\,\delta(-\frac{Eh^3}{12(1-\nu^2)}\int_0^{L_1}\int_0^{L_2}\nu\frac{\partial^2\vec{x}}{\partial {s_1}^2}\cdot\frac{\partial^2\vec{x}}{\partial {s_2}^2}ds_1\,ds_2)\\
&= -\frac{Eh^3}{12(1-\nu^2)}\nu\int_{t_1}^{t_2}\int_0^{L_1}\int_0^{L_2}\frac{\partial^2\vec{x}}{\partial {s_2}^2}\cdot\frac{\partial^2}{\partial {s_1}^2}\delta\vec{x}\,ds_1\,ds_2\,dt\\
&\quad-\frac{Eh^3}{12(1-\nu^2)}\nu\int_{t_1}^{t_2}\int_0^{L_1}\int_0^{L_2}\frac{\partial^2\vec{x}}{\partial {s_1}^2}\cdot\frac{\partial^2}{\partial {s_2}^2}\delta\vec{x}\,ds_1\,ds_2\,dt\\
&= -\frac{Eh^3}{12(1-\nu^2)}\nu\int_{t_1}^{t_2}\int_0^{L_2}\frac{\partial^2\vec{x}}{\partial {s_2}^2}\Big|_0^{L_1}\cdot\frac{\partial}{\partial s_1}\delta\vec{x}\,ds_2\,dt
\end{aligned}
\tag{4.79}
$$

$$
\begin{aligned}
&+\frac{Eh^3}{12(1-\nu^2)}\nu \int_{t_1}^{t_2}\int_0^{L_1}\int_0^{L_2} \frac{\partial^3\vec{x}}{\partial s_1\partial s_2{}^2}\cdot\frac{\partial}{\partial s_1}\delta\vec{x}\,ds_1\,ds_2\,dt\\
&-\frac{Eh^3}{12(1-\nu^2)}\nu \int_{t_1}^{t_2}\int_0^{L_1} \frac{\partial^2\vec{x}}{\partial s_1{}^2}\Big|_0^{L_2}\cdot\frac{\partial}{\partial s_2}\delta\vec{x}\,ds_1\,dt\\
&+\frac{Eh^3}{12(1-\nu^2)}\nu \int_{t_1}^{t_2}\int_0^{L_1}\int_0^{L_2} \frac{\partial^3\vec{x}}{\partial s_1{}^2\partial s_2}\cdot\frac{\partial}{\partial s_2}\delta\vec{x}\,ds_1\,ds_2\,dt\\
=&-\frac{Eh^3}{12(1-\nu^2)}\nu \int_{t_1}^{t_2}\int_0^{L_2} \frac{\partial^2\vec{x}}{\partial s_2{}^2}\Big|_0^{L_1}\cdot\frac{\partial}{\partial s_1}\delta\vec{x}\,ds_2\,dt\\
&+\frac{Eh^3}{12(1-\nu^2)}\nu \int_{t_1}^{t_2}\int_0^{L_2} \frac{\partial^3\vec{x}}{\partial s_1\partial s_2{}^2}\Big|_0^{L_1}\cdot\delta\vec{x}\,ds_2\,dt\\
&-\frac{Eh^3}{12(1-\nu^2)}\nu \int_{t_1}^{t_2}\int_0^{L_1}\int_0^{L_2} \frac{\partial^4\vec{x}}{\partial s_1{}^2\partial s_2{}^2}\cdot\delta\vec{x}\,ds_1\,ds_2\,dt\\
&-\frac{Eh^3}{12(1-\nu^2)}\nu \int_{t_1}^{t_2}\int_0^{L_1} \frac{\partial^2\vec{x}}{\partial s_1{}^2}\Big|_0^{L_2}\cdot\frac{\partial}{\partial s_2}\delta\vec{x}\,ds_1\,dt\\
&+\frac{Eh^3}{12(1-\nu^2)}\nu \int_{t_1}^{t_2}\int_0^{L_1} \frac{\partial^3\vec{x}}{\partial s_1{}^2\partial s_2}\Big|_0^{L_2}\cdot\delta\vec{x}\,ds_1\,dt\\
&-\frac{Eh^3}{12(1-\nu^2)}\nu \int_{t_1}^{t_2}\int_0^{L_1}\int_0^{L_2} \frac{\partial^4\vec{x}}{\partial s_1{}^2\partial s_2{}^2}\cdot\delta\vec{x}\,ds_1\,ds_2\,dt
\end{aligned}
$$

$$
\begin{aligned}
\Theta_9 =& \int_{t_1}^{t_2} dt\,\delta(-\frac{Eh^3}{12(1-\nu^2)}\int_0^{L_1}\int_0^{L_2}(1-\nu)\left(\frac{\partial^2\vec{x}}{\partial s_1\partial s_2}\cdot\frac{\partial^2\vec{x}}{\partial s_1\partial s_2}\right)ds_1\,ds_2) \qquad (4.80)\\
=&-\frac{Eh^3}{12(1-\nu^2)}2(1-\nu)\int_{t_1}^{t_2}\int_0^{L_1}\int_0^{L_2}\frac{\partial^2\vec{x}}{\partial s_1\partial s_2}\cdot\frac{\partial^2}{\partial s_1\partial s_2}\delta\vec{x}\,ds_1\,ds_2\,dt\\
=&-\frac{Eh^3}{12(1-\nu^2)}2(1-\nu)\int_{t_1}^{t_2}\int_0^{L_2}\frac{\partial^2\vec{x}}{\partial s_1\partial s_2}\Big|_0^{L_1}\cdot\frac{\partial}{\partial s_2}\delta\vec{x}\,ds_2\,dt\\
&+\frac{Eh^3}{12(1-\nu^2)}2(1-\nu)\int_{t_1}^{t_2}\int_0^{L_1}\int_0^{L_2}\frac{\partial^3\vec{x}}{\partial s_1{}^2\partial s_2}\cdot\frac{\partial}{\partial s_2}\delta\vec{x}\,ds_1\,ds_2\,dt\\
=&-\frac{Eh^3}{12(1-\nu^2)}2(1-\nu)\int_{t_1}^{t_2}\frac{\partial^2\vec{x}}{\partial s_1\partial s_2}\Big|_0^{L_1}\Big|_0^{L_2}\cdot\delta\vec{x}\,ds_2\,dt\\
&+\frac{Eh^3}{12(1-\nu^2)}2(1-\nu)\int_{t_1}^{t_2}\int_0^{L_2}\frac{\partial^3\vec{x}}{\partial s_1\partial s_2{}^2}\Big|_0^{L_1}\cdot\delta\vec{x}\,ds_2\,dt\\
&+\frac{Eh^3}{12(1-\nu^2)}2(1-\nu)\int_{t_1}^{t_2}\int_0^{L_1}\frac{\partial^3\vec{x}}{\partial s_1{}^2\partial s_2}\Big|_0^{L_2}\cdot\delta\vec{x}\,ds_1\,dt\\
&-\frac{Eh^3}{12(1-\nu^2)}2(1-\nu)\int_{t_1}^{t_2}\int_0^{L_1}\int_0^{L_2}\frac{\partial^4\vec{x}}{\partial s_1{}^2\partial s_2{}^2}\cdot\delta\vec{x}\,ds_1\,ds_2\,dt.
\end{aligned}
$$

With the preceding manipulation of the terms of the variational indicator, the terms can now be grouped to form the equation of motion and boundary conditions,

$$\begin{aligned} V.I. = &\int_{t_1}^{t_2}\int_0^{L_1}\int_0^{L_2} \vec{\Psi}_1 \cdot \delta\vec{x}\, ds_1\, ds_2\, dt + \int_0^{L_1}\int_0^{L_2} \vec{\Psi}_2\big|_{t_1}^{t_2} \cdot \delta\vec{x}\, ds_1\, ds_2 \\ &+ \int_{t_1}^{t_2}\int_0^{L_2} \vec{\Psi}_3\big|_0^{L_1} \cdot \delta\vec{x}\, ds_2\, dt + \int_{t_1}^{t_2}\int_0^{L_1} \vec{\Psi}_4\big|_0^{L_2} \cdot \delta\vec{x}\, ds_1\, dt \\ &+ \int_{t_1}^{t_2}\int_0^{L_2} \vec{\Psi}_5\big|_0^{L_1} \cdot \frac{\partial}{\partial s_1}\delta\vec{x}\, ds_2\, dt + \int_{t_1}^{t_2}\int_0^{L_1} \vec{\Psi}_6\big|_0^{L_2} \cdot \frac{\partial}{\partial s_2}\delta\vec{x}\, ds_1\, dt \\ &+ \int_{t_1}^{t_2} \vec{\Psi}_7\big|_0^{L_1}\big|_0^{L_2} \cdot \delta\vec{x}\, ds_2\, dt = 0. \end{aligned} \tag{4.81}$$

In order for the above expression to hold, all of the $\vec{\Psi}_i$ must be zero. While $\vec{\Psi}_1$ yields the equation of motion, the boundary conditions come from the other $\vec{\Psi}$. With some cancellation of terms, we write the equation of motion

$$\begin{aligned} &\rho h\frac{\partial^2\vec{x}}{\partial t^2} - \frac{Eh}{1-\nu^2}\frac{\partial}{\partial s_1}\left[\left(1-\left(\frac{\partial\vec{x}}{\partial s_1}\cdot\frac{\partial\vec{x}}{\partial s_1}\right)^{-\frac{1}{2}}\right)\frac{\partial\vec{x}}{\partial s_1}\right] \\ &-\frac{Eh}{1-\nu^2}\frac{\partial}{\partial s_2}\left[\left(1-\left(\frac{\partial\vec{x}}{\partial s_2}\cdot\frac{\partial\vec{x}}{\partial s_2}\right)^{-\frac{1}{2}}\right)\frac{\partial\vec{x}}{\partial s_2}\right] \\ &-\frac{Eh}{1-\nu^2}\nu\frac{\partial}{\partial s_1}\left[\left(\left(\frac{\partial\vec{x}}{\partial s_2}\cdot\frac{\partial\vec{x}}{\partial s_2}\right)^{\frac{1}{2}}-1\right)\left(\frac{\partial\vec{x}}{\partial s_1}\cdot\frac{\partial\vec{x}}{\partial s_1}\right)^{-\frac{1}{2}}\frac{\partial\vec{x}}{\partial s_1}\right] \\ &-\frac{Eh}{1-\nu^2}\nu\frac{\partial}{\partial s_2}\left[\left(\left(\frac{\partial\vec{x}}{\partial s_1}\cdot\frac{\partial\vec{x}}{\partial s_1}\right)^{\frac{1}{2}}-1\right)\left(\frac{\partial\vec{x}}{\partial s_2}\cdot\frac{\partial\vec{x}}{\partial s_2}\right)^{-\frac{1}{2}}\frac{\partial\vec{x}}{\partial s_2}\right] \\ &-\frac{Eh}{1-\nu^2}\frac{1-\nu}{2}\frac{\partial}{\partial s_1}\left[\left(\frac{\partial\vec{x}}{\partial s_1}\cdot\frac{\partial\vec{x}}{\partial s_2}\right)\frac{\partial\vec{x}}{\partial s_2}\right] - \frac{Eh}{1-\nu^2}\frac{1-\nu}{2}\frac{\partial}{\partial s_2}\left[\left(\frac{\partial\vec{x}}{\partial s_1}\cdot\frac{\partial\vec{x}}{\partial s_2}\right)\frac{\partial\vec{x}}{\partial s_1}\right] \\ &+\frac{Eh^3}{12(1-\nu^2)}\frac{\partial^4\vec{x}}{\partial {s_1}^4} + \frac{Eh^3}{12(1-\nu^2)}\frac{\partial^4\vec{x}}{\partial {s_2}^4} + 2\frac{Eh^3}{12(1-\nu^2)}\frac{\partial^4\vec{x}}{\partial {s_1}^2\partial {s_2}^2} = \vec{F}. \end{aligned} \tag{4.82}$$

As we consider the case of small extension, we make linearizations such

$$\left(\left(\frac{\partial\vec{x}}{\partial s_2}\cdot\frac{\partial\vec{x}}{\partial s_2}\right)^{\frac{1}{2}}-1\right)\left(\frac{\partial\vec{x}}{\partial s_1}\cdot\frac{\partial\vec{x}}{\partial s_1}\right)^{-\frac{1}{2}} = \left(1-\left(\frac{\partial\vec{x}}{\partial s_2}\cdot\frac{\partial\vec{x}}{\partial s_2}\right)^{-\frac{1}{2}}\right). \tag{4.83}$$

The equations of motion and associated boundary conditions are then written as follows.

Equation of Motion:

$$\begin{aligned}
&\rho h\frac{\partial^2\vec{x}}{\partial t^2}+\frac{Eh^3}{12(1-\nu^2)}\left(\frac{\partial^4\vec{x}}{\partial {s_1}^4}+2\frac{\partial^4\vec{x}}{\partial {s_1}^2\partial {s_2}^2}+\frac{\partial^4\vec{x}}{\partial {s_2}^4}\right)\\
&\quad-\frac{Eh}{1-\nu^2}\frac{\partial}{\partial s_1}\left(\left[\left(1-\left(\frac{\partial\vec{x}}{\partial s_1}\cdot\frac{\partial\vec{x}}{\partial s_1}\right)^{-\frac{1}{2}}\right)+\nu\left(1-\left(\frac{\partial\vec{x}}{\partial s_2}\cdot\frac{\partial\vec{x}}{\partial s_2}\right)^{-\frac{1}{2}}\right)\right]\frac{\partial\vec{x}}{\partial s_1}\right)\\
&\quad-\frac{Eh}{1-\nu^2}\frac{\partial}{\partial s_2}\left(\left[\left(1-\left(\frac{\partial\vec{x}}{\partial s_2}\cdot\frac{\partial\vec{x}}{\partial s_2}\right)^{-\frac{1}{2}}\right)+\nu\left(1-\left(\frac{\partial\vec{x}}{\partial s_1}\cdot\frac{\partial\vec{x}}{\partial s_1}\right)^{-\frac{1}{2}}\right)\right]\frac{\partial\vec{x}}{\partial s_2}\right)\\
&\quad-\frac{Eh}{1-\nu^2}\frac{1-\nu}{2}\left(\frac{\partial}{\partial s_1}\left[\left(\frac{\partial\vec{x}}{\partial s_1}\cdot\frac{\partial\vec{x}}{\partial s_2}\right)\frac{\partial\vec{x}}{\partial s_2}\right]+\frac{\partial}{\partial s_2}\left[\left(\frac{\partial\vec{x}}{\partial s_1}\cdot\frac{\partial\vec{x}}{\partial s_2}\right)\frac{\partial\vec{x}}{\partial s_1}\right]\right)=\vec{F}
\end{aligned}\tag{4.84}$$

Boundary Conditions:

At $s_1 = 0, L_1$*:*

$$\begin{aligned}
&-\frac{Eh}{1-\nu^2}\left[\left(1-\left(\frac{\partial\vec{x}}{\partial s_1}\cdot\frac{\partial\vec{x}}{\partial s_1}\right)^{-\frac{1}{2}}\right)+\nu\left(1-\left(\frac{\partial\vec{x}}{\partial s_2}\cdot\frac{\partial\vec{x}}{\partial s_2}\right)^{-\frac{1}{2}}\right)\right]\frac{\partial\vec{x}}{\partial s_1}\\
&\quad-\frac{Eh}{1-\nu^2}\frac{1-\nu}{2}\left(\frac{\partial\vec{x}}{\partial s_1}\cdot\frac{\partial\vec{x}}{\partial s_2}\right)\frac{\partial\vec{x}}{\partial s_2}+\frac{Eh^3}{12(1-\nu^2)}\frac{\partial^3\vec{x}}{\partial {s_1}^3}\\
&\quad+\frac{Eh^3}{12(1-\nu^2)}(2-\nu)\frac{\partial^3\vec{x}}{\partial s_1\partial {s_2}^2}=0
\end{aligned}\tag{4.85}$$

$$\frac{\partial^2\vec{x}}{\partial {s_1}^2}+\nu\frac{\partial^2\vec{x}}{\partial {s_2}^2}=0\tag{4.86}$$

At $s_2 = 0, L_2$*:*

$$\begin{aligned}
&-\frac{Eh}{1-\nu^2}\left[\left(1-\left(\frac{\partial\vec{x}}{\partial s_2}\cdot\frac{\partial\vec{x}}{\partial s_2}\right)^{-\frac{1}{2}}\right)+\nu\left(1-\left(\frac{\partial\vec{x}}{\partial s_1}\cdot\frac{\partial\vec{x}}{\partial s_1}\right)^{-\frac{1}{2}}\right)\right]\frac{\partial\vec{x}}{\partial s_2}\\
&\quad-\frac{Eh}{1-\nu^2}\frac{1-\nu}{2}\left(\frac{\partial\vec{x}}{\partial s_1}\cdot\frac{\partial\vec{x}}{\partial s_2}\right)\frac{\partial\vec{x}}{\partial s_1}+\frac{Eh^3}{12(1-\nu^2)}\frac{\partial^3\vec{x}}{\partial {s_2}^3}\\
&\quad+\frac{Eh^3}{12(1-\nu^2)}(2-\nu)\frac{\partial^3\vec{x}}{\partial {s_1}^2\partial s_2}=0
\end{aligned}\tag{4.87}$$

$$\frac{\partial^2\vec{x}}{\partial {s_2}^2}+\nu\frac{\partial^2\vec{x}}{\partial {s_1}^2}=0\tag{4.88}$$

At Corners:

$$\frac{\partial^2 \vec{x}}{\partial s_1 \partial s_2} = 0 \tag{4.89}$$

There are thus four independent structural parameters.

$$\begin{aligned}
e1 &= \rho h \\
e2 &= \frac{Eh^3}{12(1-\nu^2)} \\
e3 &= \frac{Eh}{1-\nu^2} \\
e4 &= \nu
\end{aligned} \tag{4.90}$$

4.3.3 The Final Three-Dimensional Equations

Equation of Motion:

$$\begin{aligned}
& e1 \frac{\partial^2 \vec{x}}{\partial t^2} + e2 \left(\frac{\partial^4 \vec{x}}{\partial {s_1}^4} + 2 \frac{\partial^4 \vec{x}}{\partial {s_1}^2 \partial {s_2}^2} + \frac{\partial^4 \vec{x}}{\partial {s_2}^4} \right) \\
& \quad - e3 \frac{\partial}{\partial s_1} \left(\left[\left(1 - \left(\frac{\partial \vec{x}}{\partial s_1} \cdot \frac{\partial \vec{x}}{\partial s_1} \right)^{-\frac{1}{2}} \right) + e4 \left(1 - \left(\frac{\partial \vec{x}}{\partial s_2} \cdot \frac{\partial \vec{x}}{\partial s_2} \right)^{-\frac{1}{2}} \right) \right] \frac{\partial \vec{x}}{\partial s_1} \right) \\
& \quad - e3 \frac{\partial}{\partial s_2} \left(\left[\left(1 - \left(\frac{\partial \vec{x}}{\partial s_2} \cdot \frac{\partial \vec{x}}{\partial s_2} \right)^{-\frac{1}{2}} \right) + e4 \left(1 - \left(\frac{\partial \vec{x}}{\partial s_1} \cdot \frac{\partial \vec{x}}{\partial s_1} \right)^{-\frac{1}{2}} \right) \right] \frac{\partial \vec{x}}{\partial s_2} \right) \\
& \quad - e3 \frac{1-e4}{2} \left(\frac{\partial}{\partial s_1} \left[\left(\frac{\partial \vec{x}}{\partial s_1} \cdot \frac{\partial \vec{x}}{\partial s_2} \right) \frac{\partial \vec{x}}{\partial s_2} \right] + \frac{\partial}{\partial s_2} \left[\left(\frac{\partial \vec{x}}{\partial s_1} \cdot \frac{\partial \vec{x}}{\partial s_2} \right) \frac{\partial \vec{x}}{\partial s_1} \right] \right) = \vec{F}
\end{aligned} \tag{4.91}$$

Boundary Conditions:

At $s_1 = 0, L_1$*:*

$$\begin{aligned}
& -e3 \left[\left(1 - \left(\frac{\partial \vec{x}}{\partial s_1} \cdot \frac{\partial \vec{x}}{\partial s_1} \right)^{-\frac{1}{2}} \right) + e4 \left(1 - \left(\frac{\partial \vec{x}}{\partial s_2} \cdot \frac{\partial \vec{x}}{\partial s_2} \right)^{-\frac{1}{2}} \right) \right] \frac{\partial \vec{x}}{\partial s_1} \\
& \quad - e3 \frac{1-e4}{2} \left(\frac{\partial \vec{x}}{\partial s_1} \cdot \frac{\partial \vec{x}}{\partial s_2} \right) \frac{\partial \vec{x}}{\partial s_2} + e2 \frac{\partial^3 \vec{x}}{\partial {s_1}^3} + e2(2-e4) \frac{\partial^3 \vec{x}}{\partial s_1 \partial {s_2}^2} = 0
\end{aligned} \tag{4.92}$$

$$\frac{\partial^2 \vec{x}}{\partial {s_1}^2} + e4\frac{\partial^2 \vec{x}}{\partial {s_2}^2} = 0 \tag{4.93}$$

At $s_2 = 0, L_2$*:*

$$\begin{aligned}
&-e3\left[\left(1-\left(\frac{\partial \vec{x}}{\partial s_2}\cdot\frac{\partial \vec{x}}{\partial s_2}\right)^{-\frac{1}{2}}\right)+e4\left(1-\left(\frac{\partial \vec{x}}{\partial s_1}\cdot\frac{\partial \vec{x}}{\partial s_1}\right)^{-\frac{1}{2}}\right)\right]\frac{\partial \vec{x}}{\partial s_2}\\
&-e3\frac{1-e4}{2}\left(\frac{\partial \vec{x}}{\partial s_1}\cdot\frac{\partial \vec{x}}{\partial s_2}\right)\frac{\partial \vec{x}}{\partial s_1}+e2\frac{\partial^3 \vec{x}}{\partial {s_2}^3}+e2(2-e4)\frac{\partial^3 \vec{x}}{\partial {s_1}^2\partial s_2}=0
\end{aligned} \tag{4.94}$$

$$\frac{\partial^2 \vec{x}}{\partial {s_2}^2} + e4\frac{\partial^2 \vec{x}}{\partial {s_1}^2} = 0 \tag{4.95}$$

At Corners:

$$\frac{\partial^2 \vec{x}}{\partial s_1 \partial s_2} = 0 \tag{4.96}$$

Definitions:

$$\begin{aligned}
e1 &= \rho h\\
e2 &= \frac{Eh^3}{12(1-\nu^2)}\\
e3 &= \frac{Eh}{1-\nu^2}\\
e4 &= \nu
\end{aligned} \tag{4.97}$$

4.4 Structural Damping

Structural damping is added through the use of the Kelvin-Voight model. In this approach, the modulus of elasticity E is replaced by an expression including some internal damping, $E(1 + G\partial/\partial t)$. Here, G would be the damping parameter. The three-dimensional damped equation of motion is thus written as follows, while the boundary conditions remain the same.

$$
\begin{aligned}
&e1\frac{\partial^2\vec{x}}{\partial t^2}+e2\left(1+G\frac{\partial}{\partial t}\right)\left(\frac{\partial^4\vec{x}}{\partial {s_1}^4}+2\frac{\partial^4\vec{x}}{\partial {s_1}^2\partial {s_2}^2}+\frac{\partial^4\vec{x}}{\partial {s_2}^4}\right) \\
&\quad -e3\left(1+G\frac{\partial}{\partial t}\right)\frac{\partial}{\partial s_1}\left(\left[\left(1-\left(\frac{\partial\vec{x}}{\partial s_1}\cdot\frac{\partial\vec{x}}{\partial s_1}\right)^{-\frac{1}{2}}\right)+e4\left(1-\left(\frac{\partial\vec{x}}{\partial s_2}\cdot\frac{\partial\vec{x}}{\partial s_2}\right)^{-\frac{1}{2}}\right)\right]\frac{\partial\vec{x}}{\partial s_1}\right) \\
&\quad -e3\left(1+G\frac{\partial}{\partial t}\right)\frac{\partial}{\partial s_2}\left(\left[\left(1-\left(\frac{\partial\vec{x}}{\partial s_2}\cdot\frac{\partial\vec{x}}{\partial s_2}\right)^{-\frac{1}{2}}\right)+e4\left(1-\left(\frac{\partial\vec{x}}{\partial s_1}\cdot\frac{\partial\vec{x}}{\partial s_1}\right)^{-\frac{1}{2}}\right)\right]\frac{\partial\vec{x}}{\partial s_2}\right) \\
&\quad -e3\frac{1-e4}{2}\left(1+G\frac{\partial}{\partial t}\right)\left(\frac{\partial}{\partial s_1}\left[\left(\frac{\partial\vec{x}}{\partial s_1}\cdot\frac{\partial\vec{x}}{\partial s_2}\right)\frac{\partial\vec{x}}{\partial s_2}\right]+\frac{\partial}{\partial s_2}\left[\left(\frac{\partial\vec{x}}{\partial s_1}\cdot\frac{\partial\vec{x}}{\partial s_2}\right)\frac{\partial\vec{x}}{\partial s_1}\right]\right)=\vec{F}
\end{aligned}
\tag{4.98}
$$

4.5 Numerical Solution Method and Fluid-dynamic Coupling

The equations of motion are solved using finite-difference formulations in both space and time. Treatment is similar to that of the fluid-dynamic solution, using implicit backwards difference time integration, and an iterative approach to solving the implicit nonlinear equations of motion. FSDS coupling of the discrete formulations for the fluid-dynamics and structural-dynamics follows an iterative procedure, alternating between the two solutions until convergence is reached.

4.5.1 SDS Discretization

We first show the second-order backwards time integration used in the implicit SDS formulation. Consider a function $\vec{Q}(\vec{x})$, which contains all of the internal forcing terms in the equation of motion except the inertial term with time derivative. The two-dimensional equation 4.48 or three-dimensional equation 4.92 is then rewritten in time-discrete form as

$$e1\frac{2\vec{x}^{n+1}-5\vec{x}^{n}+4\vec{x}^{n-1}-\vec{x}^{n-2}}{\Delta t^2}+\vec{Q}(\vec{x}^{n+1})=\vec{F}^{n+1}. \tag{4.99}$$

As the equation is solved iteratively, diagonal terms in $\vec{Q}$ are collected on the left-hand side, with off-diagonal terms on the right-hand side.

The first and second spatial derivatives used are the same second-order formulations used in the fluid-dynamic solver and described in § 3.3.2. Higher derivatives needed for the structural solution are also second-order finite differences, defined as

Fourth Derivative Centered:

$$\frac{\partial^4 x}{\partial s^4} = \frac{x_{i+2} - 4x_{i+1} + 6x_i - 4x_{i-1} + x_{i-2}}{\Delta s^4} \tag{4.100}$$

Bi-directional Second Derivative Centered:

$$\begin{aligned}\frac{\partial^4 x}{\partial s_1^2 \partial s_2^2} = \frac{1}{\Delta s_1^2 \Delta s_2^2} (&x_{i+1,j+1} - 2x_{i+1,j} + x_{i+1,j-1} \\ &-2x_{i,j+1} + 4x_{i,j} - 2x_{i,j-1} + x_{i-1,j+1} - 2x_{i-1,j} + x_{i-1,j-1})\end{aligned} \tag{4.101}$$

Third Derivative Forward:

$$\frac{\partial^3 x}{\partial s^3} = \frac{-5x_i + 18x_{i+1} - 24x_{i+2} + 14x_{i+3} - 3x_{i+4}}{2\Delta s^3} \tag{4.102}$$

Third Derivative Backward:

$$\frac{\partial^3 x}{\partial s^3} = \frac{5x_i - 18x_{i+1} + 24x_{i+2} - 14x_{i+3} + 3x_{i+4}}{2\Delta s^3}. \tag{4.103}$$

4.5.2 SDS Solution Method

A standard solution solves the discrete form of the governing equations, given in two-dimensions by equations 4.48, 4.49, and 4.50, using an iterative Gauss-Seidel solver. In so doing, the nonlinear term uses the stretching expression, $\left(1 - (\partial\vec{x}/\partial s \cdot \partial\vec{x}/\partial s)^{-1/2}\right)$, from the previous iteration in both the equation of motion and the boundary condition. Such a formulation is found to have a stability limit on the grid dimension related to the ratio of extensional to bending rigidity, $(e3L^2)/e2$. Thus, the iterative method is only stable for a given rigidity ratio on a sufficiently fine grid, as is further discussed in Chapter 5.

Alternate Solution Method for Two-Dimensional SDS

For select cases requiring a very high rigidity ratio, an alternate solution method is used which eases the grid size restriction. The method is formulated so that the stretching expression does not lag in the iterative process. Considering the equation of motion 4.48, with $\vec{x} = (y, z)$, we consider the position to change little from the previous time step as

$$\vec{x}^{n+1} = \vec{x}^n + \delta\vec{x} = (y^n + \delta y, z^n + \delta z). \tag{4.104}$$

The stretching expression can now be written as

$$\left(1 - \left(\frac{\partial \vec{x}}{\partial s} \cdot \frac{\partial \vec{x}}{\partial s}\right)^{-1/2}\right)^{n+1} = \left[1 - \left(\left(\frac{\partial y^n}{\partial s} + \frac{\partial \delta y}{\partial s}\right)^2 + \left(\frac{\partial z^n}{\partial s} + \frac{\partial \delta z}{\partial s}\right)^2\right)^{-1/2}\right]$$
$$= \left[1 - \left(\frac{\partial {y^n}^2}{\partial s} + 2\frac{\partial y^n}{\partial s}\frac{\partial \delta y}{\partial s} + \frac{\partial \delta y^2}{\partial s} + \frac{\partial {z^n}^2}{\partial s} + 2\frac{\partial z^n}{\partial s}\frac{\partial \delta z}{\partial s} + \frac{\partial \delta z^2}{\partial s}\right)^{-1/2}\right]. \tag{4.105}$$

Eliminating the terms which are second order in $\delta\vec{x}$, and using $\alpha = (\partial y^n/\partial s)^2 + (\partial z^n/\partial s)^2$, the stretching expression becomes

$$\left[1 - \left(\frac{\partial {y^n}^2}{\partial s} + 2\frac{\partial y^n}{\partial s}\frac{\partial \delta y}{\partial s} + \frac{\partial {z^n}^2}{\partial s} + 2\frac{\partial z^n}{\partial s}\frac{\partial \delta z}{\partial s}\right)^{-1/2}\right]$$
$$= \left[1 - \alpha^{-1/2}\left(1 + \frac{2}{\alpha}\left(\frac{\partial y^n}{\partial s}\frac{\partial \delta y}{\partial s} + \frac{\partial z^n}{\partial s}\frac{\partial \delta z}{\partial s}\right)\right)^{-1/2}\right]. \tag{4.106}$$

Using a binomial expansion around $\delta\vec{x} = 0$, we obtain a final expression for the stretching term which is linear in terms of $\delta\vec{x}$,

$$\left(1 - \left(\frac{\partial \vec{x}}{\partial s} \cdot \frac{\partial \vec{x}}{\partial s}\right)^{-1/2}\right)^{n+1} = \left[1 - \alpha^{-1/2}\left(1 - \frac{1}{\alpha}\frac{\partial y^n}{\partial s}\frac{\partial \delta y}{\partial s} - \frac{1}{\alpha}\frac{\partial z^n}{\partial s}\frac{\partial \delta z}{\partial s}\right)\right]. \tag{4.107}$$

The nonlinear expression in the equations of motion contains the product of the stretching term and the first derivative of the position vector, $\partial\vec{x}/\partial s$. This product is now linearized around $\delta\vec{x}=0$, first considering the y-component,

$$\begin{aligned}
&\left(1-\left(\frac{\partial\vec{x}}{\partial s}\cdot\frac{\partial\vec{x}}{\partial s}\right)^{-1/2}\right)^{n+1}\frac{\partial y}{\partial s}^{n+1} \\
&=\left[1-\alpha^{-1/2}\left(1-\frac{1}{\alpha}\frac{\partial y^n}{\partial s}\frac{\partial\delta y}{\partial s}-\frac{1}{\alpha}\frac{\partial z^n}{\partial s}\frac{\partial\delta z}{\partial s}\right)\right]\left(\frac{\partial y}{\partial s}^{n}+\frac{\partial\delta y}{\partial s}\right) \\
&=\left[1-\alpha^{-1/2}\left(1-\frac{1}{\alpha}\frac{\partial z^n}{\partial s}\frac{\partial\delta z}{\partial s}\right)\right]\frac{\partial y^n}{\partial s}+\left[\alpha^{-1/2}\frac{1}{\alpha}\frac{\partial y^n}{\partial s}^{2}+(1-\alpha^{-1/2})\right]\frac{\partial\delta y}{\partial s}.
\end{aligned} \tag{4.108}$$

Replacing $\delta\vec{x}$ with $\vec{x}^{n+1}-\vec{x}^{n}$, we obtain from the above expression, and the equivalent z-component expression,

$$\left(1-\left(\frac{\partial\vec{x}}{\partial s}\cdot\frac{\partial\vec{x}}{\partial s}\right)^{-1/2}\right)^{n+1}\frac{\partial\vec{x}}{\partial s}^{n+1}=\left(\beta_y+\gamma_y\frac{\partial y}{\partial s}^{n+1},\beta_z+\gamma_z\frac{\partial z}{\partial s}^{n+1}\right), \tag{4.109}$$

where

$$\begin{aligned}
\beta_y&=\alpha^{-3/2}\left(\frac{\partial z^n}{\partial s}\left(\frac{\partial z^{n+1}}{\partial s}-\frac{\partial z^n}{\partial s}\right)-\frac{\partial y^n}{\partial s}^{2}\right)\frac{\partial y^n}{\partial s} \\
\gamma_y&=\alpha^{-3/2}\frac{\partial y^n}{\partial s}^{2}+(1-\alpha^{-1/2}) \\
\beta_z&=\alpha^{-3/2}\left(\frac{\partial y^n}{\partial s}\left(\frac{\partial y^{n+1}}{\partial s}-\frac{\partial y^n}{\partial s}\right)-\frac{\partial z^n}{\partial s}^{2}\right)\frac{\partial z^n}{\partial s} \\
\gamma_z&=\alpha^{-3/2}\frac{\partial z^n}{\partial s}^{2}+(1-\alpha^{-1/2}).
\end{aligned} \tag{4.110}$$

This formulation of equations 4.109 and 4.110 stabilizes the iterative scheme in solving the two-dimensional structural equations. The boundary conditions are slightly altered in this scheme, in that the extensional strain is constrained to be zero at the free end. The resultant free-end boundary conditions are thus $\partial^2\vec{x}/\partial s^2=\partial^3\vec{x}/\partial s^3=0$, and contain no stretching term.

This method allows simulation of very high rigidity ratios on relatively small grids, an advantage when very high extensional rigidity and very low bending rigidity are required to capture the essential physics. The method, however, is not as robust as the standard approach, and encounters difficulty with extreme events such as snapping and recoil. Such issues are discussed further with the validation in Chapter 5.

4.5.3 FSDS Coupling

Fluid-dynamic influence to the structural equation is through the external forcing term in the equation of motion, given by equation 4.48 in two-dimensions and equation 4.92 in three-dimensions. The solved body position is then used to reformulate the fluid-dynamic grid, marking the structural influence on the flow. The converged solution is one where the body position is compatible with the fluid-dynamic forcing, and the flow field is compatible with body position and motion.

The Solution Procedure

Inclusion of the structural solution alters slightly the solution procedure detailed in § 3.4.3. It now proceeds as follows.

1. Calculate the fluid-dynamic forcing and solve the structural equations of motion for the new body position.
2. Set the grid and the velocity boundary conditions using the new structural solution.
3. Calculate the Poisson source term and pressure boundary condition from the velocity field.
4. Solve the Poisson equation for the pressure.
5. Solve the Navier-Stokes equations with the new pressure field to update the velocity field.
6. Return to Step 1 unless tolerance is reached in terms of velocity change, mass conservation, and body position (3 iterations minimum).
7. Advance time step and return to Step 1.

While the fluid-dynamic grid is a clustered O-grid for resolution at the sharp leading and trailing edges, the structural grid used is evenly spaced to allow direct use of the derived equations of motion. Interpolation between the grids is thus necessary. Setting the fluid-dynamic grid requires interpolation of the structural position, while the calculated fluid-dynamic forcing must be interpolated back onto the structural grid. In both cases cubic spline interpolation is used.

Dynamic coupling is through the external forcing term in the structural solution defined as force-per-length (or force-per-area for the three-dimensional case) by

$$\vec{F}_f = [\Delta\tau]\hat{n}, \tag{4.111}$$

where $\hat{n}$ is the upward facing normal and $[\Delta\tau]$ is the difference between the fluid-dynamic stress tensor at the top and bottom of the body. Elements of the stress tensor are defined by the fluid dynamics at the body surface as

$$\tau_{ij} = \nu\rho_f\left(\frac{\partial u_i}{\partial\xi_j} + \frac{\partial u_j}{\partial\xi_i}\right) - \delta_{ij}p. \tag{4.112}$$

Kinematic coupling comes from the structural motion dictating the velocity boundary condition for the flow field.

Added Mass Concern

A stability problem is encountered with this iteratively coupled method when the body mass $e1$ is reduced. As the added mass becomes a more significant inertial effect, a larger portion of the inertia is represented on the right-hand side of the structural equation. Clearly, if the exact value of the added mass were known, it could be included in the left-hand side of the structural equation, and the effect subtracted from the forcing term. For the two-dimensional equation of motion, with m_a as the added mass, this would be

$$(e1 + m_a)\frac{\partial^2\vec{x}}{\partial t^2} + e2\frac{\partial^4\vec{x}}{\partial s^4} - e3\frac{\partial}{\partial s}\left[\left(1 - \left(\frac{\partial\vec{x}}{\partial s}\cdot\frac{\partial\vec{x}}{\partial s}\right)^{-\frac{1}{2}}\right)\frac{\partial\vec{x}}{\partial s}\right] = \vec{F}_{hyd} + m_a\frac{\partial^2\vec{x}}{\partial t^2} \tag{4.113}$$

For the present problem, however, the added mass is difficult to define. There is no relevant strip theory as for a long cylinder, and the added mass for a waving membrane is a function of the wavelength. As such, an assumed constant added mass $\tilde{m}_a$ is used, with the acceleration term on the right-hand side being that from the previous $(m-1)$ iteration,

$$\begin{aligned}(e1+\tilde{m}_a)\frac{\partial^2\vec{x}}{\partial t^2} &+ e2\frac{\partial^4\vec{x}}{\partial s^4} - e3\frac{\partial}{\partial s}\left[\left(1-\left(\frac{\partial\vec{x}}{\partial s}\cdot\frac{\partial\vec{x}}{\partial s}\right)^{-\frac{1}{2}}\right)\frac{\partial\vec{x}}{\partial s}\right] = \\ &\vec{F}_{hyd}+\tilde{m}_a\left(\frac{\partial^2\vec{x}}{\partial t^2}\right)^{m-1}.\end{aligned} \tag{4.114}$$

As the solution converges, $(\partial^2\vec{x}/\partial t^2)^m = (\partial^2\vec{x}/\partial t^2)^{m-1}$, so the assumed added mass terms on both sides of the equation become equivalent. Understanding this, the accuracy of the assumed added mass does not impact the solution, so long as there is convergence. This procedure is effective in stabilizing the coupled solution, even with vanishing body mass.

4.5.4 FSDS Nondimensionalization

In considering the coupled system, we nondimensionalize the structural parameters by the fluid-dynamics. All nondimensionalizations are made using the fluid density ρ_f, the flow speed V, and the body length L. As such, the nondimensional parameters of the coupled system are

$$\begin{aligned}\mu &= \frac{e1}{\rho_f L} = \frac{\rho_s h}{\rho_f L}\\ K_B &= \frac{e2}{\rho_f U^2 L^3} = \frac{EI}{\rho_f U^2 L^3} = \left[\frac{EI}{(1-\nu_s^2)\rho_f U^2 L^3}\right]\\ K_S &= \frac{e3}{\rho_f U^2 L} = \frac{Eh}{\rho_f U^2 L} = \left[\frac{Eh}{(1-\nu_s^2)\rho_f U^2 L}\right]\\ Re &= \frac{UL}{\nu}\\ \nu_s &= e4,\end{aligned} \tag{4.115}$$

where ν is the fluid viscosity and ν_s is the Poisson ratio, a nondimensional quantity which is only relevant in the three-dimensional simulations. The three-dimensional nondimensionalizations for K_B and K_S are given in brackets. Discussion of coupled theory and simulations will use these nondimensionalizations of equation 4.115.

Chapter 5

Verification and Validation of the Fluid (FDS), Structure (SDS), and Coupled (FSDS) Models

A series of simulations is performed for the purpose of verifying and validating the accuracy and consistency of the FDS, SDS, and FSDS capabilities. The test cases are such that the displayed success of the simulations indicates accuracy of the simulations performed in the present flexible thin-foil study. In select cases for both the FDS and SDS simulations, a convergence study is performed, demonstrating near second-order convergence with both spatial and temporal discretization.

5.1 FDS Verification and Validation

Validation for the fluid-dynamic solver derived in Chapter 3 is obtained through the simulation of several problems studied previously both experimentally and numerically. The problems include those for both stationary bodies and those with imposed motion. Validation is made for both the dynamic interaction (hydrodynamic forcing of the body) and the flow characteristics. Problems are chosen using both a cylindrical body and the thin-foil resolved at the sharp edges.

5.1.1 Flow Over a Fixed Cylinder

The classical problem of vortex shedding from a fixed cylinder has been very well studied. The only relevant nondimensional input parameter for the two-dimensional problem is the Reynolds number, $Re = UD/\nu$, where U is the steady incoming flow, D the cylinder diameter, and ν the kinematic viscosity. A number of studies at $Re = 100$ have been performed, as this is an often used problem for benchmarking of numerical codes. At this Reynolds number, periodic vortex shedding is well-established, but turbulence in the wake vortices is not yet present (see [10] for an explanation of the regimes). A compilation of results for this problem was given by Zhou and Graham [78]. That information is presented in Table 5.1, along with the present result. The quantities compared are the Strouhal number, or nondimensional frequency of vortex shedding, $St = fD/U$; the drag coefficient, $c_d = F_{Stream}/(0.5\rho DU^2)$, and the oscillating lift coefficient, $c_l = F_{Cross}/(0.5\rho DU^2)$. It can be seen that the results of the present study compare well to these other experimental and computational studies. Such accuracy indicates successful capture of the physical process of flow separation, time accuracy of the unsteady wake flow, and accurate calculation of the hydrodynamic forcing on the body.

5.1.2 Periodically Forced Cylinder

The problem of a cylinder in forced periodic motion was used for a full convergence test, indicating the spatial and temporal second order accuracy of the numerical model. This problem of a two-dimensional cylinder forced periodically in one direction in an otherwise still fluid was the subject of an extensive numerical and experimental study by Dutsch *et al.*[18]. These results of [18] have previously been used for benchmarking in the studies of Uzunoglu *et al.*[68] and Guilmineau & Queutey [27]. The relevant input parameters for a cylinder of diameter D being forced at a frequency ω and amplitude A are the Reynolds number, $Re = A\omega D/\nu$, and the Keulegan-Carpenter number, $KC = 2\pi A/D$. A number of flow regimes have been identified based on these parameters. The combination used in the present study,

Study	St	$\overline{C_d}$	$C_{l_{rms}}$
Lienhard (experiment)	0.155-0.173	1.35-1.49	-
Arkell & Graham	-	1.33	0.17
Beaudan & Moin	-	1.35	0.24
Chaplin (method 1)	0.152	1.82	0.20
Chaplin (method 2)	-	1.82	0.20
Gushchin	-	1.38	-
Karniadakis	-	1.42	0.26
Kravchenko	-	-	0.23
Mittal	-	-	0.23
Savvides (method 1)	-	1.30	0.16
Savvides (method 2)	-	1.32	0.14
Sherwin	-	1.36	0.24
Stansby	0.169	1.36	-
Younis (method 1)	-	1.46	0.34
Younis (method 2)	0.168/0.174	1.43/1.45	-
Zhou & Graham (method 1)	0.162	1.37	0.20
Zhou & Graham (method 2)	0.162	1.48	0.22
Present Study	0.171	1.40	0.24

Table 5.1: Data compilation of cylinder flow at $Re = 100$. All but data of present study are from Zhou and Graham [78]. The first entry is from experiment and the remainder are computational.

$Re = 100$ and $KC = 5$, puts the system solidly in a region of periodic symmetric vortex shedding. The quantities used for comparison are the drag and added mass coefficients. These are determined by separating the hydrodynamic forcing in the direction of imposed motion into a component in phase with the velocity and a component in phase with the acceleration. This idea follows Morison's equation, enabling the hydrodynamic forcing to be written as in [18], with the drag coefficient c_d and added mass coefficient c_i following

$$F_x(t) = -\frac{1}{2}\rho D\dot{x}|\dot{x}|c_d - \frac{1}{4}\pi\rho D^2\ddot{x}c_i. \tag{5.1}$$

Given a long oscillating time history of the hydrodynamic forcing and cylinder position, velocity, and acceleration, the drag and added mass coefficients can be calculated by isolating the components in phase with the velocity and acceleration, respectively. These are

$$c_d = \frac{\int_{t_0}^{t_f} F_x\dot{x}dt}{\frac{1}{2}\rho D\int_{t_0}^{t_f}\dot{x}^2|\dot{x}|dt} \tag{5.2}$$

$$c_i = \frac{\int_{t_0}^{t_f} F_x\ddot{x}dt}{\frac{1}{4}\pi\rho D^2\int_{t_0}^{t_f}\ddot{x}^2dt}. \tag{5.3}$$

Convergence tests of the hydrodynamic numerical model were pursued using this forced cylinder problem. It has been shown in Chapter 3 that derivatives in the numerical formulation contain errors of second-order both in terms of grid spacing and time step. A series of runs were pursued to test for this second-order convergence of the solution.

Grid Size Convergence

While maintaining a constant time step of $dt = 0.01D/(A\omega)$, the radial and circumferential grid dimensions were varied concurrently, creating an $N \times N$ grid. The domain size was kept constant as a circle of diameter $12D$. Grid clustering at the cylinder body, which is normally used, was removed for this convergence test, so that radial grid spacing was even along each locus. Runs were performed for

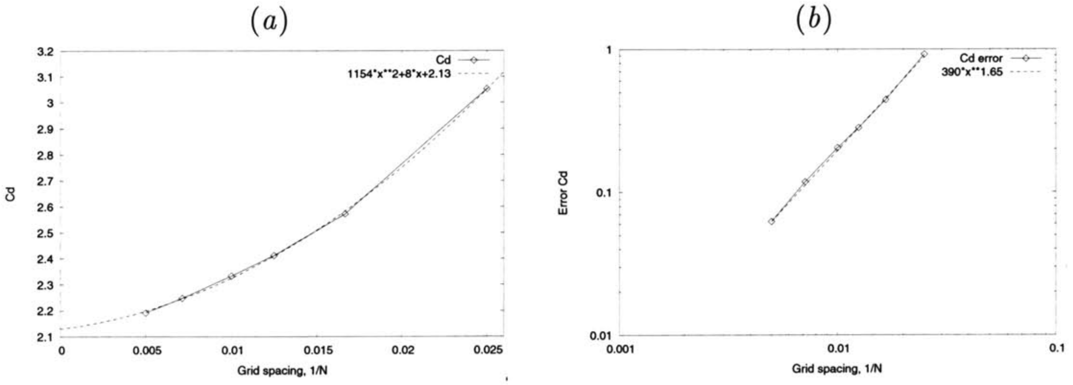

Figure 5-1: (a) Convergence of drag coefficient with decreasing grid spacing and quadratic polynomial curve fit. (b) Drag error from the intercept with power curve fit.

$N = \{40, 60, 80, 100, 140, 200\}$. Figure 5-1$(a)$ shows the convergence of the drag coefficient with grid spacing with a quadratic polynomial curve fit that indicates an intercept at $c_d = 2.13$. A plot of the error from this intercept is given in figure 5-1(b), indicating error as $e_{c_d} \sim \Delta x^{1.65}$.

Plots of the added mass coefficient with grid spacing are given in figure 5-2. When fitting the quadratic to all points an intercept of $c_i = 1.51$ is found, with a corresponding error fit indicating $e_{c_i} \sim \Delta x^{1.06}$. However, figure 5-2$(a)$ indicates that the polynomial fit is not accurately capturing the trend of the more accurate low grid spacing data, and consequently not predicting an accurate intercept. We proceed by considering the convergence of c_i for the four most accurate points, representing $N = \{80, 100, 140, 200\}$. Figure 5-3$(a)$ shows the better fit to the more accurate data, and an intercept of $c_i = 1.471$. The corresponding error plot of figure 5-3(b) shows convergence of the error as $e_{c_i} \sim \Delta x^{1.92}$. It is not anticipated that exact second-order convergence would be observed throughout the entire range of grid spacing, particularly with simulation of nonlinear equations. As the larger grid spacings are unable to resolve elements of the near body flow physics, consistent convergence of the added mass is not observed until N is sufficiently high, $N \geq 80$. The spatially second-order nature of the model is reflected in both error trends as $e_{c_d} \sim \Delta x^{1.65}$ and $e_{c_i} \sim \Delta x^{1.92}$.

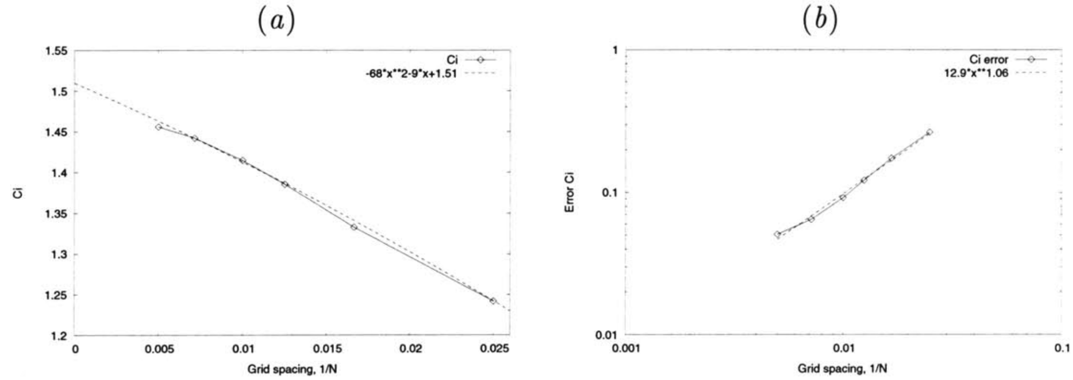

Figure 5-2: (a) Convergence of added mass coefficient with decreasing grid spacing and quadratic polynomial curve fit. (b) Added mass error from the intercept with power curve fit.

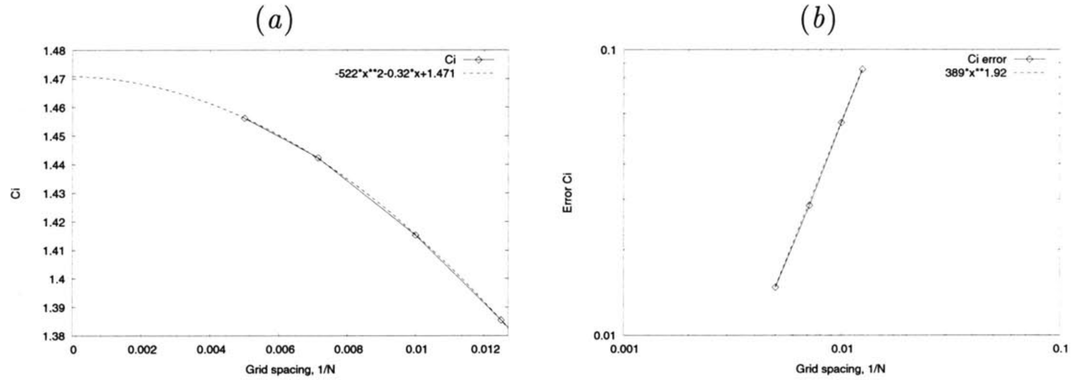

Figure 5-3: (a) Convergence of added mass coefficient with decreasing grid spacing and quadratic polynomial curve fit, using the four most accurate grids as $N = \{80, 100, 140, 200\}$. ($b$) Added mass error from the intercept with power curve fit.

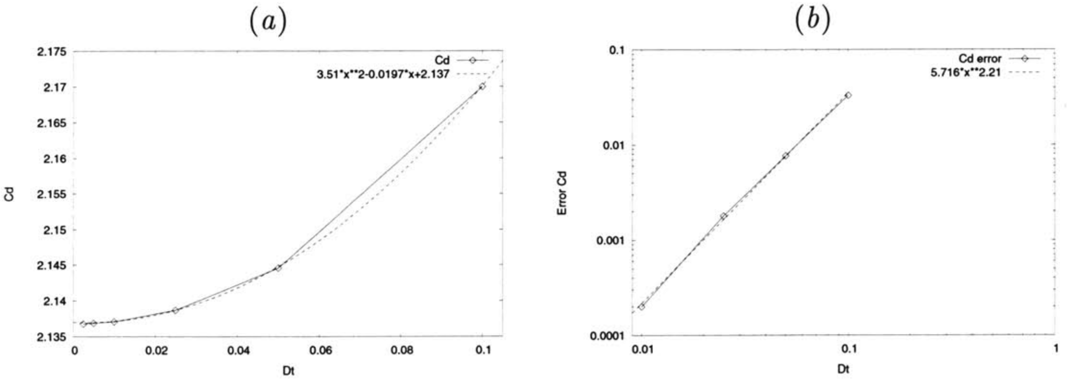

Figure 5-4: (*a*) Convergence of drag coefficient with decreasing time step and quadratic polynomial curve fit. (*b*) Drag error from the intercept with power curve fit.

Time Step Convergence

Holding the grid dimension constant (and using clustering at the inner boundary) runs were performed for a series of time steps to test the convergence. Using $dt = \{0.1, 0.05, 0.025, 0.01, 0.005, 0.0025\}$, the values of c_d and c_i were calculated. Figure 5-4(*a*) shows convergence of the drag coefficient with time step, and the quadratic polynomial fit indicates an intercept of $c_d = 2.137$. The error from the intercept is plotted in figure 5-4(*b*), with the two smallest time steps omitted due to full convergence. The error power curve fit shows convergence as $e_{c_d} \sim \Delta t^{2.21}$. Convergence of the added mass coefficient with time step and quadratic polynomial fit are shown in figure 5-5(*a*), indicating an intercept of $c_d = 1.466$. The power fit to the corresponding error plot of figure 5-5(*b*) shows convergence as $e_{c_i} \sim \Delta t^{1.84}$. The error convergence with time step found for the flow coefficients reflect the second-order numerical formulation.

Domain Size Convergence

In order to obtain a 'best' answer of c_d and c_i for comparison to the previous studies, a test of the behavior of the answer with increasing domain size was conducted. It is known that proximity of the domain boundary to active areas of the flow can influence the result, particularly with the Dirichlet boundary condition used in this

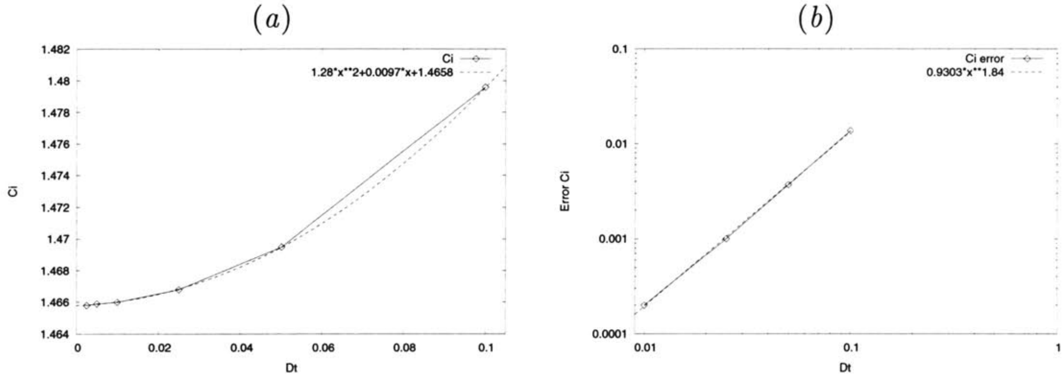

Figure 5-5: (a) Convergence of added mass coefficient with decreasing time step and quadratic polynomial curve fit. (b) Added mass error from the intercept with power curve fit.

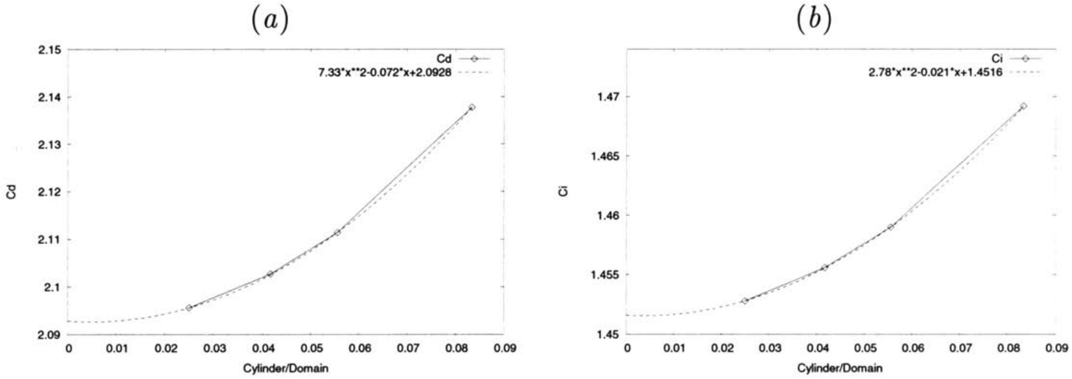

Figure 5-6: Convergence of the (a) drag coefficient and (b) added mass coefficient with increasing domain size, and quadratic polynomial curve fit.

benchmarking test. A series of runs was performed at a fixed time step $dt = 0.005$ and equivalent clustered grids at a range of domain sizes. The grid size in the radial direction was increased with domain size to maintain equivalent grid spacing in the active flow region. With the outer domain boundary as a circle, the range of domain to cylinder diameter used was $D_{dom}/D_{cyl} = \{12, 18, 24, 40\}$. The calculated c_d and c_i are plotted in Figure 5-6, and show convergence with increasing domain size to $c_d = 2.09$ and $c_i = 1.45$. These "best" values are precisely the highest resolution values found in [18], and used for benchmarking in [68] and [27].

The full convergence testing of the hydrodynamic model has shown the second-order nature of the solution both in terms of grid spacing and time step. The convergence of the answer with increasing distance of the outer domain boundary was

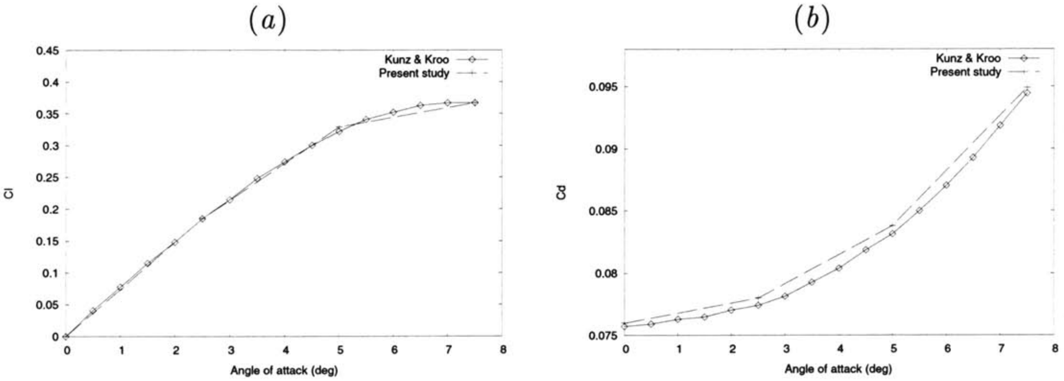

Figure 5-7: Plot of (*a*) lift coefficient and (*b*) drag coefficient for a NACA0008 foil over a range of angles of attack. The present results are found to compare very well with those of Kunz & Kroo [35].

also displayed. Accuracy of the simulation is verified by matching of the theoretically most accurate solution to that of a previously accepted benchmarking solution.

5.1.3 Rigid Thin Foil at Angle of Attack

Owing to the rather extreme geometry to be treated in the present study, confirmation of the accuracy of the model for the thin bodies to be used was also sought. The thin-foil to be used in this research is of a $1:100$ thickness to length ratio. The flow is to be fully resolved around the sharp edges, with no explicit enforcement of the Kutta condition. To ensure accuracy of the treatment at these sharp edges, comparisons are made to previous studies involving flow over rigid thin foils.

Comparison was made to earlier numerical and experimental studies of fixed foils at an angle of attack to steady incoming flow. The first comparison is made to a two-dimensional numerical simulation of flow over a NACA0008 foil at $Re = UL/\nu = 2000$, done by Kunz & Kroo [35]. The drag and lift coefficients were calculated using the present model over the same range of angles of attack for the NACA0008 foil. These results are presented with those of [35] in figure 5-7. It is clear from the figure that the present model is accurately calculating the steady flow about the foil through the point of stall.

Tests were also made of an impulsively started thin foil at a range of angles

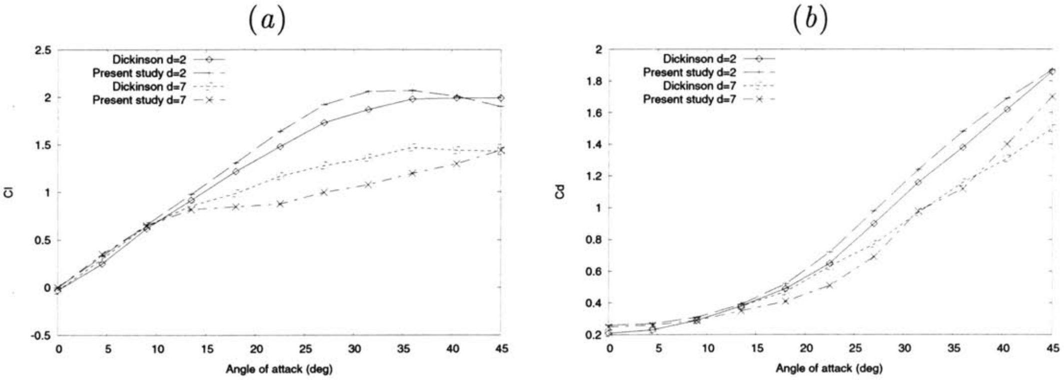

Figure 5-8: Plot of (*a*) lift coefficient and (*b*) drag coefficient for early (2 chord lengths travelled) and late (7 chord lengths travelled) times after an impulsive start (fast acceleration from rest). Results are from the experiment of Dickinson & Gotz [14] and the present numerical simulation, and show a reduction of lift and drag in time at angles over 13.5^o.

of attack and compared to the experimental work of Dickinson & Gotz [14]. The foil was constantly accelerated over 0.32 convective time units until reaching the desired velocity at $Re = 192$. The impulsive conditions and Reynolds number of the simulation exactly matched those reported for the experiment. While the simulation was two-dimensional, the experiment was set up to minimize three-dimensional effects. The form of the foil was given in [14] as "bluntly rounded on the leading edge and sharply tapered at the trailing edge" with a 0.02 thickness ratio; the simulation sought equivalence in form by using a NACA0002 foil, possessing those same characteristics. Drag and lift on the foil are presented in [14] at an early stage (after 2 chord lengths of travel) and a late stage (after 7 chord lengths of travel) over a range of angles of attack from 0^o to 90^o in 4.5^o increments. A gradual decreasing in time of both lift and drag was found for angles of attack greater than 13.5^o. The simulation was run at the same angles of attack, up to 45^o. The lift and drag coefficients for the early and late times are shown in figure 5-8 for experiment of [14] and the simulation results.

The plots show good agreement for both lift and drag at small angles of attack. The separation of the early and late forcing values at $\sim 15^o$ is clear in both the experimental and simulated results. The simulated results generally follow the trends found in the experiments, but indicate some difference in the values, particularly in

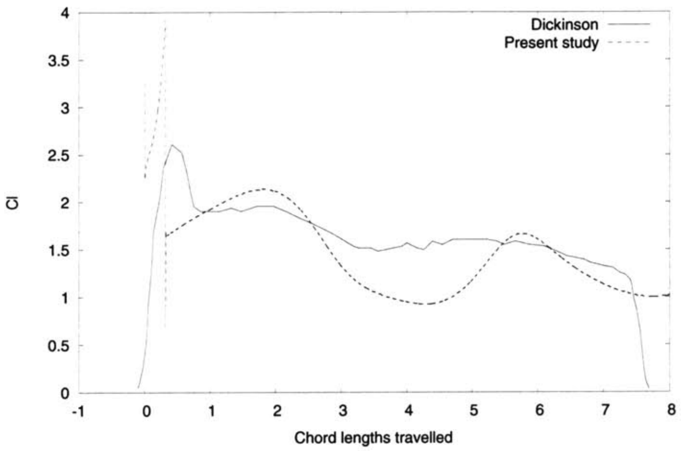

Figure 5-9: Plot of Cl vs. the distance travelled by the foil at a 31.5^o angle of attack. Traces are shown for the simulation, and for the experiment (taken from [14]). Differences in the impulse and subsequent history are clear, particularly the smoother transitions of the experiment yielding less pronounced transient effects.

the lift at higher angles of attack at the later time. Plots of the experimental time history of the forcing, given in [14], indicates an unsteady process at these larger angles of attack, one likely to be largely influenced by the manner of the impulsive start. Figure 5-9 shows the time history of the lift coefficient for the experiment and simulation. While the simulation is able to exactly linearly ramp up the velocity (constant acceleration), the experiment must transition the acceleration from zero to the constant value (and back to zero) over a finite period of time. The unsteady lift response show in figure 5-9 is likely to be affected by the exact nature of the impulsive start, and can be expected to exhibit some differences between the simulation and experiment. Such differences, and those associated with the finite span of the experimental foil, can account for the modest differences in the lift and drag plots of figure 5-8. Success of the simulation indicates the ability of the numerical model to capture unsteady hydrodynamic effects when using of a thin foil, an important component to the present study.

5.1.4 Rigid Flapping Foil

Anderson [2] performed low Reynolds number experiments for a large span (~two-dimensional) rigid NACA0012 foil, flapping in both heave and pitch. Using PIV, a velocity field was obtained from the experiment, allowing comparison of the vortical flow with numerical simulation. The case considered was at $Re = 1100$, for a heave amplitude of $0.75L$ and pitch amplitude of 30^o. The heave leads the pitch by a phase difference of 75^o, and the flapping is at a Strouhal frequency of $St = 0.32$.

The velocity vectors from FDS simulation results are plotted with the PIV vectors from experiment in figure 5-10. The vortex development and release into the wake occur at the equivalent phase and location for the simulation and experimental case. Overall, the figure shows a very good qualitative comparison of the near-body and wake vortical flow characteristics.

5.2 SDS Verification and Validation

Verification and validation are sought for the structural numerical model derived in Chapter 4. Problems independent of fluid dynamics are sought for comparison. One good type of problem is that of the body pinned at one end, and under the influence of gravity. This two-dimensional 'swinging chain' problem becomes a swinging membrane problem in three dimensions. A steady displacement problem is also used in the validation of the three-dimensional model, testing the accuracy of the nonlinear plate structural treatment.

5.2.1 Description of the Hanging Chain Problem and Simulation Challenges

The problem we consider is of a chain, or inextensible highly flexible string, pinned at the upper end, and under the influence of gravity. The variation of the tension force from the maximum value at the pinned end to zero at the free end is a significant similarity between this problem and that of such a body in a free stream. This

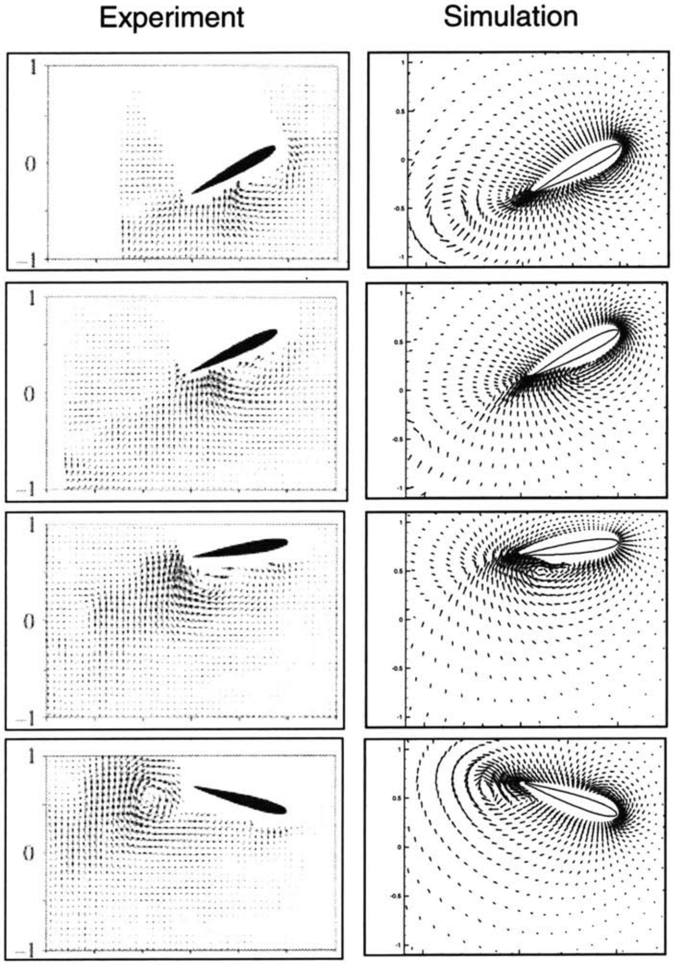
Experiment

Simulation

Figure 5-10: A series of plots of the vector velocity field for a two-dimensional NACA0012 foil flapping in heave and pitch. The left series represents the PIV experimental data of Anderson [2], while the right column is simulation results using the present numerical model. The Reynolds number is 1100, and the heave leads the pitch by 75^o.

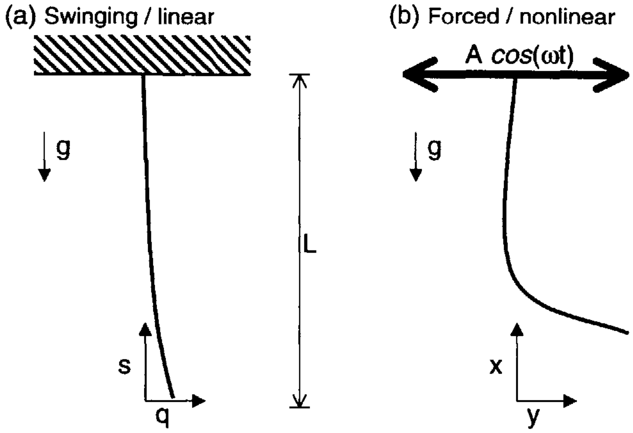

Figure 5-11: A diagram of the swinging chain or string problem. The body is pinned at the upper end and subject to the influence of gravity: (a) represents an initially displaced body in the linear regime (small displacement); (b) represents a body with periodic lateral forcing at the fixed end, outside of the linear regime (large displacements).

swinging chain problem, in its linear form, has an analytical solution for the natural modes as a Bessel equation [29][22]. Considering the swinging chain of figure 5-11(a), the equation, where el is the mass per length (as in Chapter 4) and g is gravity, is

$$el\frac{\partial^2 q}{\partial t^2} - \frac{\partial}{\partial s}\left(el\, g\, s\frac{\partial q}{\partial s}\right) = 0. \tag{5.4}$$

The modal solutions take the form of Bessel functions,

$$q(s) = CJ_o\left(2\omega\sqrt{\frac{s}{g}}\right), \tag{5.5}$$

where the boundary condition $q(L) = 0$ yields

$$J_o\left(2\omega\sqrt{\frac{L}{g}}\right) = 0. \tag{5.6}$$

The natural modes of the linear swinging problem are defined in table 5.2.

The desired structural properties for accurate simulation of the swinging chain are near inextensibility and near perfect bending flexibility. As would be expected,

Mode n	$2\omega\sqrt{\frac{L}{g}}$	ω^*	T^*
1	2.405	1.203	5.223
2	5.520	2.760	2.277
3	8.654	4.327	1.452
4	11.792	5.896	1.066
5	14.931	7.466	0.842

Table 5.2: Definition for the modes of linear hanging chain of equations 5.5 and 5.6. Also includes the nondimensional natural frequency (nondimensionalized by $\sqrt{g/L}$) and period.

intermediate values of either of these properties alter the physics from that of the ideal swinging chain. Stability of the numerical scheme is dependent on the ratio of the extensional rigidity to bending rigidity, $(e3\,L^2)/e2$, as defined in Chapter 4, equation 4.51. There is a maximum value for this ratio which increases with grid resolution. As such, there is a trade off between the degree to which the body is inextensible, perfectly flexible, and computational intensity. It is found with the hanging chain problem that bending rigidity increases the modal natural frequencies by increasing the restoring force, particularly influencing the higher modes. On the other hand, extensional flexibility is found to facilitate transfer of energy from lower to higher modes, causing the system to evolve differently from the inextensible one.

A sense of the influence of the bending and extensional stiffness can be gained from examining the linear equations. The equation of motion and frequency for the linear extensional mode, where x is displacement in the axial direction, are

$$e1\frac{\partial^2 x}{\partial t^2} - e3\frac{\partial^2 x}{\partial s^2} = 0 \tag{5.7}$$

$$\omega = k_s\sqrt{\frac{e3}{e1}}. \tag{5.8}$$

In this case we are most concerned with the lowest mode, where $k_s = \pi/(2L)$, as this will have the lowest frequency. The equation of motion and frequency for the linear normal modes, where y is the displacement in the normal direction and τ is a tension considered constant for simplicity, are

$$e1\frac{\partial^2 y}{\partial t^2} + e2\frac{\partial^4 y}{\partial s^4} - \tau\frac{\partial^2 y}{\partial s^2} = 0 \tag{5.9}$$

$$\omega = k_n\sqrt{\frac{\tau}{e1} + \frac{e2}{e1}{k_n}^2}. \tag{5.10}$$

In comparing the relative importance of the two terms in the frequency expression, the tension can be considered $\tau \sim e1\,g\,L$. For sufficiently high wavenumbers the bending rigidity will exert it's influence over the dynamics and siginificantly increase the natural frequency.

Dimensional expressions for the frequencies have been presented in equations 5.6, 5.8, and 5.10. This allows observation of the fact that the natural swinging frequency is independent of the body mass $e1$ (as with a pendulum), while the stretching and elastic bending natural frequencies are functions of the mass. Henceforth, we consider all quantities in nondimensional form, using $e1$, L, and g for nondimensionalization. As such, we have nondimensional bending rigidity $e2^* = e2/(e1\,gL^3)$, extensional rigidity $e3^* = e3/(e1\,gL)$, and time $t* = t\sqrt{g/L}$. The subsequent discussion will consider all quantities nondimensional and the * will no longer be used to indicate nondimensional quantities.

5.2.2 Small Amplitude Hanging Chain: Comparison to Analytic Result

We first examine the effect of bending rigidity on the natural frequencies of the first few modes. The linear swinging chain is initially displaced with an amplitude of A in all of the first four modes. The initial displacement is

$$q(s) = A\left(J_o(2.405\sqrt{s}) - J_o(5.520\sqrt{s}) + J_o(8.654\sqrt{s}) - J_o(11.792\sqrt{s})\right), \tag{5.11}$$

where the alternating sign is chosen to avoid large initial slope at the tail. Three values of A were used, as $(0.01, 0.05, 0.1)$, and the power spectra for the three cases is

Mode n	ω_{theory}	ω_{num}	$error$
1	1.20	1.20	0%
2	2.76	2.81	1.8%
3	4.33	4.71	8.8%
4	5.90	6.91	17.1%

Table 5.3: The theoretical modal natural frequencies for the swinging chain from equations 5.5 and 5.6, and those measured from the numerical simulation with parameters $(A, e2, e3) = (0.01, 0.0005, 50)$.

shown in figure 5-12. If the displacements of all modes were in the linear regime, and the body was inextensible, the modes would operate independently, each maintaining the initial amplitude. It is expected that this would be more the case at smaller initial displacement amplitudes and higher extensional rigidity, as these conditions correspond to the conditions which yield the Bessel function solution of equation 5.5. Figure 5-12 shows that, for the small amplitude case, the first three modes oscillate with 97%, 94%, and 87% of the initial displacement amplitude, where the fourth mode oscillates with only 25% of the initial displacement amplitude. The frequencies for the lowest amplitude case, and error from the corresponding theoretical frequencies are given in table 5.3. It is evident that accuracy in this simulation is quite good for the first two modes, falling off to 17% frequency error for the fourth mode.

In determining the difficulty in capturing the fourth mode, we examine the influence of the extensional flexibility and bending rigidity. For the simulations of figure 5-12, a grid of $N = 200$ is used, limiting the ratio of extensional to bending rigidity to $e3/e2 = 100\,000$. The lowest stretching mode of equation 5.7, with extensional rigidity $e3 = 50$, yields a natural frequency of $\omega_s = 11.11$. Where the vertical swinging displacement will have twice the frequency of the horizontal displacement, we consider half this stretching frequency, $\omega_s/2 = 5.56$, and its proximity to the frequency of the fourth swinging mode, $\omega_4 = 5.896$. As such, energy from the fourth swinging mode interacts with the stretching mode.

We look at the fourth bending mode to assess the influence of the bending rigidity on the frequency. Considering this fourth mode, with wavenumber $k_n = 7\pi/2$, the frequency in the absence of tension, with $e2 = 0.0005$, would be $\omega_b = 2.7$, according (*a*) A=0.01

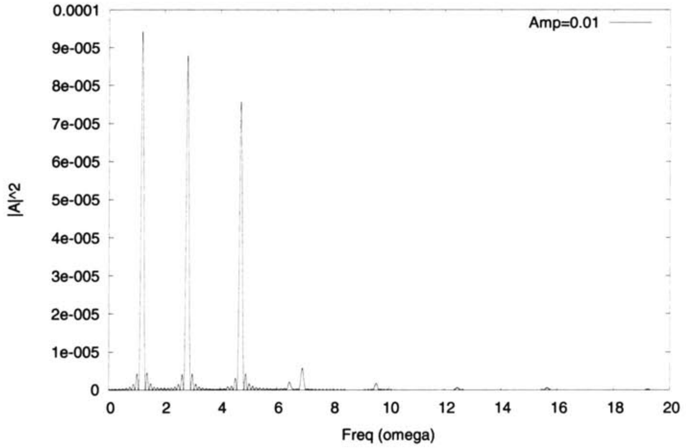

(*b*) A=0.05

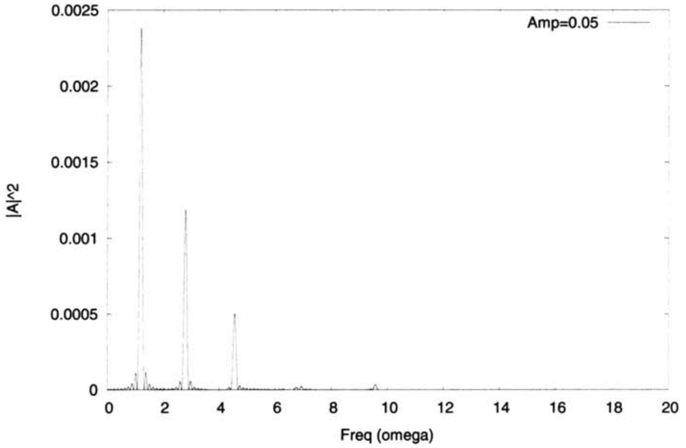

(*c*) A=0.1

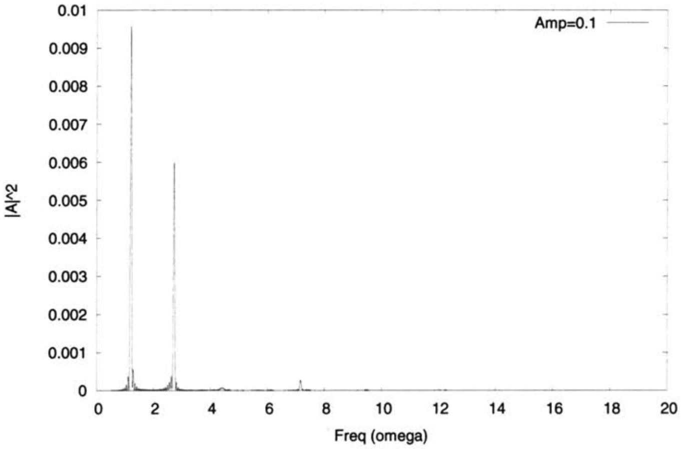

Figure 5-12: Power spectral density of a hanging chain initially displaced in the first four modes with amplitude of (*a*)0.01 (*b*)0.05 and (*c*)0.1. Frequency data spans 100 nondimensional time units.

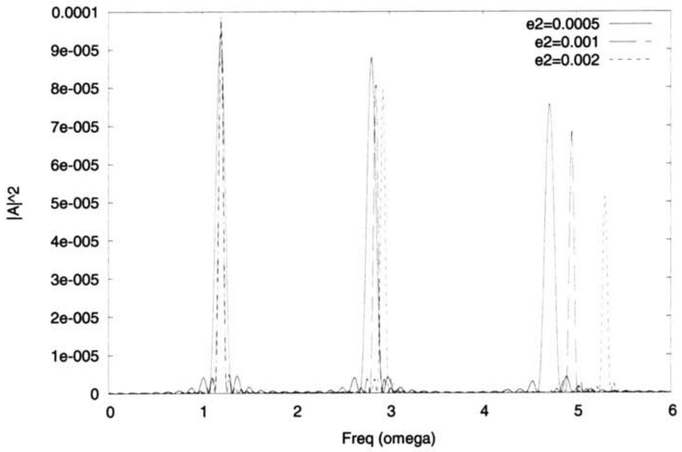

Figure 5-13: Power spectral density of hanging chain initially displaced in the first four modes with amplitude of $A = 0.01$, and frequency data spanning 100 nondimensional time units. The three curves are for $(e2, e3) = (0.0005, 50), (0.001, 100), (0.002, 200)$.

to equation 5.10. This frequency being the same order of the natural swinging fourth mode frequency indicates that the bending rigidity will be contributing significantly to the restoring force and subsequent modal frequency. As such, if we estimate the tension as half the maximum value in equation 5.10, then the first term in the radical has the value 0.5. The second term, for this fourth mode, will have a value of 0.06, suggesting an increase in frequency on the order of that reported in table 5.3. An illustration of the influence of bending rigidity on the first three modes can be seen in the power spectrum of figure 5-13, where bending rigidities of $e2 = 0.0005$, 0.001, and 0.002 are used. The added restoring force of the bending rigidity is seen to increase the higher mode frequencies. Thus, the loss of accuracy in the higher modes associated with both finite bending rigidity and finite extensional rigidity has been demonstrated.

5.2.3 Chain Released from Horizontal

We now turn to a highly nonlinear problem with the hanging chain to examine the influence of finite bending and extensional rigidity on the evolution. The problem is of the release of a chain from a horizontal configuration. Through such simulation, the effect of the bending and stretching rigidity on the solution is studied. It is clear that the influence of these properties will be in situations where they play a significant role in the system dynamics. A measure of the participation of the bending and stretching in the system dynamics is the amount of energy which enters these modes. Consider, for example, the snapping and recoil of such a nearly inextensible body. At the point of snap, where the kinetic energy goes away, the energy must be transferred to potential energy in the stretching mode. When this happens, the dynamics can no longer be considered governed by inextensibility and the value of the extensional rigidity will influence the evolution. When a snapping body recoils, energy is translated back into the kinetic domain at the higher modes associated with the stretching mode frequencies. Such evolution of energy to higher modes through transfer to the stretching mode is apparent in this study of chain release from the horizontal.

The released chain is first examined with values of bending rigidity $e2 = 0.005$ and extensional rigidity $e3 = 500$. The time history of the different energy components is given in figure 5-14(a). The bottom of the swing is the point of minimum gravitational potential energy, where the tendency toward stretching is expected. At the first such minimum a slight stretching event can be seen in the stretching potential energy curve, though with little observable energy transfer to higher modes. However, near the second minimum of the gravitational potential energy, a significant transfer of energy to the stretching mode is apparent. After such event, it is clear that this energy exchanges between the kinetic and structural potential (both stretching and bending) modes at a much higher frequency. These high frequency dynamics are dependent on the values of the extensional and bending rigidities, while the early time low-frequency dynamics are general for very high extensional rigidity and very low bending rigidity. Solution schemes that contain numerical dissipation have been used in order to control prevalence of the high frequency components, as discussed in [22]. In experiment and observation, these high frequency components are controlled through physical dissipation. For the present end, where the structural code is coupled to a viscous fluid, there will be plenty of modeled physical dissipation for the higher modes. However, these test cases of the uncoupled structural model require the modeled Kelvin-Voight structural dissipation discussed in § 4.4. Two different structural damping values are used in simulations of the plots figure 5-14(b)(c). It is clear that the damping controls the higher modes. For structural damping, the rate of energy dissipation in the system will be dependent exclusively on the extensional and bending rigidities, while for external fluid damping energy is dissipated out of any mode of body motion.

We now examine the swinging evolution with varying the extensional rigidity for a fixed bending rigidity of $e2 = 0.01$. Figure 5-15(a) and (b) show the time history of the tail position for simulations with five different extensional stiffnesses. The kinematics convergence with increasing stiffness. Figure 5-15(c) shows this convergence through a plot of the RMS difference from the highest stiffness case ($e3 = 1000$). For the duration of the simulation, it's clear that the doubling of the stiffness from $e3 = 500$ to $e3 = 1000$ has negligible influence on the kinematics. The kinematics will diverge, however, as the energy in this undamped case migrates to the higher modes for long duration. Such divergence will not be an issue for the damped case. This can be observed in the evolution and RMS error plots for the case damped as $G = 0.01$ as shown in figure 5-16. The plots show faster convergence of the solution with extensional stiffness, indicating that error associated with extensional flexibility is reduced with damping.

Convergence with lowering bending rigidity is now sought for a fixed extensional rigidity. We consider the case with extensional rigidity of $e3 = 50$ and Kelvin-Voight damping of $G = 0.01$. With damping serving to suppress the higher modes, convergence is found with lowering the bending rigidity as $e2 = (0.01, 0.005, 0.0025, 0.001, 0.0005, 0.00025, 0.0001)$. The cases of lowest bending rigidity also required a increase in the grid size to $N = 400$ for $e2 = 0.00025$ and $N = 500$ for $e2 = 0.0001$, to accommodate the larger ratios of $e3/e2$. Plots of the time history of the end position are shown with the RMS error plots in figure 5-17, showing convergence with decreasing bending rigidity (as the inverse becomes large).

We have demonstrated the convergence of the of the kinematics with increasing extensional stiffness and decreasing bending rigidity. It is, in fact, the reduction of (*a*) G=0

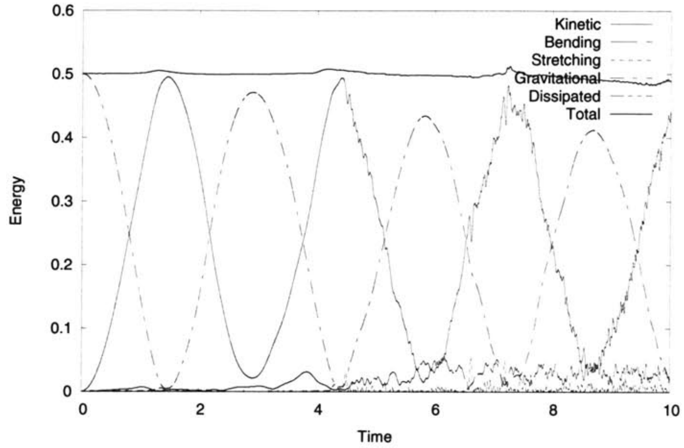

(*b*) G=0.001

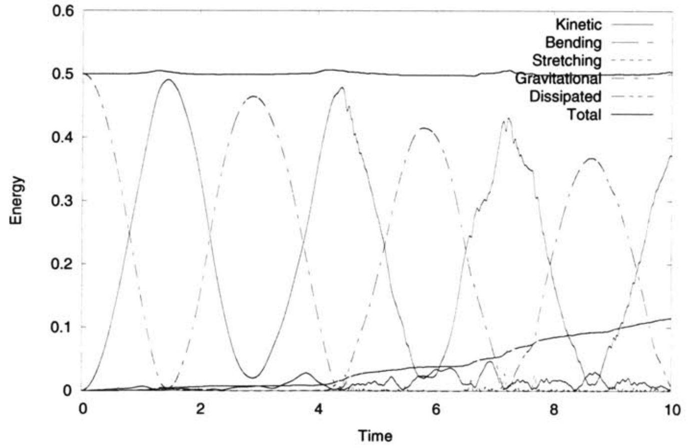

(*c*) G=0.01

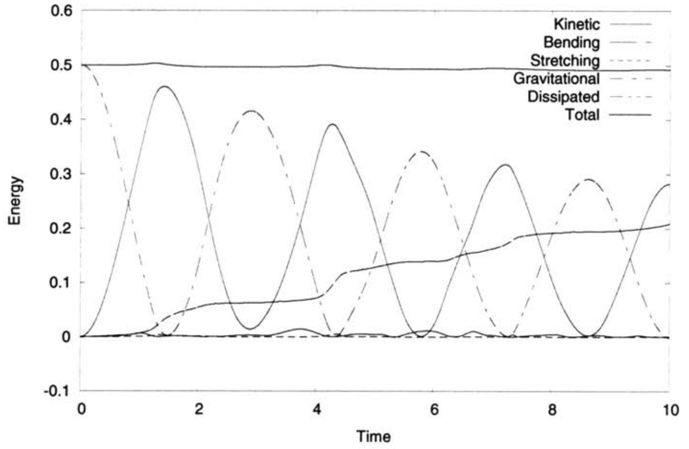

Figure 5-14: Time history of the system energy components (and total) for the horizontally released chain with $(e2, e3) = (0.005, 500)$ using three different Kelvin-Voight structural damping values, G as defined in § 4.4.

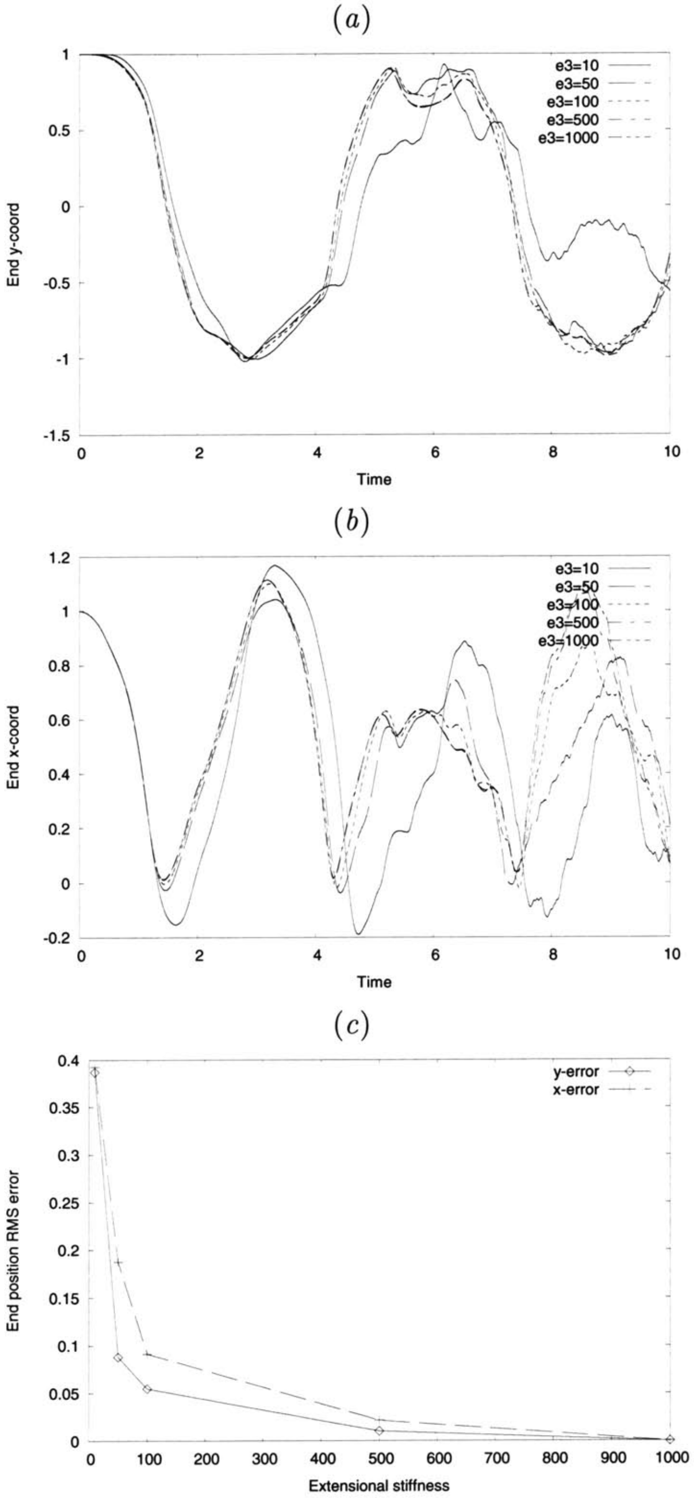

Figure 5-15: Time history of the end position for the horizontally released undamped chain for bending rigidity $e2 = 0.01$ and extensional rigidities $e3 = (10, 50, 100, 500, 1000)$. Plots of (a) the y-coordinate, (b) the x-coordinate, and (c) the RMS difference from the highest stiffness case over the 10 time unit duration.

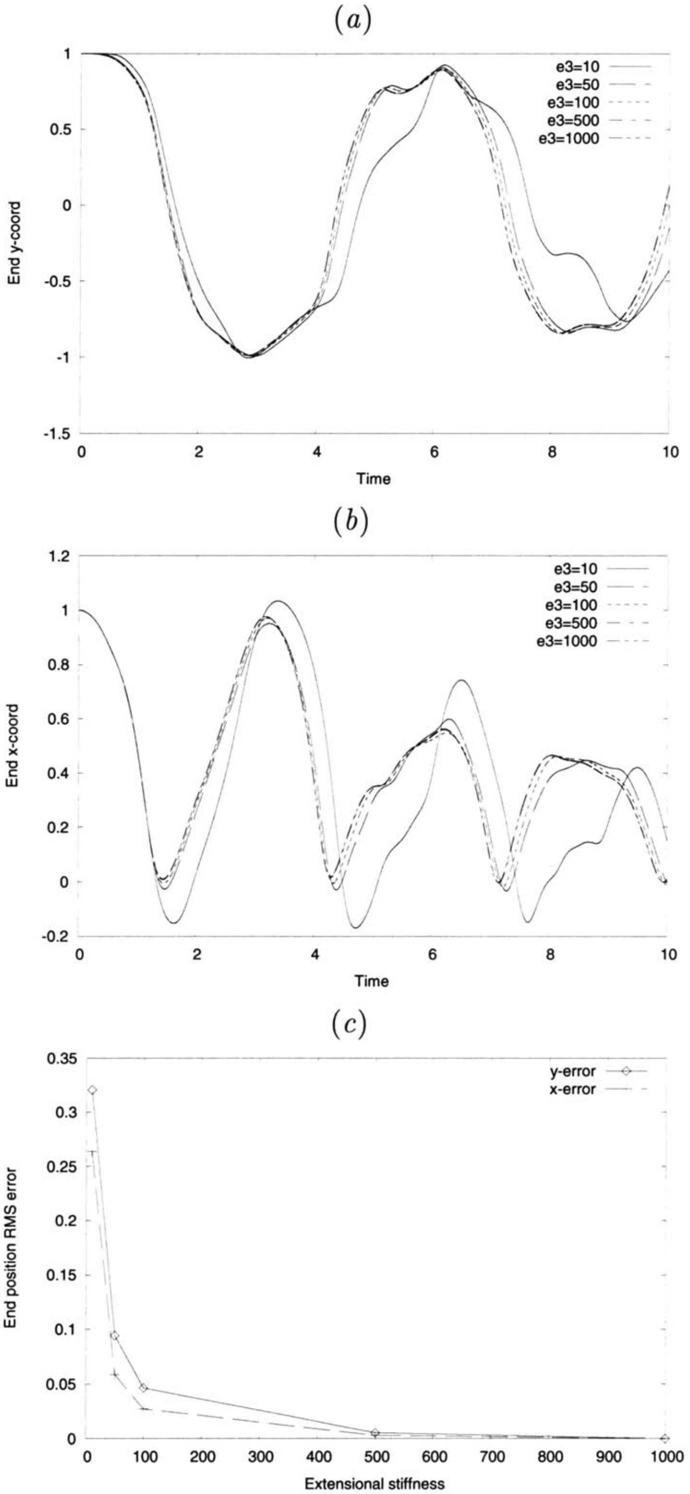

Figure 5-16: Time history of the end position for the horizontally released chain for bending rigidity $e2 = 0.01$, Kelvin-Voight damping of $G = 0.01$, and extensional rigidities $e3 = (10, 50, 100, 500, 1000)$. Plots of (a) the y-coordinate, (b) the x-coordinate, and (c) the RMS difference from the highest stiffness case over the 10 time unit duration.

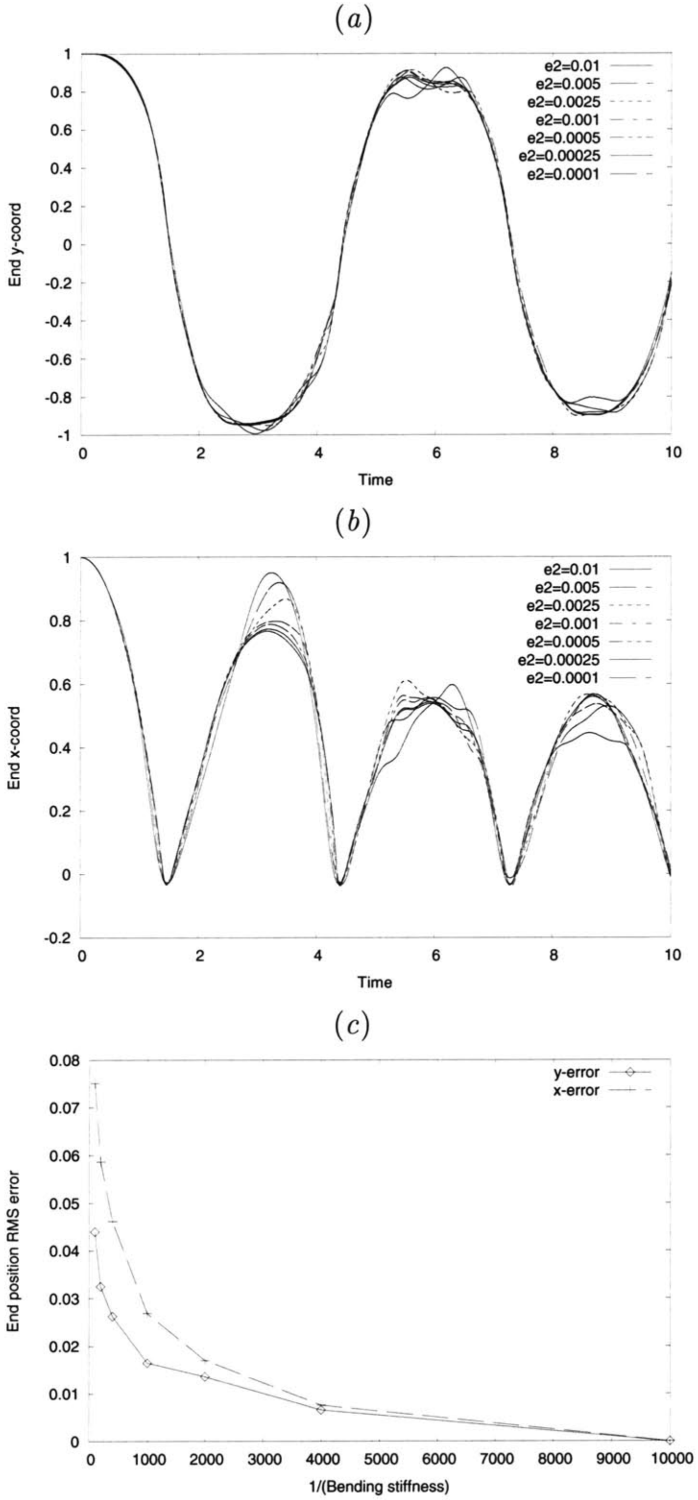

Figure 5-17: Time history of the end position for the horizontally released chain for extensional rigidity $e3 = 50$, Kelvin-Voight damping of $G = 0.01$, and bending rigidities $e2 = (0.01, 0.005, 0.0025, 0.001, 0.0005, 0.00025, 0.0001)$. Plots of (a) the y-coordinate, (b) the x-coordinate, and (c) the RMS difference from the lowest bending rigidity case over the 10 time unit duration.

energy in these modes that makes the evolution of the system lose dependence on the values of the rigidities. This reduction of modal energy with the increasing of extensional rigidity and decreasing of bending rigidity can be seen in figure 5-18, where the mean energy over the duration of the simulation is shown. As such, we have shown a correspondence between negligible energy content in a structural mode and convergence of the kinematics with that extreme for the structural parameter. For the structural parameter being sufficiently extreme, the evolution of the system is no longer dependent on its value.

Comparison to Experiment

In Koh et. al. [31] an experiment and simulation were performed where a pinned-pinned catenary is released at one end under the influence of gravity. A time history of the cable tension was obtained from a strain gauge located near the pinned end, a distance 2.5% of the cable length. For their numerical simulation, the need for a dissipative integration scheme was again indicated in order to reduce transfer of energy to high frequency modes.

Running the identical case using the present numerical scheme, we use modelled physical dissipation with damping parameter $G = 0.01$, as was found effective in the preceding discussion. Figure 5-19 shows the time history of the near-end tension from the experiment and numerics of Koh and the numerics of the present work. It's clear that the Koh numerical results and the present numerical results with $G = 0.01$ are very similar. Both numerical results differ a little from the experimental result, particularly in the higher frequency components, but give generally good prediction of the measured tension.

5.2.4 Horizontally Forced Chain

We now turn our attention to the hanging chain periodically forced at its upper end in the horizontal direction, as in figure 5-11(*b*). This is a problem that has been studied experimentally and numerically in [29] and [22]. The past studies were directed toward

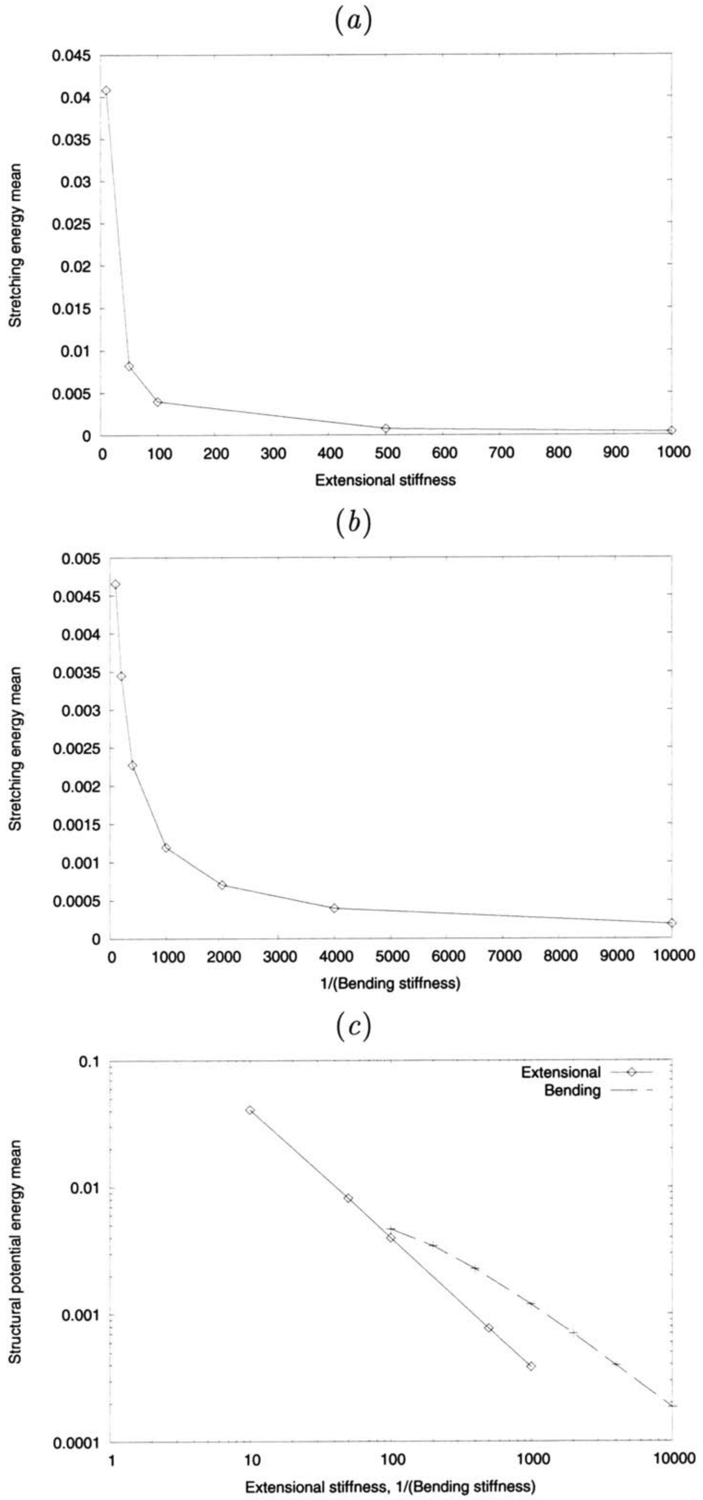

Figure 5-18: Structural potential energy averaged over the 10 time units of the simulation. (*a*) for bending stiffness $e2 = 0.01$ and damping $G = 0.01$ while varying extensional stiffness, (*b*) for extensional stiffness $e3 = 50$ and damping $G = 0.01$ while varying bending stiffness, and (*c*) on a log-log plot.

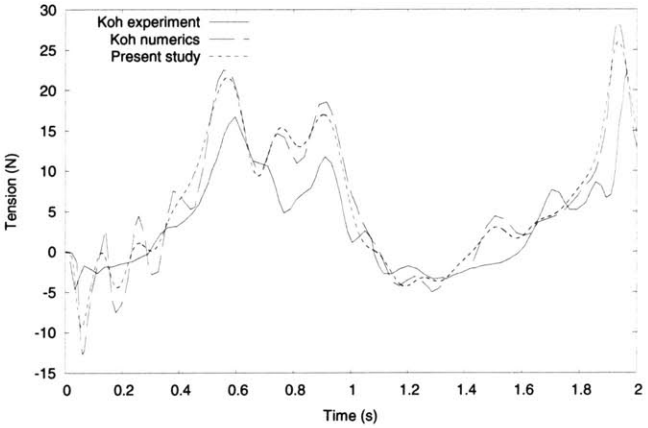

Figure 5-19: Shows the pin-end tension time history. The present numerical study follows closely the numerical results of Koh et. al.[31], which differs only slightly from the experimental measurement.

experimental validation of numerical simulations of a nonlinear swinging chain. A single event of loop closing at the free end of the forced chain has been used in the validation effort. This same event is sought in use of the present numerical model. The associated kinematics are far more extreme than those to be encountered in the coupled flapping simulation, as the hydrodynamic grid could not handle such an extreme configuration as the body closing on itself. Consequently, the structural parameters required to resolve the kinematics are also extreme, requiring large grids to allow high ratios of $e3/e2$. Again, convergence of the kinematics can be related to disappearance of the energy from the structural potential domain.

The particular problem, and comparison of a single event, is a difficult criterion for such a nonlinear system. The evolution of the nonperiodic response of this system is quite sensitive to the physical and numerical conditions, as described in [29] and [22]. As such, comparison of a single event at a specified time is a rigorous path for validation. Convergence of this problem using the present model is toward the loop closing event at the proper time, as $e3/e2$ becomes very large. Figure 5-20 displays the loop very nearly closing at the experimentally observed time of $t \simeq 3.4s$. For this simulation, a rigidity ratio of $e3/e2 = 4 \times 10^7$ was used, requiring a grid of $N = 4000$ for numerical stability. While this is an impractical grid size for the coupled hydrodynamic model, the problems to be investigated do not require resolution of

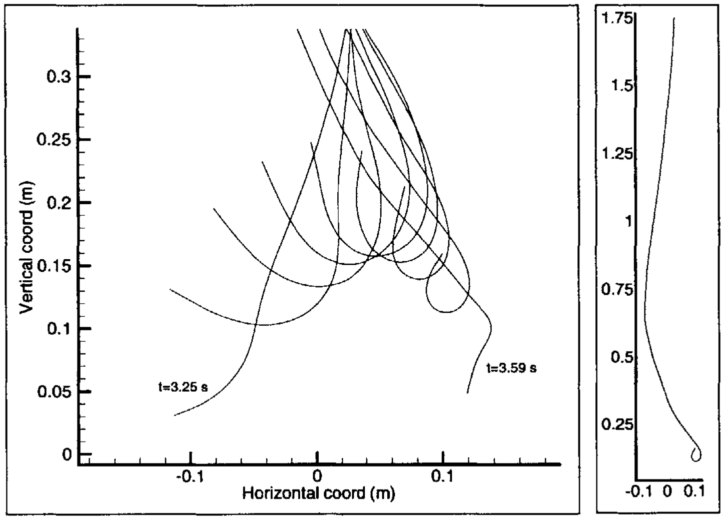

Figure 5-20: The simulated loop closing event using $e3/e2 = 4 \times 10^7$ and $N = 4000$ compares well to the shaking chain experiment ([29],[22]). The snapshot showing the entire length of chain displays the extreme nature of this event in terms of the tight loop closing.

configurations such as that of figure 5-20. With this problem, the capability of the structural model has been shown to exceed the requirements of the coupled model.

Alternate Two-Dimensional Solution Method

In order to capture the loop closing event with the horizontally forced chain, it is necessary to use a very high rigidity ratio. The standard numerical solution method requires very large grids for stability with these large rigidity ratios. The alternate solution method described in § 4.5.2 allows use of such large rigidity ratios on smaller grids, but is not as robust to accurate simulation of extreme events such as snapping and recoil.

We repeat the highest rigidity ratio case ($e3/e2 = 4 \times 10^7$) of the horizontally forced chain, this time using the alternate solution method and a grid dimension of $N = 100$, forty times smaller than that required for the standard solution method. Again, we capture the loop closing event at $t \simeq 3.4s$, as can be seen in figure 5-21. While the loop closing event occurs at the time observed in experiment, the loop is slightly larger and shifted upward when using $N = 100$ as opposed to $N = 4000$. The

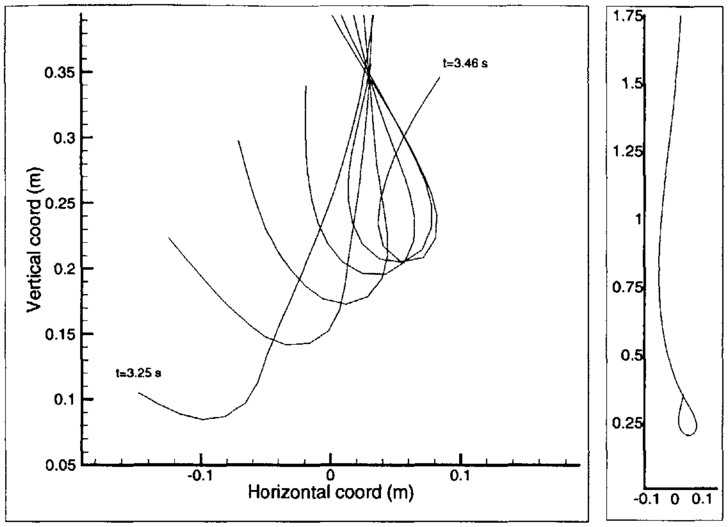

Figure 5-21: The simulated loop closing event using $e3/e2 = 4 \times 10^7$ and $N = 100$ with the alternate solution method, with snapshot showing entire length of chain.

differences in the evolution of the simulation using the two grid sizes can be seen in the time history of the horizontal and vertical position of the free end, given in figure 5-22. These differences indicate the loss of accuracy of the low resolution simulation using the smaller grid, particulary as the length scale of the bending dynamics approaches that of the grid spacing at the time of loop closing. Despite some loss of accuracy, we have resolved this extreme event of loop closing at the time found experimentally in a computationally rapid simulation.

5.2.5 3D Membrane Released from Horizontal

The horizontally released chain problem is extended to a square membrane which is pinned along one edge. Two cases are run for this problem. The first, less refined, case has nondimensional structural properties (defined by equation 4.97) as bending rigidity $e2 = 0.05$, extensional rigidity $e3 = 50$, Poisson ratio $e4 = 0.3$ and Kelvin-Voight damping of $G = 0.01$, calculated on a 25×25 grid. The second, more refined case, uses $e2 = 0.01$, $e3 = 100$, $e4 = 0.3$, and $G = 0.001$, calculated on a 50×50 grid. A series of snapshots of the swinging membrane simulation using the coarse grid is shown in Figure 5-23. The contours of extensional strain on this plot indicate

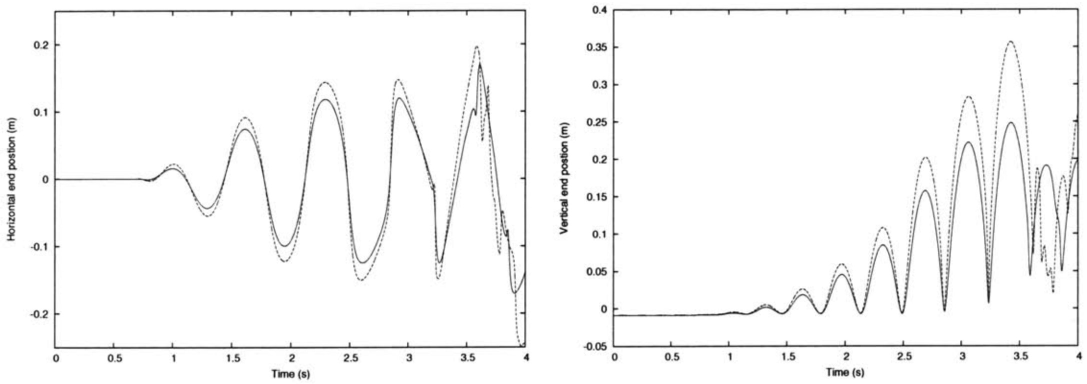

Figure 5-22: The horizontal and vertical position of the free end in the shaking chain simulation with $e3/e2 = 4 \times 10^7$, using the standard solution method with $N = 4000$ (——), and the alternate solution method with $N = 100$ (— —). Differences indicate loss of accuracy for the lower resolution simulation, and the breakdown of this lower resolution simulation after the loop closing event.

the increase in tension at the bottom of the swing. The three dimensional effects are evident in the curvature of the end, and the variation of the strain toward the edges.

A plot of the end corner trajectory for the two swinging membrane cases is shown with the two-dimensional chain end trajectory in figure 5-24(a-b). The rigidities of the chain used in this plot are equivalent to those of the fine plate, and a similar trajectory is found. The energy budget for the fine plate simulation is given in figure 5-24(c). Only a small amount of energy enters the structural bending and extensional modes, suggesting only small influence of the structural properties on the evolution of the swinging plate.

5.2.6 Fully Bounded Linear and Nonlinear Plate

We now turn to the problem of a rectangular plate bounded on all four edges, allowing comparison to previous linear and nonlinear treatments. The linear development in Shames and Dym [53] considers only the bending rigidity as a restoring force, and no contribution from tension associated with the strain in displacement. The nonlinear von Karman plate system used by Kirby and Yosibash [30] does consider the effect of tension from extensional strain, allowing comparison of the present model using a nonlinear problem.

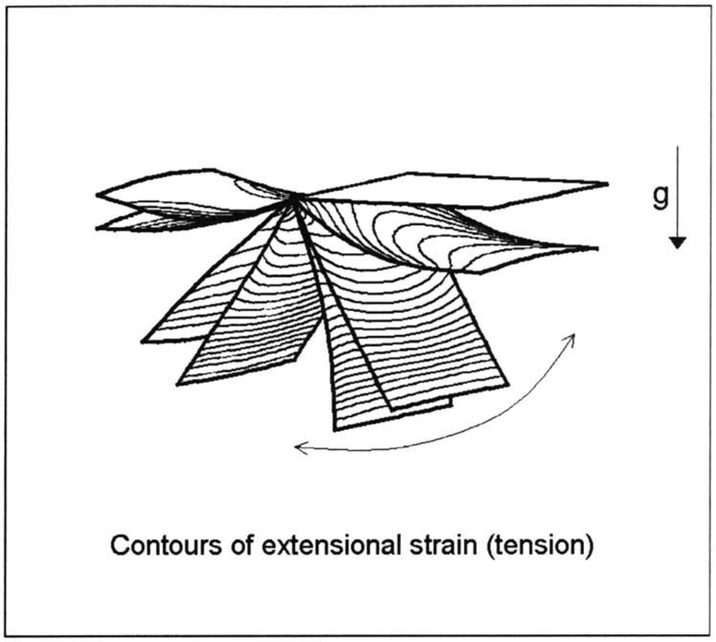

Figure 5-23: A series of snapshots of the swinging membrane separated by 0.7 nondimensional time units. Contours are of extensional strain, and show the increase of strain at the bottom of the swing, as well as the spanwise variation of the strain. This is the coarse simulation using $e2 = 0.05$ and $e3 = 50$ with a 25×25 grid.

Linear Comparison Here we consider two problems solved in Shames and Dym [53]. The first is of the square plate clamped on all edges and subject to a uniform normal load, q. The steady state displacement at the plate center is given by linear theory as

$$y_{max} = 0.0202\frac{q(L/2)^4}{e2} = 0.00126\frac{qL^4}{e2}, \tag{5.12}$$

where $e2$ is the bending rigidity and L is the side length. The case to be used in the nonlinear model for comparison must be one for which the bending rigidity dominates the tension force. Using $e2 = 1$, $q = 1$, and $L = 1$, equation 5.12 predicts $y_{max} = 0.00126$. Using $e3 = 1000$, the first clamped mode ($k = 2\pi$) will have a tension restoring force of less than 0.01% the bending restoring force. For such low extensional rigidity the answer obtained from the numerical simulation is independent of the value of $e3$. The problem was run on $N \times N$ grids for $N = (11, 15, 21, 25, 31)$ to

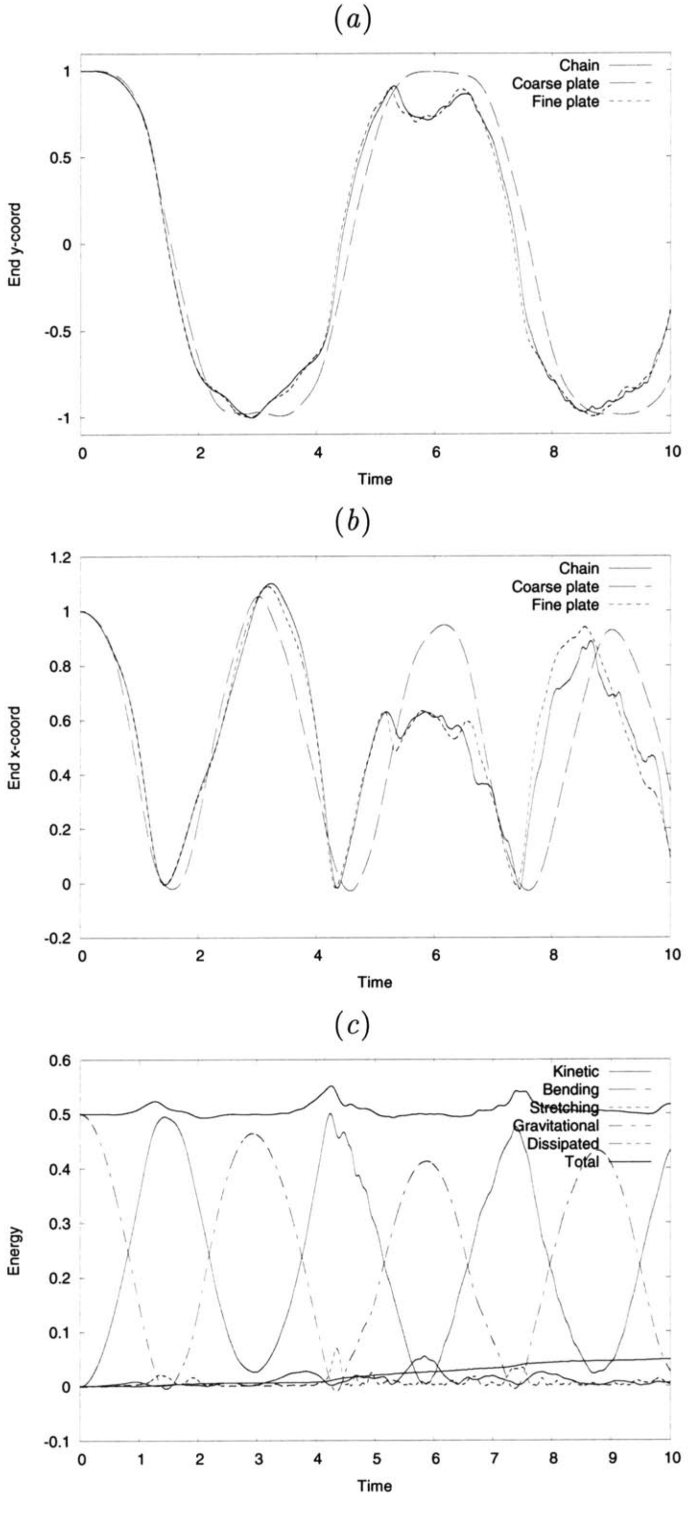

Figure 5-24: Time history of the plate end corner position and chain end in (*a*) and (*b*). The coarse plate on a 25×25 grid has bending rigidity $e2 = 0.05$, extensional rigidity $e3 = 50$, Poisson ratio $e4 = 0.3$ and damping of $G = 0.01$. The fine plate on a 50×50 grid has $e2 = 0.01$, $e3 = 100$, $e4 = 0.3$, and $G = 0.001$. The chain has $e2 = 0.01$, $e3 = 100$, and $G = 0$. The fine plate energy budget is given in (*c*).

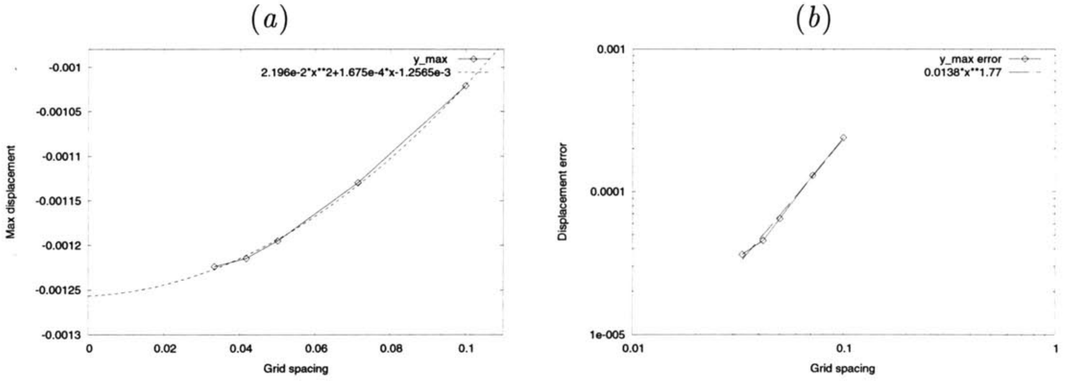

Figure 5-25: (a) Maximum steady state displacement for clamped plate under uniform load with varying grid spacing. Using $e2 = 1$, $e3 = 1000$, $q = 1$, and $L = 1$ on an $N \times N$ grid with $N = (11, 15, 21, 25, 31)$. (b) Error from the $y_{max} = 0.00126$ intercept with $e_{ymax} = 0.0138\Delta x^{1.77}$ curve fit.

examine the convergence with grid spacing. A plot of maximum displacement with grid spacing is given in figure 5-25(a), and a quadratic polynomial curve fit indicates an intercept of $y_{max} = 0.00126$, the value predicted from the linear formulation. The error from this intercept value is plotted in figure 5-25(b), along with the the curve fit of $e_{ymax} \sim \Delta x^{1.77}$ which indicates near second-order convergence with grid spacing.

We now look at the linear problem with simply supported edges to examine the frequency of the first mode, and convergence with time step. From the linear development in Shames and Dym [53], the frequency of the first mode for the square plate is

$$\omega = 19.9 \frac{1}{L^2} \sqrt{\frac{e2}{e1}}. \tag{5.13}$$

Using $e1 = 1$, $e2 = 1$, $e3 = 1000$, and $L = 1$, and initially displacing the first mode at $A = 0.01$, the linearly derived frequency is $\omega = 19.9$. On a 25×25 grid, runs are made with time step of $\Delta t = (.01, .005, .0025, .001)$. A plot of the frequency with time step is given in figure 5-26(a), and a polynomial fit indicates an intercept of $\omega = 19.81$, a 0.45% difference from the linear solution. The error from this intercept is plotted in figure 5-26(b), and the curve fit of $e_\omega \sim \Delta t^{1.95}$ indicates second-order convergence with time step.

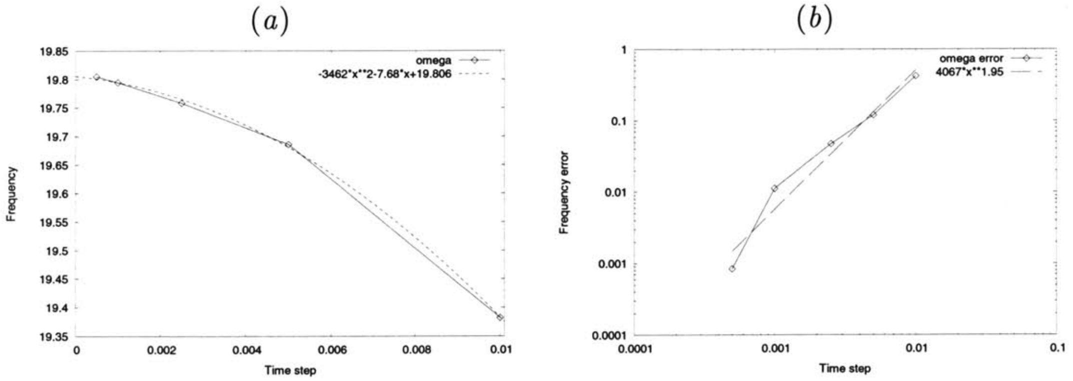

Figure 5-26: (a) Frequency of the first mode of the simply supported square plate for $e1 = 1$, $e2 = 1$, $e3 = 1000$, and $L = 1$, using $\Delta t = (.01, .005, .0025, .001)$. (b) Error of the frequency from the $\omega = 19.81$ intercept with $e_\omega = 4067\Delta t^{1.95}$ curve fit.

Nonlinear Comparison We again compare maximum displacement of a clamped plate under uniform load, this time in the regime where nonlinear effects are important. The work of Kirby and Yosibash [30] uses a nonlinear formulation to look at this problem. An equivalent system is obtained using the present model by using $e2 = 0.01$, $e3 = 48$, and $q = 0.2368$. The work of [30] indicates a maximum displacement of $y_{max} = 0.02615$ for these parameters. With such displacement, the magnitude of the tension associated restoring force is $\sim 16\%$ the magnitude of the bending restoring force for the $k = 2\pi$ mode. This indicates the importance of the nonlinearity for this problem, and the linear prediction of equation 5.12 is for $y_{max} = 0.0298$ which represents a 14% error.

We examine convergence with grid spacing for $N \times N$ with $N = (11, 15, 21, 25, 31, 35, 41, 51, 81)$. A plot of maximum displacement with grid spacing is given in figure 5-27(a). The quadratic polynomial curve fit indicates an intercept of $y_{max} = 0.02619$, a 0.15% difference from the value indicated in [30]. The error from this intercept value is plotted in figure 5-27(b), with the the power curve fit showing error convergence as $e_{ymax} \sim \Delta x^{1.46}$. For this case, where the nonlinear terms of the governing equation become significant, the error is observed to converge as $\sim \frac{3}{2}$ power with grid spacing. The spatial derivatives in the formulation are all taken with second-order accuracy, but as the stretching nonlinearity contains fractional exponents, convergence of the solution error is not guaranteed at the same

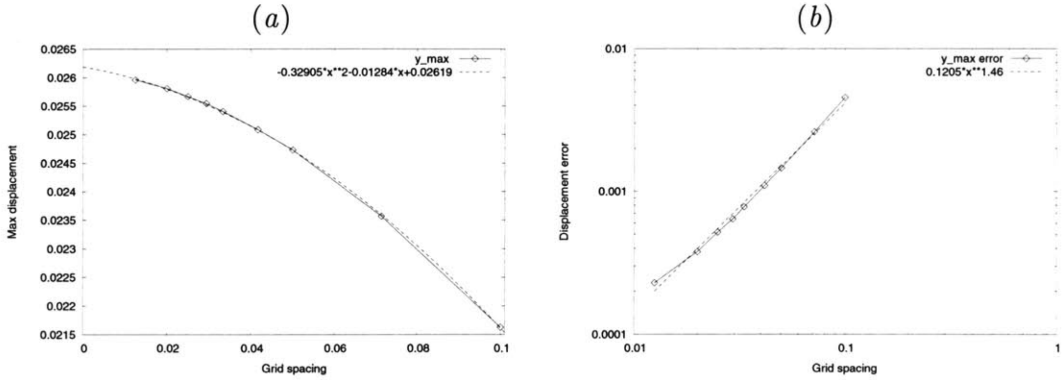

Figure 5-27: (*a*) Maximum steady state displacement for clamped plate under uniform load with varying grid spacing in the nonlinear regime. For comparison to [30], using $e2 = 0.011$, $e3 = 48$, $q = 0.2368$, and $L = 1$ on an $N \times N$ grid with $N = (11, 15, 21, 25, 31, 35, 41, 51, 81)$. (*b*) Error from the $y_{max} = 0.02619$ intercept with $e_{ymax} = 0.1205\Delta x^{1.46}$ curve fit.

rate. Thus, while error convergence for this nonlinear problem is better than first-order, it falls short of second-order.

5.3 FSDS Verification

5.3.1 Verification Problem: Flexible Foil with Impulsive Cross-flow

The problem used for two-dimensional FSDS verification is that of a thin foil pinned on one end subject to an impulsively started cross-flow. When the flow is started, energy is transferred to the structure in the form of both kinetic and potential energy. The progression of the coupled solution in time is depicted in the series of vorticity plots of figure 5-28(*a*), which show the vortices shedding and interacting with the non-linear body motion as it aligns with the incoming flow. This simulation is performed at $Re = 1000$ with relatively high values for the mass ratio ($\mu = 1$) and bending rigidity ($K_B = 0.1$), resulting in significant energy exchange between the fluid and structural domains. A high value for the structural extensional rigidity ($K_S = 100$), impedes significant energy content in the extensional mode.

5.3.2 Energy Conservation with Grid Resolution

A particularly good measure of accuracy of the coupled simulation is energy conservation. We perform the FSDS-2D for this problem of a pinned thin foil with impulsively started cross flow using two different resolution grids of $N = (60 \times 120)$ and $N = (100 \times 200)$. The energy budget for the lower and higher resolution FSDS is given in figure 5-28(b). Significant energy content appears in all components except the structural extensional mode, indicating the near inextensibility. The structural energies and the outer boundary flux (representing energy input to the system through a pressure gradient) are not significantly influenced by the grid resolution, while the fluid kinetic energy and fluid dissipation both show lower values on the lower resolution grid. This additional energy loss, or numerical dissipation, is displayed in the curves of total loss. At the end of the simulation, the low resolution numerical dissipation is 53% of the physical viscous dissipation, while the high resolution numerical dissipation is 24% of the viscous dissipation, indicating improved Reynolds number accuracy. This higher resolution $N = (100 \times 200)$ grid is used for all two-dimensional simulations of the present study. The three-dimensional simulations use a coarser $N = ([48\times]60 \times 120)$ grid, yielding some Reynolds number accuracy for computational efficiency.

5.3.3 FSDS-3D Verification

We now consider a related three-dimensional problem to test the energy conservation of the coupled FSDS-3D simulation tool, using a grid of $N = (48 \times 60 \times 120)$. For this case, we use a three-dimensional initial displacement as

$$z(s_1, s_2)_0 = A_0 s_1 \left(1 + sin\left(\frac{2\pi}{B} s_2\right)\right), \tag{5.14}$$

with the simulation domain of width B, periodic in the spanwise s_2 direction. We use a domain width equal to the length, so that $B/L = 1$ and an initial displacement amplitude scaled by $A_0 = 0.1$, so that the trailing edge displacement ranges from $0 \rightarrow 0.2$, and the body presents a small angle displacement to the impulsively started

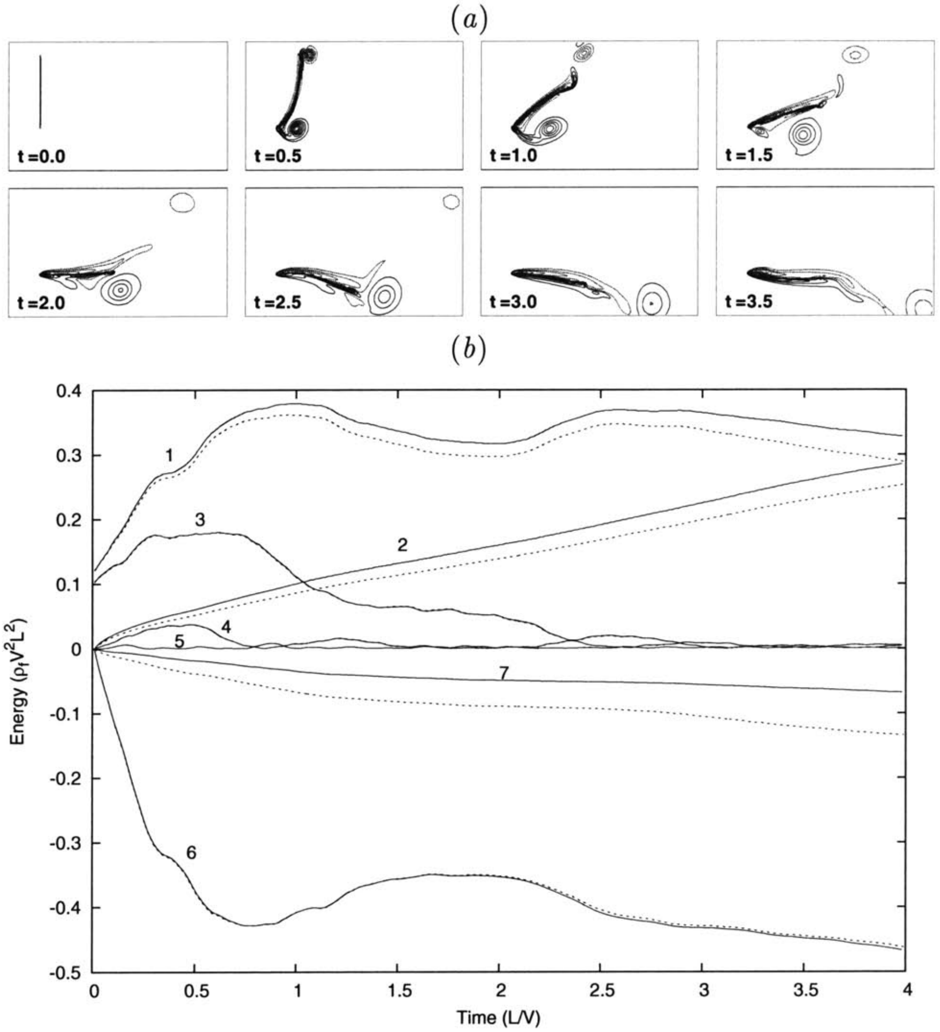

Figure 5-28: (*a*) Vorticity contour series for impulsively started cross flow. (*b*) Energy budget time history using grids of $N = (60 \times 120)$ (– – –) and $N = (100 \times 200)$ (——), with fluid kinetic (1), fluid dissipated (2), structural kinetic (3), structural bending potential (4), structural extensional potential (5), outer boundary flux (6), and total loss (7) energies.

flow. The simulation parameters of $Re = 1000$, $\mu = 1$, and $K_B = 0.1$ are the same as in the two-dimensional verification, while the extensional rigidity is reduced to $K_S = 1$ to allow spanwise variation to the displacement in the periodic domain, and the Poisson ratio used is $\nu_s = 0.3$. The system experiences a high frequency oscillation of the spanwise displacement as it settles toward a flow-aligned configuration, as can be seen in the time history of the displacement at the trailing edge point of the initial maximum, given in figure 5-29(a). A three-dimensional perspective of the displacement can be seen in figure 5-30 in a series of shaded plots from $t = 1.5 \rightarrow 2$. The complicated three-dimensional structure of the associated vortex wake can be seen in the plot of vortex contours representing positive and negative vorticity in the wake, given in figure 5-31. A spanwise and streamwise variation to the vortex structure is seen in the vorticity plot. The energy budget plot of figure 5-29(b) shows good energy conservation for this highly three-dimensional simulation. The total energy loss due to numerical dissipation for the entire simulation is 16% of that lost due to physical viscous dissipation. The energy plot shows that this good energy conservation is found in a simulation that experiences significant energy exchange between the fluid and structural domains. Structural energy enters the fluid domain as fluid kinetic energy, and experiences significant viscous dissipation, reducing the amount of energy in the oscillation. Even though we have reduced the extensional rigidity to allow spanwise variation, we again see very little participation of the structural extensional potential energy in the energy budget. The simulation verifies the ability of FSDS-3D to successfully simulate the fluid-structure interaction with three-dimensional structural displacement and three-dimensional flow characteristics while conserving energy in the system.

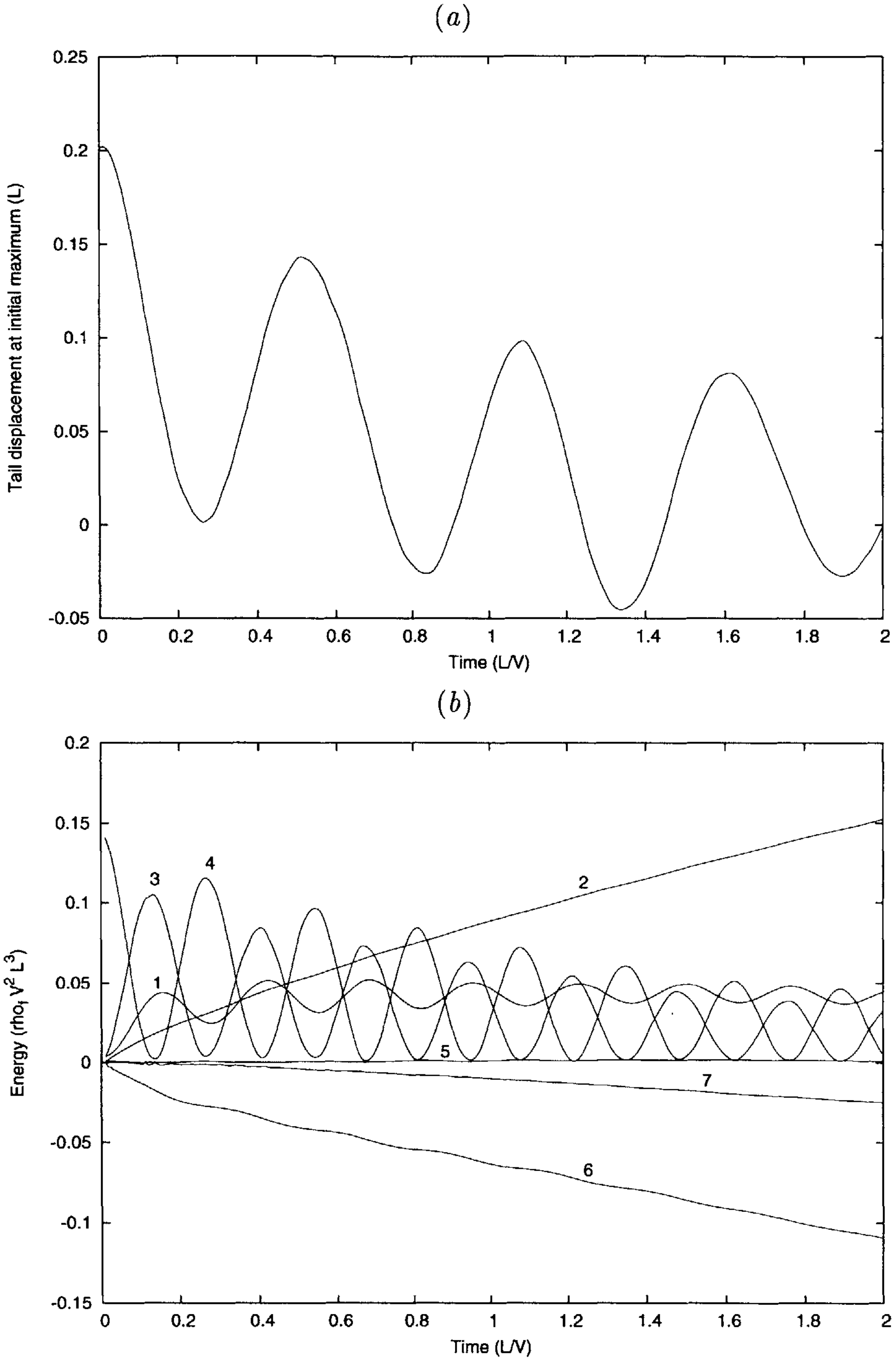

Figure 5-29: (*a*) Time history of the trailing edge displacement at the spanwise position of initial maximum. (*b*) Energy budget time history with fluid kinetic (1), fluid dissipated (2), structural kinetic (3), structural bending potential (4), structural extensional potential (5), outer boundary flux (6), and total loss (7) energies.

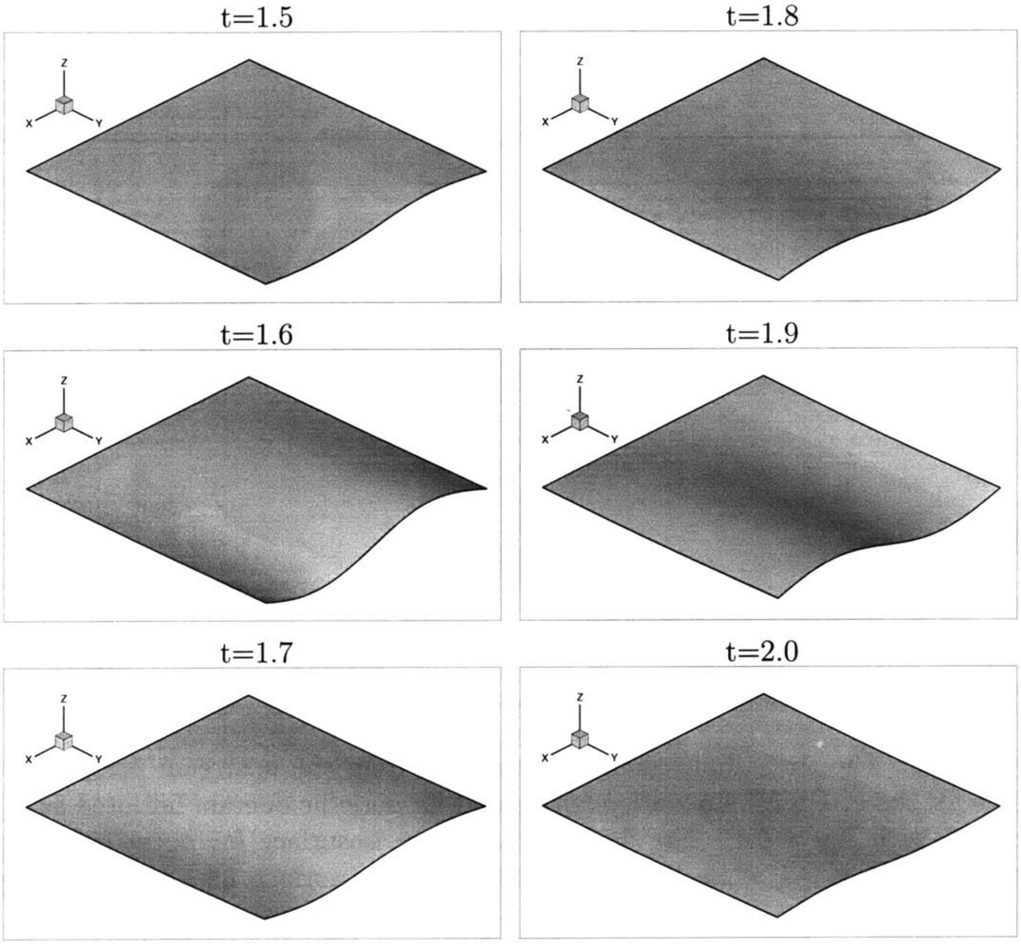

Figure 5-30: Shaded surface from downstream perspective for the FSDS-3D simulation with spanwise periodic domain initiated as equation 5.14 with $A_0 = 0.1$.

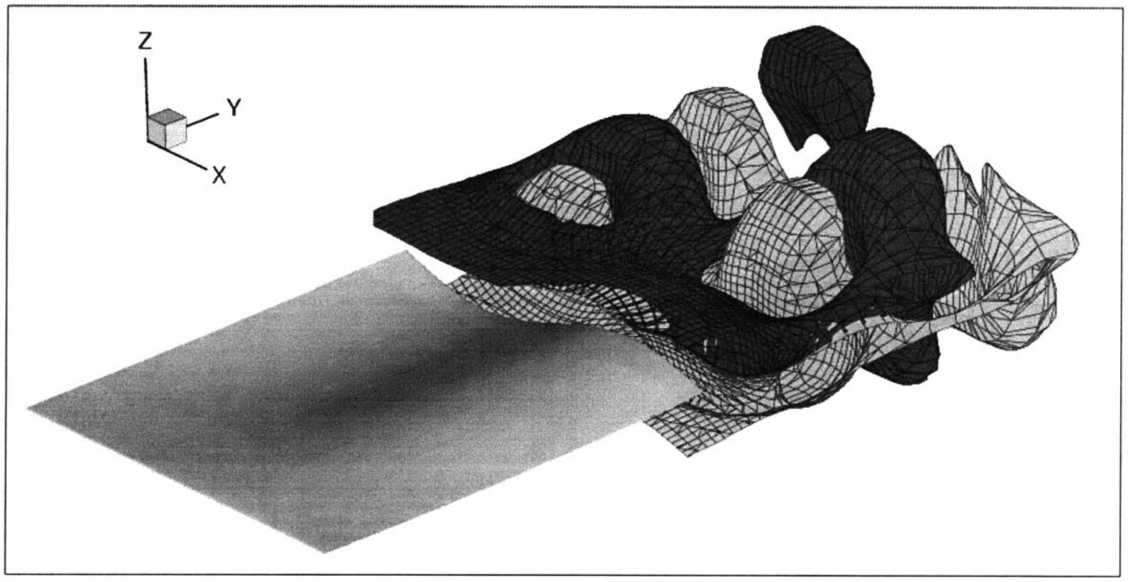

Figure 5-31: The three-dimensional vortex wake from the upstream perspective at $t = 1.9$ for the FSDS-3D simulation with spanwise periodic domain initiated as equation 5.14 with $A_0 = 0.1$. The dark surface is an isosurface for negative spanwise vorticity of $\omega_x = -1$ while the light surface is an isosurface for positive spanwise vorticity of $\omega_x = +1$.

Chapter 6

The Two-Dimensional Passive Flapping Foil

The case of a two-dimensional thin passive foil is studied in an unbounded uniform flow. We consider the problem in the near inextensible limit, examining the effects of structure-to-fluid mass ratio, bending rigidity, and Reynolds number. Understanding the responses of this system is a key foundation to eventual exploitation of the natural modal behavior in engineering endeavors. The limit of very low bending rigidity represents the flag flapping problem, a problem of import in the natural world, as well as engineering and industrial applications. Larger bending rigidity cases relate to the flow-structure interaction of the fish-like swimming problem involving flexible foils.

6.1 Introduction to the Passive Flapping Problem

6.1.1 Problem Statement

We consider the problem of a two-dimensional thin membrane, pinned on the leading edge and free on the trailing edge, excited by a uniform incompressible viscous inflow in an unbounded domain, shown in figure 6-1. The body is sufficiently thin that the thickness function with length is unimportant to the result. The structural proper-

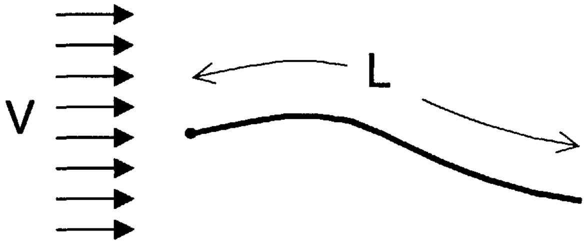

Figure 6-1: Depiction of the problem of the flapping two-dimensional flexible thin foil of length L in uniform incoming flow V in an unbounded fluid domain. The foil is pinned at the leading edge and free at the trailing edge.

ties of the membrane in this two-dimensional study are the length, mass-per-length, bending rigidity, and extensional rigidity. The extensional rigidity is considered to be very high, and is included in the nonlinear numerical model as a means of maintaining continuity and transmitting force tangentially, as detailed in Chapter 4.

The geometrically nonlinear equation of motion for the two-dimensional flag is

$$\rho_s h \frac{\partial^2 \vec{x}}{\partial t^2} - \frac{\partial}{\partial s}\left(T(s)\frac{\partial \vec{x}}{\partial s}\right) + EI\frac{\partial^4 \vec{x}}{\partial s^4} = \vec{F}_f, \tag{6.1}$$

with s as the Lagrangian coordinate along the length, and the body position vector $\vec{x}$ fixed at the pinned leading edge. Here, ρ_s is the structural density, h is the flag thickness, $T(s)$ is the tension in the body, and EI is the structural bending rigidity. Fluid coupling is through the forcing term defined as

$$\vec{F}_f = [\Delta \tau]\hat{n}, \tag{6.2}$$

where $\hat{n}$ is the upward facing normal and $[\Delta\tau]$ is the difference between the fluid dynamic stress tensor at the top and bottom of the body. Elements of the stress tensor are defined by the fluid dynamics at the body surface as

$$\tau_{ij} = \nu \rho_f \left(\frac{\partial u_i}{\partial \xi_j} + \frac{\partial u_j}{\partial \xi_i}\right) - \delta_{ij} p. \tag{6.3}$$

Equations 6.2 and 6.3 contain all of the physical influence of the fluid flow to the structure. This includes viscous damping and boundary layer drag, inertial added mass effect, and the influence of separation with vortices shedding into the wake.

The fluid dynamics are obtained as the solution to the incompressible fluid momentum and mass conservation equations, the Navier–Stokes equations, written as

$$\begin{aligned} \frac{\partial \vec{v}}{\partial t} + (\vec{v} \cdot \vec{\nabla})\vec{v} &= -\frac{1}{\rho_f}\vec{\nabla}p + \nu\nabla^2\vec{v}, & (6.4) \\ \vec{\nabla} \cdot \vec{v} &= 0. & (6.5) \end{aligned}$$

The velocity boundary conditions complete the picture as

$$\begin{aligned} \vec{v} &= \frac{\partial \vec{x}}{\partial t} \quad \text{on flag boundary} & (6.6) \\ \vec{v} &= V \quad \text{at } \infty. & (6.7) \end{aligned}$$

It is through this inner boundary condition, equation 6.6, that the structural influence is imparted to the fluid, as the flow is necessarily solved as one consistent with such structural motion. While dynamic continuity between the fluid and structural domains is contained in equations 6.1-6.3, kinematic continuity between the domains is contained in equations 6.4-6.7. This set of equations govern the coupled fluid and structural motion of the system depicted in figure 6-1.

6.1.2 Linear stability analysis

Following the work of Triantafyllou [63] and Coene [13] we write the equation of motion, considering z to be the displacement from the streamwise y axis, as

$$\rho_s h \frac{\partial^2 z}{\partial t^2} - \frac{\partial}{\partial y}\left(T\frac{\partial z}{\partial y}\right) + EI\frac{\partial^4 z}{\partial y^4} + m_a\left(\frac{\partial}{\partial t} + V\frac{\partial}{\partial y}\right)^2 z = 0. \qquad (6.8)$$

The only difference between this equation and those of Triantafyllou and Coene is that we have allowed for variation of the tension in the streamwise direction. Unlike the soap film problem where the gravity influences the tension, the present study has only the fluid forcing contributing to the tension. If we assume a Blasius laminar boundary layer to represent the fluid forcing, the tension can be written as

$$T(y) = 1.3\rho_f V^2 L Re^{-1/2}\left(1-\sqrt{\frac{y}{L}}\right), \tag{6.9}$$

where

$$Re = \frac{VL}{\nu}. \tag{6.10}$$

In seeking a solution to equation 6.8 which lends itself to physical interpretation, we avoid the variable tension expression of equation 6.9, instead using a constant of equation 6.9 evaluated at the leading edge. Using a constant value for tension, we revert to the equation used in the previous studies, the notable difference being the quantifying of the tension in terms of the fluid dynamics. The equation of motion is now written with the last term expanded as

$$\begin{aligned} \rho_s h\frac{\partial^2 z}{\partial t^2} &- 1.3\rho_f V^2 L Re^{-1/2}\frac{\partial^2 z}{\partial y^2} + EI\frac{\partial^4 z}{\partial y^4} \\ &+ m_a\frac{\partial^2 z}{\partial t^2} + 2m_a V\frac{\partial^2 z}{\partial y \partial t} + m_a V^2\frac{\partial^2 z}{\partial y^2} = 0. \end{aligned} \tag{6.11}$$

The three expanded final terms represent the fluid dynamic effects of inertial added mass, Coriolis force, and centrifugal force, respectively (see [63]). Grouping the terms we have

$$(\rho_s h + m_a)\frac{\partial^2 z}{\partial t^2} + (m_a V^2 - 1.3\rho_f V^2 L Re^{-1/2})\frac{\partial^2 z}{\partial y^2} + EI\frac{\partial^4 z}{\partial y^4} + 2m_a V\frac{\partial^2 z}{\partial y \partial t} = 0. \tag{6.12}$$

In the second term, the countering effects of the Kelvin-Helmholtz instability and the restoring action of the drag-induced tension can be seen. The variables (y, z, t) of the equation of motion are now nondimensionalized by the length L and free stream velocity V, obtaining

$$(\rho_s h + m_a)\frac{V^2}{L}\frac{\partial^2 z}{\partial t^2} \quad + \quad (m_a V^2 - 1.3\rho_f V^2 L Re^{-1/2})\frac{1}{L}\frac{\partial^2 z}{\partial y^2} + EI\frac{1}{L^3}\frac{\partial^4 z}{\partial y^4}$$

$$+2m_a V \frac{V}{L} \frac{\partial^2 z}{\partial y \partial t} = 0. \tag{6.13}$$

Dividing through by $V^2 \rho_f$ we get the final form of the nondimensional equation,

$$(\mu + c_m) \frac{\partial^2 z}{\partial t^2} + \left(c_m - 1.3Re^{-1/2}\right) \frac{\partial^2 z}{\partial y^2} + K_B \frac{\partial^4 z}{\partial y^4} + 2c_m \frac{\partial^2 z}{\partial y \partial t} = 0, \tag{6.14}$$

where $c_m = m_a/(\rho_f L)$.

We assume a travelling-wave mode, $z = Ae^{i(ky-\omega t)}$, where k and ω are nondimensional wavenumber and frequency. The equation of motion then yields the dispersion relation as

$$(\mu + c_m)\,\omega^2 + \left(c_m - 1.3Re^{-1/2}\right) k^2 - K_B k^4 - 2c_m \omega k = 0. \tag{6.15}$$

The frequency is thus

$$\begin{aligned} \omega &= \frac{c_m k}{\mu + c_m} \pm \frac{1}{\mu + c_m} \sqrt{c_m^2 k^2 - (\mu + c_m)\left(c_m k^2 - 1.3Re^{-1/2} k^2 - K_B k^4\right)} \\ &= \frac{c_m k}{\mu + c_m} \pm \frac{k}{\mu + c_m} \sqrt{-\mu c_m + (\mu + c_m)\left(1.3Re^{-1/2} + K_B k^2\right)}. \end{aligned} \tag{6.16}$$

Unstable flapping modes are realized when the argument of the radical is negative, satisfying

$$\frac{\mu c_m}{\mu + c_m} > 1.3Re^{-1/2} + K_B k^2. \tag{6.17}$$

From equation 6.16 we see the expected result that the tension and bending rigidity are stabilizing effects, while the centrifugal force is the destabilizing effect of the Kelvin-Helmholtz instability. All three of these effects are scaled by the total inertia, the sum of structural mass and added mass. An additional stabilizing effect comes from the Coriolis force (the first term in the radical), which scales only with the added mass. As the expression in the radical can never become negative when $\mu = 0$, the system cannot realize unstable flapping without structural mass. Zhu & Peskin [79] indicate that the periodic energy exchange between potential energy and kinetic energy cannot be sustained unless the structure itself can take on kinetic energy, that having the kinetic energy in terms of added mass is not sufficient. The present analysis shows why that is the case. The fluid added mass is convecting with the flow velocity, and, thus, influences the system differently from structural mass. It is in fact the added mass which brings about the flapping instability, but this instability cannot be realized on a massless body.

The added mass coefficient is given from the potential flow solution of an infinite waving plate as derived by Coene [13],

$$c_m = \frac{m_a}{\rho_f L} = \frac{2}{k}. \tag{6.18}$$

The added mass is thus a function of the wavenumber and dependent on the flapping mode. This is an important distinction from the cable problem, in which the added mass is estimated from the cable cross section. The criterion for existence of flapping in the flag can now be rewritten in terms of the mode as

$$\frac{\mu}{\frac{1}{2}\mu k + 1} > 1.3 Re^{-1/2} + K_B k^2. \tag{6.19}$$

Equation 6.19 shows the stabilizing effect of lower mass ratio (the left hand side decreases with decreasing μ), lower Reynolds number, and higher bending rigidity. Recall that Zhang *et al.* [76] and Zhu & Peskin [79] found increasing the length to be destabilizing, an adjustment which decreases μ, increases Re, and decreases K_B. The change to both the Re and K_B will be destabilizing, and the observed trend comes from the combination of effects.

Rearranging equation 6.19 we obtain the mass ratio limit for flapping

$$\mu > \frac{1.3 Re^{-1/2} + K_B k^2}{1 - 0.65 Re^{-1/2} k - 0.5 K_B k^3}. \tag{6.20}$$

In the cases where the mass ratio is small compared with the added mass, the flapping

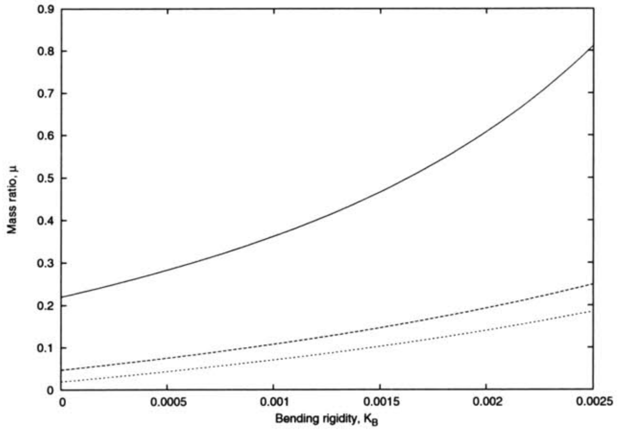

Figure 6-2: Critical mass ratio for flapping vs. bending rigidity K_B for $Re = 100$ (——), $Re = 1000$ (— —), $Re = 5000$ (- - -), using the expression of (6.20) for the $k = 2\pi$ mode.

criterion of equation 6.17 or 6.19 reduces to

$$\mu > 1.3 Re^{-1/2} + K_B k^2. \tag{6.21}$$

When bending rigidity can be neglected, the resultant simple relation becomes independent of the wavenumber, and existence of flapping becomes only a function of the two parameters μ and Re as

$$\mu > 1.3 Re^{-1/2}. \tag{6.22}$$

A plot of the stability relation of equation 6.20 is shown in figure 6-2, depicting the relationship between critical mass ratio μ and bending rigidity K_B for the $k = 2\pi$ mode at $Re = 100, 1000, 5000$. The plot shows the increased stability with lower Reynolds number and higher bending rigidity, with the intercepts at zero K_B representing the restoring influence of the viscous tension.

The linear analysis performed above would be more physically accurate if it were to include varying tension along the body, as well as the effect of global lift. A pin-ended thin body at an angle of attack will experience lift which tends toward flow alignment. A method for including this lift effect is laid out in the analysis of

Argentina & Mahadevan [4], but their approach has not yet been applied to the regime of interest in the present study. Rather than refining the linear analysis further, we continue the study using FSDS, simulations which incorporate both the global lift wake effects and variable tension in the body.

6.2 Overview of the FSDS Study and Response Results

6.2.1 Systematic Investigative Approach

Using the predictions of the linear analysis of § 6.1.2, we pursue FSDS to confirm the stability criteria in relation to the system parameters, and to examine the response moving away from the critical point into the flapping regime. All simulations use a fluid-dynamic grid dimension of $(N_\rho \times N_\theta) = (100 \times 200)$ and a structural grid dimension of $N_s = 200$. One interest is in the limit of low bending rigidity, where the viscous tension dominates the restoring force, characteristic of the flag problem. In order to minimize the influence of bending rigidity, the lowest possible value should be used. As noted in Chapter 4, a finite value of bending rigidity must be used to ensure robustness of the structural numerical model, and a minimum bending rigidity of $K_B = 0.0001$ could be used for robust solution while maintaining essential inextensibility of the structure, using $K_S = 10$. The linear analysis of figure 6-2 predicts that, using this bending rigidity at $Re = 1000$, 90% of the total restoring effect is due to the viscous tension. For rigidity ratios larger than this $K_S/K_B = 100\,000$, larger grid dimensions must be used to ensure stability.

Considering the prediction of equation 6.21, we seek to define the stability and response trends as a function of the parameters μ, Re, and K_B. Simulations are initiated with the body straight, and displaced linearly from pinned leading edge to the trailing edge with nondimensional displacement of $A_0 = 0.1$. The flow is impulsively started, with a small gradient buffer zone around the body used to minimize transients. With the mass ratio μ as the control parameter, we look to examine the range of response with increasing μ from stability into the flapping regime. Changes to this response trend with μ are then studied for varying values of both Re and K_B. With a fixed, low bending rigidity of $K_B = 0.0001$, the trend is studied from low to relatively high Reynolds numbers as $Re = 100, 500, 1000, 2500, 5000$. Alternatively, with a fixed Reynolds number of $Re = 1000$, the trend is studied through two decades of increasing bending rigidity as $K_B = 0.0001, 0.001, 0.01$. An intensive study is performed at $Re = 1000$ and $K_B = 0.0001$, carefully tracking the trends in response, as well as the associated physical phenomena.

6.2.2 The Three Response Regimes

The FSDS simulations are initiated with the body straight, at an angle of attack with tail amplitude $A_0 = 0.1$. As the simulation proceeds the body is initially displaced by the fluid dynamic forcing toward alignment with the incoming flow, and either settles to a stable-straight configuration, or experiences sustained flapping. We identify three distinct regimes of response: (I) fixed-point stability; (II) limit-cycle flapping; and (III) chaotic flapping. The differences in the response among the three regimes can be seen in figure 6-3, which plots the time history of the cross-stream displacement of the trailing edge or tail for one case from each response regime. In regime (I) the body settles to the steady-straight configuration with no cross-stream displacement of the trailing edge, while in regime (II) the response settles to a period-one limit-cycle oscillation of constant frequency and amplitude. In regime (III) the trailing edge displacement exhibits sustained nonperiodic behavior characteristic of chaos.

For the case of $K_B = 0.0001$ and $Re = 1000$ we present in figure 6-4 the results from a series of simulations through a range of mass ratios, $\mu = 0.025$ to $\mu = 0.3$, covering the three response regimes. For each mass ratio, a time history of the two-dimensional tail position is given for twenty nondimensional time units. Additionally, a phase plot is given of the cross-stream tail displacement against the cross-stream tail velocity, as well as a power spectrum of the cross-stream tail displacement. For the stable fixed-point region (I) response of $\mu = 0.025$ the phase plot spirals in to a point, corresponding to the steady-straight configuration. For the region (II) response

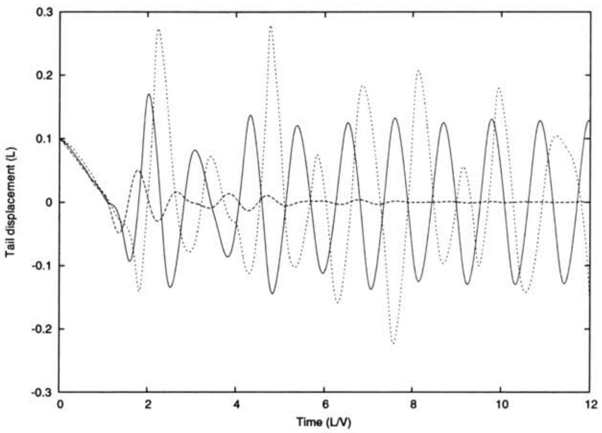

Figure 6-3: Time history of cross-stream tail displacement for (I) fixed-point stability with $\mu = 0.025$ (— —), (II) limit-cycle flapping with $\mu = 0.1$ (——), and (III) chaotic flapping with $\mu = 0.2$ (- - -), with $Re = 1000$ and $K_B = 0.0001$.

of $\mu = 0.05$, the phase plot spirals to a limit-cycle trajectory, and the power spectrum exhibits a distinct frequency peak for the tail flapping. The amplitude of the tail flapping increases with μ in region (II), and the phase plane trajectories become larger, while shifting slightly down in frequency. For $\mu = 0.125$ and higher, the system is in the chaotic region (III) where the plot in the phase plane does not trend to a specific trajectory and multiple frequency peaks are seen in the power spectrum.

Trends of the response with mass ratio are shown in figure 6-5. This includes the value of the dominant frequency from the power spectra, the tail amplitude taken as an average of the extrema, the Strouhal number $St = f2A/V$, and the largest Lyapunov exponent. The Lyapunov exponent indicates the divergence of nearby trajectories in phase space, and is calculated using the method of Wolf *et al.* [73]. Considering that the difference between two nearly identical states of the flapping body can be measured by their distance, d, in the n-dimensional phase space, then the largest Lyapunov exponent, λ, is estimated by the evolution of this distance, $d(t)$, as

$$d(t) = d(t_0)e^{\lambda(t-t_0)}. \tag{6.23}$$

The value for d is approximated using the time history of the cross-stream tail dis-

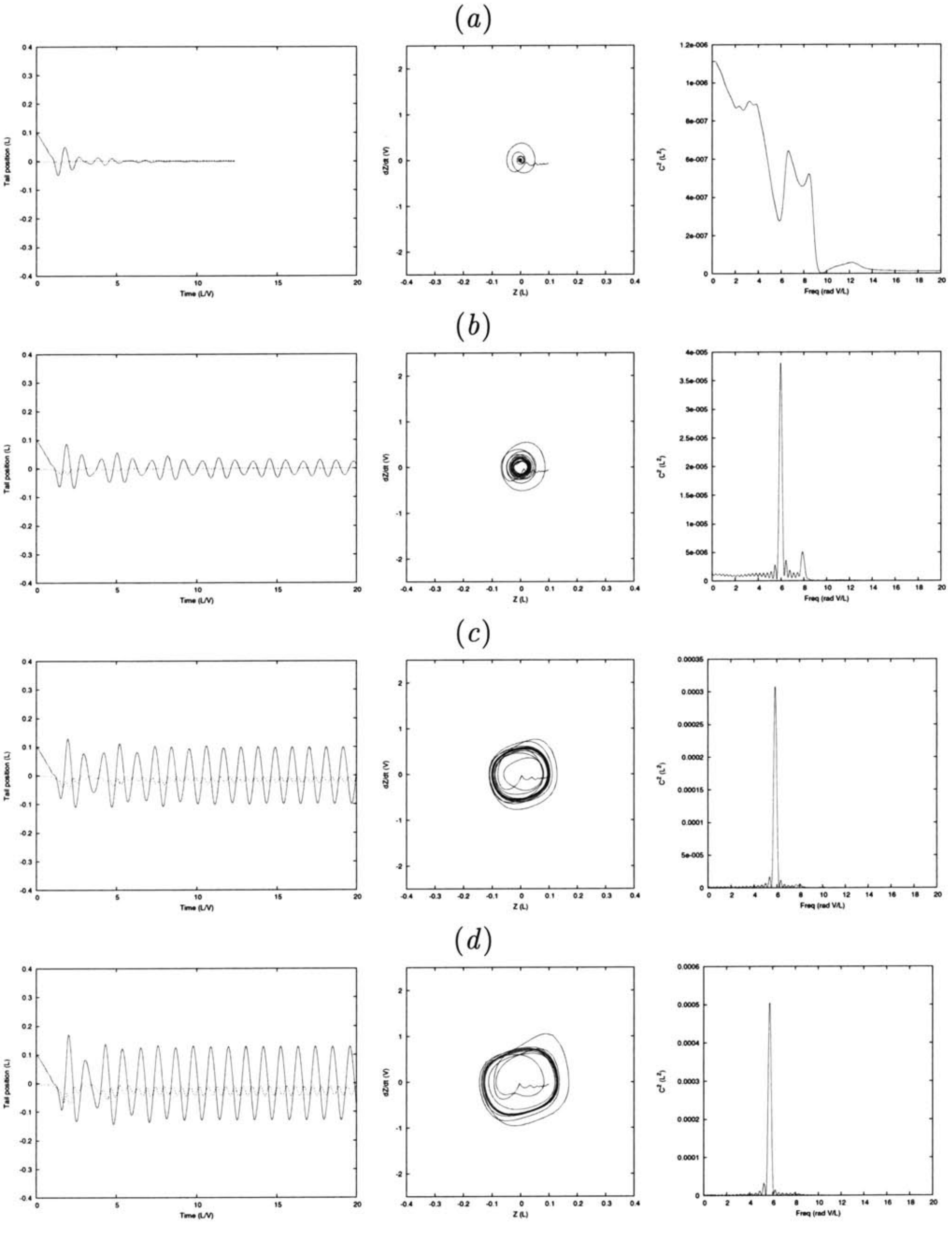

Figure 6-4: Time history of cross-stream (——) and streamwise (– – –) tail position, phase plot of cross-stream displacement and velocity, and frequency power spectrum of cross-stream displacement, for $\mu = 0.025$ (a), $\mu = 0.05$ (b), $\mu = 0.075$ (c), $\mu = 0.1$ (d), $\mu = 0.125$ (e), $\mu = 0.15$ (f), $\mu = 0.175$ (g), $\mu = 0.2$ (h), $\mu = 0.25$ (i), and $\mu = 0.3$ (j), with $Re = 1000$ and $K_B = 0.0001$.

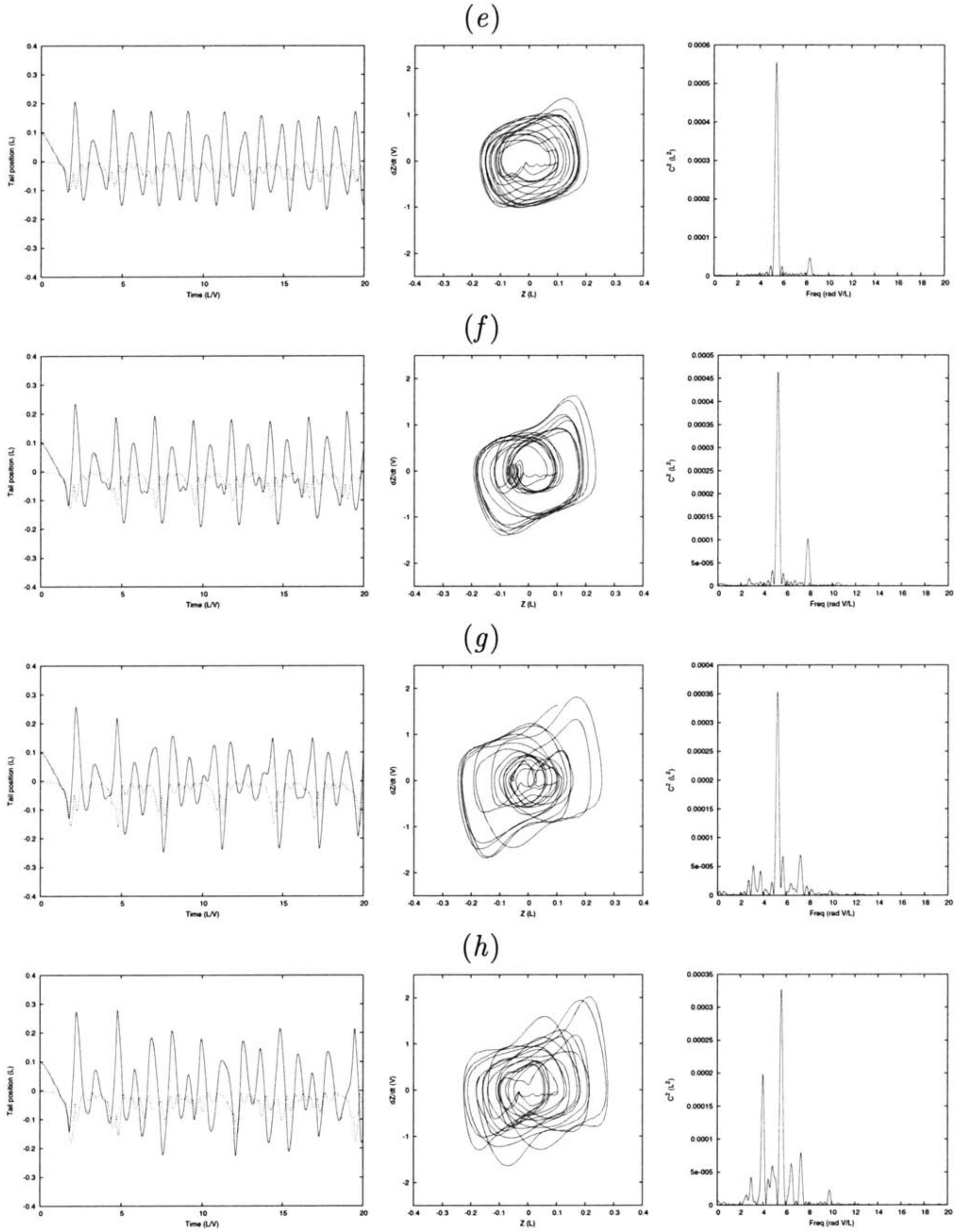

Figure 6-4: (continued)

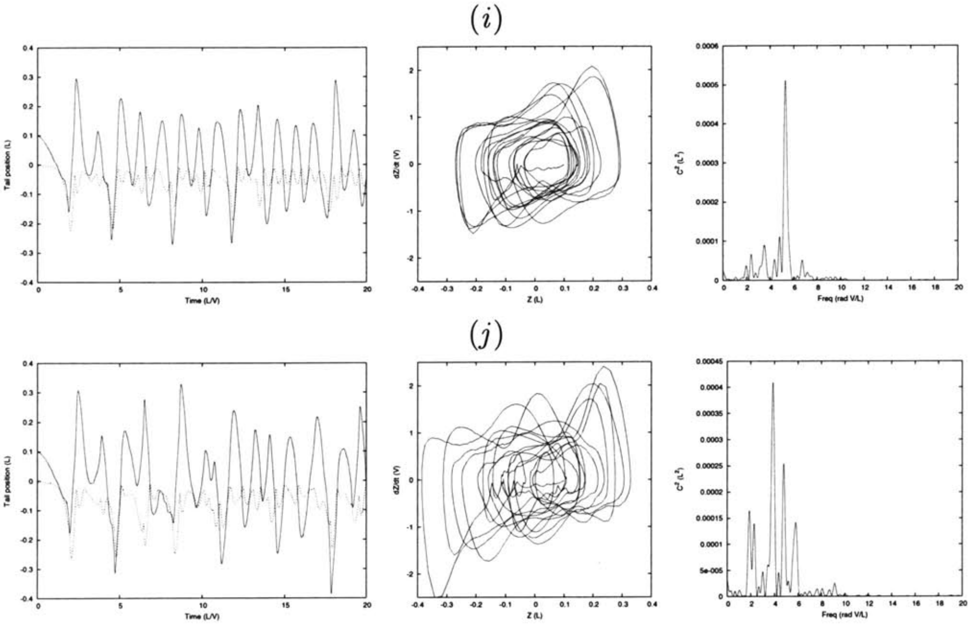

Figure 6-4: (continued)

placement, and modelling the physics as a ten-dimensional system using the time delay technique of [73]. A negative value of λ indicates convergence of the nearly identical states, while a positive value indicates divergence.

We see in figure 6-5 that the flapping amplitude initially increases with mass ratio away from the critical point, levelling out at $A \simeq 0.15$, similar to the trend found away from stability in [70]. As the dominant frequency is reduced only slightly with increasing mass ratio, the Strouhal number follows a trend similar to the amplitude, levelling to a value between $St = 0.2$ and $St = 0.3$. The Lyapunov exponent, initially negative for the region (I) point of $\mu = 0.025$, plateaus to zero for the region (II) range of $\mu = 0.05$ to $\mu = 0.1$, and takes on increasing positive values for $\mu = 0.125$ and above.

6.2.3 Regime Transitions in Parameter Space

Fixed-point stability

The differences in initial evolution between the fixed-point stable mode and the flapping modes are shown in figure 6-6. The figure displays the body response at 0.4

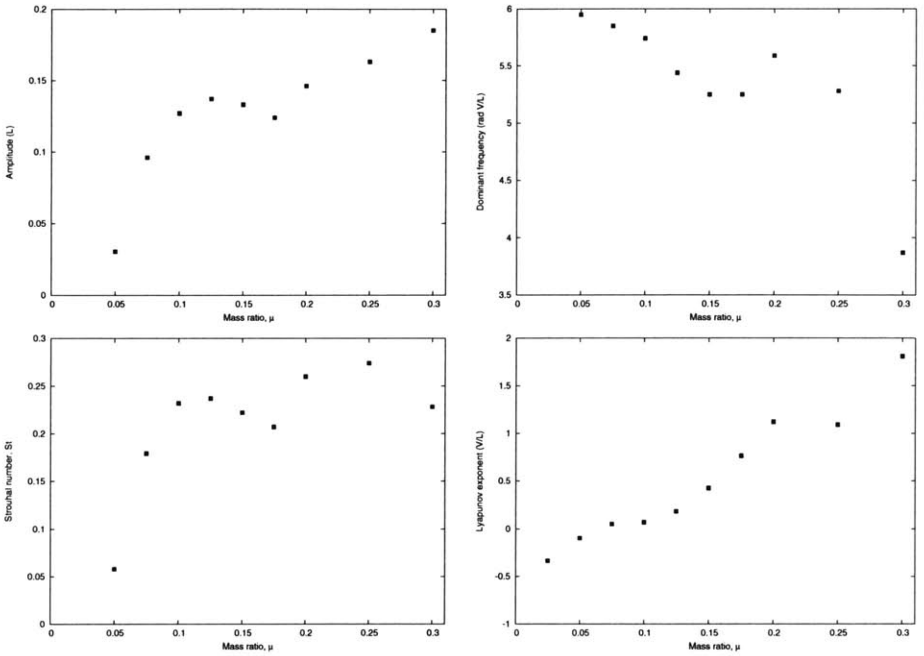

Figure 6-5: Flapping amplitude, frequency, Strouhal number, and largest Lyapunov exponent as a function of the mass ratio. All values are taken from the cross-stream tail displacement time series of figure 6-4, with $Re = 1000$ and $K_B = 0.0001$.

intervals from $t = 0$ to $t = 2$, as well as a vorticity contour plot at $t = 10$, for a case of fixed-point stability in figure 6-6(a) and a case of limit-cycle flapping in figure 6-6(b). The settling of the body into the flow-aligned configuration can be seen in the stable case, while continued oscillation around this configuration can be seen in the flapping case. The vorticity plot at $t = 10$ in the stable case indicates a steady symmetric velocity deficit wake, contrasting the unsteady vortex wake of the flapping case. It is this difference between sustained steady vs. sustained unsteady evolution which defines whether the FSDS simulates a stable fixed point or an unstable flapping system.

A plot showing the FSDS flapping stability limit in $\mu - Re$ space for the low bending rigidity of $K_B = 0.0001$ is given in figure 6-7(a). The stability limit of equation 6.22 is also plotted, showing good prediction of the critical mass ratio. It is not surprising that the proportionality of equation 6.22 holds for stability. In the case of very low bending rigidity, the only two relevant parameters are the mass ratio μ and the Reynolds number Re. In seeking some natural relationship between

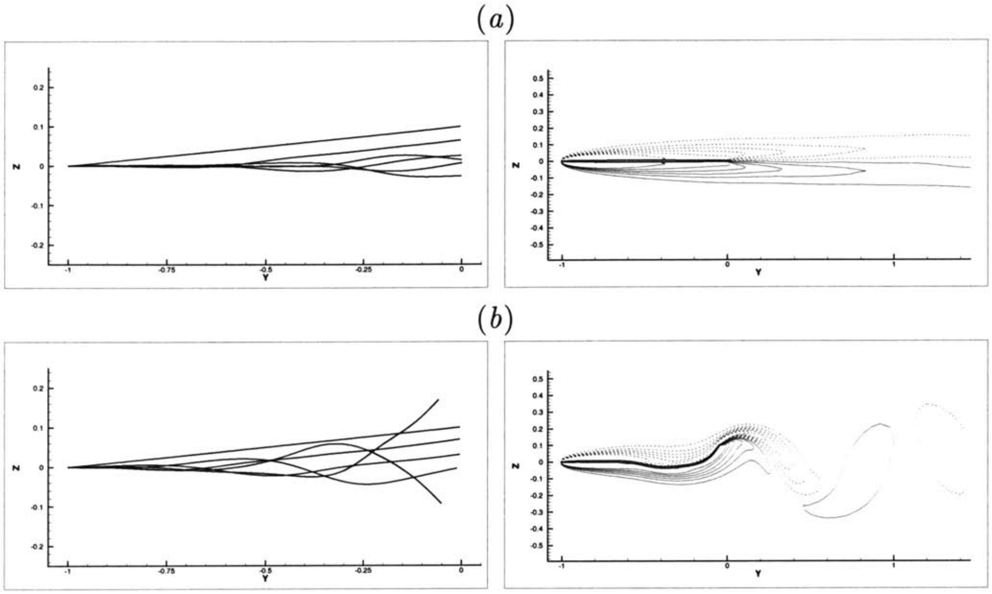

Figure 6-6: Body response at time intervals of 0.4 from $t = 0$ to $t = 2$ and vorticity plot at $t = 10$ for a fixed-point stable (a) and flapping unstable (b) case. Dashed lines indicate negative vorticity. Simulations for $Re = 1000$ and $K_B = 0.0001$ with $\mu = 0.025$ (a) and $\mu = 0.1$ (b).

these parameters, a new mass ratio can be considered which is scaled to the Blasius boundary layer thickness rather than the body length.

$$\tilde{\mu} = \frac{\rho h}{\rho_f L Re^{-1/2}} = \mu Re^{1/2} \tag{6.24}$$

This modified mass ratio is the logical choice for a critical mass ratio which has Reynolds number dependence, and the numerical results of figure 6-7(a) confirm $\tilde{\mu} = 1.3$ to be the critical value for the onset of flapping.

We now consider the effect of the bending rigidity, which we have predicted in equation 6.21 through our linear analysis to be a function of the nondimensional wavenumber. Considering $k = 2\pi$, the wavelength being found close to the body length in [76], [70], and the present simulations, we find the critical mass ratio for stability transition with bending rigidity to be predicted by

$$\mu_{crit} = 1.3Re^{-1/2} + K_B 4\pi^2, \tag{6.25}$$

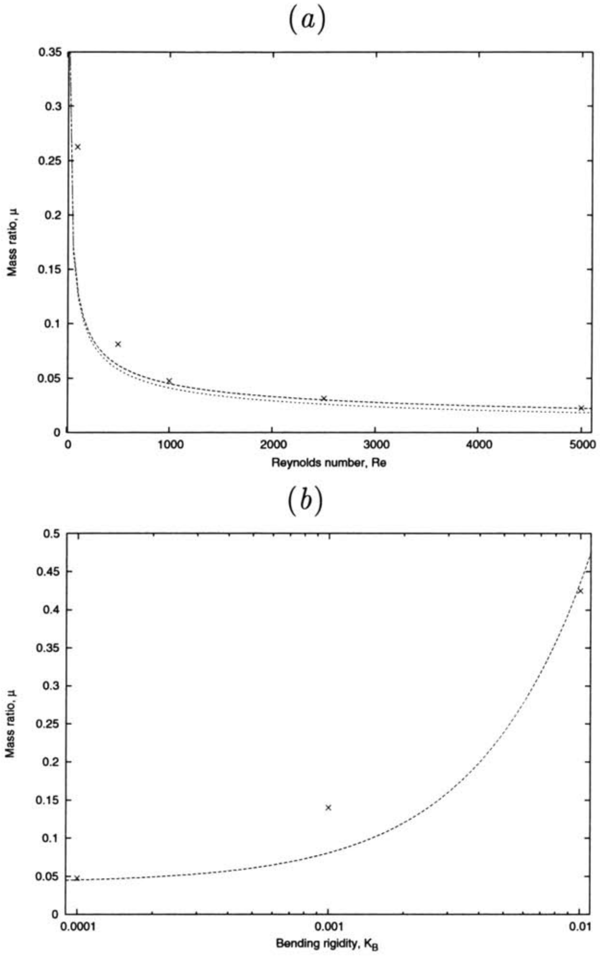

Figure 6-7: FSDS results for the critical mass ratio (×), above which unstable flapping is realized. (*a*) For $K_B = 0.0001$ and a range of Reynolds numbers, plotted with $1.3Re^{-1/2}$ (– – –) and $1.3Re^{-1/2} + K_B 4\pi^2$ (— —). (*b*) For $Re = 1000$ and a range of bending rigidities, plotted with $1.3Re^{-1/2} + K_B 4\pi^2$ (— —).

as plotted in figure 6-7(*a*). Little difference in the stability curves excluding and including bending rigidity of figure 6-7(*a*) indicates that the bending rigidity at the low value of $K_B = 0.0001$ has little influence on the stability. To examine the influence of bending rigidity on the system stability, we consider cases of larger bending rigidity. For the fixed Reynolds number $Re = 1000$, we plot FSDS stability data for increasing bending rigidity in figure 6-7(*b*). The plot shows that the critical mass ratio given by equation 6.25 continues to be a good prediction for two orders of magnitude higher rigidity.

Experimental data for stability transition from [70] at $Re \sim 100\,000$ and from [54]

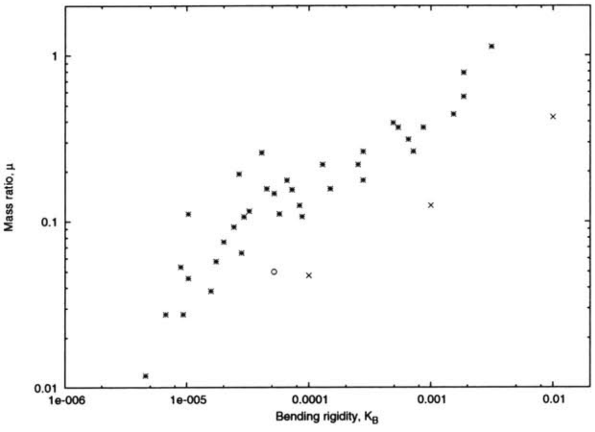

Figure 6-8: Mass ratio above which flapping is realized for a range of bending rigidities. Experimental results from [70] ($*$) at *Re* $\sim$ 100 000, from [54] ($\circ$) at *Re* $\sim$ 50 000, and FSDS results ($\times$) at *Re* $= 1000$.

at *Re* $\sim$ 50 000 were put in terms of K_B and μ for comparison to the present FSDS. We plot these experimental data with the FSDS data at *Re* $= 1000$ in figure 6-8. The trend of critical mass ratio with bending rigidity from FSDS is shown to follow that of the experimental data, but with a shift downward. As the prediction of equation 6.25 is for a higher critical mass ratio for the lower Reynolds number, we look to the physics not modelled in the linear analysis for an explanation. The wake dynamics, which are not considered in the linear analysis, will be altered as the rate of dissipation of the shed vorticity will be less for the higher Reynolds numbers. Additionally, smaller scale vortex structures will form at the higher Reynolds numbers. This effect was observed in the experiments of [76] at *Re* $= 20\,000$, but not was not in the equivalent simulations of [79] at *Re* $= 200$. The higher Reynolds number experiments display the periodic shedding of small scale vortices in the wake while the body is in a non-flapping state. Such small scale periodic shedding, which relieves the wake instability without body flapping, could account for the higher critical mass ratios of *Re* $\sim 10^5$ over *Re* $\sim 10^3$.

The influence of the relevant nondimensional parameters on the physical effects relating to stability of the system are well predicted by the linear analysis of § 6.1.2. The importance of the mass ratio on the appearance of the flapping instability is displayed. The question addressed in [54] of whether flapping will happen in the dense medium of water, is really just one of whether a dense enough flexible material exists to obtain the necessary mass ratios. Varying the nondimensional parameters, as we do in the present study, has a direct influence on the physical effects of the problem given by equation 6.14.

Low Bending Rigidity Regime Map

The stability and response results for the low bending rigidity case are summarized in the diagram of figure 6-9 on the $Re-\mu$ plane. While we considered a large number of mass ratio cases for the detailed investigation at $Re = 1000$, we performed select runs at higher and lower Reynolds numbers to help indicate the trends in response transition. The figure shows the three response regimes of (I) fixed-point stability, (II) limit-cycle flapping, and (III) chaotic flapping. The curve of transition from stable to limit-cycle response is plotted as μ_{crit} from equation 6.25. We find that the mass ratio for transition to chaos is roughly proportional to that for stability transition, such that $\mu_{chaos} \simeq 2.5\mu_{crit}$. The mass ratio for chaotic transition is thus considered as

$$\mu_{chaos} = 2.5\mu_{crit} = 3.25Re^{-1/2} + K_B 10\pi^2. \tag{6.26}$$

These transition curves of equations 6.25 and 6.26 fit the data well for all but the lowest Reynolds number, $Re = 100$, where the critical mass ratio for transition to limit-cycle flapping is underpredicted, and no chaotic response was found with FSDS up through $\mu = 0.5$. The changes associated with regime transition with increasing mass ratio are indicated in figure 6-9, including the vortex wake patterns and sign of the largest Lyapunov exponent. As the mass ratio is increased, the velocity deficit wake of the fixed point becomes a limit-cycle alternating vortex pattern of the von Karman wake. Increasing the mass ratio further, into the chaotic regime, the wake is characterized by nonperiodic vortex clustering. The value of the largest Lyapunov exponent indicates the response regime, as it is negative for the stable fixed point,

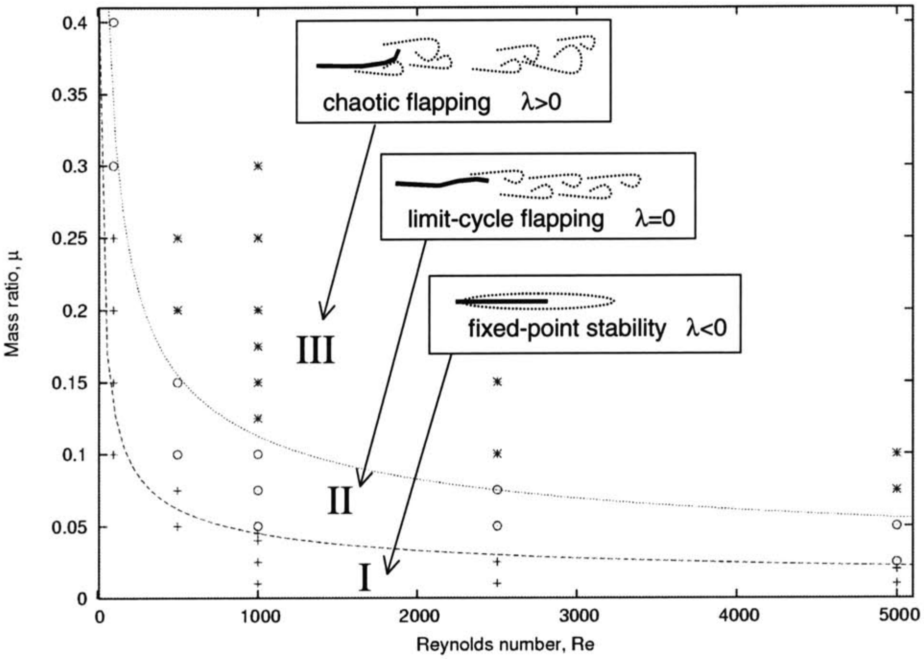

Figure 6-9: Bifurcation diagram for $K_B = 0.0001$ shows the fixed-point stability limit given by equation 6.25 (— —), and the curve indicating transition from limit cycle to chaotic response given by equation 6.26 ($\cdots\cdots$); with FSDS data indicating response as **I** a stable fixed point (+), **II** a periodic limit cycle ($\odot$), or **III** chaotic flapping ($*$). Wake patterns and the sign of the largest Lyapunov exponent are indicated for each response regime.

zero for the limit cycle, and positive for chaotic flapping.

Influence of Bending Rigidity

While we have considered earlier in this section the influence of bending rigidity on the stability, we now examine in more detail the differences in flapping response as relates to the bending rigidity. Using $Re = 1000$ and $K_S = 10$, the mass ratios associated with regime transitions are considered as a function of the bending rigidity. We utilize three bending rigidities in the study, $K_B = 0.0001, 0.001, 0.01$, representing three different orders of magnitude. While the lowest bending rigidity approaches the perfectly flexible limit with tension dominating the restoring force, the highest bending rigidity behaves as a beam with beam bending dominating the restoring force.

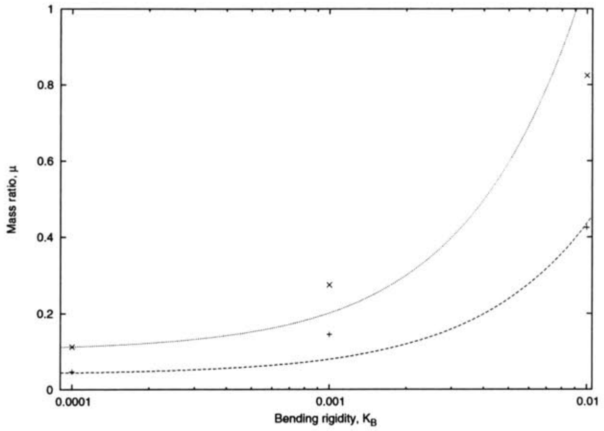

Figure 6-10: Critical mass ratio for regime transition from stable fixed point to limit-cycle flapping (+), and from limit-cycle to chaotic flapping (×), from FSDS simulations with $Re = 1000$. Also plotted are the fit curves of equation 6.25 (— —) and equation 6.26 (· · · · · ·).

The regime transitions are plotted in figure 6-10, which shows an increase in the critical mass ratio with bending rigidity for transition to limit-cycle flapping and to chaotic flapping. The equations 6.25 and 6.26 are also plotted, and make a good estimate of the regime transitions through the range of bending rigidities. We see from the combination of figure 6-10 and figure 6-9, that these equations predicting regime transition with a linear relationship to bending rigidity and inverse root relationship to Reynolds number hold well for the range of parameter space considered in this study. Figure 6-10 confirms that the higher bending rigidity cases are inherently more stable than those at lower bending rigidities, a result predicted by the linear analysis of § 6.1.2.

6.3 Physical Phenomena of the Flapping Problem

The following discussion details some of the key physics associated with this flapping response and regime transition. We consider the bistable phenomenon observed in prior studies, and examine the dynamical features of the two unsteady flapping regimes and the mechanics of the transition from limit-cycle to chaotic flapping.

6.3.1 Subcritical Bifurcation as a Duffing Oscillator

The experiments of [76], [70], and [54] at $Re \sim 10^4 - 10^5$ all observe subcritical bifurcation, a significant region of bistability where stable straight and unstable flapping modes can both be realized depending on the initial conditions. The phenomenon is also observed in the low Reynolds number numerical simulations of [79]. For FSDS simulations at $Re = 1000$, we observe no significant region of bistability for $K_B = 0.0001$, while we do observe bistability for $K_B = 0.001$. When $\mu = 0.145$ we observe convergence to a sustained limit-cycle flapping state with amplitude of $A = 0.05$ when the simulation is initiated with a tail displacement of $A_0 = 0.25$. However, when the simulation is initiated with a tail displacement of $A_0 = 0.001$, the body maintains this straight configuration, without tendency to the flapping limit-cycle. Plots of the body position through several flapping cycles at $t \sim 40$ are shown in figure 6-11(a) for both the flapping and stable cases.

In considering the restoring effects in our linear analysis of § 6.1.2, we used a simple model for the tension which assumed it to be constant in both space and time. With the flapping action of the limit-cycle, and associated shedding of vortices from the trailing edge, there will be an oscillatory component to the drag on the body, and therefore to the body tension and its restoring effect. The change in the tension profile between the stable-straight and flapping cases can be seen in figure 6-11(b), where a snapshot of the flapping tension at $t = 50.4$ is plotted with the stable straight tension profile and that predicted by Blasius boundary layer theory. The differences between the stable straight and flapping tension profiles indicate a significant difference in the restoring force between the two cases, a phenomenon which will alter the stability.

This oscillation of the restoring force with oscillation of the system is analogous to oscillation of a nonlinear spring. A common model to describe hysteresis in response is the Duffing equation, a forced mass-spring-dashpot system where the spring is nonlinear, written as

$$x_{tt} + bx_t + k(1 - \gamma x^2)x = F\cos(\omega t). \tag{6.27}$$

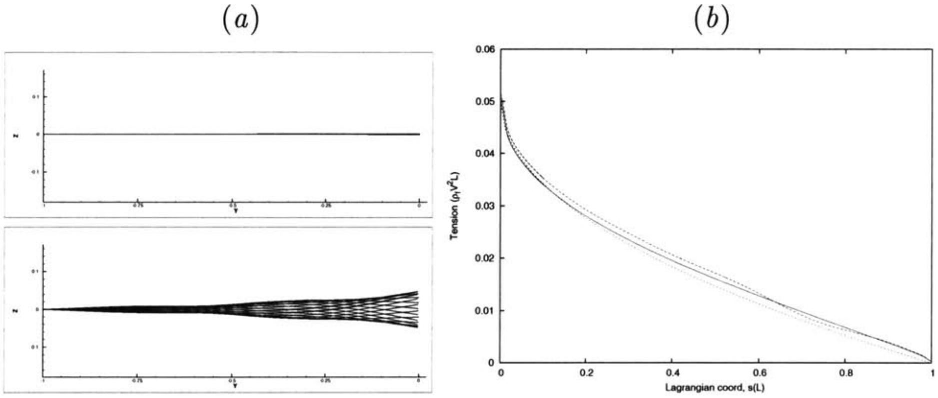

Figure 6-11: Bistable results with $K_B = 0.001$, $Re = 1000$, and $\mu = 0.145$ for the $A_0 = 0.001$ initial condition stable straight case and the $A_0 = 0.25$ initial condition flapping case. (a) Flapping position through several flapping cycles at $t \sim 40$ for the stable straight case (top) and the flapping case (bottom). (b) Tension profile with length coordinate for the converged stable straight case (——) and a snapshot of the flapping case (— —) at $t = 50.4$, along with the Blasius tension prediction (- - -).

For positive γ the spring will be softening, and amplitude hysteresis can be realized for forcing frequencies less than the natural frequency (see for example [17]). The analogous nonlinear restoring term for our flag analysis of § 6.1.2 is

$$-T\left(1-\gamma\left(\frac{\partial^2 z}{\partial y^2}\right)^2\right)\frac{\partial^2 z}{\partial y^2}, \tag{6.28}$$

with a positive value of γ again indicating a softening spring. Defining $\tilde{T}$ as

$$\tilde{T} = T\left(1-\gamma\left(\frac{\partial^2 z}{\partial y^2}\right)^2\right), \tag{6.29}$$

we consider this as a model for the measured value of the tension for the flapping case of $K_B = 0.001$ and $\mu = 0.145$. We plot together in figure 6-12(a) the FSDS time history of measured tension and $(\partial^2 z/\partial y^2)^2$, evaluated at $s = 0.72$, the position which experiences maximum curvature. The opposite phase of the two plots indicates that the tension decreases as the body curvature increases, and γ has a positive value as a softening spring. We find a fit of $\tilde{T}$ to the measured tension at $s = 0.72$ using $T = 0.11$ and $\gamma = 0.32$, as shown in the plot of figure 6-12(b). The flapping flag thus acts in the

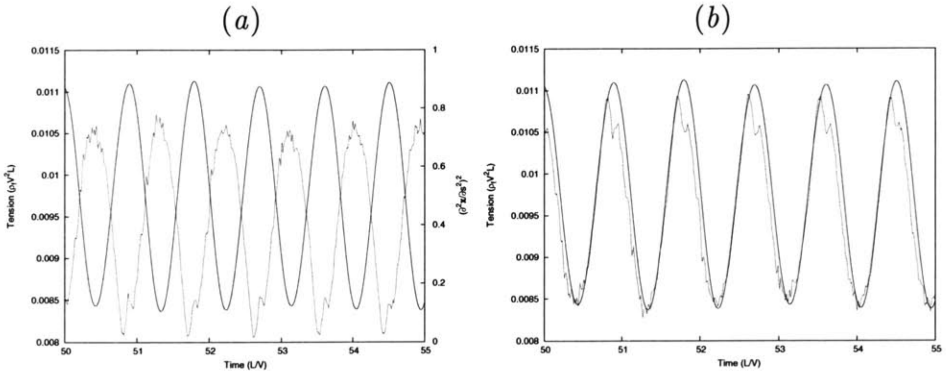

Figure 6-12: Time history of tension and body curvature at $s = 0.72$ for $K_B = 0.001$, $Re = 1000$, and $\mu = 0.145$, for the flapping case of $A_0 = 0.25$. (a) Measured tension (——), plotted with $(\partial^2 z/\partial y^2)^2$ ($\cdots$). (b) Measured tension (——), plotted with $\tilde{T}$ ($\cdots$) of (6.29), using $T = 0.11$ and $\gamma = 0.32$.

same manner as a softening spring in the Duffing equation, explaining the existence of hysteretic behavior. While the higher Reynolds number experiments exhibit a much more significant bistable region than the present work, they also have considerably larger onset response amplitudes. The Duffing model predicts the existence and size of the hysteresis region to be similarly tied to the response amplitude through the magnitude of the external forcing. While the FSDS simulation at $K_B = 0.0001$, which does not display bistability, has an onset flapping amplitude of $A = 0.03$, the FSDS at $K_B = 0.001$, which displays bistability, has an onset flapping amplitude of $A = 0.07$. The high Reynolds numbers experiments, however, which display significant regions of bistability, have onset flapping amplitudes of $A = 0.38$ for [76], $A = 0.35$ for [70], and $A = 0.23$ for [54].

6.3.2 Limit-cycle Flapping and the Energy Budget

The limit-cycle flapping of region (II) is marked by the convergence of the flapping to a single-frequency oscillation which exactly repeats itself. The corresponding phase plot in figure 6-4 traces out a single-loop closed line when the flapping is converged. A sequence of plots for the region (II) case of $\mu = 0.1$, showing the body flapping and contours of vorticity in the fluid, is given in figure 6-13. Response is of a travelling wave of increasing amplitude from leading edge to trailing edge, as was observed in

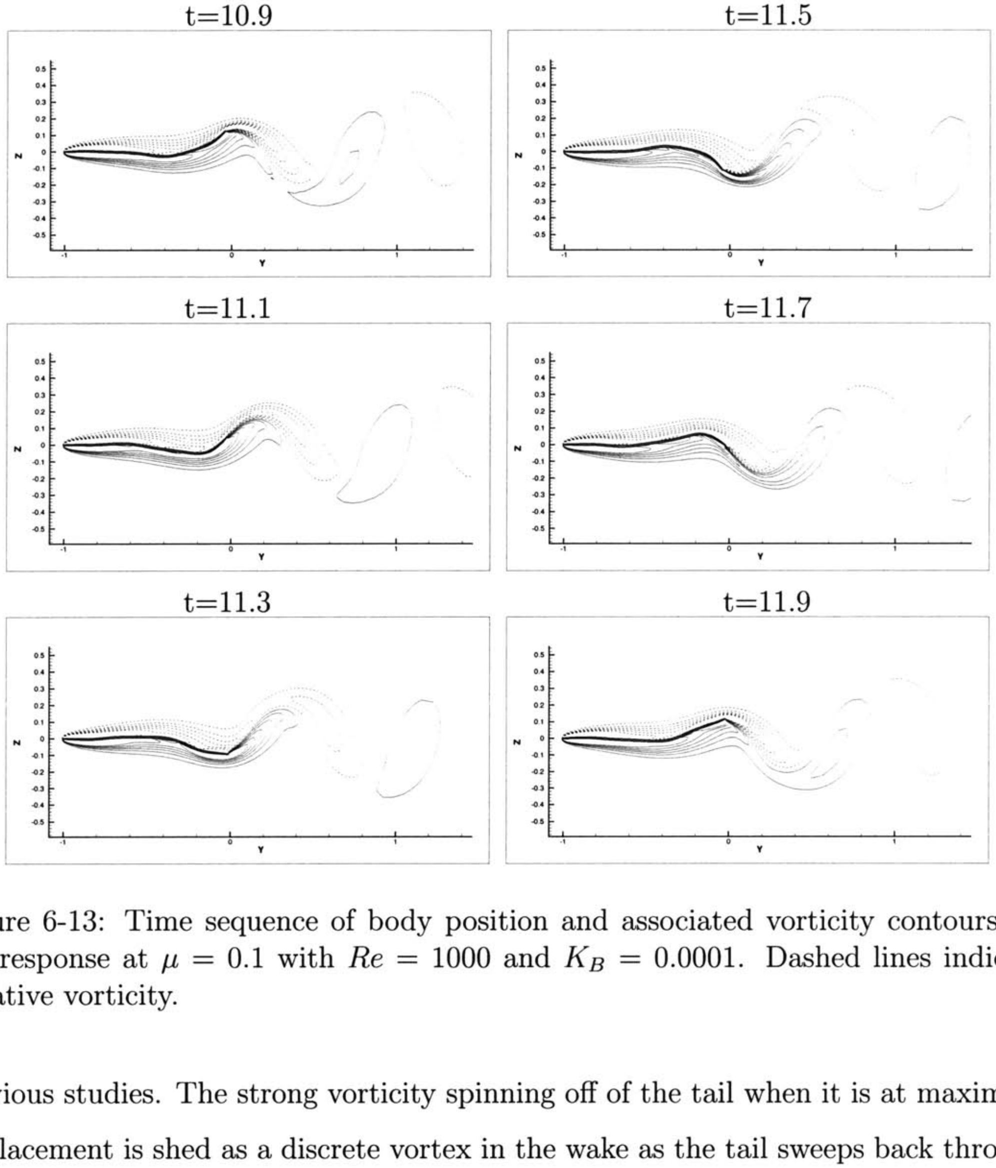

Figure 6-13: Time sequence of body position and associated vorticity contours for the response at $\mu = 0.1$ with $Re = 1000$ and $K_B = 0.0001$. Dashed lines indicate negative vorticity.

previous studies. The strong vorticity spinning off of the tail when it is at maximum displacement is shed as a discrete vortex in the wake as the tail sweeps back through the zero point. This process is repeated in symmetry as the tail passes through maximum displacement in the opposite direction. A von Karman vortex street, consisting of a continuous series of alternately signed vortices, is the resulting wake.

When looking at a limit of very low bending rigidity and very high extensional rigidity, there is limited participation of structural potential energy in the energy budget. Thus, the oscillation consists primarily of an exchange of energy between the total kinetic energy (fluid and structure) and the fluid potential energy in the form of the pressure gradient driving the flow. To examine this, we decompose the kinetic and potential energies to isolate the oscillating components. The oscillating

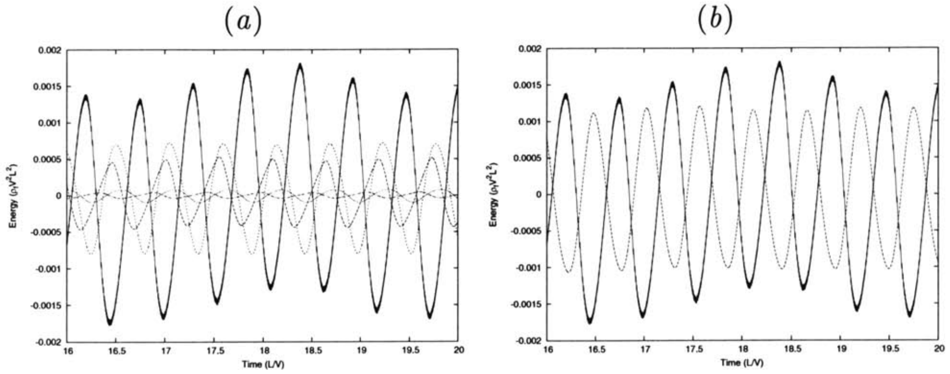

Figure 6-14: Time history of the oscillating part of the energy components for $\mu = 0.1$ with $Re = 1000$ and $K_B = 0.0001$, from $t = 16 \rightarrow 20$. (a) Plot of fluid potential (——), fluid kinetic (— —), structural kinetic (- - -), structural bending potential (· · · · · ·), and structural stretching potential (—·—) energies. (b) Plot of fluid potential (——), and total kinetic (— —) energies.

energy components for the $\mu = 0.1$ case are plotted in figure 6-14(a) from $t = 16 \rightarrow 20$, close to limit-cycle convergence. The plot shows very little participation of the structural potential energy, with the majority of the energy exchange being between the fluid potential energy and the fluid and structural kinetic energy. The sum of the kinetic energies are plotted with the fluid potential energy in figure 6-14(b), showing the near balance in the magnitude of the oscillation. The minimal participation of the structural potential energies is a reflection of the bending and extensional rigidities approaching their infinitesimal and infinite limits, respectively, where the actual values of these parameters do not significantly influence the system evolution.

Variation with Reynolds Number

We now consider how the limit-cycle flapping and associated energy budget change with changing Reynolds number, by comparing the largest limit cycle realized for each Reynolds number for the case of $K_B = 0.0001$. The value of μ and the cross-stream tail displacement amplitude for each case is given in figure 6-15(a), showing the convergence of the largest limit-cycle mass ratio to $\mu \simeq 0.05$ and the convergence of the amplitude to $A \simeq 0.1$, for increasing Reynolds number.

We consider a value for the oscillating energy to be that which is exchanged

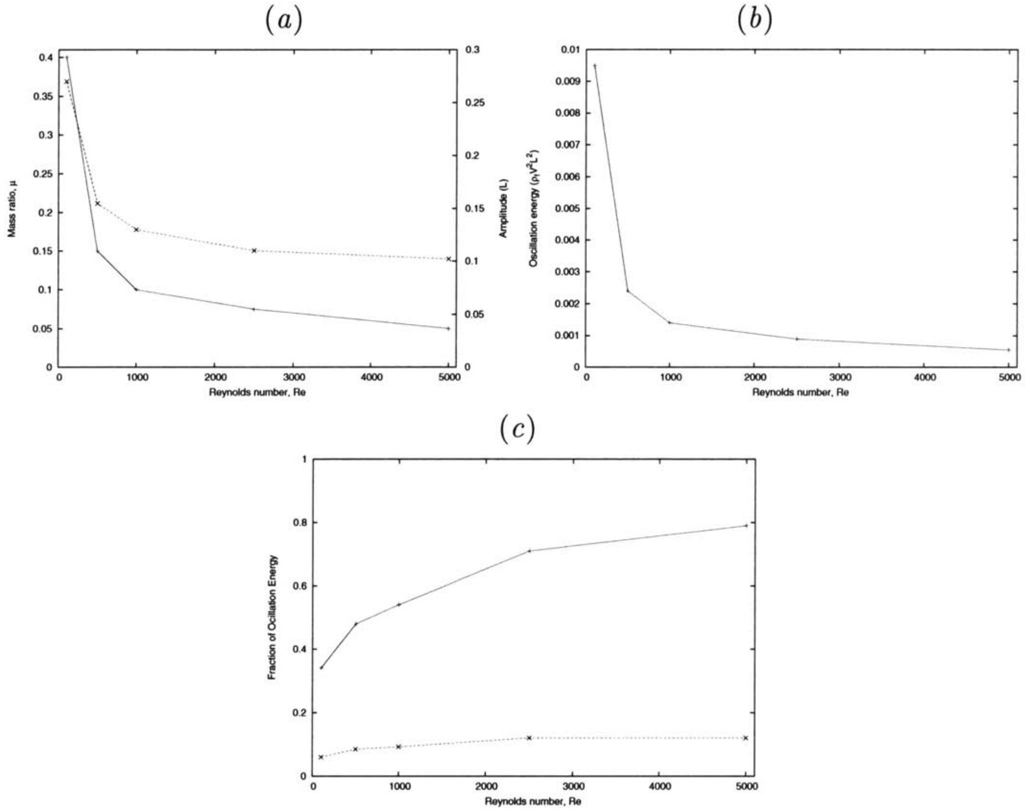

Figure 6-15: Plots for the largest limit cycle realized with $K_B = 0.0001$ for a range of Reynolds number. (*a*) Mass ratio (—+—) and trailing edge amplitude (× — —) with Reynolds number. (*b*) The total oscillation energy (—+—) with Reynolds number. (*c*) The fraction of the total oscillation energy which goes into structural kinetic (—+—) and structural potential (× — —) energy.

through different modes of the system during the limit-cycle oscillation. The total oscillation energy is found by isolating the oscillating part of the energy components, and is plotted for the different Reynolds number cases in figure 6-15(*b*). The oscillation energy is decreasing with Reynolds number, as the oscillation amplitude for the largest limit-cycle is also decreasing. It is now interesting to consider the participation of the structural energy components in the oscillating energy budget. The structural kinetic and structural potential energies are plotted in figure 6-15(*c*) as a fraction of the total oscillating energy. A purely structural oscillation would have a fractional value of 1 for both kinetic and potential energies as the total energy would be alternately transferred between the two modes. For the present fluid-structural case at low bending rigidity, we can see in figure 6-15(*c*) that the structural potential energy has a maximum participation in the energy oscillation of about 10%. This indicates that the potential energy oscillation is primarily in the fluid dynamics in the form of oscillation to the pressure gradient driving the system, as seen in figure 6-14. The structural kinetic energy fraction increases with the Reynolds number, up to 80% of the oscillating energy for $Re = 5000$. This fraction is a measure of the structural mass participation to the total mass (structural and added mass) oscillating in the system. The trend of increasing structural kinetic energy fraction accompanies a decrease in the mass ratio plotted in figure 6-15(*a*), which at first seems contradictory. The explanation for increasing structural kinetic energy fraction despite the decreasing mass ratio is that the added mass is also decreasing. As the discussion of § 6.1.2 predicts an inverse relationship between the added mass and the wavenumber, we look to the mode shapes to determine whether the added mass would also be decreasing with increasing Reynolds number. Figure 6-16 displays the body at maximum tail displacement for the largest limit cycle case through the range of Reynolds numbers. The figure shows an increase in the wavenumber of response with increasing Reynolds number. For the lowest Reynolds number case of $Re = 100$, the body represents 1/4 of a wavelength, while for the highest Reynolds number case of $Re = 5000$, the wavelength is smaller than the body length. We conclude that the increase of the structural kinetic energy fraction with increasing Reynolds number

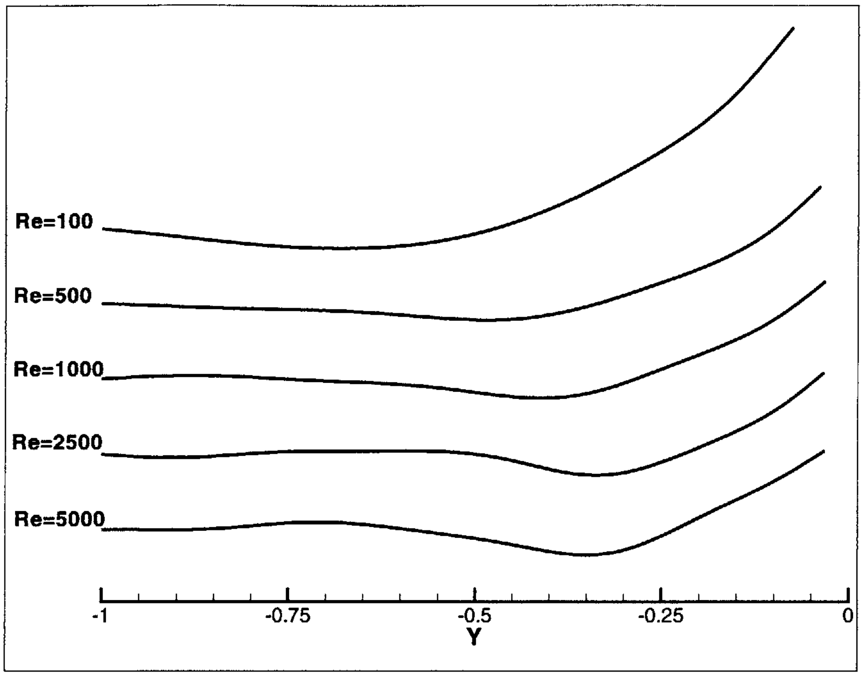

Figure 6-16: Mode shape for the largest limit cycle with $K_B = 0.0001$ for the range of Reynolds numbers. Body displacement is shown for the phase point of maximum trailing edge amplitude.

is due to a reduction in the added mass associated with higher wavenumber modes. For the higher Reynolds number cases, the limit cycle at this low bending rigidity becomes primarily an oscillation of the energy between the structural kinetic energy and the fluid potential energy in the form of an oscillation to the pressure gradient driving the flow.

Influence of Bending Rigidity

The influence of bending rigidity on the limit-cycle flapping is now examined in terms of the flapping characteristics and the associated energy budget. The range of the region (II) limit-cycle flapping is examined by plotting in figure 6-17 the flapping amplitude, frequency, and Strouhal number for the lowest and highest mass ratios within the region for each of the three bending rigidities. A significant trend in the flapping frequency is seen with increasing bending rigidity. While the frequency for a given bending rigidity changes little through the limit-cycle regime, this frequency

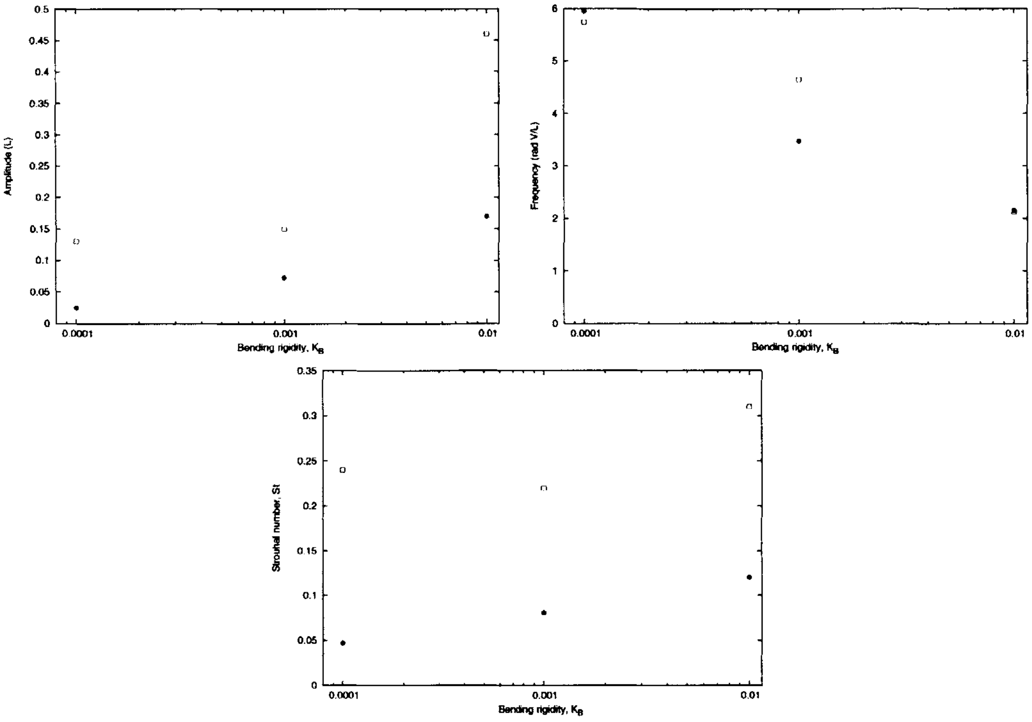

Figure 6-17: Flapping amplitude, frequency, and Strouhal number for the lowest (●) and highest (□) mass ratios in the limit-cycle flapping regime. Results for $Re = 1000$ through a range of bending rigidities representing three different orders of magnitude.

trends lower for the higher bending rigidities. The Strouhal number for transition to chaos remains in the range of $St \sim 0.2 \rightarrow 0.3$, so the flapping amplitude at transition becomes large for the higher bending rigidities. In fact, for the highest bending rigidity of $K_B = 0.01$ the flapping amplitude at transition is very high, nearly $0.5L$ suggesting the disappearance of chaos at high bending rigidities.

Three series of plots showing the body position through a flapping cycle are given in figure 6-18, one series for each bending rigidity representing the highest mass ratio within the limit-cycle regime. All cases reveal a streamwise travelling wave increasing in amplitude from head to tail. While the two lower bending rigidity cases display a wavelength approximately equal to the body length, the high bending rigidity case displays a wavelength of approximately two body lengths. The higher bending rigidity thus results in a limit-cycle being carried to much larger amplitudes, as well as a significantly longer wavelength mode shape.

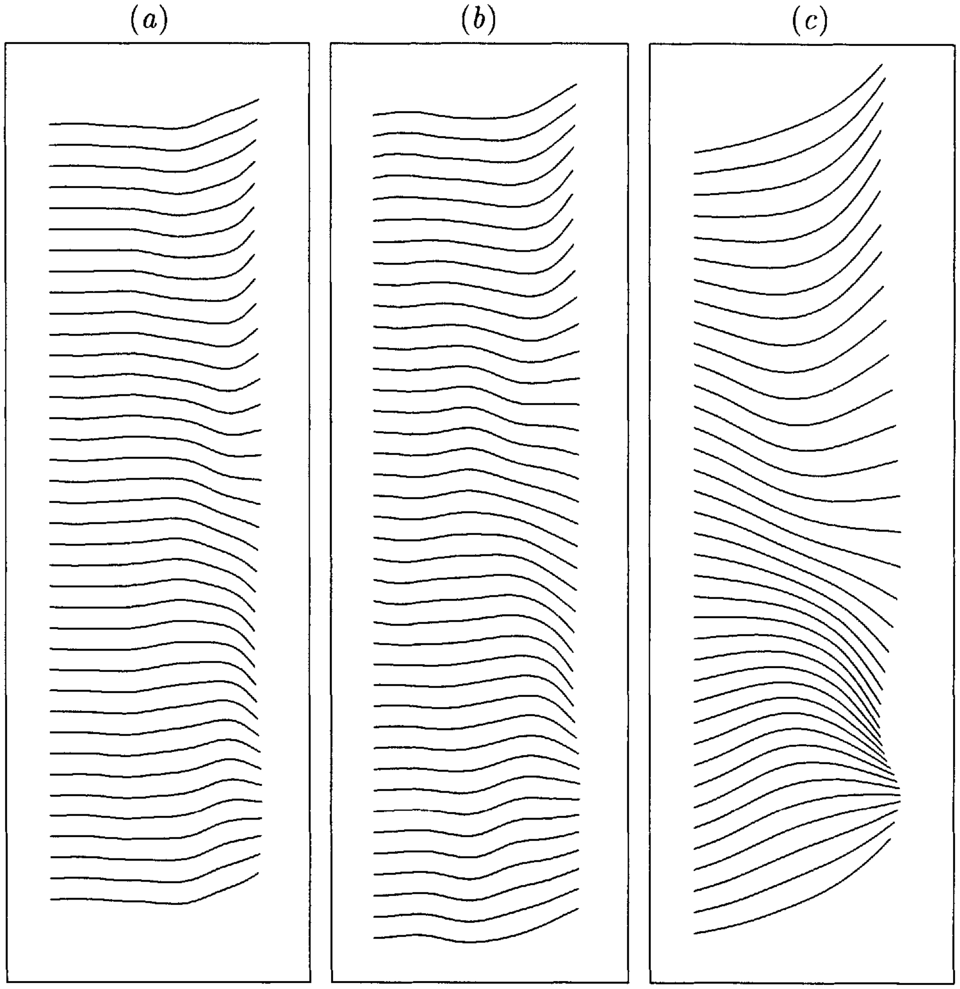

Figure 6-18: Plots showing the body displacement through one complete flapping cycle for the highest mass ratio case within the limit-cycle flapping regime, with time advancing downward. For simulation parameters of (*a*) $K_B = 0.0001$ and $\mu = 0.1$, (*b*) $K_B = 0.001$ and $\mu = 0.25$, and (*c*) $K_B = 0.01$ and $mu = 0.75$.

The trends with bending rigidity relating to the energy oscillation for the largest largest limit-cycle flapping (before transition to chaos) are given in figure 6-19, analogous to those given for Reynolds number in figure 6-15. We can see in figure 6-19(*a*) the convergence of both the value of μ and of the cross-stream tail displacement amplitude as the bending rigidity is reduced. This convergence corresponds to the reduction of the influence of the bending rigidity to the system, as the flow induced tension becomes the dominant restoring effect. A dramatic increase to the oscillation energy in the system seen in figure 6-19(*b*) accompanies the high amplitude response at the highest bending rigidity, indicating a high-energy limit cycle. The fractional participation of the structural kinetic and structural potential energies to the total oscillation energy are given in figure 6-19(*c*). The structural potential energy fraction increases from 9% to 36% as the bending rigidity increases from $K_B = 0.0001$ to $K_B = 0.001$, becoming a more significant influence to the system. However, as the rigidity increases further to $K_B = 0.01$, the structural potential energy fraction drops to 22% due to the dramatic increase in the total oscillation energy. The curve indicates the trend of the significance of the potential energy stored in the structure decreasing for very high and very low rigidity. This follows the idea that for very low (perfectly flexible) and very high (rigid body) bending rigidity, it is the limit value which is the important influence, not the exact value of the bending rigidity. The structural kinetic energy fraction does not change much through the range of bending rigidities, remaining close to 60%, indicating that the proportion between structural mass and added mass is little changed. As the μ for the largest limit cycle increased with bending rigidity, the added mass increases in proportion. The change to the added mass comes from the change in the mode shape with bending rigidity apparent in figure 6-18. As was indicated for the lowest Reynolds numbers, the longer wavelength responses at the higher bending rigidities have a higher associated added mass.

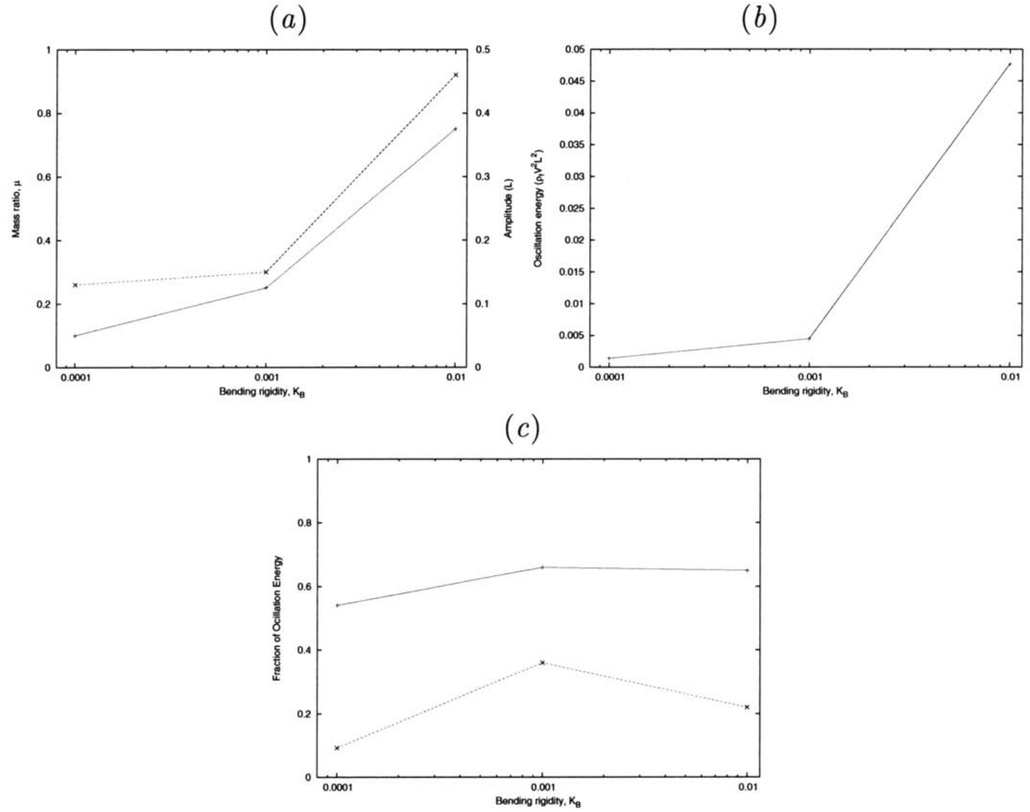

Figure 6-19: Plots for the largest limit cycle realized with $Re = 1000$ for a range of bending rigidities. (*a*) Mass ratio (—+—) and trailing edge amplitude (× — —) with bending rigidity. (*b*) The total oscillation energy (—+—) with bending rigidity. (*c*) The fraction of the total oscillation energy which goes into structural kinetic (—+—) and structural potential (× — —) energy.

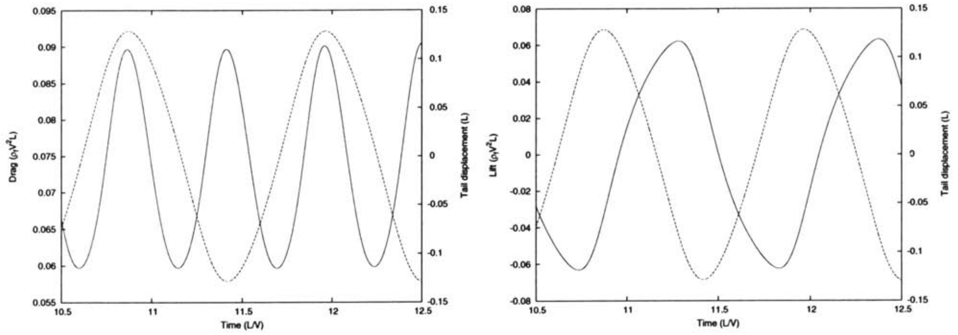

Figure 6-20: Time history of the nondimensional drag and lift forces during limit cycle shedding for $\mu = 0.1$ with $Re = 1000$ and $K_B = 0.0001$. Drag and lift forcing (——) plotted with the tail displacement (— —).

6.3.3 Fluid-dynamic Drag and Lift

The fluid-dynamic forcing to the body varies both with the Reynolds number and with the structural parameters as they influence the flapping mode. We have displayed in figure 6-13 the shedding of body generated vorticity into the wake through the flapping cycle in the limit-cycle regime. Associated with this periodic shedding of vortices into the wake, there is a time varying fluid-dynamic forcing in both the streamwise (drag) and cross-stream (lift) directions. The time history of the drag and lift through this shedding process are plotted with the cross-stream tail displacement in figure 6-20. While the lift fluctuation is at the frequency of the flapping, the drag fluctuation is at twice the frequency, reflecting that the upward flap and downward flap influence the drag identically during symmetric flapping. The drag plot indicates that for this limit cycle the drag is always positive, with the drag minimum being 2/3 the drag maximum. Maximum drag corresponds to the phase of maximum tail displacement, while drag minimum corresponds to the tail zero crossing. Conversely, the lift force is near zero at the point of maximum displacement, and builds to a maximum during the sweep from up to down (or down to up). The lift maxima at $t = 11.3$ and $t = 11.85$ correspond to the phase of vortex separation from the tail, as can be seen in figure 6-13.

We consider the drag and lift of the passively flapping body through the range of parameters considered in our study. Drag and lift coefficients are considered as the force nondimensionalized by $1/2\rho_f V^2 L$, and are given in terms of the mean drag coefficient, $< Cd >$, and the root-mean-square of the drag and lift fluctuations, Cd_{rms} and Cl_{rms}. Plots of the force coefficients with mass ratio for the five Reynolds numbers considered, $Re = 100, 500, 1000, 2500, 5000$, at the lowest bending rigidity of $K_B = 0.0001$ are given in figure 6-21. The trend of $< Cd >$ with mass ratio is similar for the range of Reynolds numbers, but shifted up in terms of both $< Cd >$ and μ for decreasing Re. The trendline shows constant mean drag for the subcritical regime, and a roughly linear increase with mass ratio in the flapping regimes. A fit to this trend is given by

$$< Cd > \simeq Cd_0 + 0.8(\mu - \mu_{crit}), \tag{6.30}$$

where Cd_0 is the subcritical drag coefficient and μ_{crit} is the transition mass ratio. While the plot of figure 6-21 shows that the mean drag, $< Cd >$, at a given mass ratio is always smaller for larger Reynolds numbers, the fluctuating components, Cd_{rms} and Cl_{rms}, are shown to be larger for larger Reynolds numbers. This follows from the skin friction drag being larger for lower Reynolds numbers, while the onset of flapping and associated fluctuating forcing occurs at lower mass ratios for higher Reynolds numbers. The increase in the fluctuating drag, Cd_{rms}, is superlinear with mass ratio, and a fit is given by

$$Cd_{rms} \simeq 1.5(\mu - \mu_{crit})^{1.5}. \tag{6.31}$$

The increase in the fluctuating lift is roughly linear, and a fit to the trend is

$$Cl_{rms} \simeq 1.5(\mu - \mu_{crit}). \tag{6.32}$$

Contour plots for $< Cd >$, Cd_{rms} and Cl_{rms} in the $Re - \mu$ plane are constructed from this same data, and given in figure 6-22. These again display the trends of decreasing $< Cd >$, and increasing Cd_{rms} and Cl_{rms} with increasing Reynolds number, and the increasing of all three forcing coefficients with increasing mass ratio.

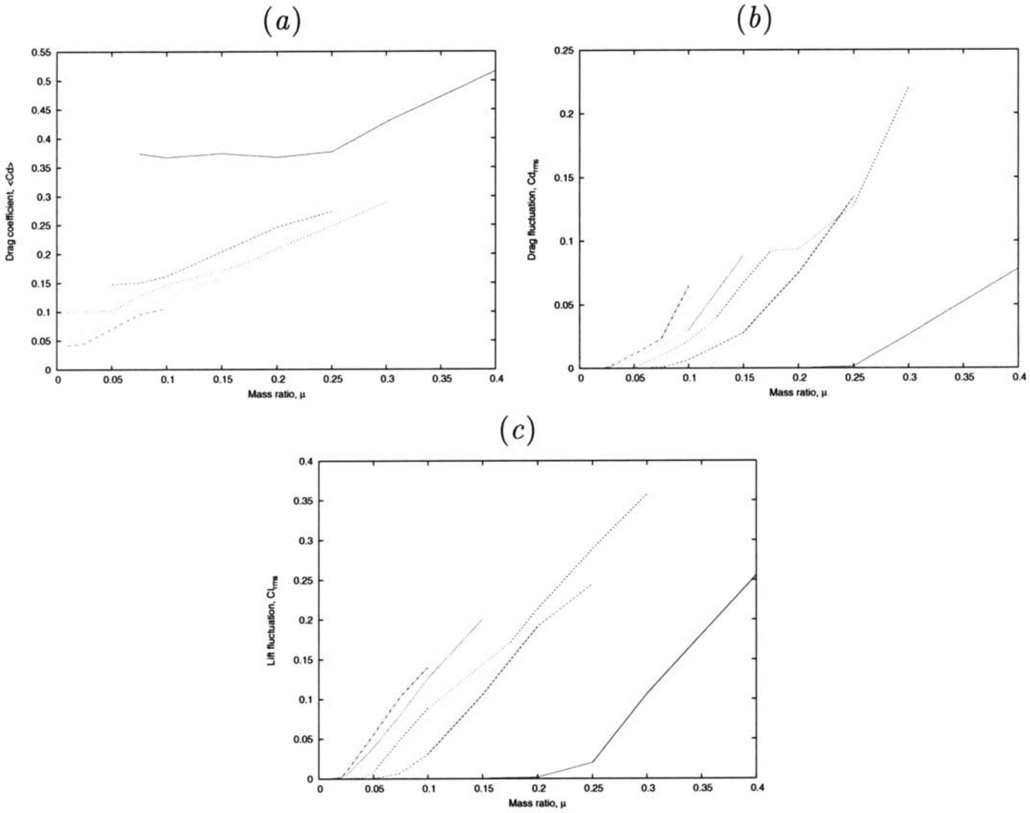

Figure 6-21: (*a*) Mean drag coefficient, (*b*) fluctuating drag coefficient, and (*c*) fluctuating lift coefficient, for the range of mass ratios with $K_B = 0.0001$, at $Re = 100$ (——), $Re = 500$ (— —), $Re = 1000$ (- - -), $Re = 2500$ (···), and $Re = 5000$ (—·—).

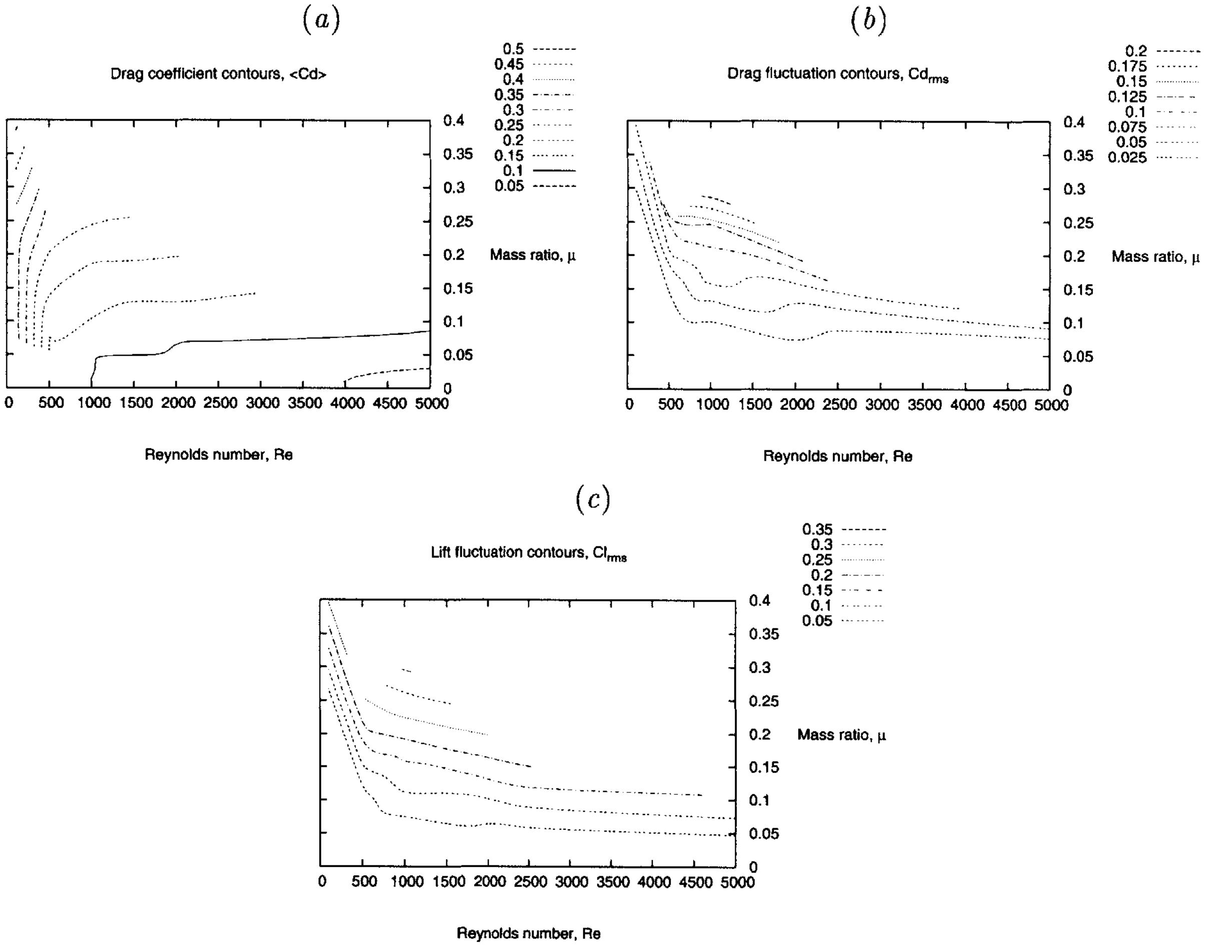

Figure 6-22: Contours of the (a) mean drag coefficient, (b) fluctuating drag coefficient, and (c) fluctuating lift coefficient, in $Re - \mu$ space with $K_B = 0.0001$,

The trend of the forcing coefficients with mass ratio through the range of bending rigidities are given in figure 6-23 for the fixed Reynolds number $Re = 1000$. The plots indicate that $< Cd >$, Cd_{rms} and Cl_{rms} show similar trends as the bending rigidity is increased, and that all three coefficients are lower for higher bending rigidities at a fixed mass ratio. The expressions of equations 6.30-6.32, continue to offer a crude prediction to the forcing coefficients, though prediction errors as great as 50% exist for the fluctuating components at the highest bending rigidity. The contour plots of the coefficients in $K_B - \mu$ space given in figure 6-24 provide a visual for their variation in terms of these two control parameters.

Trends in the drag and lift coefficients in the parametric region considered in this study are predicted by equations 6.30, 6.31, and 6.32. The μ_{crit} used in these expressions can be taken as the prediction of equation 6.25, and the subcritical drag coefficient from the Blasius prediction as $Cd_0 = 2.7Re^{-1/2}$. Substituting these expressions, we have predictions in the flapping regimes for the three forcing coefficients in terms of the relevant system parameters as

$$\begin{aligned} < Cd > &\simeq 2.7Re^{-1/2} + 0.8(\mu - 1.3Re^{-1/2} - K_B 4\pi^2) && (6.33) \\ Cd_{rms} &\simeq 1.5(\mu - 1.3Re^{-1/2} - K_B 4\pi^2)^{1.5} && (6.34) \\ Cl_{rms} &\simeq 1.5(\mu - 1.3Re^{-1/2} - K_B 4\pi^2), && (6.35) \end{aligned}$$

while $< Cd >= 2.7Re^{-1/2}$ and $Cd_{rms} = Cl_{rms} = 0$ in the non-flapping regime.

6.3.4 Transition to Chaos and the Vortex Wake

Examining figure 6-4 reveals that the period-one limit cycle is broken up as mass ratio goes to $\mu = 0.125$ and higher. We see from figure 6-5 that this corresponds to a Strouhal number of $St = 0.23$. Consider that the natural frequency of the fluid dynamics is defined by a universal Strouhal number, as discussed by Sarpkaya in [52], $St = 2Af/V \simeq 0.2$. This being the case, we are observing a change in the dynamics of the system as the flapping frequency enters the neighborhood of the natural wake frequency. Changes in the behavior of nonlinear systems near resonance is a common

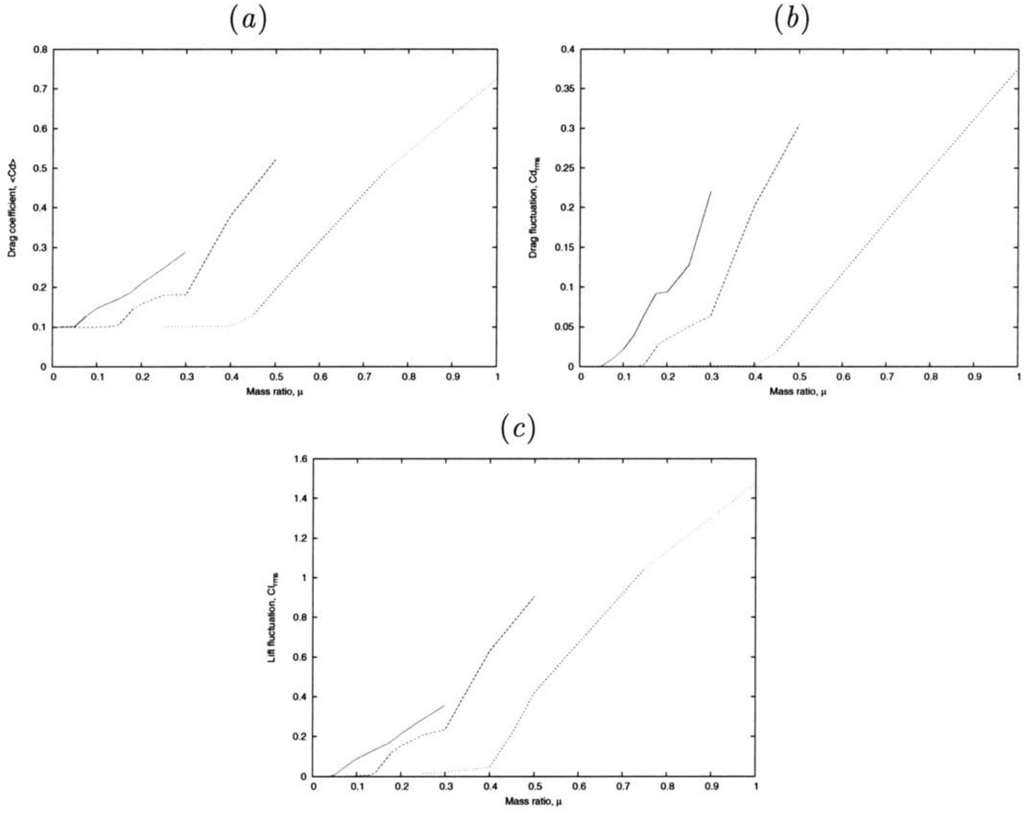

Figure 6-23: (a) Mean drag coefficient, (b) fluctuating drag coefficient, and (c) fluctuating lift coefficient, for the range of mass ratios with $Re = 1000$, at $K_B = 0.0001$ (——), $K_B = 0.001$ (— —), and $K_B = 0.01$ (- - -).

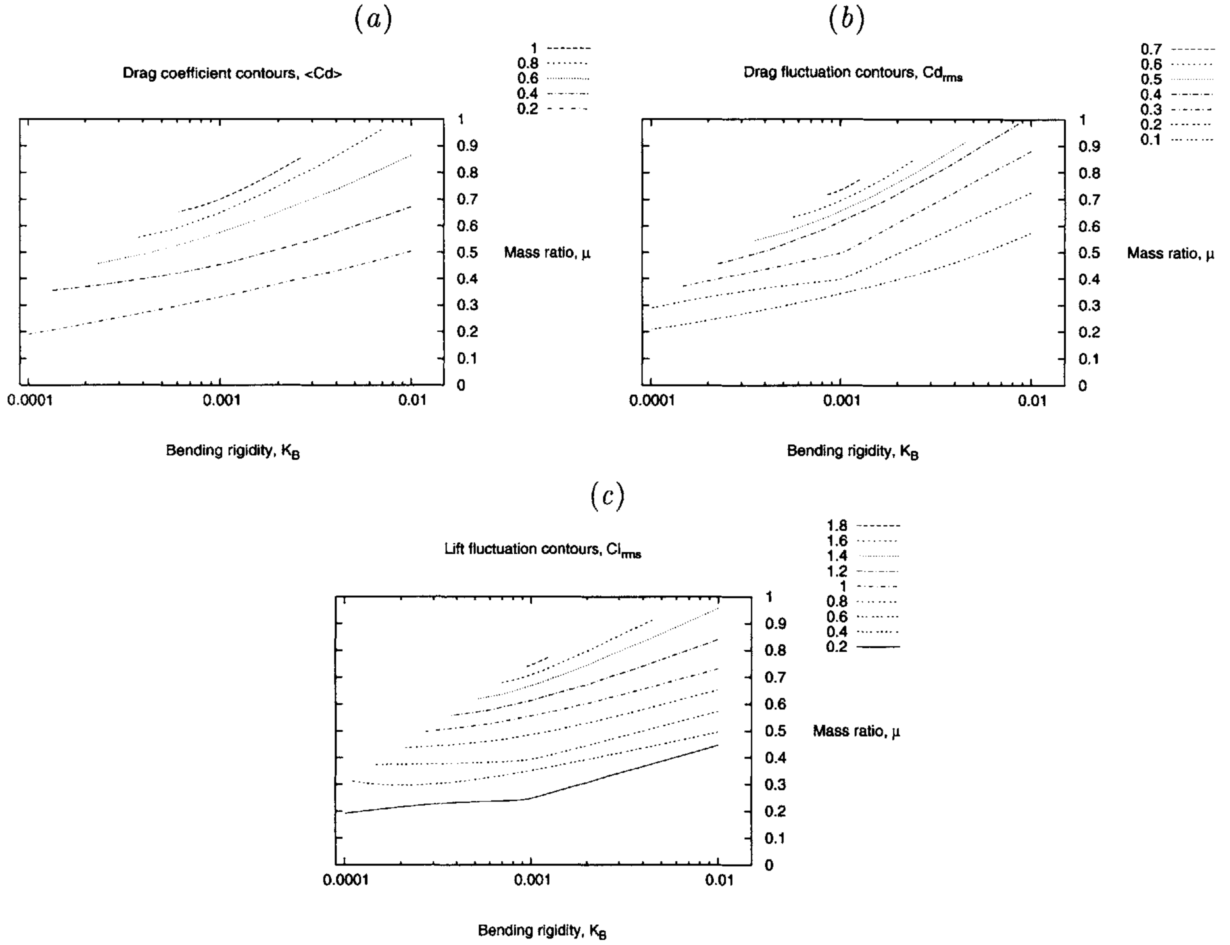

Figure 6-24: Contours of the (a) mean drag coefficient, (b) fluctuating drag coefficient, and (c) fluctuating lift coefficient, in $K_B - \mu$ space with $Re = 1000$,

phenomenon (see for example [45]). The particular case of vortex induced vibration of flexible cylinders reveals distinctly nonlinear behavior as the structural natural frequency approaches the wake frequency ([52], [71]).

As described in the review of Procaccia [48], many nonlinear systems share behavior in the transition from a period-one limit cycle to chaos. One of these behaviors is successive period doubling, as shown in [45]. Such period doubling would be expected to show up as a signal at 1/2 of the dominant limit-cycle frequency. What we observe, however, at $\mu = 0.125$ and $\mu = 0.15$ is the appearance of a second significant frequency component with a value of 3/2 that of the dominant frequency. The signal is period-two periodic but without a significant component at the period-two frequency (as $sin((2\pi/T)t) + sin((3\pi/T)t)$ is periodic in $2T$). As soon as the limit cycle is broken, for $\mu > 0.1$, the largest Lyapunov exponent takes on a positive value. This indicates a direct transition from a period-one limit cycle to a chaotic system, or a very narrow transition region.

Calling the dominant limit-cycle frequency ω_L, the appearance of the second frequency component at $3\omega_L/2$ suggests a nonlinear combination of the dominant frequency with the period-doubled frequency of $\omega_L/2$. A constraint on the realization of the $\omega_L/2$ subharmonic could be effecting an immediate transfer of that energy to the $3\omega_L/2$ component. It has been well established that there exist specific wake modes which represent stable patterns of vortex distribution into the wake. These are covered in detail by Williamson & Roshko [72]. The specific case of the $\omega_L/2$ subharmonic mode is addressed, and it is argued that lack of symmetry would preclude its being a natural mode.

With all of the cases for $\mu > 0.1$, with the $3\omega_L/2$ superharmonic, being Lyapunov unstable, the system tends to this chaotic attractor. We now consider the vortex wake associated with this mode. The case for $\mu = 0.15$, with the strong superharmonic, is examined between the period-two cycle of $t = 4.9 \rightarrow 7.3$. The three peaks through the two-cycle can be seen in the $\mu = 0.15$ time series plot, along with a triple-loop in the corresponding phase plot of figure 6-4. Figure 6-25 gives a sequence of plots showing the body flapping and vorticity contours. While the vortex pattern is not symmetric, it is notable that the hesitation, or small tail wiggle, at $t = 6.5$ creates a dead zone in the vortex wake. The result is a separation between vortex clusters in the wake, a phenomenon that can be seen in the expanded view of the final frame in figure 6-25. Flapping with the dominant frequency and $\omega_L/2$ subharmonic would have more even distribution of the vortices in an asymmetric wake, and the system avoids such a mode.

The differences between the wakes with the $3\omega_L/2$ harmonic vs. the $\omega_L/2$ harmonic were examined by forcing the body to oscillate (as a straight rigid foil) in these two modes. The signals used were $Asin(\omega t) + 0.5Asin(1.5\omega t)$ and $Asin(\omega t) + 0.5Asin(0.5\omega t)$. The time history of the tail displacement and the vortex wake at the end of the simulation, at $t = 10$, are given in figure 6-26. The plot of the 3/2 superharmonic mode shows vortex clustering in the wake. A series of three strong vortices (positive-negative-positive) is shed in a diagonal formation, separated by a region of weaker negative vorticity. The 1/2 subharmonic mode, on the other hand, shows evenly spaced alternating vortices with three shed in the upper part of the wake followed by one shed in the lower part of the wake. While the construction of these forced 3/2 superharmonic and 1/2 subharmonic modes was somewhat arbitrary, they do display the anticipated differences. The indication is that wake clustering is the preferred mode to the asymmetric evenly spaced pattern, and thus the period-doubled energy of the flapping flag feeds into the 3/2 superharmonic.

6.3.5 Snapping and Recovery

Increasing the mass ratio to values of $\mu = 0.175$ and above results in broadband response, as is seen in the power spectrum plots of figure 6-4. Associated with this are further increases in the Lyapunov exponent, and a noticeably less regular time series and phase plot. The larger mass ratio time series indicate intermittent large and violent (indicated by the rapid change in direction) snapping events interspersed with smaller oscillations. This behavior is the same as observed in typical chaotic flapping often encountered in our everyday lives.

For the purpose of this study, we define a snapping event as a spike in the magni-

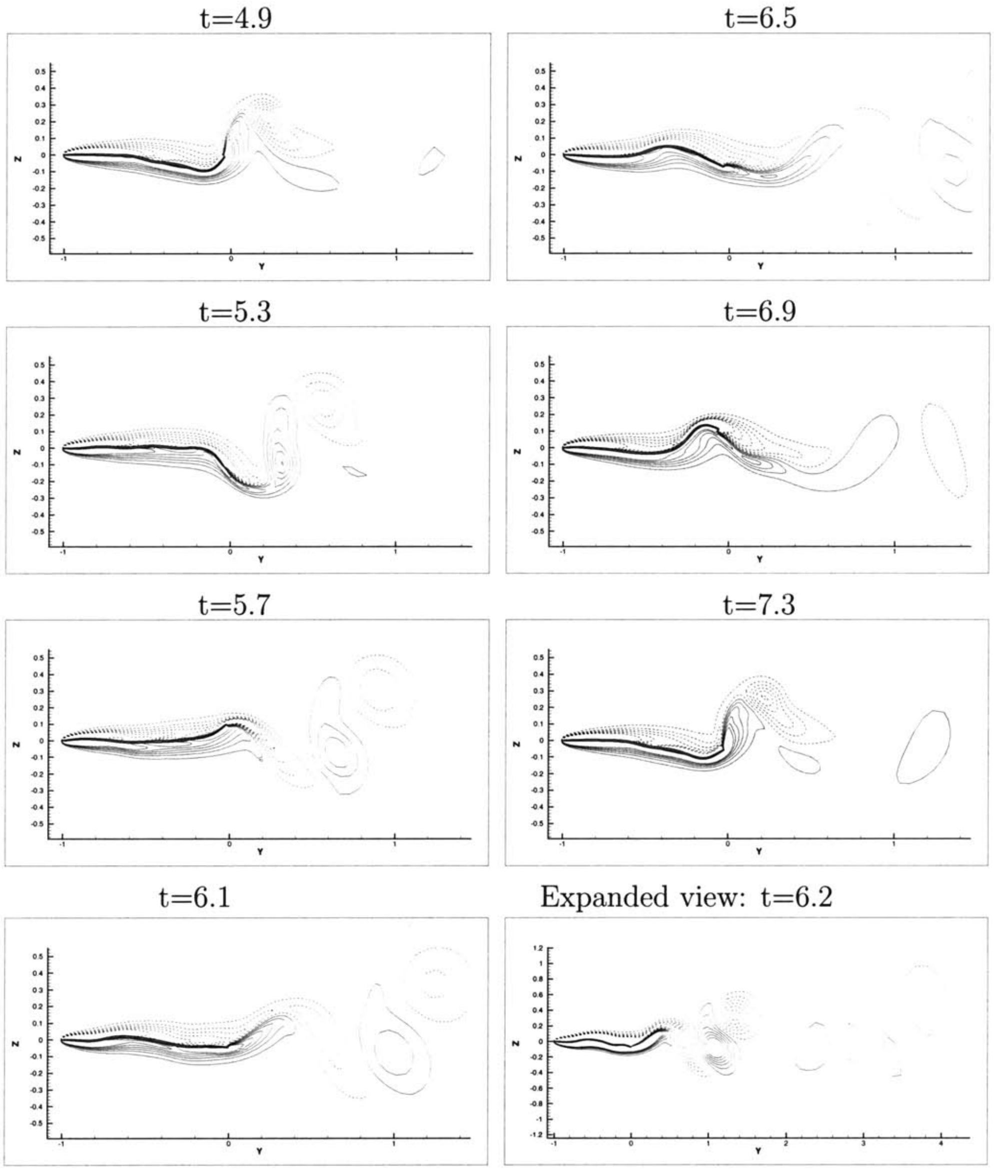
t=4.9

t=6.5

t=5.3

t=6.9

t=5.7

t=7.3

t=6.1

Expanded view: t=6.2

Figure 6-25: Time sequence of body position and associated vorticity contours for the response at $\mu = 0.15$ with $Re = 1000$ and $K_B = 0.0001$. Dashed lines indicate negative vorticity. The final frame is an expanded view using higher resolution vorticity contours.

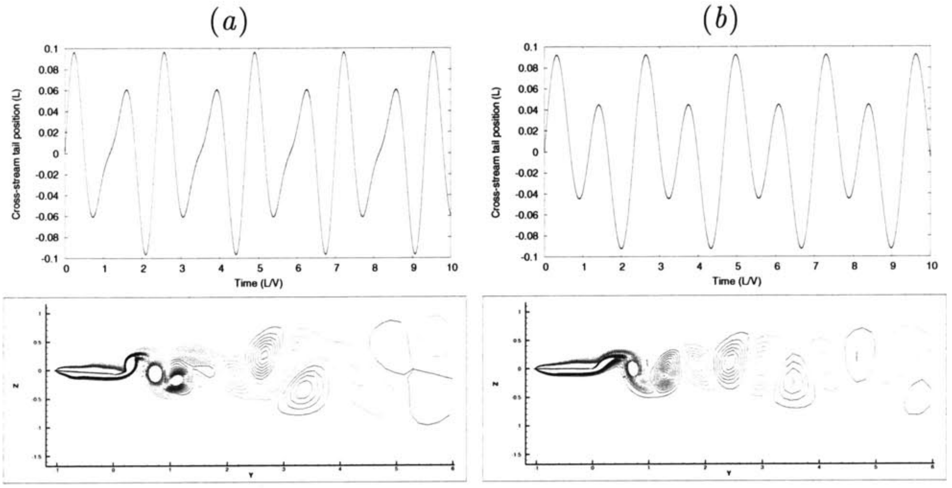

Figure 6-26: Upper plots are the time history of cross-stream tail displacement for the rigid foil forced in (a) the 3/2 superharmonic mode $Asin(\omega t) + 0.5Asin(1.5\omega t)$ and (b) the 1/2 subharmonic mode $Asin(\omega t) + 0.5Asin(0.5\omega t)$. Lower plots are the corresponding vortex wake at $t = 10$, with dashed lines representing negative vorticity.

Mass ratio, μ	Snapping events
0.1	0
0.125	0
0.15	0
0.175	1
0.2	2
0.25	4
0.3	6

Table 6.1: Number of snapping events for each mass ratio from $t = 0 \to 20$, for $Re = 1000$ and $K_B = 0.0001$.

tude of the trailing edge acceleration which exceeds $30V^2/L$. The idea of 'snapping' connotates a rapid acceleration, and this criteria does well to select events with the characterization discussed below. By this definition, the limit-cycle regime does not include snapping events, and the number of snapping events in a simulation of 20 convective time units is given in table 6.1 for the mass ratios $\mu = 0.1 \to 0.3$, with $Re = 1000$ and $K_B = 0.0001$. The data indicate that snapping ceases to happen up through $\mu = 0.15$, and that the frequency of the events then increases with increasing mass ratio.

We examine in detail the snapping event at $t \simeq 18$ for the case of $\mu = 0.3$. A plot

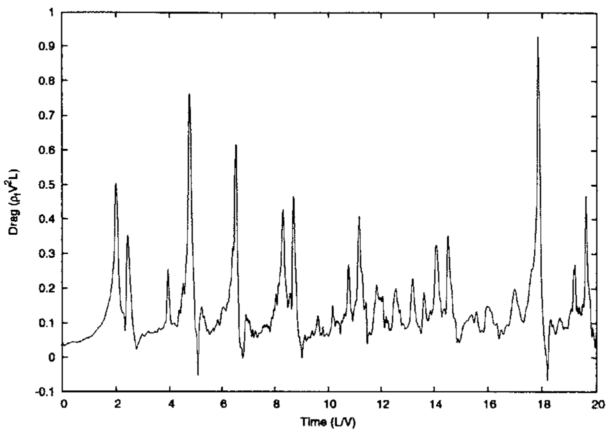

Figure 6-27: Time history of the drag for $\mu = 0.3$ with $Re = 1000$ and $K_B = 0.0001$, as measured by the total fluid dynamic forcing on the body in the streamwise direction.

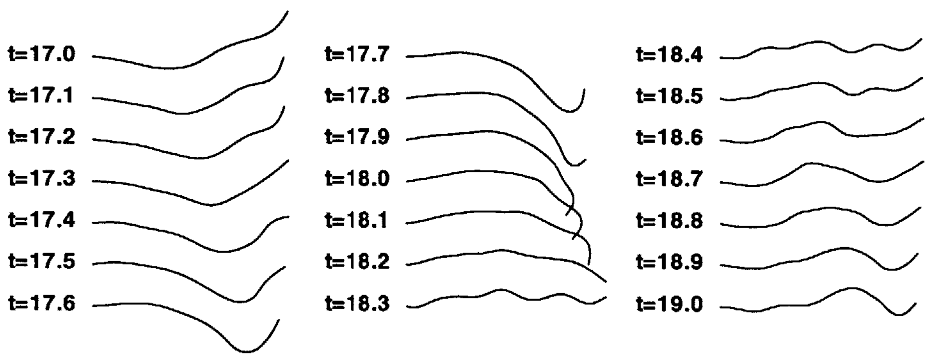

Figure 6-28: Time sequence of body position for $\mu = 0.3$ with $Re = 1000$ and $K_B = 0.0001$.

of the time history of the drag for this case is given in figure 6-27, showing a near impulsive increase in drag at $t = 17.85$, followed by a rapid decrease to negative drag values, with a minimum at $t = 18.2$. A series of plots showing the body configuration from $t = 17 \rightarrow 19$ are given in figure 6-28. These plots show a large wave travelling down the body, creating a hook in the tail at $t = 17.7$. This hook then snaps at $t = 17.85$, corresponding to the spike in drag force. We observe recoil behaviour beginning at $t = 18.2$, when the drag becomes negative. This is characterized by a dynamic buckling of the body, indicated by the spontaneous appearance of a high wavenumber mode shape which is essentially stationary for a short period of time, before rolling out to the tail as a travelling wave beginning at $t = 18.5$.

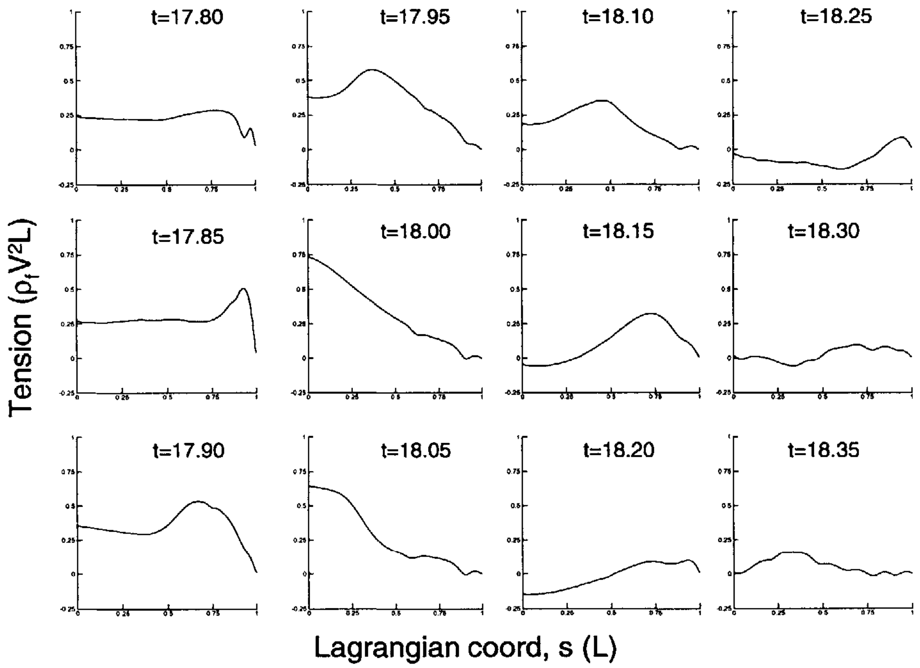

Figure 6-29: Time sequence of body tension as a function of the Lagrangian length coordinate, with $s = 0$ as the leading edge and $s = 1$ as the trailing edge, for $\mu = 0.3$ with $Re = 1000$ and $K_B = 0.0001$.

To further understand the snapping dynamics, we look at the cable tension along the length through the snapping event. A series of plots of the tension with the Lagrangian length coordinate are given in figure 6-29. A high tension impulse appears near the tail at the time of snapping, $t = 17.85$, and pushes toward the leading edge as the body arrests itself, with maximum tension at the leading edge experienced at $t = 18.0$. After this time the body begins to recoil, and the tension at the leading edge drops rapidly, becoming negative at $t = 18.15$ and remaining so until $t = 18.3$. It is during this period where the dynamic buckling is observed. These rapid changes in the tension, loss of positive tension and associated high mode buckling are characteristic of the cable snapping problem, as described by Zhu *et al.* in [81].

The vortex wake associated with the snapping event is displayed in the vorticity plots of figure 6-30 at $t = 18.0$ and $t = 18.5$. A very strong positive vortex is generated during the snapping event, and this is pinched off at $t = 18.0$ as seen in figure 6-30(a). As the tail sweeps back up to the centerline and pauses, a strong

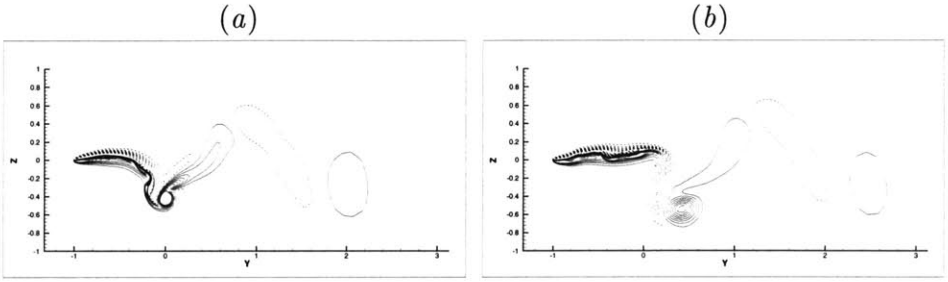

Figure 6-30: Vorticity contours in the wake at (a) $t = 18.0$ and (b) $t = 18.5$ for $\mu = 0.3$ with $Re = 1000$ and $K_B = 0.0001$. Dashed lines indicate negative vorticity.

Figure 6-31: Depiction of sample points for frequency analysis of the flapping body. Point A is the trailing edge of the body, whose cross-stream displacement is used for analysis, while point B is at the centerline of the wake, two body lengths downstream of the trailing edge equilibrium position, where the cross-stream flow velocity is used for analysis.

negative vortex is formed and released into the wake. As can be seen in figure 6-30(b) this vortex pair is displaced well below the centerline of the wake, and it continues to migrate downward as a vortex dipole. We thus see that these violent snapping events in the chaotic regime have associated rapid variation in the fluid dynamic forcing and internal tension, as well as distribution of high strength vortices away from the wake centerline.

6.3.6 Wake Frequency and Vortex Patterns

Frequency analysis of the flapping system was given in § 6.2 in terms of the cross-stream tail displacement. For the same case of $Re = 1000$ and $K_B = 0.0001$, we now consider the frequency of the variations in the wake by looking at the cross-stream velocity at a fixed point in the wake centerline two body lengths downstream from the trailing edge equilibrium position. Figure 6-31 depicts the location of the wake frequency point and that taken at the trailing edge of the body.

A series plots of the frequency spectrum are given in figure 6-32, for the flapping range of mass ratios. The plots display the power spectrum for the cross-stream flow velocity in the wake, overlaying the power spectrum of the cross-stream trailing edge displacement, each normalized by its peak power for comparison of the spectra. For the limit-cycle response at $\mu = 0.05 \rightarrow 0.1$, there is little difference between the tail displacement spectrum and the wake velocity spectrum. The width of the peaks are equivalent in this range, and the small superharmonic secondary peak at $\mu = 0.05$, associated with non-sinusoidal oscillation, is clear for both spectra. Slight differences between the tail and wake spectra are observed for the higher mass ratios in the chaotic regime. At the onset of chaos, at $\mu = 0.125$ and $\mu = 0.15$, a more significant signal is seen at the period-doubled frequency (the 1/2 subharmonic) in the wake spectrum than in the tail spectrum. The 3/2 superharmonic still remains the dominant secondary peak for these cases, however, a phenomenon discussed in § 6.3.4. The plots of the spectra for the broadband chaotic response at $\mu = 0.175 \rightarrow 0.3$, show that while the dominant frequency remains the same for the wake spectra as the tail spectra, and the broadband character remains, the magnitude of the subsidiary peaks in the wake spectra does not match that of the tail spectra. In particular, the spectra of $\mu = 0.2$ indicates a secondary peak as a subharmonic for the tail spectrum and a secondary peak as a superharmonic for the wake spectrum. These differences reflect the nonlinear nature of the energy transport in the system, with the frequency content evolving as the energy moves through the system.

The vortex wake of the range of mass ratios for this case of $Re = 1000$ and $K_B = 0.0001$ is plotted in terms of vorticity contours in figure 6-33. It can be seen from the plots that the wake observation point B is positioned sufficiently downstream that the vortices are fully developed, but near enough that the vortices are still strong. The change from the regular vortex pattern of a von Karman vortex street to the irregular pattern associated with chaotic flapping can be seen as the mass ratio increases. As the Strouhal number increases with mass ratio in the limit cycle regime, the vortices in the von Karman street become larger, but without a proportional increase in their spacing. While the vortices in the street at $\mu = 0.05$ are extended in the

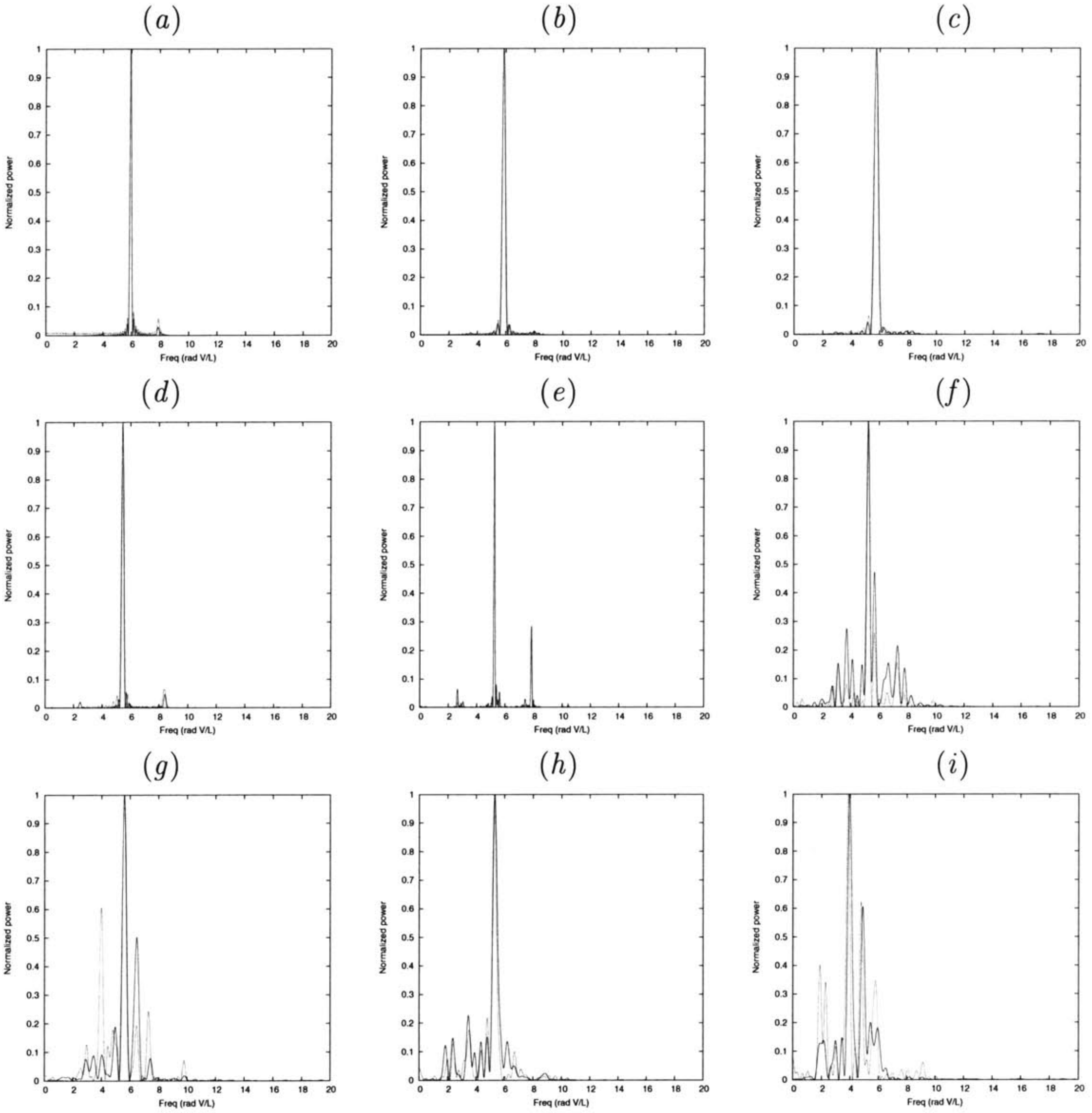

Figure 6-32: Normalized frequency power spectrum for the cross-stream velocity (— —) at the wake centerline $2L$ downstream from the equilibrium tail position, and the cross-stream tail displacement ($\cdots$). Runs at Re = 1000, K_B = 0.0001 and (a) $\mu = 0.05$, (b) $\mu = 0.075$, (c) $\mu = 0.1$,(d) $\mu = 0.125$, (e) $\mu = 0.15$, (f) $\mu = 0.175$m, (g) $\mu = 0.2$, (h) $\mu = 0.25$, and (i) $\mu = 0.3$.

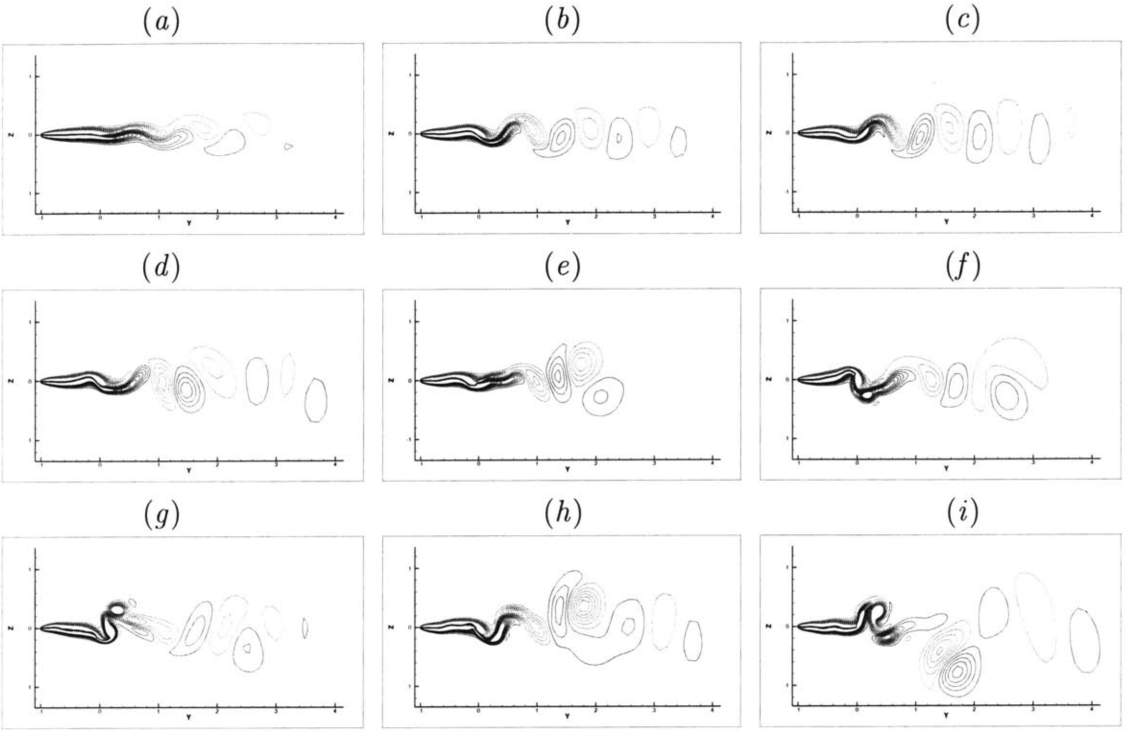

Figure 6-33: Vorticity contours in the flapping wake for the fully developed flow at $Re = 1000$, $K_B = 0.0001$ and (a) $\mu = 0.05$, (b) $\mu = 0.075$, (c) $\mu = 0.1$,(d) $\mu = 0.125$, (e) $\mu = 0.15$, (f) $\mu = 0.175$m, (g) $\mu = 0.2$, (h) $\mu = 0.25$, and (i) $\mu = 0.3$. All plots are to the same scale, with dashed contours indicating negative vorticity.

streamwise direction, those in the street at $\mu = 0.1$ are extended in the cross-stream direction. This pattern of regularly distributed larger, stronger vortices extended in the cross-stream direction eventually breaks down at $\mu = 0.125$, and an irregular vortex pattern develops. The breakdown in the regular vortex wake is accompanied by the appearance of alternate frequency components, as seen in figure 6-32. Eventual broadband response has associated widening of the disorganized wake, with some vortices being distributed far from the wake centerline, as discussed in § 6.3.5.

6.4 Summary of the Two-dimensional Flapping Problem

We examine the problem of a thin flexible foil in uniform flow, and find it controlled by the nondimensional parameters of Reynolds number $Re = VL/\nu$, mass ratio $\mu = \rho_s h/(\rho_f L)$, and bending rigidity $K_B = EI/(\rho_f V^2 L^3)$. Linear analysis indicates the influence of the relevant nondimensional parameters, the destabilizing effect of higher mass ratio and Reynolds number, and the stabilizing effect of higher bending rigidity. The predictions of this stability analysis are confirmed through the results of the numerical simulation, and we suggest equation 6.25 as a good prediction of the critical mass ratio, above which flapping will be realized. The region of bistability found in previous experimental studies at higher Reynolds numbers is not as prevalent in the present FSDS study at $Re = 1000$. The existence of hysteresis is shown to be analogous to that of the Duffing softening spring model, with the larger onset flapping amplitudes for the higher Reynolds number experiments explaining the more pronounced region of bistability.

A systematic series of runs is performed for varying mass ratios at the low bending rigidity of $K_B = 10^{-4}$ for $Re = 1000$. The results reveal three distinct regimes of response, defined by (I) fixed-point stability, (II) limit-cycle flapping, and (III) chaotic flapping. When the mass ratio is increased above the critical value for the stable fixed point a travelling-wave flapping limit cycle is observed. This period-one limit cycle increases in amplitude with mass ratio, while maintaining roughly the same frequency, until the Strouhal number of the system reaches the value of the natural wake frequency. This nonlinear resonance condition at $\mu > 0.1$ results in a direct transition from a period-one limit cycle to chaos, and select runs at alternate Reynolds numbers suggest a transition mass ratio given by equation 6.26. The breaking up of the limit cycle shows as the appearance of a 3/2 superharmonic to the limit-cycle frequency. Where the period-doubled 1/2 subharmonic does not represent a natural wake frequency, the energy is transferred to this 3/2 component and the resulting system is chaotic. The chaos is measured by a positive value of the largest

Lyapunov exponent, which increases further with increasing mass ratio. Eventual broadband response is characterized by irregular flapping motion with intermittent violent snapping events, including large rapid changes in tension, dynamic buckling, and shedding of strong vortices away from the wake centerline. Examination of the forcing through the flapping regime indicates that the mean drag force decreases with increasing Reynolds number, while the fluctuation components of the drag and lift both increase with Reynolds number. All three forcing components are found to decrease with increasing bending rigidity, and a prediction of the forcing components in terms of the relevant parameters is given by equations 6.33-6.35.

Chapter 7

The Three-Dimensional Passive Flapping Foil

The case of a three-dimensional passive thin foil is now considered, examining the three-dimensionality of the flapping instability and the associated three-dimensional wake. The two-dimensional linear analysis is extended to three-dimensions, examining the stability of spanwise modes. Three-dimensional FSDS simulations are performed using spanwise periodicity, and the mode shapes, stability and three-dimensional flow characteristics are examined.

7.1 Introduction to the Three-Dimensional Flapping Problem

7.1.1 Problem Statement

As with the two-dimensional problem, we consider a thin membrane pinned at the leading edge and free at the trailing edge, under the influence of a uniform incompressible viscous inflow, as shown in figure 7-1. The problem as considered in the present study is spanwise periodic both for the structure and the flow, meaning that one spanwise edge of the body and the flow domain is connected to the other spanwise edge. The resulting infinite series of identical domains is depicted in figure 7-2.

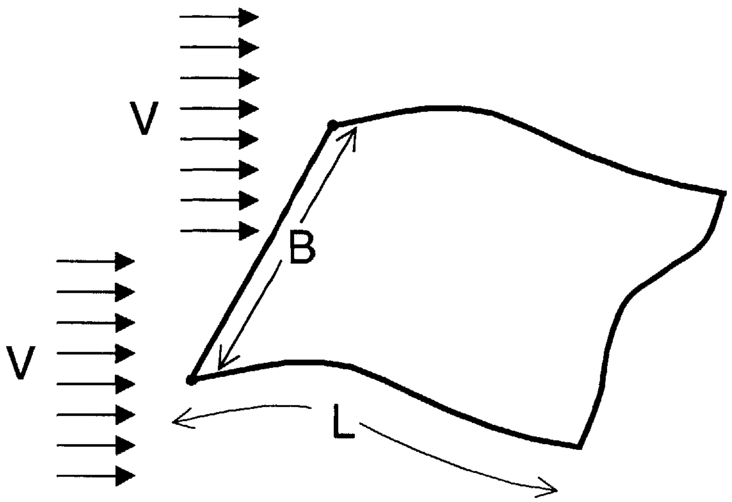

Figure 7-1: Depiction of the problem of the flapping three-dimensional flexible thin foil of length L and span B in uniform incoming flow V in an unbounded fluid domain. The body is pinned at the leading edge and free at the trailing edge.

When using such a spanwise periodic domain, continuing to consider the body to be inextensible would prohibit any spanwise variation to the structural displacement, as such variation necessitates spanwise strain. The study thus considers a body which has a moderate degree of extensibility, thus allowing spanwise variation to the displacement.

The governing equation for this three-dimensional flexible plate is different from the two-dimensional equation, and is written as

$$\begin{aligned}\rho_s h\frac{\partial^2\vec{x}}{\partial t^2} &- \frac{\partial}{\partial s_1}\left(T_1\frac{\partial\vec{x}}{\partial s_1}\right) - \frac{\partial}{\partial s_2}\left(T_2\frac{\partial\vec{x}}{\partial s_2}\right) + \frac{EI}{1-\nu_s^2}\left(\frac{\partial^4\vec{x}}{\partial s_1^4} + 2\frac{\partial^4\vec{x}}{\partial s_1^2\partial s_2^2} + \frac{\partial^4\vec{x}}{\partial s_2^4}\right)\\ &-\frac{\partial}{\partial s_1}\left(M\frac{\partial\vec{x}}{\partial s_2}\right) - \frac{\partial}{\partial s_2}\left(M\frac{\partial\vec{x}}{\partial s_1}\right) = \vec{F}_f, \end{aligned}\tag{7.1}$$

with s_1 as the Lagrangian coordinate along the length, s_2 as the Lagrangian coordinate along the span, and $\vec{x}$ as the body position vector. Structural parameters are, again, ρ_s for the structural density, h for the body thickness, EI for bending rigidity, and ν_s for the Poisson ratio, while internal efforts in the equation are T_1 for tension in the s_1 direction, T_2 for tension in s_2 direction, and M for the moment due to shear stress

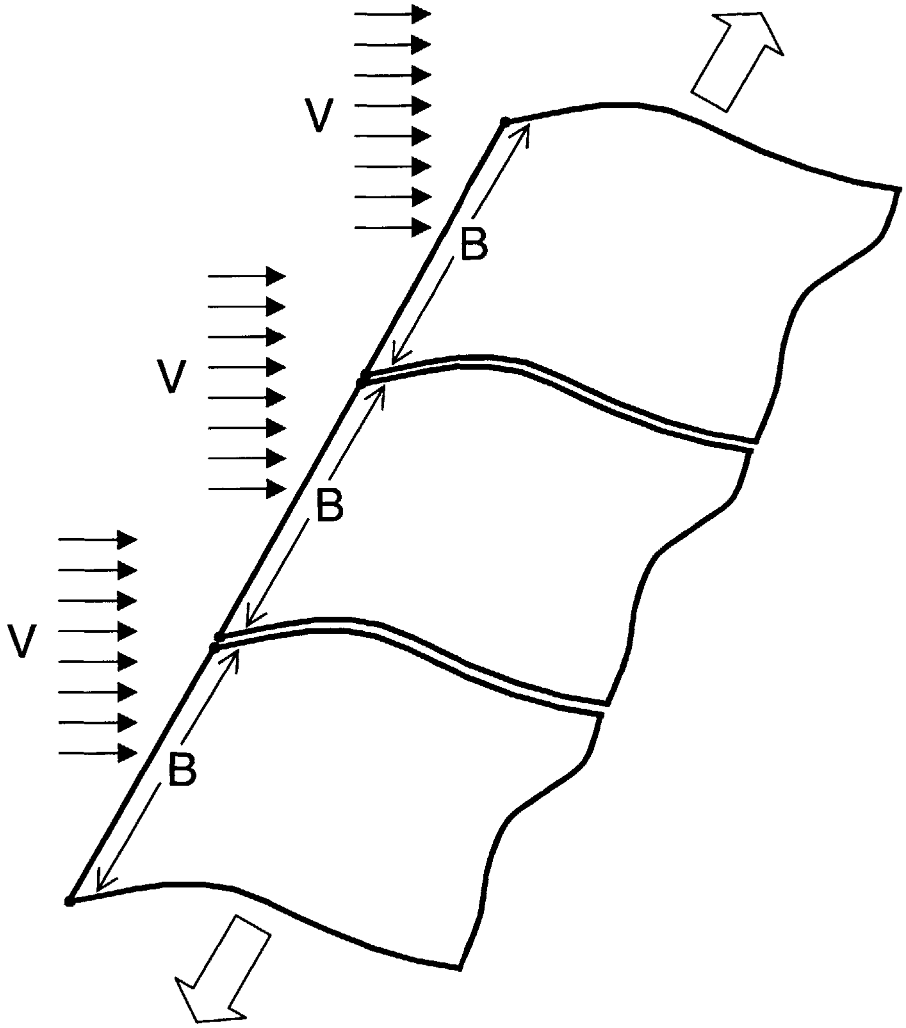

Figure 7-2: Depiction of the consequence of spanwise periodicity, as used in the simulations. An infinite series of identical domains results from the use of a spanwise periodic domain.

in the membrane plane.

The fluid-dynamic governing equations and associated forcing to the structure are the same as detailed in § 6.1.1 for the two-dimensional problem, with the forcing as

$$\vec{F}_f = [\Delta\tau]\hat{n}, \tag{7.2}$$

where $\hat{n}$ is the upward normal and $[\Delta\tau]$ is the difference between the fluid dynamic stress tensor at the top and bottom of the body. Elements of the stress tensor are derived from the fluid dynamics at the surface as

$$\tau_{ij} = \nu\rho_f\left(\frac{\partial u_i}{\partial\xi_j} + \frac{\partial u_j}{\partial\xi_i}\right) - \delta_{ij}p. \tag{7.3}$$

The fluid dynamics come from solution to the Navier-Stokes equations,

$$\begin{aligned} \frac{\partial\vec{v}}{\partial t} + (\vec{v}\cdot\vec{\nabla})\vec{v} &= -\frac{1}{\rho_f}\vec{\nabla}p + \nu\nabla^2\vec{v}, && (7.4)\\ \vec{\nabla}\cdot\vec{v} &= 0, && (7.5) \end{aligned}$$

with velocity boundary conditions at the body defined by the body motion, $\vec{v} = \partial\vec{x}/\partial t$, and at infinity as the mean flow, $\vec{v} = V$. As described in § 6.1.1 for the two-dimensional problem, these governing equations, coupled by the external forcing to the structure and the kinematic boundary condition of the flow field, describe the complete flapping problem, including effects of added mass, viscous drag, and vortex shedding into the wake.

7.1.2 Three-Dimensional Linear Stability Analysis

We perform a linear analysis for a tensioned membrane with bending rigidity, starting with the linear equation of motion,

$$\begin{aligned} \rho_s h\frac{\partial^2 z}{\partial t^2} &- \left(T_y\frac{\partial^2}{\partial y^2} + T_x\frac{\partial^2}{\partial x^2}\right)z + \frac{EI}{1-\nu_s^2}\left(\frac{\partial^4}{\partial y^4} + 2\frac{\partial^4}{\partial y^2\partial x^2} + \frac{\partial^4}{\partial x^4}\right)z\\ &+ m_a\left(\frac{\partial}{\partial t} + V\frac{\partial}{\partial y}\right)^2 z = 0, && (7.6) \end{aligned}$$

where T_y and T_x are the membrane tensions in the lengthwise y and spanwise x directions, V is the mean flow, and z is the membrane displacement, considered to be small in this analysis. We rearrange the terms as

$$\begin{aligned}(\rho_s h + m_a)\frac{\partial^2 z}{\partial t^2} &+ \left(m_a V^2 - T_y\right)\frac{\partial^2 z}{\partial y^2} + (-T_x)\frac{\partial^2 z}{\partial x^2} + \frac{EI}{1-\nu_s^2}\frac{\partial^4 z}{\partial y^4} + 2\frac{EI}{1-\nu_s^2}\frac{\partial^4 z}{\partial y^2 \partial x^2} \\ &+ \frac{EI}{1-\nu_s^2}\frac{\partial^4 z}{\partial x^4} + 2m_a V\frac{\partial^2 z}{\partial y \partial t} = 0. \qquad (7.7)\end{aligned}$$

As with the two-dimensional analysis, we consider for the analysis that the tension is constant, though different for the streamwise and spanwise directions. We will simulate the problem with FSDS-3D using spanwise periodicity, so we consider this case when determining the tension. The significance of spanwise periodicity is that the the projection length of the span will remain constant, which has two consequences. First, streamwise tension will induce a spanwise tension in the membrane scaled by the Poisson ratio. Second, any spanwise variation to the displacement will necessarily have spanwise strain, and associated tension.

The streamwise tension is taken as the Blasius boundary-layer tension as in the two-dimensional study,

$$T_y = 1.3\rho_f V^2 L Re^{-1/2}. \qquad (7.8)$$

The spanwise tension comes from both the spanwise strain and the streamwise tension through Hooke's law as

$$T_x = \frac{Eh}{1-\nu_s^2}\epsilon_{xx} + 1.3\nu_s \rho_f V^2 L Re^{-1/2}, \qquad (7.9)$$

where ν_s is the Poisson ratio. The spanwise strain comes from spanwise variation in the displacement, and is estimated from a sawtooth approximation to a wave of amplitude A_x and wavelength λ_x,

$$\epsilon_{xx} = \frac{\left(\left(\frac{\lambda_x}{4}\right)^2 + A_x^2\right)^{1/2}}{\frac{\lambda_x}{4}} - 1 = \frac{\left(\left(\frac{\pi}{2k_x}\right)^2 + A_x^2\right)^{1/2}}{\frac{\pi}{2k_x}} - 1. \tag{7.10}$$

The variables (x, y, z, t) of the equation of motion are now nondimensionalized by L and V, yielding

$$\begin{aligned} &(\rho_s h + m_a)\frac{V^2}{L}\frac{\partial^2 z}{\partial t^2} + \left(m_a V^2 - T_y\right)\frac{1}{L}\frac{\partial^2 z}{\partial y^2} + (-T_x)\frac{1}{L}\frac{\partial^2 z}{\partial x^2} + \frac{EI}{1-\nu_s^2}\frac{1}{L^3}\frac{\partial^4 z}{\partial y^4} \\ &+2\frac{EI}{1-\nu_s^2}\frac{1}{L^3}\frac{\partial^4 z}{\partial y^2 \partial x^2} + \frac{EI}{1-\nu_s^2}\frac{1}{L^3}\frac{\partial^4 z}{\partial x^4} + 2m_a V\frac{V}{L}\frac{\partial^2 z}{\partial y \partial t} = 0. \end{aligned} \tag{7.11}$$

Dividing by $V^2 \rho_f$, we obtain

$$\begin{aligned} (\mu + c_m)\frac{\partial^2 z}{\partial t^2} \; &+ \; \left(c_m - 1.3Re^{-1/2}\right)\frac{\partial^2 z}{\partial y^2} + \left(-K_S\epsilon_{xx} - 1.3\nu_s Re^{-1/2}\right)\frac{\partial^2 z}{\partial x^2} \\ &+ \; K_B\frac{\partial^4 z}{\partial y^4} + 2K_B\frac{\partial^4 z}{\partial y^2 \partial x^2} + K_B\frac{\partial^4 z}{\partial x^4} + 2c_m\frac{\partial^2 z}{\partial y \partial t} = 0, \end{aligned} \tag{7.12}$$

where

$$\mu = \frac{\rho_s h}{\rho_f L}, \quad c_m = \frac{m_a}{\rho_f L}, \quad K_B = \frac{EI}{(1-\nu_s^2)\rho_f V^2 L^3}, \text{ and } K_S = \frac{Eh}{(1-\nu_s^2)\rho_f V^2 L}. \tag{7.13}$$

We now consider the mode which is a travelling wave in the streamwise y direction and a standing wave in the spanwise x direction, given by $z = Ae^{i(k_y y - \omega t)}(e^{ik_x x} + e^{-ik_x x})/2$ or $z = Ae^{i(k_y y - \omega t)}cos(k_x x)$. Using this mode in the equation of motion, we obtain the dispersion relation

$$\begin{aligned} (\mu + c_m)\omega^2 \; &+ \; \left(c_m - 1.3Re^{-1/2}\right)k_y^2 + \left(-K_S\epsilon_{xx} - 1.3\nu_s Re^{-1/2}\right)k_x^2 - K_B k_y^4 \\ &- \; 2K_B k_y^2 k_x^2 - K_B k_x^4 - 2c_m k_y \omega = 0. \end{aligned} \tag{7.14}$$

Alternatively, if we consider the mode of a travelling wave at an angle to the base flow or y direction, given by $z = Ae^{i(k_y y + k_x x - \omega t)}$, the dispersion relation of equation 7.14 remains the same. The frequency found through solution of the dispersion relation is

$$\begin{aligned}
\omega &= \frac{c_m k_y}{\mu + c_m} \pm \frac{1}{\mu + c_m}\Big[c_m^2 k_y^2 - (\mu + c_m)\Big(c_m k_y^2 - 1.3Re^{-1/2}k_y^2 \\
&\quad - K_S \epsilon_{xx} k_x^2 - 1.3\nu_s Re^{-1/2} k_x^2 - K_B k_y^4 - 2K_B k_y^2 k_x^2 - K_B k_x^4\Big)\Big]^{1/2} \\
&= \frac{c_m k_y}{\mu + c_m} \pm \frac{1}{\mu + c_m}\Big[-\mu c_m k_y^2 + (\mu + c_m)\Big(1.3Re^{-1/2}k_y^2 \\
&\quad + K_S \epsilon_{xx} k_x^2 + 1.3\nu_s Re^{-1/2} k_x^2 + K_B k_y^4 + 2K_B k_y^2 k_x^2 + K_B k_x^4\Big)\Big]^{1/2} \qquad (7.15)
\end{aligned}$$

A flapping instability is realized when the value in the square root of the second term is negative. This is achieved with realization of the inequality

$$\frac{\mu c_m k_y^2}{\mu + c_m} > 1.3Re^{-1/2}k_y^2 + K_S \epsilon_{xx} k_x^2 + 1.3\nu_s Re^{-1/2} k_x^2 + K_B k_y^4 + 2K_B k_y^2 k_x^2 + K_B k_x^4. \qquad (7.16)$$

This reduces to precisely the two-dimensional expression when the wave is entirely in the stream-wise direction, with $k_x = 0$. It can be seen in equation 7.16 that any mode with spanwise variation (non zero k_x) is more stable than the streamwise mode.

We consider the three-dimensional stability limit from equation 7.16 for the case of $Re = 1000$, $K_B = 0.0001$, $K_S = 1$, $\nu_s = 0.3$, $k_y = 2\pi$, and $c_m = 2/k_y = 0.32$, for a range of k_x and A_x. While both A_x and k_x influence the spanwise tension through ϵ_{xx} as shown in equation 7.10, the restoring force associated with this tension operates as the product of this tension and the square of k_x. The critical mass ratios are plotted in figure 7-3, which shows the increased stability of the high cross-stream modes. Also shown is an increase in stability for higher amplitudes, suggesting that higher spanwise modes will be restricted to lower oscillation amplitudes. For mass ratios $\mu > 0.1$, all modes where $k_x \leq k_y = 2\pi$, corresponding to cross-stream or spanwise wavelengths longer than the chord length, are predicted to be unstable flapping modes.

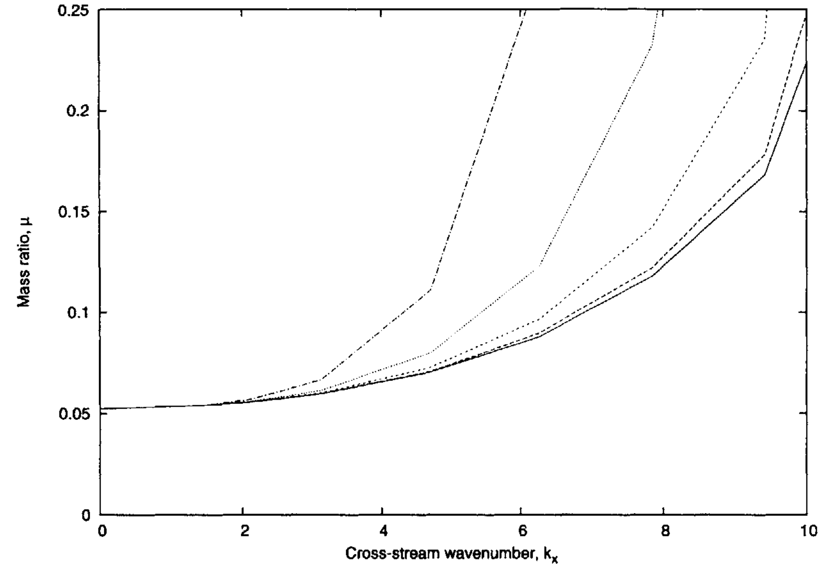

Figure 7-3: Critical mass ratio vs. cross-stream wavenumber, from equation 7.16 of the linear analysis for flapping of three-dimensional flag with $Re = 1000$, $K_B = 0.0001$, $K_S = 1$, $\nu_s = 0.3$, $k_y = 2\pi$, and $c_m = 2/k_y = 0.32$. Plotted for spanwise amplitude of $A_x = 0$ (——), $A_x = 0.01$ (— —), $A_x = 0.025$ (- - -), $A_x = 0.05$ (···), and $A_x = 0.1$ (—·—)

7.2 The FSDS-3D Response Results and Analysis

7.2.1 Investigative Approach and Simulation Constraints

Three-dimensional flapping modes are now examined with the simulation tool FSDS-3D. While the development of this tool is covered in Chapters 3 and 4, the capability of the fluid and structural components, as well as the coupled implementation, is displayed in Chapter 5. Using our understanding of the two-dimensional system response, derived from the work of Chapter 6, combined with the predictions of the three-dimensional linear analysis of § 7.1.2, we are able to perform a targeted set of simulations to understand the three-dimensional trends and behavior. Such a targeted approach is necessary using FSDS-3D, as the computational cost of the three-dimensional simulations prohibits covering parameter space to the extent that was done in the two-dimensional study. All simulations are performed at $Re = 1000$, $K_B = 0.0001$, $K_S = 1$, and $\nu_s = 0.3$, using a spanwise periodic domain of width B.

A consequence of the domain periodicity is that the simulation can only evolve with characteristics that are periodic in B or two-dimensional (without spanwise variation). A lower extensional rigidity is used in the three-dimensional case than for the two-dimensional study, so that the strain associated with spanwise variation results in a lower tension, as explained in § 7.1.2. The simulations are used first to examine the initial stability of isolated spanwise wave modes for comparison to the prediction of the linear stability analysis, and second to investigate the natural modal responses expected in an evolved system.

To examine the stability of a mode of a specific spanwise wavenumber, the initial condition is set to excite that wavenumber. A spanwise sinusoidal variation to the streamwise linear initial displacement is used, such that

$$z(s_1, s_2)_0 = A_0 s_1 sin(k_2 s_2), \tag{7.17}$$

where k_2 corresponds to the k_x of the linear analysis. The FSDS-3D domain is spanwise periodic, and in this study the domain width is set to the spanwise wavelength, so $B = \lambda_2 = 2\pi/k_2$. A small matrix of runs are made varying the parameters of aspect ratio B/L and mass ratio μ to determine the stability and initial growth of the isolated spanwise wave modes for comparison to the linear analysis.

The study of the natural response modes of the system examines the characteristics of the system response to varying initial and ambient conditions. Select simulations which excite both standing wave and travelling wave modes are examined, along with mixed modes including two-dimensional bias. Through this study, we identify the base modes of response, along with hybrid response modes, and the tendency of the system evolution.

7.2.2 Initial Modal Stability

Isolated three-dimensional modes of spanwise standing waves are excited by using the initial condition of equation 7.17, where the width of the periodic domain is set to the spanwise wavelength as $B = \lambda_2 = 2\pi/k_2$. The stability transition prediction of

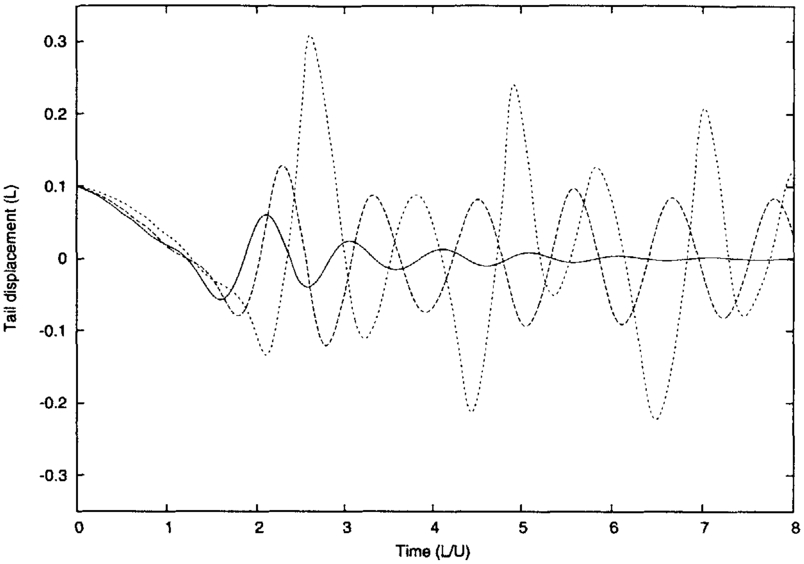

Figure 7-4: Time history of the cross-stream tail displacement for the two-dimensional mode, $k_2 = 0$, using FSDS-2D with $Re = 1000$, $K_B = 0.0001$, and $K_S = 1$, for $\mu = 0.025$ (——), $\mu = 0.075$ (— —), and $\mu = 0.2$ (- - -).

equation 7.16 is used as a guideline for examining the relationship between spanwise wavenumber and the modal stability. Using fixed values $Re = 1000$, $K_B = 0.0001$, $K_S = 1$, and $\nu_s = 0.3$, we consider a small matrix of B/L and μ values in order to test the stability prediction of the linear analysis.

We first consider the two-dimensional case where $k_2 = 0$, which the linear prediction of equation 7.16 and figure 7-3 indicates is the least stable with the lowest critical mass ratio. We perform FSDS-2D for mass ratios of $\mu = 0.025, 0.075, 0.2$, with all other parameters as previously indicated, and an initial linear displacement with tail amplitude of $0.1L$. A time history of the cross-stream tail displacement for these three cases is plotted in figure 7-4. The plot indicates fixed-point stability for $\mu = 0.025$, convergence to limit-cycle flapping for $\mu = 0.075$, and chaotic flapping for $\mu = 0.2$. The transitions follow those of the two-dimensional study of chapter 6.

We now seek to understand the stability of modes of finite spanwise wavelength, by considering the cases of $B/L = 5$ ($k_2 = 1.26$) and $B/L = 1$ ($k_2 = 6.28$). For the mass ratio of $\mu = 0.075$, the linear prediction depicted in figure 7-3 indicates that the wider span case of $k_2 = 1.26$ should be in the flapping regime, while the narrow span

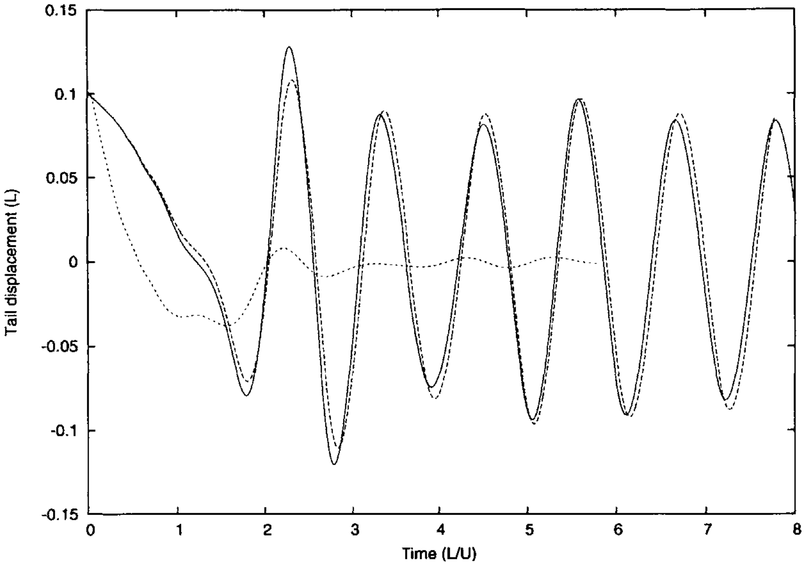

Figure 7-5: Time history of the cross-stream tail displacement at the spanwise standing wave antinode for $\mu = 0.075$ and $B/L = 5$ or $k_2 = 1.26$ (— —), and $B/L = 1$ or $k_2 = 6.28$ (- - -), and the two-dimensional $k_2 = 0$ (——).

case of $k_2 = 6.28$ should be in the fixed-point stable regime. The three-dimensional modes are excited through the initial condition of equation 7.17, representing a spanwise standing wave with initial maximum tail amplitude of $0.1L$. Figure 7-5 plots the cross-stream tail displacement at the antinode for the wide and narrow span cases, along with the two-dimensional tail displacement. The plot indicates that the maximum displacement of the wider span case very nearly matches the displacement of the two-dimensional case, converging to limit-cycle flapping. This reflects the prediction of figure 7-3 that for the low spanwise wavenumber of $k_2 = 1.26$, the stability characteristics are near convergence to that of two-dimensional flapping. The maximum trailing edge displacement for the narrow span case, however, trends to zero, indicating the stability for $k_2 = 6.28$ which is predicted by figure 7-3 for the mass ratio of $\mu = 0.075$.

We now examine the flapping stability for the wide span $B/L = 5$ and narrow span $B/L = 1$ cases with the mass ratio increased to $\mu = 0.2$, using the same standing wave initial condition. The time history of the antinode trailing edge displacement for these three-dimensional cases is plotted in figure 7-6 along with that of the two-dimensional

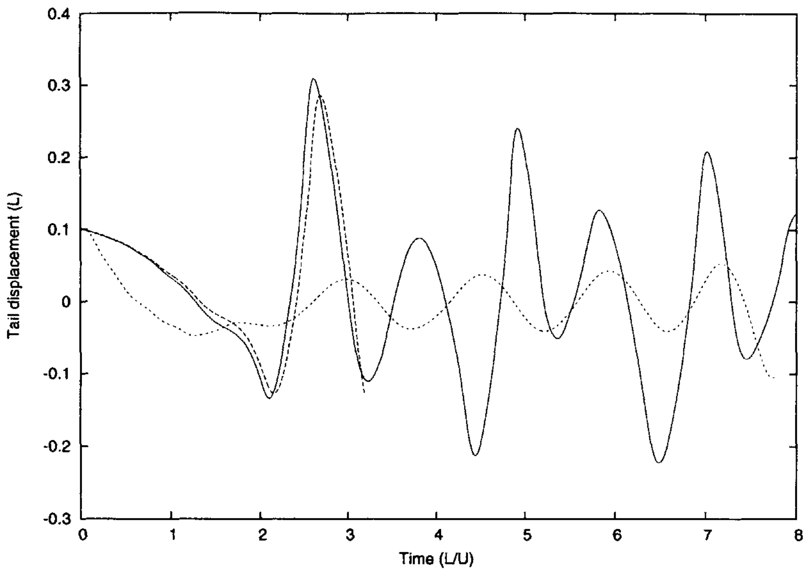

Figure 7-6: Time history of the cross-stream tail displacement at the spanwise standing wave antinode for $\mu = 0.2$ and $B/L = 5$ or $k_2 = 1.26$ (— —), and $B/L = 1$ or $k_2 = 6.28$ (- - -), and the two-dimensional $k_2 = 0$ (——).

simulation with $\mu = 0.2$. Again, it can be seen that the antinode displacement for the wide span case follows closely that of the two-dimensional case, until the simulation breaks down at $t \simeq 3.2$ due to rapid spanwise changes to the displacement. For the narrow span case of $B/L = 1$ and $\mu = 0.2$, the antinode time history of figure 7-6 suggests that the body initially takes on a limit-cycle flapping mode.

The three-dimensional stability results are summarized in the plot of figure 7-7, in the plane of spanwise wavenumber and mass ratio. The eight data points, representing three runs from two-dimensional simulation at $k_2 = 0$, three runs for $B/L = 5$ and $k_2 = 1.26$, and two runs for $B/L = 1$ and $k_2 = 6.28$, are plotted with the linear prediction for stability transition of equation 7.16. The prediction can be seen to hold for the limited data obtained in this study, indicating that the linear analysis of § 7.1.2 captures the essential physics associated with stability of the three-dimensional problem.

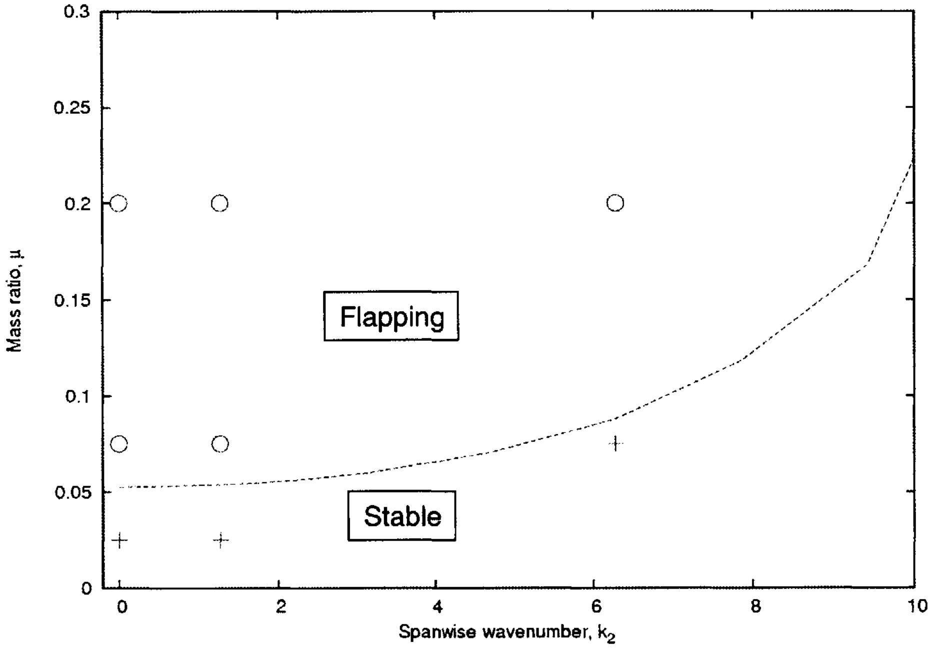

Figure 7-7: Bifurcation diagram for three-dimensional flapping initiated as isolated standing wave modes with equation 7.17, with with $Re = 1000$, $K_B = 0.0001$, $K_S = 1$, and $\nu_s = 0.3$, through a range of spanwise wavenumber k_2 and mass ratio μ. FSDS data indicate responses as stable (+), or flapping (⊙). Also plotted is the prediction of stability transition from equation 7.16 (— —).

7.2.3 Modal Response

Our study of the modal response of the system includes an examination of the body displacement and wake characteristics associated with modes excited by several different initial and ambient conditions. Cases which excite multiple modes display the tendency of the system energy, and thus suggest the natural modes of the evolved system. The study reveals three base modes, each with unique wake structure, which make up the building blocks for the system response. These base modes are the spanwise standing wave, the spanwise travelling wave, and the two-dimensional response, and are characterized in the response discussion below.

The Spanwise Standing Wave

The runs described in § 7.2.2 are initiated to excite a standing wave response, with the initial displacement given by equation 7.17. The symmetry of the initial displacement and ambient conditions offer no spanwise directional nor two-dimensional bias, and thus excite solely a standing wave response. We examine this response by considering the converged limit-cycle case of $\mu = 0.075$ and $B/L = 5$ ($k_2 = 1.26$). The displacement of the three-dimensional body through a complete flapping cycle can be seen in figure 7-8, which shows a series of shaded surface plots from $t = 6.2$ to $t = 7.2$ from the downstream perspective. The limit-cycle mode can be seen to consist of a travelling wave of increasing amplitude in the streamwise y-direction, modulated in amplitude as a standing wave in the spanwise x-direction.

The two-dimensional limit-cycle flapping results of Chapter 6 revealed that the periodic flapping had an associated alternating vortex shedding pattern of a von Karman vortex street. The standing wave modulation to the three-dimensional limit-cycle flapping suggests that the sign of these vortices alternates with the phase in the spanwise direction. This can be seen in the plot of vorticity contours for the spanwise standing wave case of $\mu = 0.075$ and $B/L = 5$ given in figure 7-9 at time $t = 7.1$. The plot shows the body and wake from the upstream perspective, with two domains shown side-by-side to aid visualization of the vortex wake pattern. Figure 7-

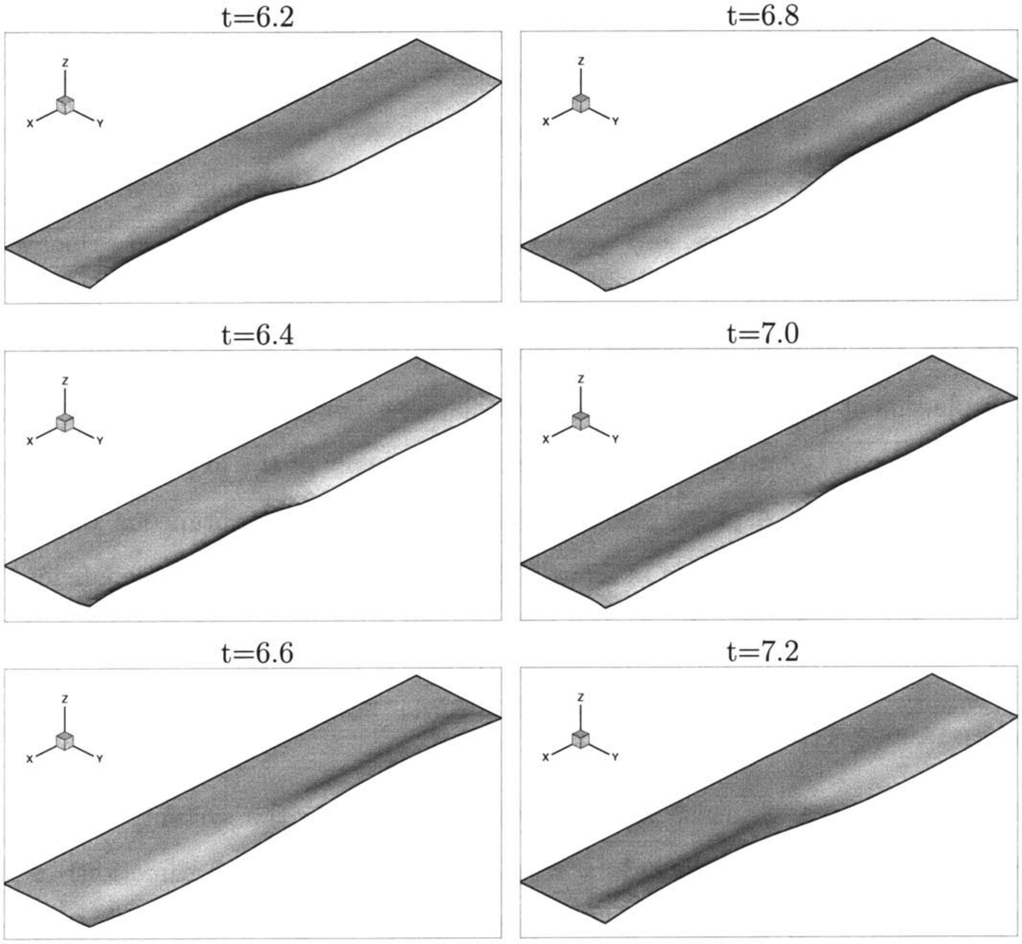

Figure 7-8: Shaded surface from downstream perspective for the spanwise standing wave flapping with $\mu = 0.075$ and $B/L = 5$ ($k_2 = 1.26$). FSDS-3D simulation with spanwise periodic domain initiated as equation 7.17 with amplitude of $0.1L$.

9(a) shows that the sign of the spanwise vorticity alternates in the spanwise direction with the standing wave modulation, and the staggered same-sign vortices are laced together at the nodes. The vortex structure splits and turns at the nodes of the wake, a phenomenon confirmed by the pattern of streamwise vorticity at the nodes, which can be seen in the contour plot of figure 7-9(b). A normal component to the vorticity in the splitting and turning can be seen in figure 7-9(c), and reflects the drawing of the vortex structure toward the wake centerline ($z = 0$) at the lacing nodes. This wake of two layers of laced cellular vortices of opposite sign has the same structure as that found by Newman & Karniadakis in [44] for the standing wave response of flow induced cable vibration, and we consider it one of the fundamental responses of the flapping system.

We can also identify the modal response by performing modal decomposition to the displacement of the trailing edge of the flapping body. Using a discrete Fourier transform we can isolate the sine and cosine components of the excited mode, which we designate mode1. A phase plot displaying the locus of instantaneous amplitudes of the two components is given in figure 7-10, and the linear trajectory confirms that it is a purely spanwise standing wave mode.

The Spanwise Travelling Wave

In order to excite a spanwise travelling wave response in the system, we alter the ambient flow condition to include a cross-flow (in the spanwise direction) of 25% the base flow strength. We consider again the case of $\mu = 0.075$ and $B/L = 5$ ($k_2 = 1.26$), and use the same initial displacement condition given by equation 7.17. A plot of the time history of the trailing edge displacement at the antinode of the initial condition, given in figure 7-12(a), indicates that the trajectory of this point is not much changed from the standing wave case. However, the series of three-dimensional shaded displacement plots of figure 7-11, shows a significantly different response from that of the standing wave given in figure 7-8. The response of this mode consists of travelling waves at an angle oblique to the body orientation, so that at any given time one spanwise point along the trailing edge will be at the maximum,

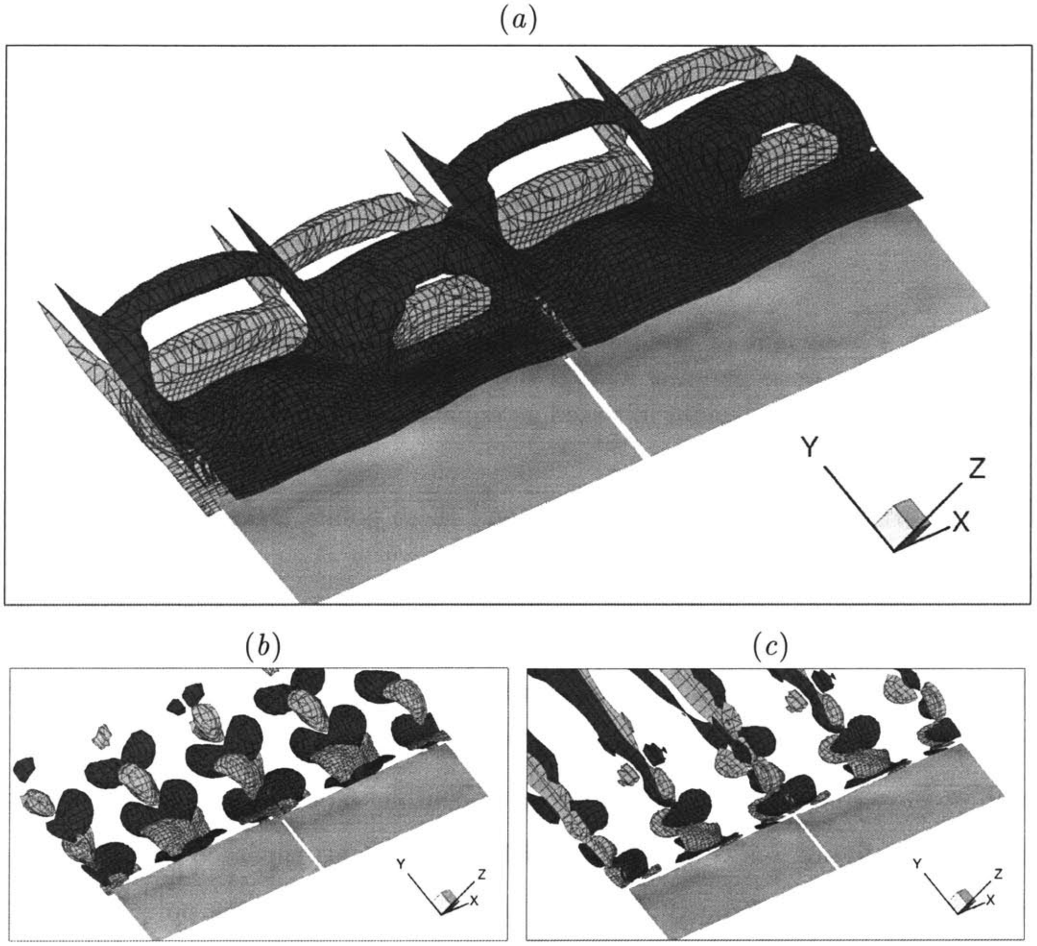

Figure 7-9: The three-dimensional vortex wake from the upstream perspective at $t = 7.1$ for the standing wave response of $\mu = 0.075$ and $B/L = 5$, with the domain repeated once in the spanwise direction. The dark and light surfaces are isosurfaces for negative and positive vorticity for (a) spanwise vorticity of $\omega_x = \pm 1$, (b) sreamwise vorticity of $\omega_y = \pm 0.25$, and (c) normal vorticity of $\omega_z = \pm 0.25$.

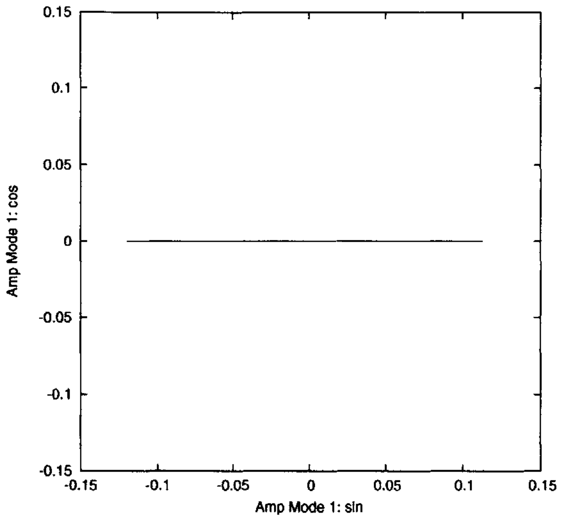

Figure 7-10: Phase plot of trailing edge displacement in sine-cosine space for the spanwise standing wave flapping with $\mu = 0.075$ and $B/L = 5$. FSDS-3D simulation with spanwise periodic domain initiated as equation 7.17 with amplitude of $0.1L$.

and one spanwise point at the minimum, and these points travel in the direction of the cross-flow.

The vortex wake associated with the travelling wave mode is different from that of the standing wave mode, in that progression in time is represented only by a shift in phase in the spanwise direction. The three-dimensional vortex wake for the travelling wave mode is seen in the vorticity contour plots given from an upstream perspective in figure 7-13. The plots, with the spanwise repeated domain, show a wake of a continuous obliquely shedding vortex street, where the point of shedding from the body travels with the wave in the spanwise direction. While the bulk of the vortex structure can be seen in the plot of the spanwise vorticity of figure 7-13(a), the plot of streamwise vorticity of figure 7-13(b) reflects the oblique angle of the shedding, and the normal vorticity of figure 7-13(c) indicates little participation of this component. A pure travelling wave mode would be expected to have no time dependence to the total drag integrated along the span, as the flow is merely being phase shifted along the span in time. The difference in drag fluctuation between the standing wave and travelling wave mode can be seen in figure 7-12(b), which does display significantly less forcing fluctuation for the travelling wave mode. The

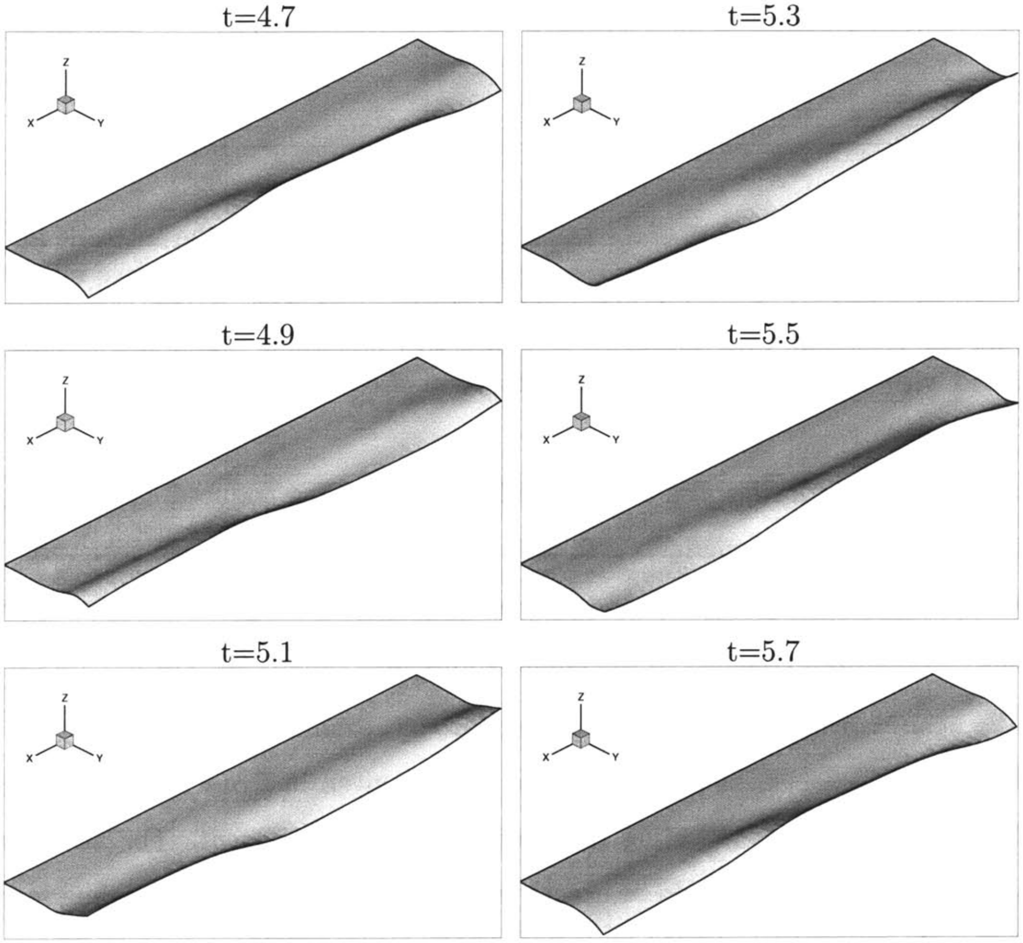

t=4.7

t=5.3

t=4.9

t=5.5

t=5.1

t=5.7

Figure 7-11: Shaded surface from downstream perspective for the spanwise travelling wave flapping with $\mu = 0.075$ and $B/L = 5$ ($k_2 = 1.26$). FSDS-3D simulation with spanwise periodic domain initiated as equation 7.17 with amplitude of $0.1L$, using a 25% cross-flow in the spanwise x-direction.

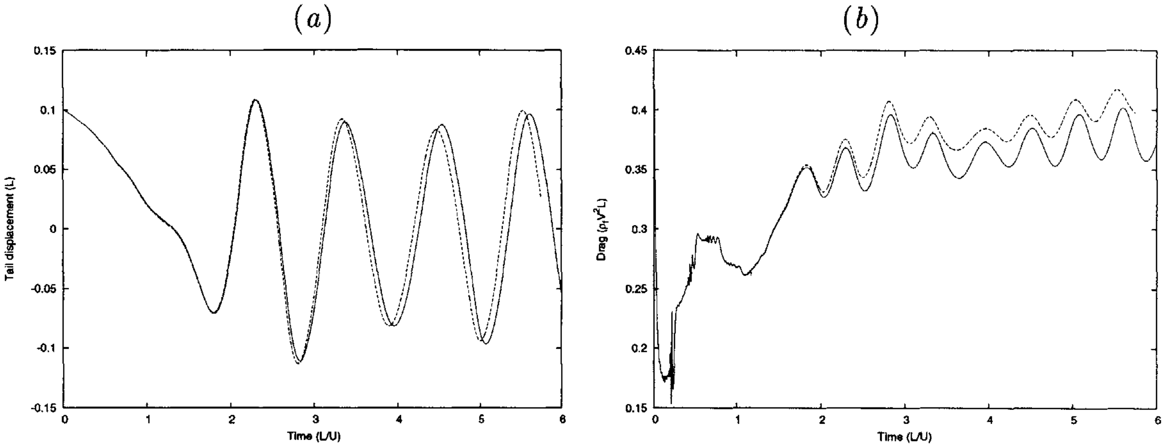

Figure 7-12: (*a*) Time history of the trailing edge displacement at the antinode for the standing wave mode (——) and the same location for the travelling wave mode (— —). (*b*) Time history of total drag for standing wave mode (——) with no cross-flow, and for the travelling wave mode (— —) with 25% cross-flow. Both simulations are initiated with the standing wave initial condition of equation 7.17.

travelling wave mode was also a response found in the flow induced cable vibration study of Newman & Karniadakis [44], with a vortex wake of the same structure. We consider this travelling wave mode with an obliquely shedding vortex street to be a second fundamental response of the flapping system.

We again consider mode identification through examining a phase plot of the trailing edge displacement sine and cosine modes, given in figure 7-14. An orbital path can now be seen, reflecting the travelling wave component. For an isolated travelling wave, the path would be exactly circular, and the system is heading toward such a path.

The Two-Dimensional Flapping Mode

Two-dimensional flapping for the three-dimensional system consists of a span-wide displacement of the body. When we consider a mixed-mode initial condition with several standing wave components, and a two-dimensional bias component, the system converges to this two-dimensional flapping mode. The case considered uses an initial

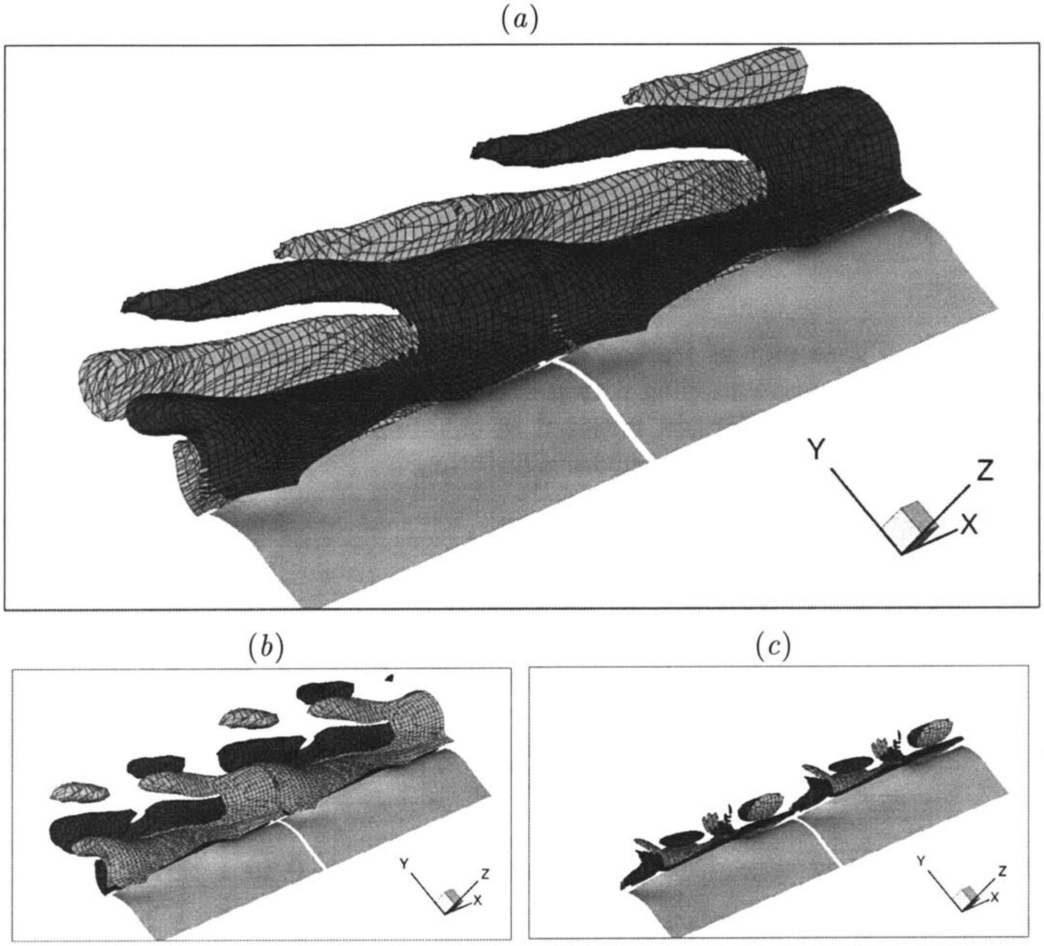

Figure 7-13: The three-dimensional vortex wake from the upstream perspective at $t = 5.7$ for the travelling wave response of $\mu = 0.075$ and $B/L = 5$, using 25% spanwise cross-flow, with the domain repeated once in the spanwise direction. The dark and light surfaces are isosurfaces for negative and positive vorticity for (a) spanwise vorticity of $\omega_x = \pm 1$, (b) sreamwise vorticity of $\omega_y = \pm 0.25$, and (c) normal vorticity of $\omega_z = \pm 0.25$.

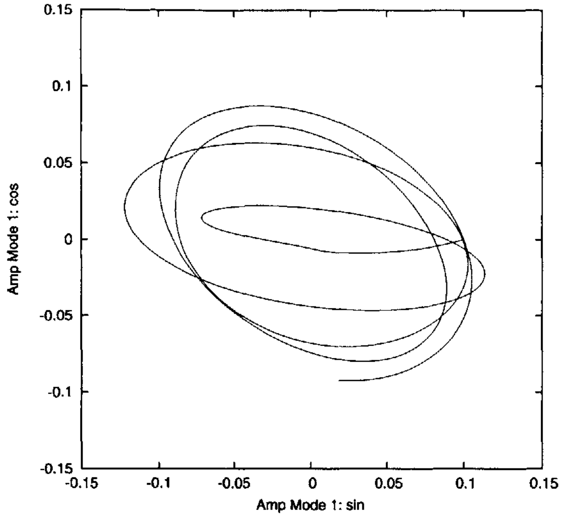

Figure 7-14: Phase plot of trailing edge displacement in sine-cosine space for the spanwise travelling wave flapping with $\mu = 0.075$ and $B/L = 5$. FSDS-3D simulation with spanwise periodic domain initiated as equation 7.17 with amplitude of $0.1L$, using a 25% cross-flow in the spanwise x-direction.

displacement of

$$\begin{aligned} z(s_1, s_2)_0 = 0.5A_0 s_1 \Bigg(1 + 0.25 \Bigg[&sin\left(\frac{2\pi}{B}s_2\right) + sin\left(2\frac{2\pi}{B}s_2\right) \\ &+sin\left(3\frac{2\pi}{B}s_2\right) + sin\left(4\frac{2\pi}{B}s_2\right) + sin\left(5\frac{2\pi}{B}s_2\right)\Bigg]\Bigg), \end{aligned} \tag{7.18}$$

so that the trailing edge displacement ranges from $z \simeq 0$ to $z \simeq A_0$. With the domain width for the simulation as $B = 5$, the mass ratio as $\mu = 0.075$, and an initial amplitude of $A_0 = 0.1$, the initial condition includes spanwise standing wave components in both the flapping and stable regimes. The energy rapidly becomes concentrated in the two-dimensional mode, which is seen to be uniform across the span in the series of shaded displacement plots of figure 7-15. The vortex wake at $t = 6.7$, plotted in figure 7-16, displays this near exact two-dimensional vortex street response, with spanwise continuous parallel vortices with little phase variation in the spanwise direction, and no significant vorticity component in the streamwise or normal directions. We consider this two-dimensional response to be our third fundamental mode of the system.

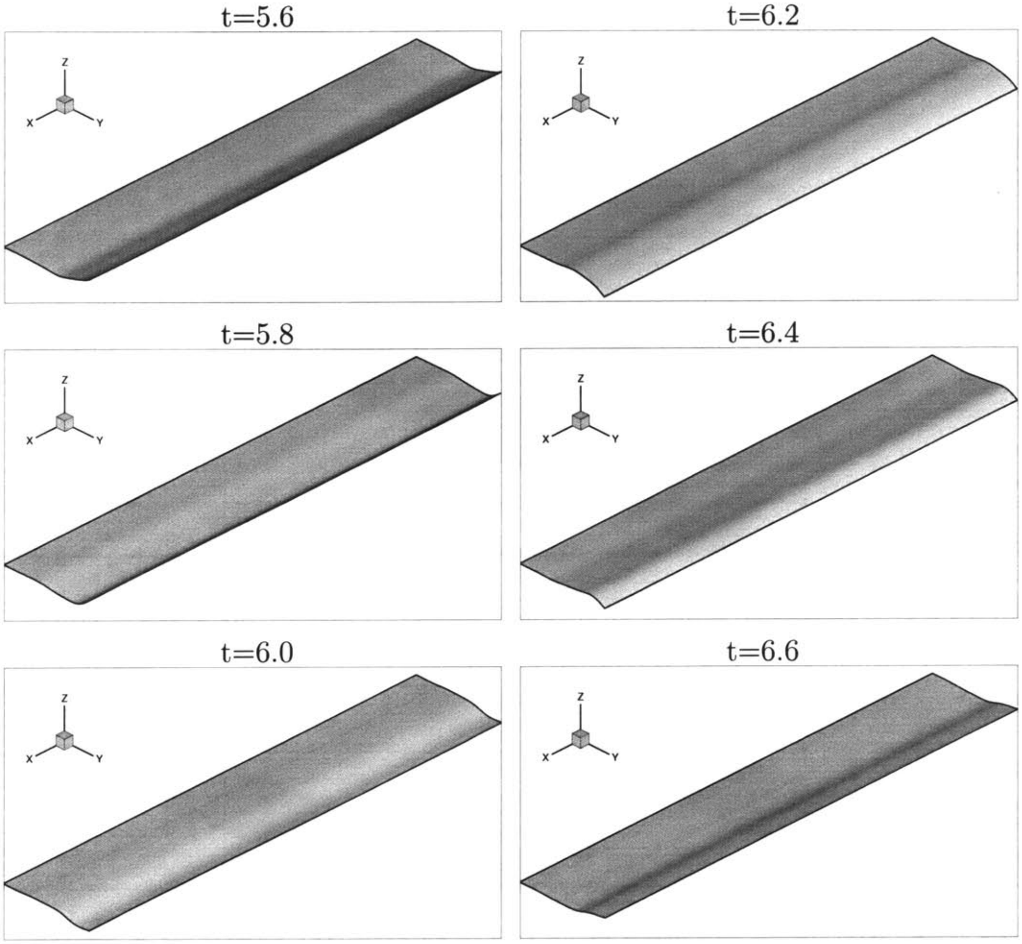
t=5.6

t=6.2

t=5.8

t=6.4

t=6.0

t=6.6

Figure 7-15: Shaded surface from downstream perspective indicating primarily two-dimensional response for system initiated with the mixed mode displacement of equation 7.18 with $B/L = 5$ and $\mu = 0.075$.

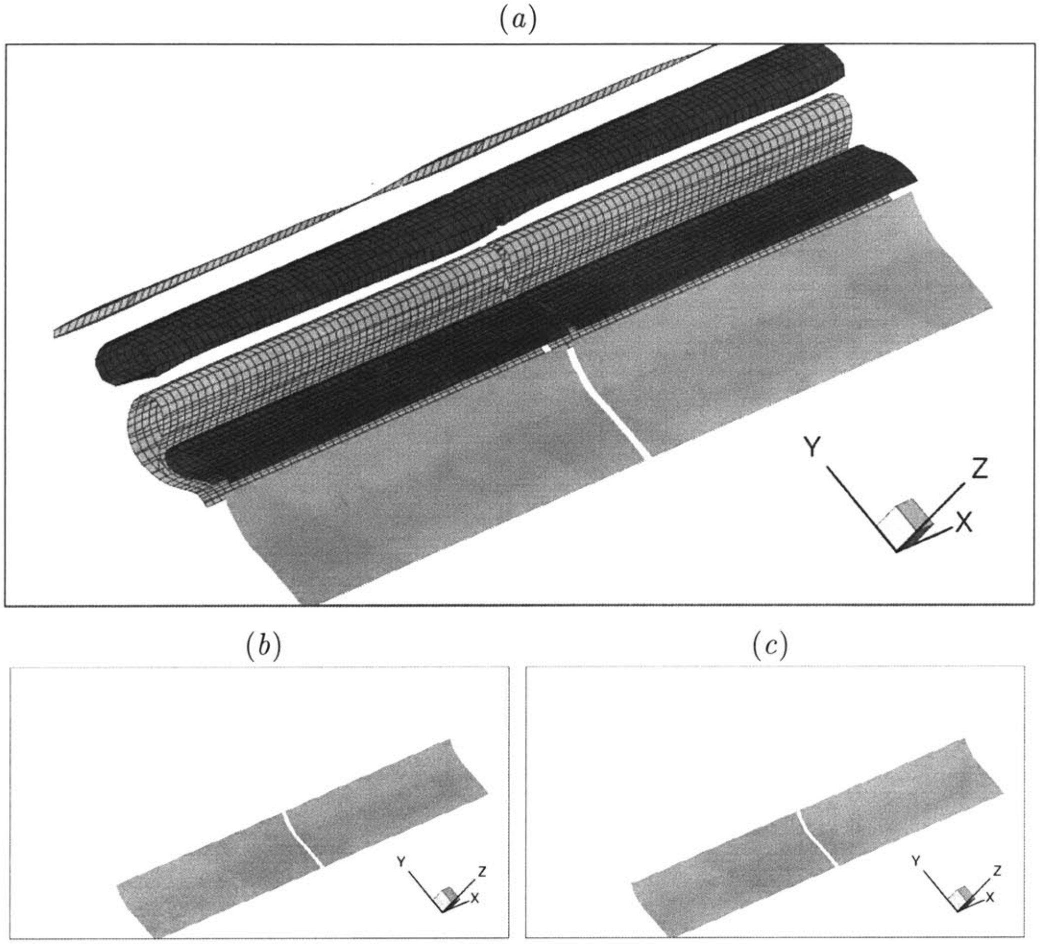

Figure 7-16: The three-dimensional vortex wake from the upstream perspective at $t = 6.7$ for the two-dimensional response of $\mu = 0.075$ and $B/L = 5$, using the mixed-mode initial displacement of equation 7.18, with the domain repeated once in the spanwise direction. The dark and light surfaces are isosurfaces for negative and positive vorticity for (a) spanwise vorticity of $\omega_x = \pm 1$, (b) sreamwise vorticity of $\omega_y = \pm 0.25$, and (c) normal vorticity of $\omega_z = \pm 0.25$.

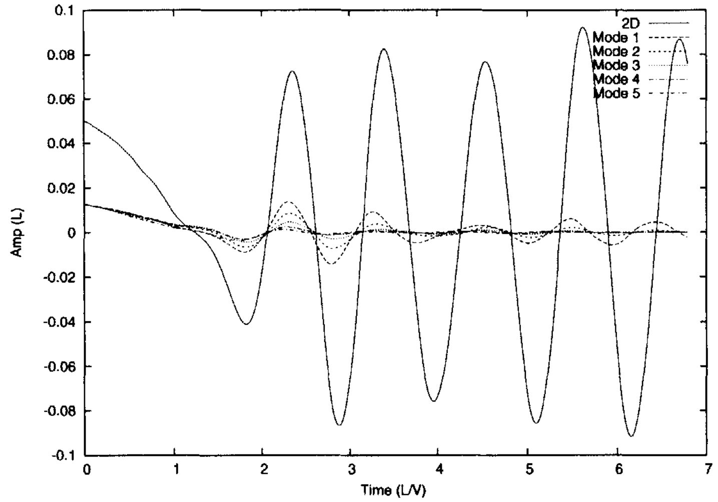

Figure 7-17: Time history of the displacement amplitude for the two-dimensional and first five sinusoidal modes which were excited by the initial condition of equation 7.18 with $B/L = 5$ and $\mu = 0.075$.

A modal decomposition of the trailing edge displacement can be used to identify the evolution of the modes which were initially excited, and the time history of the modal amplitudes are given in figure 7-17. The plot shows an initial increase in the amplitude of the two-dimensional mode, as well as for mode1 and mode2, while the higher modes are initially damped, following the trend predicted by the linear analysis. Mode1 and mode2 do not continue their growth indefinitely, instead ceding their energy to the two-dimensional mode as the simulation continues. Thus, the three-dimensional modes do not become well established.

A Second Mixed-Mode Case We now consider a second mixed-mode case, where the initial condition is not so biased to the two-dimensional mode. The initial displacement is given by

$$\begin{aligned} z(s_1, s_2)_0 = 0.125 + 0.125 &\left[sin\left(\frac{2\pi}{B}s_2\right) + sin\left(2\frac{2\pi}{B}s_2\right) \right. \\ &\left. + sin\left(3\frac{2\pi}{B}s_2\right) + sin\left(4\frac{2\pi}{B}s_2\right) + sin\left(5\frac{2\pi}{B}s_2\right) \right], \end{aligned} \quad (7.19)$$

so that all modes, including the two-dimensional mode, are initiated with the same amplitude. The vortex wake at $t = 9.8$ is given in the vorticity contour plots of figure 7-18, and show a slight increase in the spanwise variation. This can be seen most distinctly in the streamwise vorticity plot of figure 7-18(b) and the normal vorticity plot of figure 7-18(c). The indication is of greater sustained energy in the three-dimensional modes than in the run intiated with displacement of equation 7.18. The time history of the decomposed modes from the trailing edge displacement is given in figure 7-19, and again displays the initial growth of the two-dimensional mode, mode1, and mode2, while the higher modes are damped. The dominance of the two-dimensional mode is again seen, as it continues to grow while the three-dimensional modes lose energy. However, as the two-dimensional mode is initially weaker than in the case initiated with equation 7.18, it does not remove energy as quickly from mode1 and mode2, and we see some lingering spanwise variation to the strictly two-dimensional flapping.

Natural Response of the System

We have described the fundamental flapping modes for the three-dimensional system to be the spanwise standing wave mode, the spanwise travelling wave mode, and the two-dimensional mode, each with a unique vortex wake structure. The wake patterns for these three fundamental modes are depicted in the drawings of figure 7-20. The three-dimensional vortex wake for the standing and travelling wave modes are the same as found in [44] for the corresponding modes of flow induced vibration of a flexible cable. While we have shown the ability to induce these modes through the initial and ambient conditions, we are also interested in the possibility of hybrid modes, and in the tendency of the system in long-time evolution. We saw above that the system initiated with a collection of standing wave modes and a two-dimensional bias (equation 7.18) quickly obtained a primarily two-dimensional response, indicating the preference of the system for this mode. Now we consider other mixed-mode excitations to further examine the system tendency.

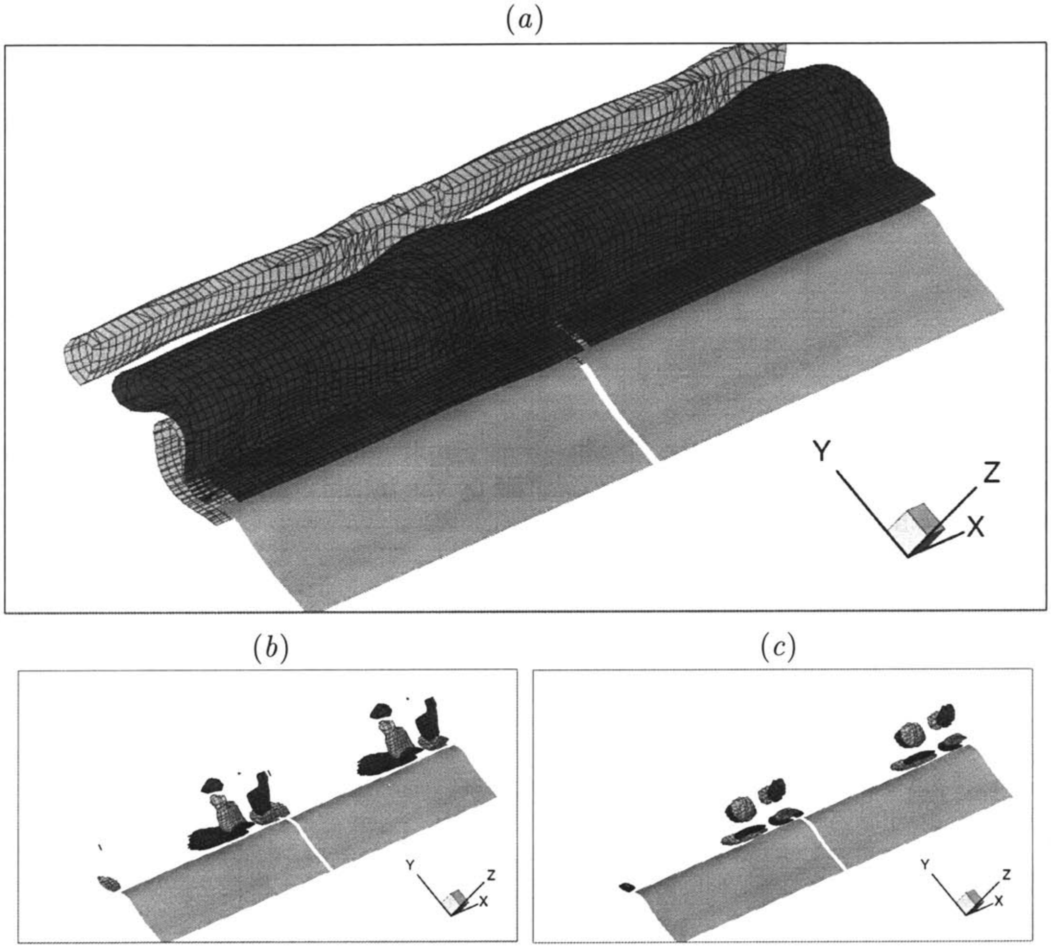

Figure 7-18: The three-dimensional vortex wake from the upstream perspective at $t = 9.8$ for the two-dimensional response of $\mu = 0.075$ and $B/L = 5$, using the mixed-mode initial displacement of equation 7.19, with the domain repeated once in the spanwise direction. The dark and light surfaces are isosurfaces for negative and positive vorticity for (*a*) spanwise vorticity of $\omega_x = \pm 1$, (*b*) sreamwise vorticity of $\omega_y = \pm 0.25$, and (*c*) normal vorticity of $\omega_z = \pm 0.25$.

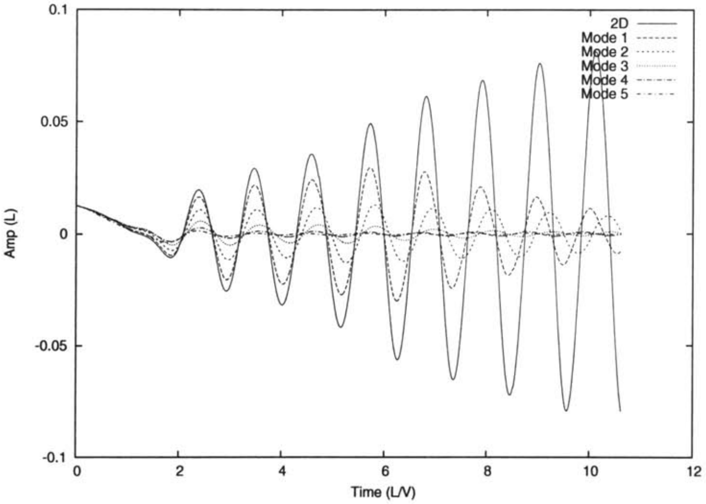

Figure 7-19: Time history of the displacement amplitude for the two-dimensional and first five sinusoidal modes which were excited by the initial condition of equation 7.19 with $B/L = 5$ and $\mu = 0.075$.

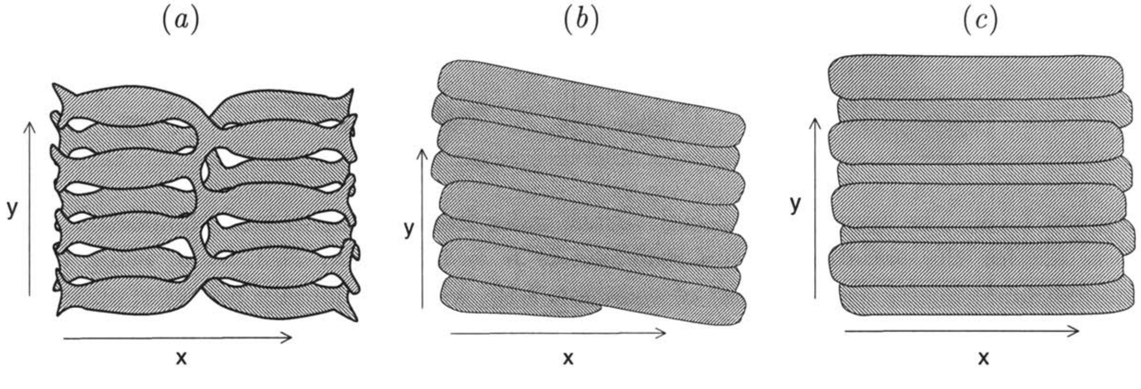

Figure 7-20: Drawing depicting the three-dimensional vortex wake pattern for the fundamental flapping modes of (*a*) spanwise standing wave, (*b*) spanwise travelling wave, and (*c*) two-dimensional flapping. The patterns should be considered to continue periodically in the spanwise x-direction.

Hybrid Travelling/Standing Wave We investigate the possibility of obtaining a travelling wave response without spanwise cross-flow by initiating a run with the body displacement of the converged travelling wave mode from the cross-flow simulation, but using no cross-flow. The flapping converges to a hybrid mode of both a travelling wave and standing wave, which can be seen in the series of shaded displacement plots given in figure 7-21. The associated vortex wake at $t = 10.5$ is plotted in figure 7-22, and shows a modulated oblique shedding pattern. The standing wave modulation to the direction of the continuous obliquely shedding vortices can be seen when comparing the vortex pattern to that of the more pure travelling wave in figure 7-13. Significant difference between the pure travelling wave and the hybrid mode can be seen in the streamwise and normal vorticity contour plots of figure 7-22(*b*) and (*c*), where elements of the standing wave wake patterns are evident. However, despite the standing wave influence to the system, the spanwise vorticity plot of figure 7-22(*a*) indicates that there is none of the vortex splitting and intersection associate with the pure standing wave mode. The result indicates a tendency of the system toward a modulated individual continuous shedding pattern.

We perform mode identification through examining a phase plot of the trailing edge displacement sine and cosine modes, given in figure 7-23. The narrow orbital path reflects the hybrid nature of the repsonse, a combination of the straight linear and circular trajectories which correspond to the standing wave and travelling wave modes.

A Second Hybrid Travelling/Standing Wave Case We again excite the hybrid mode combining a travelling and standing wave using a different initial condition. Instead of using initial displacement from a previously established travelling wave mode, we use the initial displacement given by equation 7.17, and also use an initial structural velocity corresponding to a spanwise travelling wave of nondimensional frequency $\omega = 2\pi$. As such, the spanwise directional symmetry is broken only by the initial velocity of the body. The converged vorticity field at $t = 9.8$ can be seen in the plots of figure 7-24, and closely resembles that of figure 7-22, indicating

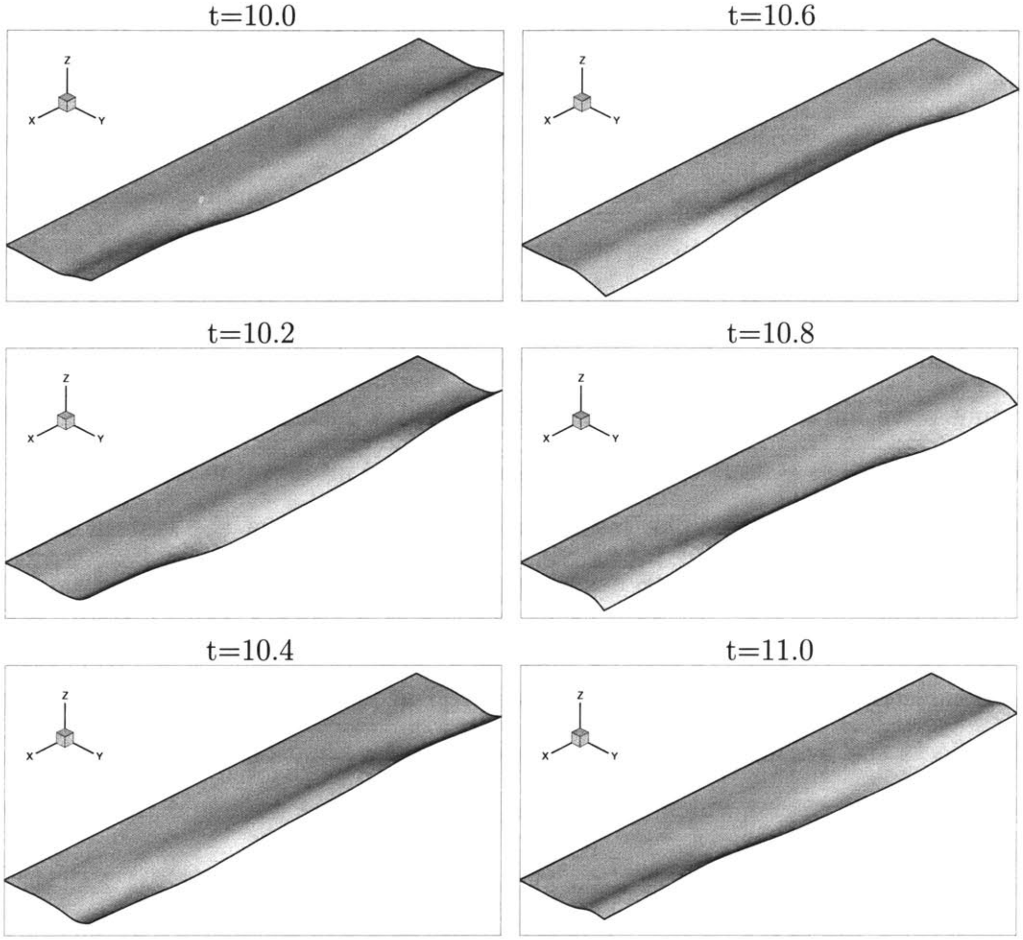

t=10.0

t=10.6

t=10.2

t=10.8

t=10.4

t=11.0

Figure 7-21: Shaded surface from downstream perspective for hybrid mode of travelling and standing wave flapping with $\mu = 0.075$, $B/L = 5$. The simulation includes no cross-flow, but breaks spanwise directional symmetry by use of a travelling wave initial displacement for the body.

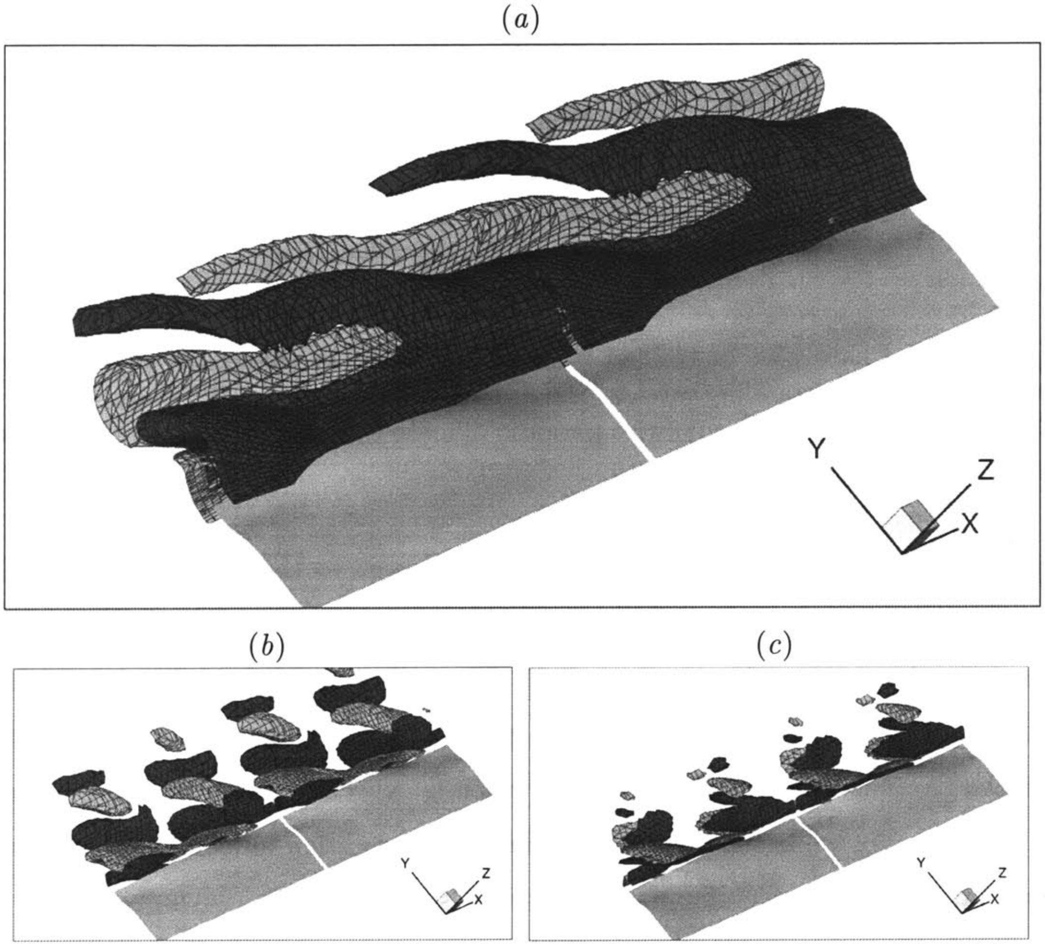

(*a*)

(*b*)

(*c*)

Figure 7-22: The three-dimensional vortex wake from the upstream perspective at $t = 10.5$ for the hybrid travelling and standing wave response of $\mu = 0.075$ and $B/L = 5$, using no spanwise cross-flow and a travelling wave initial displacement, with the domain repeated once in the spanwise direction. The dark and light surfaces are isosurfaces for negative and positive vorticity for (*a*) spanwise vorticity of $\omega_x = \pm 1$, (*b*) sreamwise vorticity of $\omega_y = \pm 0.25$, and (*c*) normal vorticity of $\omega_z = \pm 0.25$.

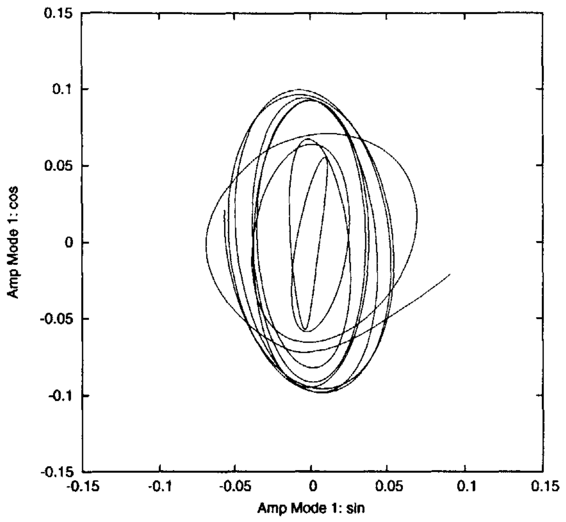

Figure 7-23: Phase plot of trailing edge displacement in sine-cosine space for the spanwise travelling/standing wave hybrid flapping mode with $\mu = 0.075$ and $B/L = 5$. FSDS-3D simulation with spanwise periodic domain initiated with a travelling wave initial displacement.

that that the two different initial conditions converge to the same flapping mode. This is confirmed by examination of the phase plot of the trailing edge displacement sine and cosine modes, given in figure 7-25. The trajectory has a similar aspect ratio to that in figure 7-23, while the rotation of the trajectory in phase space indicates that the flapping mode is phase shifted, which is expected as the initial conditions are different. So, while the difference in the initial condition influences the spanwise phase shift, the converged flapping mode is the same.

Hybrid 2D/Standing Wave The system is initiated with a mixed mode initial displacement of a spanwise standing wave and spanwise travelling wave of the same wavelength, combined with a two-dimensional bias. The flapping converges to a sustained hybrid mode combining two-dimensional and standing wave response, seen in the shaded displacement plot of figure 7-26. The vortex wake associated with this response plotted in figure 7-27 is a spanwise sinuous vortex street, a standing wave modulation to the two-dimensional wake. The strength of the standing wave modulation, as compared to that of the near-purely two-dimensional wake of figure 7-

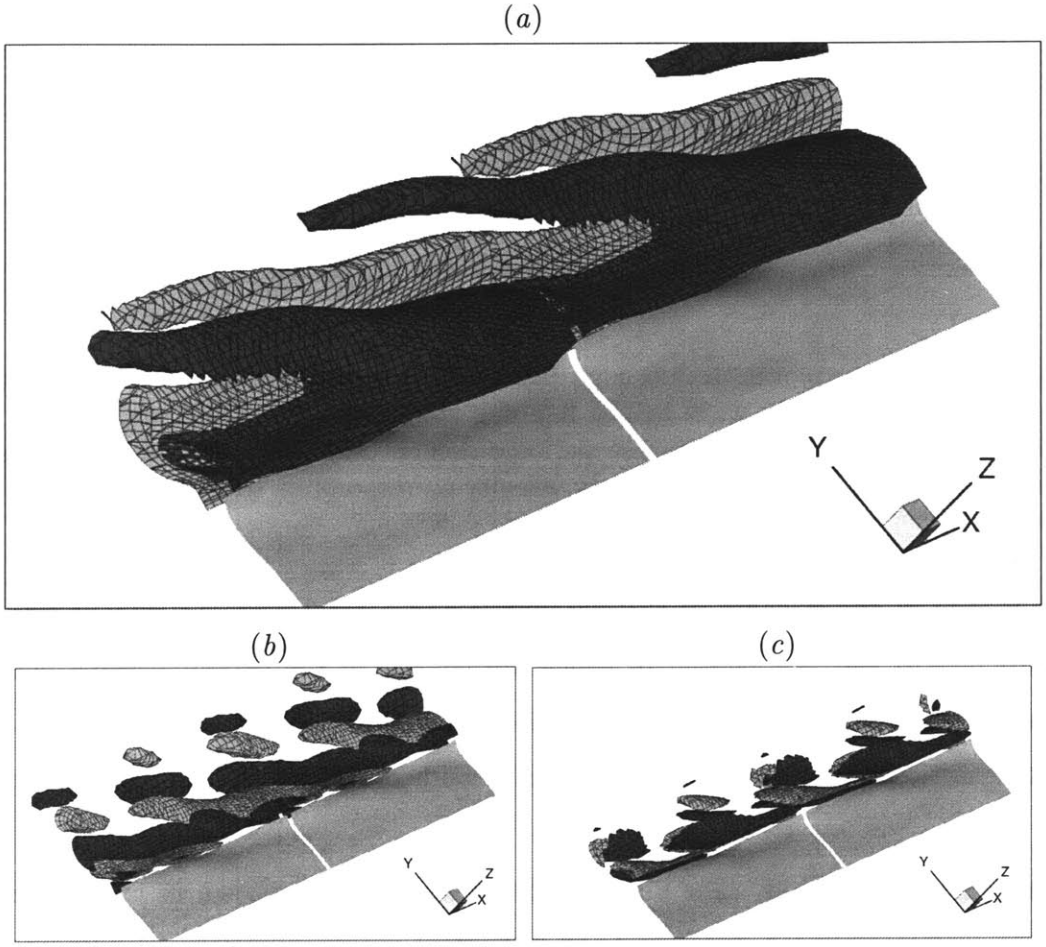

Figure 7-24: The three-dimensional vortex wake from the upstream perspective at $t = 9.8$ for the hybrid travelling and standing wave response of $\mu = 0.075$ and $B/L = 5$, using initial displacement of equation 7.17 and initial body velocity corresponding to a travelling wave of $\omega = 2\pi$, with the domain repeated once in the spanwise direction. The dark and light surfaces are isosurfaces for negative and positive vorticity for (*a*) spanwise vorticity of $\omega_x = \pm 1$, (*b*) sreamwise vorticity of $\omega_y = \pm 0.25$, and (*c*) normal vorticity of $\omega_z = \pm 0.25$.

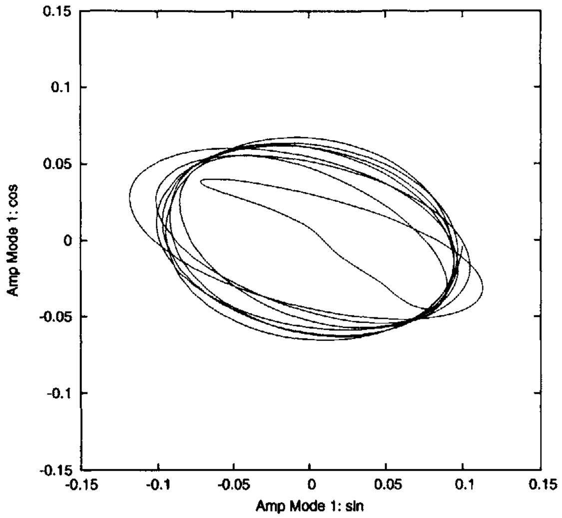

Figure 7-25: Phase plot of trailing edge displacement in sine-cosine space for the spanwise travelling/standing wave hybrid flapping mode with $\mu = 0.075$ and $B/L = 5$. FSDS-3D simulation with spanwise periodic domain initiated with initial displacement of equation 7.17 and initial body velocity corresponding to a travelling wave of $\omega = 2\pi$.

16, is seen in the strength of the streamwise and normal vorticity components of figure 7-27(b) and (c), neither of which are evident in the two-dimensional wake. Again, despite the strength of the modulation, we see no indication of vortex splitting or intersection, as the wake is dominated by a mode of individual continuous vortices.

Long-time Evolution The mixed-mode excitations have shown us the tendency of the system toward a vortex wake of individual continuous vortex structures. A similar tendency in the long time evolution was found in the vibrating cable study of [44], which tended to the travelling wave mode. We find that these structures can be modulated in direction and shape by a standing wave component, but do not display the laced pattern with vortex splitting that is associated with the pure standing wave response. There is also no indication of a hybrid mode combining a travelling wave and two-dimensional mode, which would result in the intersection of the continuous vortex patterns. The simulations suggest a preference of the system toward individual continuous vortex structures, and we thus anticipate the long-time evolved system to be dominated by either a travelling wave or a two-dimensional response. Standing

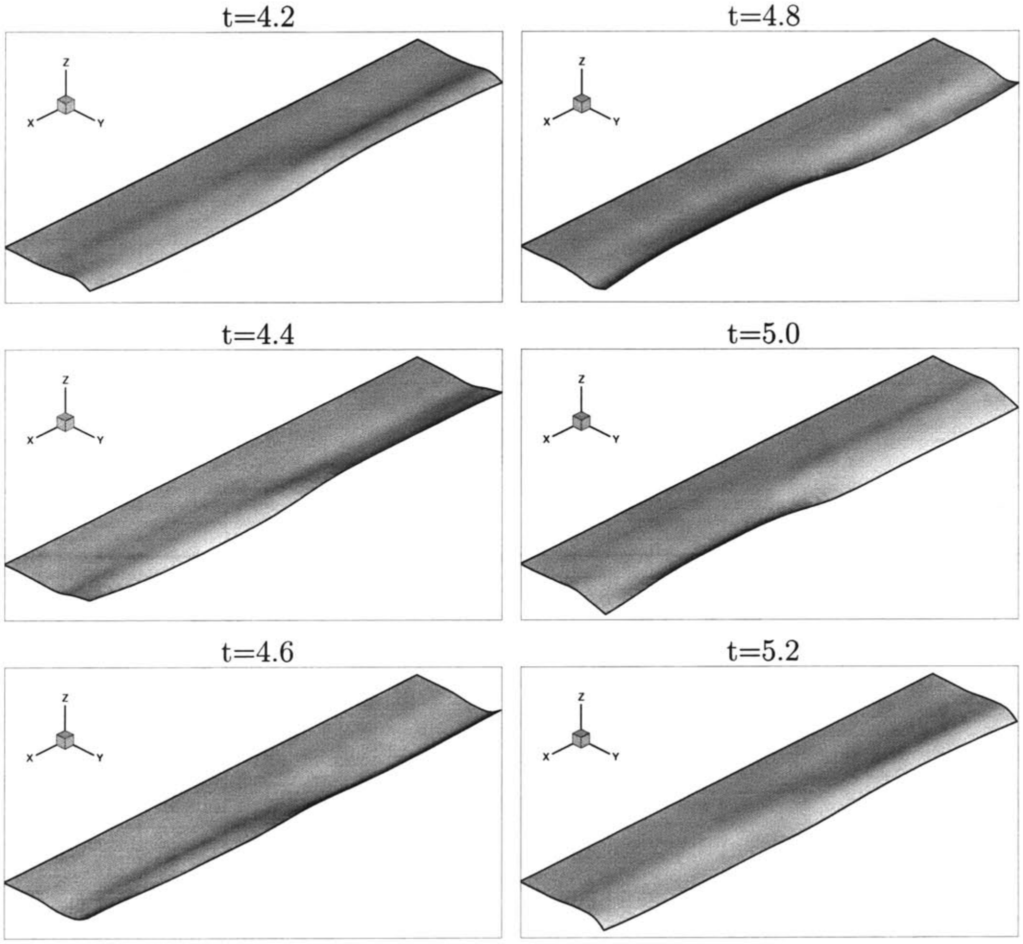
t=4.2

t=4.8

t=4.4

t=5.0

t=4.6

t=5.2

Figure 7-26: Shaded surface from downstream perspective indicating the mixed two-dimensional and standing wave response for the system initiated with the mixed mode displacement of standing wave, travelling wave, and two-dimensional bias, with $B/L = 5$ and $\mu = 0.075$.

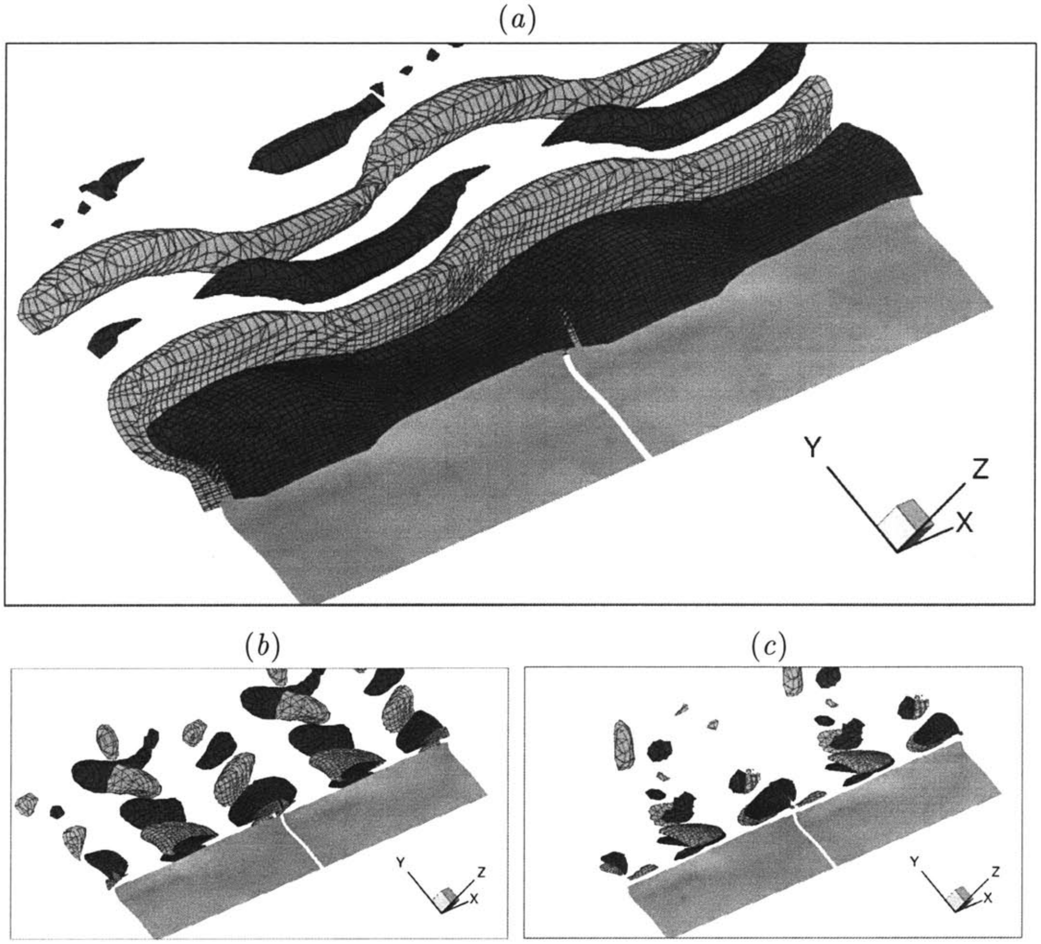

Figure 7-27: The three-dimensional vortex wake from the upstream perspective at $t = 4.7$ for the hybrid two-dimensional and standing wave response of $\mu = 0.075$ and $B/L = 5$, using mixed-mode initial displacement of standing wave, travelling wave, and two-dimensional bias, with the domain repeated once in the spanwise direction. The dark and light surfaces are isosurfaces for negative and positive vorticity for (a) spanwise vorticity of $\omega_x = \pm 1$, (b) sreamwise vorticity of $\omega_y = \pm 0.25$, and (c) normal vorticity of $\omega_z = \pm 0.25$.

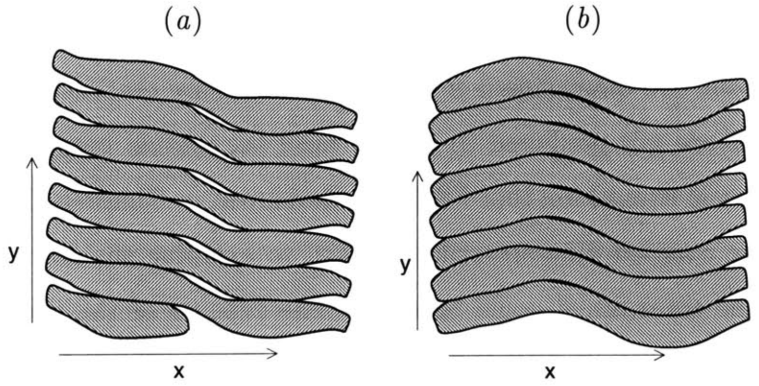

Figure 7-28: Drawing depicting the three-dimensional vortex wake pattern for the hybrid flapping modes of (*a*) travelling/standing wave, and (*b*) two-dimensional/standing wave. The patterns should be considered to continue periodically in the spanwise x-direction.

wave modulation to the response is likely dependent on the ambient conditions, and the wakes for such hybrid modes are depicted in the drawings of figure 7-28(*a*) for the travelling wave hybrid mode, and figure 7-28(*b*) for the two-dimensional hybrid mode. The present study is limited to results periodic in the domain span, so there is an artificial maximum wavelength for the travelling wave and associated minimum shedding angle. A true infinite span body would be able to take on modes covering the full spectrum of travelling wave response, but our results suggest that the system will converge to a single travelling wave or two-dimensional mode, thus avoiding an intersecting vortex pattern in the wake.

7.3 Summary of the Three-dimensional Flapping Problem

The problem of the passive flapping of a thin flexible foil, which was studied in detail in two-dimensions in Chapter 6, has been reformulated in three-dimensions, now including variation in the spanwise direction. The linear analysis of the problem indicates the importance of this spanwise variation, as stability is found to be a function of the spanwise wavenumber. With stability increasing with wavenumber, the theory converges to the two-dimensional theory as the wavenumber goes to zero. We thus have that the two-dimensional or span-wide modes are the least stable, and high spanwise modes are not predicted to appear until the system becomes quite unstable. The numerical simulation tool FSDS-3D developed in Chapters 3 and 4, is used to calculate the coupled fluid-structural system to examine the stability and characteristics of the three-dimensional flapping. The expense of the three-dimensional calculations limits the number of runs possible, but a targeted set of runs confirms the trend of the linear stability prediction of equation 7.16. Investigation of the modes of the flapping response indicates the three fundamental flapping modes of spanwise standing wave, spanwise travelling wave, and two-dimensional flapping, all displaying the streamwise travelling wave of increasing amplitude from leading to trailing edge. While the wake of the spanwise standing wave mode consists of two layers of laced cellular vortices, the spanwise travelling wave wake consists of continuous individual vortices shedding at an oblique angle, and the two-dimensional wake consists of continuous individual parallel shedding vortices. Mixed-mode excitation reveals hybrid modes of standing wave modulation to the continuous individual shedding vortices of the travelling wave and two-dimensional mode. The tendency of the system is found toward continuous individual vortex structures without splitting or intersection, so that the pure standing wave mode is not expected in an evolved system.

Chapter 8

Conclusions

In the following discussion, we consider the contribution of the newly developed FSDS simulation tool, and summarize the findings of the study of the passive flapping of a thin flexible foil. The findings include the predictions of the linear analyses performed and characterization of the flapping physics from simulation at $Re \sim O(10^3)$, for both the two-dimensional and three-dimensional problems. We conclude with a section discussing the direction for future work in studying the flapping problem with the FSDS capability.

8.1 Contribution of the FSDS

The fluid-structure direct simulation (FSDS) tool developed for this study is capable of accurately calculating the viscous flow about a flexible thin body, the dynamics of the fluid-structure interaction, and the nonlinear body motion. Two versions of the coupled solver are derived, one for two-dimensional simulations, and one for three-dimensional simulations using spanwise periodicity. Verification and validation are performed for each the fluid and structural solver individually, as well as for the coupled solver in both two and three dimensions.

The fluid-dynamic direct simulation (FDS) is developed to simulate viscous flow around thin bodies of arbitrary orientation or configuration with a computational grid fixed at the body boundary. The solver is able to accommodate motion of the flexible body, while maintaining grid clustering for simulation accuracy at the boundary, particularly around the sharp leading and trailing edges. The solver is developed for both two-dimensional and three-dimensional simulations. Parallel processing is implemented through domain decomposition in one direction for the two-dimensional solver, and in two directions for the three-dimensional solver, allowing fast wall-clock calculation using hundreds of processors. Verification and validation of the FDS solver is performed using several problems involving both cylinders and thin foils. Convergence testing confirms near second-order convergence of the solution with both temporal and spatial discretization.

The structural direct simulation (SDS) is derived as a geometrically nonlinear thin-body solver using Hamilton's Principle. With no linearization around an equilibrium position, the solver allows arbitrary orientation and configuration of the body. Two versions of SDS are developed, for the simulation of two-dimensional and three-dimensional bodies, linearized around small body thickness and small extensional strain. Verification and validation of the structural solver is performed primarily using problems of a hanging/swinging body under the influence of gravity. Comparison to an analytical linear solution and nonlinear experiments and other simulations indicate the capability of the tool for accurately simulating a range of problems. Near second-order convergence is found for the simulation result with both temporal and spatial discretization.

The coupling between the fluid and structural solvers in the FSDS capability is achieved through use of the body surface fluid-dynamic forcing in the SDS, and use of the solved body motion for the boundary position and velocity in the FDS. Stability of the coupled implementation is achieved through an implicit iterative procedure which alternates solution of the fluid and structure until convergence to tolerance. This iterative method also permits use of an assumed added mass in the structural solver, allowing stable solution of the system with very low structural masses. Verification of the coupled FSDS for both two-dimensional and three-dimensional problems is made through displaying energy conservation as the thin structure responds to an impulsively started uniform flow, experiencing considerable exchange of energy between the fluid and structural domains.

8.2 Summary of Findings

The system of the passive flapping of a flexible thin foil in a uniform stream is considered as a fundamental fluid-structure interaction problem with direct implications to engineering and industrial applications. On one level, this is the consideration of the elusive physics of the flag flapping problem, but extends to manufacture and handling of textiles and paper, as well as the engineering of flexible foils for vehicle applications. Recent advances in computational capability positions us to be able to develop and utilize our FSDS simulation tool to understand the key physical mechanisms associated with the passive flapping problem. The study is approached by first considering the two-dimensional canonical problem of a passive thin flexible foil in a uniform stream, and then extending the understanding by including three-dimensional effects.

After clearly defining the two-dimensional canonical problem, we set about pursuing a linear analysis to indicate the relevant physical mechanisms and associated nondimensional parameters, and their influence to the system stability. For our problem, where the body is very thin and essentially inextensible, we have three relevant nondimensional parameters for the system. These are mass ratio, $\mu = \rho_s h/(\rho_f L)$; the Reynolds number, $Re = UL/\nu$; and the bending rigidity, $K_B = EI/(\rho_f U^2 L^3)$. The linear analysis predicts a stabilizing influence of lower mass ratio, lower Reynolds number, and higher bending rigidity. We consider the case of vanishing bending rigidity, where the restoring force is dominated by the flow-induced tension, to represent the "flag flapping" problem. A systematic series of simulations at $Re \sim O(10^3)$ for the two-dimensional problem are pursued, varying the relevant nondimensional parameters. Initiating the simulations with the body at a slight angle of attack to the impulsively started flow, the progression of the solution toward sustained flapping or a steady-straight configuration indicates the stability of a given run. We find that the trend of the linear analysis is confirmed, giving a prediction for the critical mass ratio as

$$\mu_{crit} = 1.3Re^{-1/2} + K_B 4\pi^2, \tag{8.1}$$

above which the system will experience sustained flapping.

Studying the range of simulation data for the two-dimensional problem reveals three distinct regimes of response. These are, in order of decreasing stability, (I) fixed-point stability, (II) limit-cycle flapping, and (III) chaotic flapping. The phenomenon of hysteresis in the transition from stability to limit-cycle flapping is found to operate as a Duffing oscillator of a nonlinear spring, and therefore is more prevalent for systems with higher initial flapping amplitudes. The limit-cycle flapping is a periodic response of the system with an associated periodic von Karman vortex street wake, while the chaotic flapping is a non-repeating response with an irregular vortex wake. The body motion of both flapping modes consists of a travelling wave of increasing amplitude from leading edge to trailing edge. Examining the trends of flapping frequency, amplitude, and Lyapunov exponent, indicates that as the Strouhal number, $St = f2A/V$, reaches the natural wake Strouhal number of $St \simeq 0.2$, the system transitions to chaos. We find that the chaotic transition occurs at a mass ratio proportional to the critical stability mass ratio, and the expression

$$\mu_{chaos} = 2.5\mu_{crit} = 3.25Re^{-1/2} + K_B 10\pi^2 \tag{8.2}$$

is a good fit to the transition mass ratio above which the flapping will be chaotic. There is no indication of period doubling in the transition to chaos, as the vortex wake associated with the period-doubled system is not a natural wake mode. The downstream wake frequency spectra are found to match well the corresponding spectra of the trailing edge displacement, indicating the direct relationship between the body motion and the wake flow.

Study of the dynamics of the fluid-structure interaction of the system through the series of two-dimensional simulations indicates trends in the energy budget and fluid-dynamic forcing with the relevant system parameters. Examining the forcing coefficients in the flapping regimes, we consider the following expressions as an estimate to the fluid-dynamic forcing on the body,

$$< Cd > \simeq 2.7Re^{-1/2} + 0.8(\mu - 1.3Re^{-1/2} - K_B 4\pi^2) \tag{8.3}$$

$$Cd_{rms} \simeq 1.5(\mu - 1.3Re^{-1/2} - K_B 4\pi^2)^{1.5} \tag{8.4}$$

$$Cl_{rms} \simeq 1.5(\mu - 1.3Re^{-1/2} - K_B 4\pi^2). \tag{8.5}$$

Well into the chaotic regime, we begin to observe snapping events, characterized by spikes in the instantaneous drag force followed by a rapid reduction in drag, sometimes to negative drag values, with associated dynamic buckling of the body. We study the physics of such events, and reveal the strong vortex structures distributed far from the wake centerline, along with the high wavenumber modes which appear when the tension in the body becomes negative. This study of the wide range of responses of the two-dimensional flapping body, along with the associated physical analyses, is the first such comprehensive study of the passive flapping problem, contributing significant new understanding.

The three-dimensional study again clearly frames the extended canonical problem, before working through a linear analysis which now includes a spanwise variation. The prediction of the linear analysis is for increased stability of the system with increasing spanwise wavenumber, indicating that the two-dimensional mode is the least stable. Investigating the stability through the spanwise periodic simulations of FSDS-3D at $Re = 1000$, we initiate the runs exciting isolated spanwise standing wave modes. The stability trends predicted by the linear analysis are corroborated by the simulation results. Studying the modal response of the three-dimensional system, we reveal three fundamental modes of response, the spanwise standing wave, the spanwise travelling wave, and two-dimensional flapping. All three modes display the travelling wave of increasing amplitude in the streamwise direction found in the two-dimensional study, but have different variation in the spanwise direction. The vortex wake of the spanwise standing wave is a pattern of alternating sign in both the streamwise and spanwise direction. The cellular vortices are laced together at the nodes in the wake, making two-layers of oppositely signed laced cellular vortices. The net motion of the spanwise travelling wave mode is one of a wave travelling along the body at an oblique angle. The associated vortex wake is one of obliquely shedding continuous vortices. The two-dimensional mode does not vary in the spanwise direction, thus displaying the von Karman vortex street of parallel shedding continuous vortices. Mixed-mode investigation is performed to understand the tendency of the system in long-time evolution. This reveals that the system trends away from modes of intersecting or cellular vortices, toward the modes of continuous vortices. We do reveal hybrid modes, where the continuous modes of the travelling wave or two-dimensional response are modulated by standing wave behavior, but do not expect intersecting vortices in the evolved response. This three-dimensional study indicates the limit to the spanwise wavenumber response which can be expected for a given set of parameters, while also indicating the physics and tendencies of the different three-dimensional response modes.

8.3 Direction for Future Work

The two-dimensional and three-dimensional FSDS represent tools suitable for studying the physics of problems involving thin flexible foils. While the two-dimensional component of the present study was quite comprehensive, there is much which can still be considered for the three-dimensional passive flapping problem. Our three-dimensional study was contained within a very narrow parameter range, and does not provide a full picture of how the flapping characteristics are likely to change outside this parameter range. The understanding of evolution of the three-dimensional system would be served by simulations which cover a larger span, combination of more spanwise modes, and carried out over a longer simulation time. The present study did not characterize chaotic flapping of the three-dimensional system, and such a pursuit would indicate the three-dimensional influence on the chaotic response studied in the two-dimensional investigation. The entire understanding of the two-dimensional and three-dimensional passive flapping problem derived from the present study would be complemented by an experimental investigation which sought to examine the flapping behavior and flow characteristics through the range of parameters and responses considered.

The present study concentrated on the passive flapping of a flexible foil, and we consider one of the benefits of the enhanced understanding to be better positioning for the engineering of driven flexible foils. The prevalence of driven flexible foils for propulsion and maneuvering in nature suggest their superiority over rigid foils. The FSDS tool could be very useful for the study of how the structural parameters of a flexible foil can affect its capability and efficiency. This can be applied for surfaces designed both for periodic propulsion and for non-periodic maneuvering, as well as combinations of the two. While the simulations can indicate performance by measuring dynamic quantities of forcing and energy input, they also indicate the associated physics of the fluid-structure interaction, a key element for engineering exploitation of the problem.

Bibliography

[1] J. J. Allen and A. J. Smits. Energy harvesting eel. *Journal of Fluids and Structures*, 15:629–640, 2001.

[2] J. M. Anderson. *Vorticity control for efficient propulsion.* PhD thesis, Massachusetts Institute of Technology, Cambridge, MA, 1996.

[3] J. M. Anderson, K. Streitlien, D. S. Barrett, and M. S. Triantafyllou. Oscillating foils of high propulsive efficiency. *Journal of Fluid Mechanics*, 360:41–72, 1998.

[4] M. Argentina and L. Mahadevan. Fluid-flow-induced flutter of a flag. *PNAS*, 102:1829–1834, 2005.

[5] D. S. Barrett, M. S. Triantafyllou, D. K. P. Yue, M. A. Grosenbaughand, and M. J. Wolfgang. Drag reduction in fish-like locomotion. *Journal of Fluid Mechanics*, 392:183–212, 1999.

[6] D. N. Beal. *Propulsion through wake synchronization using a flapping foil.* PhD thesis, Massachusetts Institute of Technology, Cambridge, MA, 2003.

[7] P. W. Bearman. Vortex shedding from oscillating bluff bodies. *Annual Review of Fluid Mechanics*, 16:195–222, 1984.

[8] A. Belmonte, M. J. Shelley, S. T. Eldakar, and C. H. Wiggins. Dynamic patterns and self-knotting of a driven hanging chain. *Physical Review Letters*, 87(11):114301, 2001.

[9] H. M. Blackburn, R. N. Govardhan, and C. H. K. Williamson. A complementary numerical and physical investigation of vortex-induced vibration. *Journal of Fluids and Structures*, 15:481–488, 2001.

[10] Robert D. Blevins. *Flow-Induced Vibration.* Van Nostrand Reinhold, New York, 1990.

[11] D. Brika and A. Laneville. Vortex-induced vibrations of a long flexible circular cylinder. *Journal of Fluid Mechanics*, 250:481–508, 1993.

[12] Paul K. Chang. *Control of Flow Separation.* Hemisphere, Washington, 1976.

[13] R. Coene. Flutter of slender bodies under axial stress. *Applied Scientific Research*, 49:175–187, 1992.

[14] M. H. Dickinson and K. G. Gotz. Unsteady aerodynamic performance of model wings at low reynolds numbers. *Journal of Experimental Biology*, 174:45–64, 1993.

[15] D. G. Dommermuth. The formation of u-shaped vortices on vortex tubes impinging on a wall with application to free surfaces. *Physics of Fluids A*, 4(4):757–769, 1992.

[16] D. G. Dommermuth. The laminar interactions of a pair of vortex tubes with a free surface. *Journal of Fluid Mechanics*, 246:91–115, 1993.

[17] P. G. Drazin. *Nonlinear Systems*, chapter 7. Cambridge University Press, New York, 1992.

[18] H. Dutsch, F. Durst, S. Becker, and H. Lienhart. Low-reynolds-number flow around an oscillating circular cylinder at low keulegan-carpenter numbers. *Journal of Fluid Mechanics*, 360:249–271, 1998.

[19] C. Evangelinos, D. Lucor, and G. E. Karniadakis. Dns-derived force distributions on flexible cylinders subject to vortex-induced vibration. *Journal of Fluids and Structures*, 14:429–440, 2000.

[20] D. J. J. Farnell, T. David, and D. C. Barton. Coupled states of flapping flags. *Journal of Fluids and Structures*, 19:29–36, 2004.

[21] D. J. J. Farnell, T. David, and D. C. Barton. Numerical simulations of a filament in a flowing soap film. *Int. J. Numer. Meth. Fluids*, 44:313–330, 2004.

[22] J. I. Gobat, M. A. Grosenbaugh, and M. S. Triantafyllou. Generalized-α time integration solutions for hanging chain dynamics. *Journal of Engineering Mechanics*, 128(6):677–687, 2002.

[23] R. Gopalkrishnan, M. S. Triantafyllou, G. S. Triantafyllou, and D. Barrett. Active vorticity control in a shear flow using a flapping foil. *Journal of Fluid Mechanics*, 274:1–21, 1994.

[24] J. Gray. Studies in animal locomotion i. the movement of fish with special reference to the eel. *Journal of Experimental Biology*, 10:88–104, 1933.

[25] J. Gray. Studies in animal locomotion vi. the propulsive powers of the dolphin. *Journal of Experimental Biology*, 13:192–199, 1936.

[26] L. Guglielmini and P. Blondeaux. Propulsive efficiency of oscillating foils. *European Journal of Mechanics B/Fluids*, 23:255–278, 2004.

[27] E. Guilmineau and P. Queutey. A numerical simulation of vortex shedding from an oscillation circular cylinder. *Journal of Fluids and Structures*, 16(6):773–794, 2002.

[28] F. S. Hover, A. H. Techet, and M. S. Triantafyllou. Forces on oscillating uniform and tapered cylinders in crossflow. *Journal of Fluid Mechanics*, 363:97–114, 1998.

[29] C. T. Howell and M. S. Triantafyllou. Stable and unstable nonlinear resonant response of hanging chains: theory and experiment. *Proceedings of the Royal Society of London, Series A*, 440:345-364, 1993.

[30] R. M. Kirby and Z. Yosibash. Solution of von-karman dynamic non-linear plate equations using a pseudo-spectral method. *Computational Methods in Applied Mechanics and Engineering*, 193:575–599, 2004.

[31] C. G. Koh, Y. Zhang, and S. T. Quek. Low-tension cable dynamics: numerical and experimental studies. *Journal of Engineering Mechanics*, 125(3):347–354, 1999.

[32] M. M. Koochesfahani. Vortical patterns in the wake of an oscillating airfoil. *AIAA Journal*, 27(9):1200–1205, 1989.

[33] G. H. Koopmann. The vortex wakes of vibrating cylinders at low reynolds numbers. *Journal of Fluid Mechanics*, 28(3):501–512, 1967.

[34] P. Koumoutsakos. Active control of vortex-wall interactions. *Physics of Fluids*, 9(12):3808–3816, 1997.

[35] P.J. Kunz and I. Kroo. Analysis and design of airfoils for use at ultra-low reynolds numbers. In T. J. Mueller, editor, *Fixed and Flapping Wing Aerodynamics for Micro Air Vehicle Applications*, pages 35–60, Reston, VA, 2001. AIAA.

[36] T. Leweke, P. W. Bearman, and C. H. K. Williamson. Preface. *Journal of Fluids and Structures*, 15:377–378, 2001.

[37] M. J. Lighthill. Note on the swimming of slender fish. *Journal of Fluid Mechanics*, 9:305–317, 1960.

[38] M. J. Lighthill. Hydromechanics of aquatic animal propulsion. *Annual Reveiw of Fluid Mechanics*, 1:413–446, 1969.

[39] H. Liu, R. Wassersug, and K. Kawachi. The three-dimensional hydrodynamics of tadpole locomotion. *Journal of Experimental Biology*, 200:2807–2819, 1997.

[40] H. Liu, R. J. Wassersug, and K. Kawachi. A computational fluid dynamics study of tadpole swimming. *Journal of Experimental Biology*, 199:1245–1260, 1996.

[41] D. Lucor, L. Imas, and G. E. Karniadakis. Vortex dislocations and force distribution of long and flexible cylinders subjected to sheared flows. *Journal of Fluids and Structures*, 15:641–650, 2001.

[42] M. J. McHenry, C. A. Pell, and J. H. Long Jr. Mechanical control of swimming speed: stiffness and axial wave form in undulating fish models. *Journal of Experimental Biology*, 198:2293–2305, 1995.

[43] K. McLetchie. Drag reduction of an elastic fish model. BS thesis, Massachusetts Institute of Technology, Cambridge, MA, 2002.

[44] D. J. Newman and G. E. Karniadakis. A direct numerical simulation study of flow past a freely vibrating cable. *Journal of Fluid Mechanics*, 344:95–136, 1997.

[45] C. L. Olson and M. G. Olsson. Dynamical symmetry breaking and chaos in duffing's equation. *Am. J. Phys.*, 59:907–911, 1991.

[46] P. Orlandi. Vortex dipole rebound from a wall. *Physics of Fluids A*, 2(8):1429–1436, 1990.

[47] M. P. Paidoussis. Dynamics of flexible cylinders in axial flow. *Journal of Fluid Mechanics*, 26:717–751, 1966.

[48] I. Procaccia. Universal properties of dynamically complex systems: the organization of chaos. *Nature*, 333:618–623, 1988.

[49] R. Ramamurti and W. Sandberg. Simulation of flow about flapping airfoils using finite element incompressible flow solver. *AIAA Journal*, 39(2):253–260, 2001.

[50] D. A. Read. Oscillating foils for propulsion and maneuvering of ships and underwater vehicles. MS thesis, Massachusetts Institute of Technology, Cambridge, MA, 2001.

[51] D. Rockwell. Vortex-body interactions. *Annual Review of Fluid Mechanics*, 30:199–229, 1998.

[52] T. Sarpkaya. Vortex-induced oscillations. *Journal of Applied Mechanics*, 46:241–258, 1979.

[53] Irving H. Shames and Clive L. Dym. *Energy and Finite Element Methods in Structural Mechanics.* Hemisphere, New York, 1985.

[54] M. Shelley, N. Vandenberghe, and J. Zhang. Heavy flags undergo spontaneous oscillations in flowing water. *Phys. Rev. Let.*, 94:094302–1–4, 2005.

[55] L. Shen, X. Zhang, D. K. P. Yue, and M. S. Triantafyllou. Turbulent flow over a flexible wall undergoing a streamwise travelling wave motion. *Journal of Fluid Mechanics*, 484:197–221, 2003.

[56] S. Taneda and Y. Tomonari. An experiment on the flow around a waving plate. *Journal of the Physical Society of Japan*, 36(6):1683–1689, 1974.

[57] G. I. Taylor. Analysis of the swimming of long and narrow animals. *Proceedings of the Royal Society of London, A*, 214:158–183, 1952.

[58] Steve Taylor. Project details: Nonlinear elastic structures. *www.math.auckland.ac.nz/ taylor/preprints/NonlinearStruc.pdf.*

[59] A. H. Techet. *Experimental visualization of the near-boundary hydrodynamics about fish-like swimming bodies.* PhD thesis, Massachusetts Institute of Technology, Cambridge, MA, 2001.

[60] A. H. Techet, F. S. Hover, and M. S. Triantafyllou. Vortical patterns behine a tapered cylinder oscillating transversely to a uniform flow. *Journal of Fluid Mechanics*, 363:79–96, 1998.

[61] J. F. Thompson, F. C. Thames, and C. W. Mastin. Tomcat - a code for numerical generation of boundary-fitted curvilear coordinate systems on fields containing any number of arbitrary two-dimensional bodies. *Journal of Computational Physics*, 24:274–302, 1977.

[62] P. T. Tokumaru and P. E. Dimotakis. Rotary control of a cylinder wake. *Journal of Fluid Mechanics*, 224:77–90, 1991.

[63] G. S. Triantafyllou. Physical condition for absolute instability in inviscid hydroelstic coupling. *Phys. Fluids*, 4:544–552, 1992.

[64] G. S. Triantafyllou, M. S. Triantafyllou, and M. A. Grosenbaugh. Optimal thrust development in oscillating foils with application to fish propulsion. *Journal of Fluids and Structures*, 7:205–224, 1993.

[65] M. S. Triantafyllou, G. S. Triantafyllou, and R. Gopalkrishnan. Wake mechanics for thrust generation in oscillating foils. *Physics of Fluids A*, 3(12):2835–2837, 1991.

[66] M. S. Triantafyllou, G. S. Triantafyllou, and D. K. P. Yue. Hydrodynamics of fishlike swimming. *Annual Reveiw of Fluid Mechanics*, 32:33–53, 2000.

[67] W. T. Tsai and D. K. P. Yue. Effects of soluble and insoluble surfactant on laminar interactions of vortical flows with a free surface. *Journal of Fluid Mechanics*, 289:315–349, 1995.

[68] B. Uzunoglu, M. Tan, and W. G. Price. Low-reynolds-number flow around an oscillating circular cylinder using a cell viscous boundary element method. *International Journal for Numerical Methods in Engineering*, 50:2317–2338, 2001.

[69] Z. J. Wang. Vortex shedding and frequency selection in flapping flight. *Journal of Fluid Mechanics*, 410:323–341, 2000.

[70] Y. Watanabe, S. Suzuki, M. Sugihara, and Y. Sueoka. An experimental study of paper flutter. *Journal of Fluids and Structures*, 16(4):529–542, 2002.

[71] C. H. K. Williamson and R. Govardhan. Vortex-induced vibrations. *Annu. Rev. Fluid Mech.*, 36:413–455, 2004.

[72] C. H. K. Williamson and A. Roshko. Vortex formation in the wake of an oscillating cylinder. *J. Fluids Struct.*, 2:355–381, 1988.

[73] A. Wolf, J. B. Swift, H. L. Swinney, and J. A. Vastano. Determining lyanpunov exponents from a time series. *Physica D*, 16:285–317, 1985.

[74] M. J. Wolfgang, J. M. Anderson, M. A. Grosenbaugh, D. K. P. Yue, and M.S. Triantafyllou. Near-body flow dynamics in swimming fish. *Journal of Experimental Biology*, 202:2303–2327, 1999.

[75] T. Y. Wu. Swimming of a waving plate. *Journal of Fluid Mechanics*, 10:321–344, 1961.

[76] J. Zhang, S. Childress, A. Libchaber, and M. Shelley. Flexible filaments in a flowing soap film as a model for one-dimensional flags in a two-dimensional wind. *Nature*, 408:835–839, 2000.

[77] Xiang Zhang. *I Surfactant effects on the interaction of a three dimensional vortex pair with a free surface; and II. Turbulent flow over a flexible body undergoing fish-like swimming motion.* PhD thesis, Massachusetts Institute of Technology, Cambridge, MA, 2001.

[78] C. Y. Zhou and J. M. R. Graham. A numerical study of cylinders in waves and currents. *Journal of Fluids and Structures*, 14:403-428, 2000.

[79] L. Zhu and C. S. Peskin. Simulation of flapping flexible filament in a flowing soap film by the immersed boundary method. *Journal of Computational Physics*, 179:452–468, 2002.

[80] L. Zhu and C. S. Peskin. Interaction of two flapping filaments in a flowing soap film. *Physics of Fluids*, 15:1954–1960, 2003.

[81] Q. Zhu, Y. Liu, A. A. Tjavaras, M. S. Triantafyllou, and D. K. P. Yue. Mechanics of nonlinear short-wave generation by a moored near-surface buoy. *J. Fluid Mech.*, 381:305–335, 1999.

[82] Q. Zhu, M. J. Wolfgang, D. K. P. Yue, and M. S. Triantafyllou. Three-dimensional flow structures and vorticity control in fish-like swimming. *Journal of Fluid Mechanics*, 468:1–28, 2002.